

*Edited by*  
*H. Alicia Kim and Robert A. Guyer*

**Nonlinear Elasticity and Hysteresis**

## *Related Titles*

Murray, E.J., Sivakumar, V., Murray, E.J.

### **Unsaturated Soils - A Fundamental Interpretation of Soil Behaviour**

2010

Print ISBN: 978-1-444-33212-4

Sailor, M.J.

### **Porous Silicon in Practice Preparation, Characterization and Applications**

2012

Print ISBN: 978-3-527-31378-5; also available in digital formats

Öchsner, A., Murch, G.E., de Lemos, M.J. (eds.)

### **Cellular and Porous Materials Thermal Properties Simulation and Prediction**

2008

Print ISBN: 978-3-527-31938-1

Zhao, D., Wan, Y., Zhou, W.

### **Ordered Mesoporous Materials**

2012

Print ISBN: 978-3-527-32635-8; also available in digital formats

Su, B., Sanchez, C., Yang, X. (eds.)

### **Hierarchically Structured Porous Materials From Nanoscience to Catalysis, Separation, Optics, Energy, and Life Science**

2012

Print ISBN: 978-3-527-32788-1; also available in digital formats

Guyer, R.A., Johnson, P.A.

### **Nonlinear Mesoscopic Elasticity The Complex Behaviour of Granular Media including Rocks and Soil**

2009

Print ISBN: 978-3-527-40703-3

*Edited by H. Alicia Kim and Robert A. Guyer*

## **Nonlinear Elasticity and Hysteresis**

Fluid-Solid Coupling in Porous Media

**WILEY-VCH**  
Verlag GmbH & Co. KGaA

## Editors

**Dr. H. Alicia Kim**  
University of Bath  
Dept. of Mech. Engineering  
BA2 7AY Bath  
United Kingdom

**Robert A. Guyer**  
Los Alamos National Laboratory  
Los Alamos  
NM 87545  
USA  
  
and  
  
University of Nevada  
Department of Physics  
1664 N. Virginia Street  
Reno  
NV 89557-0220  
USA

## Cover

The image was kindly supplied by  
Schreiber N., Gierlinger N., Putz N.,  
Fratzl P., Neinhuis C., Burgert I.  
(2010) *The Plant Journal*. **61**:854–861.  
Copyright by Blackwell Publishing Ltd.

■ All books published by **Wiley-VCH** are carefully produced. Nevertheless, authors, editors, and publisher do not warrant the information contained in these books, including this book, to be free of errors. Readers are advised to keep in mind that statements, data, illustrations, procedural details or other items may inadvertently be inaccurate.

**Library of Congress Card No.:** applied for

## British Library Cataloguing-in-Publication Data

A catalogue record for this book is available from the British Library.

## Bibliographic information published by the Deutsche Nationalbibliothek

The Deutsche Nationalbibliothek lists this publication in the Deutsche Nationalbibliografie; detailed bibliographic data are available on the Internet at <<http://dnb.d-nb.de>>.

© 2015 Wiley-VCH Verlag GmbH & Co.  
KGaA, Boschstr. 12, 69469 Weinheim,  
Germany

All rights reserved (including those of translation into other languages). No part of this book may be reproduced in any form – by photoprinting, microfilm, or any other means – nor transmitted or translated into a machine language without written permission from the publishers. Registered names, trademarks, etc. used in this book, even when not specifically marked as such, are not to be considered unprotected by law.

**Print ISBN:** 978-3-527-33302-8

**ePDF ISBN:** 978-3-527-66509-9

**ePub ISBN:** 978-3-527-66508-2

**Mobi ISBN:** 978-3-527-66507-5

**oBook ISBN:** 978-3-527-66506-8

**Cover Design** Adam Design, Weinheim  
**Typesetting** Laserwords Private Limited,  
Chennai, India  
**Printing and Binding** Markono Print  
Media Pte Ltd, Singapore

Printed on acid-free paper

## Contents

**Preface** *XI*

**List of Contributors** *XV*

<b>1</b>	<b>Dynamic Pressure and Temperature Responses of Porous Sedimentary Rocks by Simultaneous Resonant Ultrasound Spectroscopy and Neutron Time-of-Flight Measurements</b>	<b>1</b>
	<i>James A. TenCate, Timothy W. Darling, and Sven C. Vogel</i>	
1.1	Introduction and Background	1
1.2	Macroscopic Measurements	3
1.2.1	Stress-Strain Measurements	3
1.2.2	Temperature Variations	4
1.2.3	Moisture Content Variations	5
1.2.4	Vibrational Excitation Variations	6
1.3	Motivation for Neutron Scattering Measurements	7
1.4	SMARTS: Simultaneous Stress–Strain and Neutron Diffraction Measurements	9
1.5	HIPPO: Simultaneous Step-Temperature Modulus/Sound Speed and Neutron Diffraction Measurements	12
1.5.1	Sample	13
1.5.2	Sample Cell	14
1.5.3	Procedure	15
1.5.4	Results	16
1.5.5	Comparison/Reference Measurements	19
1.6	Discussion and Conclusions	21
	Acknowledgments	23
	References	23
<b>2</b>	<b>Adsorption, Cavitation, and Elasticity in Mesoporous Materials</b>	<b>27</b>
	<i>Annie Grosman and Camille Ortega</i>	
2.1	Experimental Evidence of Collective Effects During Evaporation	28
2.1.1	Porous Vycor Glass	28
2.1.2	Porous Silicon	30
2.1.3	SBA-15 Silica	31

2.2	Adsorption-Induced Strain	33
2.3	Thermodynamics of the Solid–Fluid Interface	34
2.3.1	The Solid–Vapor Interface	37
2.3.2	The Solid–Liquid Interface	40
2.4	Stress Effect on the Adsorption Process	43
2.4.1	Supported and Free Standing Porous Si Layers	43
2.4.2	Monitoring of the External Stress	45
2.5	Cavitation in Metastable Fluids Confined to Linear Mesopores	47
2.5.1	The Elemental Isotherms	47
2.5.2	Si/A/B and Si/B/A Configurations	48
2.5.2.1	Si/A/B Configuration	49
2.5.2.2	Si/B/A Configuration	50
2.5.3	Nature of the Nucleation Process	51
2.5.3.1	Homogeneous Nucleation	51
2.5.3.2	Heterogeneous Nucleation and Elastic Strain	52
	References	55
<b>3</b>	<b>Theoretical Modeling of Fluid–Solid Coupling in Porous Materials</b>	<b>57</b>
	<i>Robert Alan Guyer and Hyunsun Alicia Kim</i>	
3.1	Introduction	57
3.2	Systems and Models	57
3.3	Problems	60
3.3.1	Systems of Interest	62
3.3.2	Quantities of Interest	62
3.4	Mechanical Response to Applied External Forces	63
3.5	Fluid in the Skeleton	66
3.6	Fluid in the Pore Space	73
3.7	Summary and Conclusion	76
	References	79
<b>4</b>	<b>Influence of Damage and Moisture on the Nonlinear Hysteretic Behavior of Quasi-Brittle Materials</b>	<b>81</b>
	<i>Jan Carmeliet</i>	
4.1	Nonlinear, Hysteretic, and Damage Behavior of Quasi-Brittle Materials	81
4.2	Macroscopic Damage Model for Quasi-Brittle Materials	85
4.3	Preisach-Mayergoyz (PM) Model for Nonlinear Hysteretic Elastic Behavior	88
4.4	Coupling the Macroscopic Damage Model and Damage-Dependent PM Model: Algorithmic Aspects	93
4.5	Moisture Dependence of Hysteretic and Damage Behavior of Quasi-Brittle Materials	94
4.5.1	Moisture-Dependent Mechanical Experiments	96
4.5.2	Moisture-Dependent Damage and PM Model	99

Acknowledgment	102
References	102

<b>5</b>	<b>Modeling the Poromechanical Behavior of Microporous and Mesoporous Solids: Application to Coal</b>	<b>105</b>
	<i>Matthieu Vandamme, Patrick Dangla, Saeid Nikoosokhan, and Laurent Brochard</i>	
5.1	Modeling of Saturated Porous Media	107
5.1.1	Macroporous Media	108
5.1.2	Generic (and Potentially Microporous) Media	110
5.1.3	Mesoporous Media	112
5.2	Application to Coal Seams	114
5.2.1	Modeling of a Representative Elementary Volume of a Coal Seam	116
5.2.2	A Source of Hysteresis: The Kinetics of Transfer Between Cleats and Coal Matrix	119
5.2.3	Simulating an Injection of Carbon dioxide in a Coal Seam	122
5.3	Conclusions and Perspectives	124
	References	125
<b>6</b>	<b>A Theoretical Approach to the Coupled Fluid–Solid Physical Response of Porous and Cellular Materials: Dynamics</b>	<b>127</b>
	<i>Mark W. Schraad</i>	
6.1	Introduction	127
6.1.1	Traditional Modeling Approaches	128
6.1.2	A Unifying Theoretical Approach	130
6.2	Theoretical Approach	131
6.2.1	Single-Field Equations and the Ensemble Averaging Process	133
6.2.2	Multifield Equations	134
6.3	Closure Models	135
6.3.1	Reynold's Stress and Body Forces	136
6.3.2	Material Stress Gradients	136
6.3.2.1	Momentum Exchange	137
6.3.2.2	Fluid-Field and Solid-Field Stresses	138
6.3.2.3	Solid Matrix Constitutive Models	139
6.4	Demonstration Simulations	139
6.5	Concluding Remarks	149
	References	150
<b>7</b>	<b>Swelling of Wood Tissue: Interactions at the Cellular Scale</b>	<b>153</b>
	<i>Dominique Derome, Jan Carmeliet, Ahmad Rafsanjani, Alessandra Patera, and Robert Alan Guyer</i>	
7.1	Introduction	153
7.2	Description of Wood	154
7.3	Absorption of Moisture in Wood	155

7.4	Swelling of Wood Tissue – Investigations by Phase Contrast Synchrotron X-Ray Tomographic Microscopy	156
7.4.1	Behavior of Homogeneous Tissues	158
7.5	Parametric Investigation of Swelling of Honeycombs – Investigation by Hygroelastic Modeling	161
7.5.1	Simulation Methodology	162
7.5.2	Layered Cell Wall	163
7.5.3	Effects of Geometric Variations	165
7.6	Beyond Recoverable Swelling and Shrinkage: Moisture-Induced Shape Memory	167
7.7	Discussion	168
7.7.1	On the Origin of Hysteresis of Sorption as a Function of Relative Humidity	168
7.7.2	On the Effects on Moisture Sorption	168
	Acknowledgment	169
	References	169
<b>8</b>	<b>Hydro-Actuated Plant Devices</b>	<b>171</b>
	<i>Khashayar Razghandi, Sebastien Turcaud, and Ingo Burgert</i>	
8.1	Introduction	171
8.2	General Aspects of Plant Material–Water Interactions	173
8.2.1	Principle Mechanics: Stress and Strain	173
8.2.2	Water as an Engine	174
8.2.2.1	Inflation	174
8.2.2.2	Swelling	176
8.2.3	Plant Cell Walls	177
8.2.4	Cell Wall–Water Interaction	179
8.2.4.1	Swelling/Shrinkage of Wood	180
8.2.5	Principles of Anisotropic Deformation	181
8.3	Systems Based on Inner Cell Pressure – Living Turgorized Cells	182
8.3.1	Cell Growth – Turgor: Plastic Deformation of the Cell Wall	182
8.3.2	Movement via Elastic Deformation of the Cell Wall	182
8.3.2.1	Stomatal Movement	183
8.3.2.2	Venus Flytrap: A Turgor-Based Rapid Movement	184
8.4	Systems Based on Water Uptake of Cell Walls	185
8.4.1	Bilayered Structures for Bending	185
8.4.1.1	Passive Hydro-Actuation in Pine Cones	186
8.4.1.2	Wheat Awns Hydro-Actuated Swimming Movement	187
8.4.2	Bilayered Structures for Twisting Movements	188
8.4.2.1	Curling of Erodium Awns	188
8.5	Systems Based on a Differential Swelling of Cell Wall Layer	190
8.5.1	Tension Wood Fibers	190
8.5.2	Contractile Roots	191
8.5.3	Ice Plant Seed Capsule	192



8.5.3.1	Ice Plant Capsule Opening as a Case Study for the Capacity of Water as a Plant Movement Actuator	194
8.6	Biomimetic Potential	195
	Acknowledgments	197
	References	197

<b>Index</b>	<b>201</b>
--------------	------------



## Preface

The subject matter of this book is the description of the behavior of porous materials in the presence of fluids. Porous materials are many, for example, soil or a sandstone, designed material such as a Nuclepore filter or MCM-41, wood fiber, or the cellular solid in the keel of an ice plant. Fluids often occupy the pore spaces in these materials and can alter the geometry/mechanical properties of the porous materials. It is this fluid–solid coupling that is discussed in the chapters herein.

We identify two important components of the fluid–solid interaction at the interface of solid and pore space. One relates to the phase change of fluid and the other relates to change of the mechanical state of solid. These changes depend on the thermodynamic state defined by  $(P, \sigma, T)$ , that is, the fluid is at pressure  $P$ , the solid is at stress  $\sigma$ , and both are at temperature  $T$ . The pressure  $P$  is the pressure of the fluid that is far from the pore walls. At low fluid pressure, the pore space is filled with unsaturated vapor (Figure 1a). As the fluid pressure increases (moving up the dotted line in Figure 1a), the fluid on approaching the pore walls is inhomogeneous, evolving from gas to gas–liquid coexistence and eventually to liquid, because of forces exerted by the solid on the fluid. On further increase in the fluid pressure, the liquid near the pore wall solidifies. This evolution is depicted in the one-dimensional pore space of Figure 2. The  $x$ -axis indicates a physical pore space discretized for illustrative purposes in layers. The fluid pressure increases from Figure 2a–d, and the fluid near the pore wall undergoes phase changes. At fluid pressure equal to the saturated vapor pressure, Figure 2d, the fluid far from the pore wall is bulk liquid and the fluid close to the wall, which has not become solid, is at an effective pressure greater than the saturated vapor pressure. The fluid at the pore wall has become solid at an effective pressure, which is much greater than the saturated vapor pressure. While this evolution of the fluid in response to the fluid pressure is taking place, the solid, at stress  $\sigma$ , is almost unchanged.

The second component of the fluid–solid interaction is the development of a mechanical force system in the solid. At the pore wall, the solid pulls on the fluid, causing the inhomogeneous fluid arrangements in Figure 2a–d. In reaction, the fluid pulls on the solid causing a strain field in the solid. This is illustrated in Figure 3, a pore space in one dimension (for simplicity) bounded by solid on either

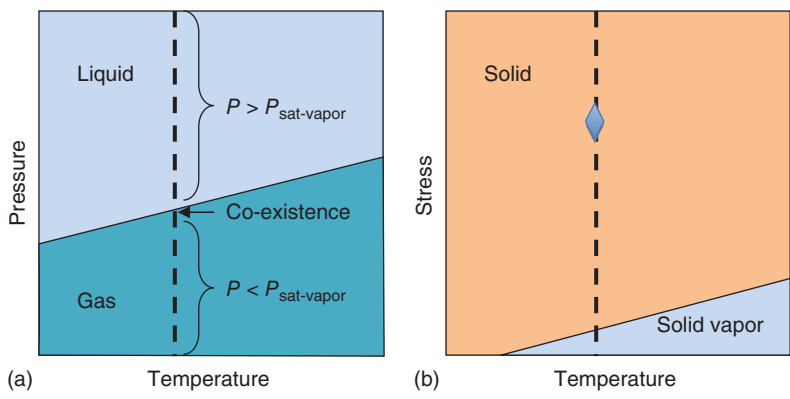


**Figure 1** (a, b) Phase diagrams of the material in a porous media system. The fluid is in principle at  $(P, T)$  and the solid, able to be addressed independently of the fluid, is in principle at  $(\sigma, T)$ .

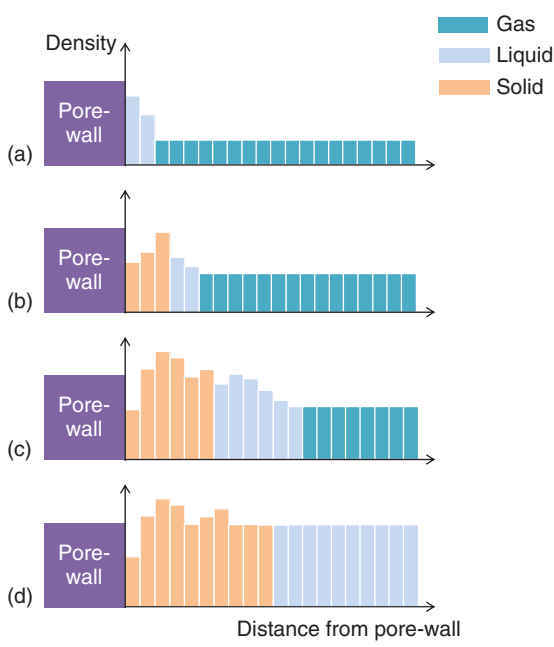


**Figure 2** Fluid configuration in a pore space near a wall as pressure increases from (a) to (d). (a) Pressure is far from the saturated vapor pressure; (b) pressure is increasing; (c) pressure is approaching the saturated vapor pressure; and (d) pressure is at saturated vapor pressure.

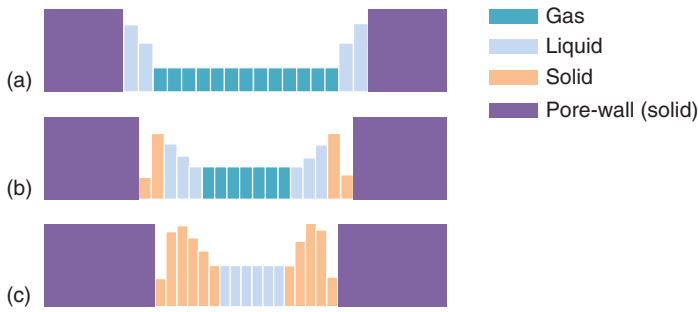


**Figure 3** Fluid configuration in a pore wall system. The phase changes within the fluid and the strain induced in the pore wall are illustrated. The fluid pressure increases from (a) very low to (c) the saturated vapor pressure.

side. As pressure approaches  $P_{\text{sat}}$ , phase changes occur that are shown in Figure 2. The solid phase of the fluid appears on the pore wall due to densification as a result of forces exerted by the pore wall system. Concomitantly, the fluid pulls the pore walls into the pore space. A strain develops in the solid. This strain, often assumed to be small and able to be neglected, is driven by the fluid and can be a complex function of the history of the fluid configurations.

The solid could be under no stresses except that caused by forces from the fluid. However, it is, in principle, possible to have a stress field in the solid that is set independent of the forces from the fluid. This possibility, illustrated in Figure 1b, is the domain of Biot theory. For the most part, this subject area is not developed in this book. An exception is the paper by Vandamme *et al.* in Chapter 5.

The interaction of fluid and solid in porous materials at local scale manifests itself as complex nonlinear phenomena at global scale. One interesting nonlinear phenomenon that this book draws attention to is hysteresis. Hysteresis can be in the response to mechanical probes such as the stress–strain curve of a dry Berea sandstone, discussed in Chapter 1. The mechanical state of a typical sandstone evolves slowly over time following finite frequency excitation. Chapter 1 presents the mechanical experiments that interrogate the internal strain of the grains using a neutron beam and reveals important features of the behavior of rocks, that is, consolidated granular media.

There are also many systems in which the coupling between fluid and solid brings about the complex behavior, and some hysteresis can arise only as a result of the coupling. Chapter 2 is an experimental and theoretical study of mesoporous silicon material and presents a thermodynamic model at the fluid–solid interface. It reports adsorption-induced strain in the solids and the reciprocal stress effect on the adsorption process. Chapter 3 develops a theory to describe the fluid–solid coupling at the local scale. The manifestation of this interaction is described and investigated using a finite element model. The inhomogeneous system composed of fluid and solid elements can accommodate a variety of circumstances such as bulk fluid in the pore space of a rock, fluid in the wall fabric of wood or a cellular solid, and fluid in the polymeric filling of a cellular solid framework. Chapter 4

continues to present a theoretical study that formulates a model for stress–strain behavior of dry quasi-brittle materials allowing damage to be created. The Preisach model is used to model the damages at microscale, and this is translated as density to the macroscopic elastic elements to interpret the macroscopic behavior in terms of evolving populating of microscopic elements. The dry quasi-brittle material model is then modified to include moisture by allowing fluid–solid coupling in the form of an effective internal stress. Chapter 5 focuses on coal that serves as a valuable model of saturated porous material. The particularly interesting feature of coal is the range of length scales of the pores from macroscopic to mesoscopic, cleats, and matrix pores. This is modeled combining thermodynamic description of two pore systems, the macroscopic cleat system and the mesoscopic matrix system, which are coupled by a Darcy flow that is driven by a pressure gradient. Chapter 6 brings an alternative perspective on mechanics of porous materials by developing a multifield model and applying it to a series of foams. The particular interest here is the behavior of coupled fluid–solid systems under dynamic loading.

Chapter 7 examines the fluid–solid coupling in the context of wood swelling. The experimental observations are obtained by the modern X-ray tomography technique at a micrometer scale, and strains at multiple scales of hierarchical wood tissues are studied as a function of moisture content. This is accompanied by a parallel modeling study that explores the role of materials' structure as moisture content changes. The final chapter, Chapter 8, also investigates biological cellular materials, that is, plants. The authors employ this coupling in numerous ways from the analog of “blowing up a balloon” to a “mechanical” thermostat. Systems that exhibit this wide range of behaviors are described, for example, systems based on inner cell pressure, systems based on water uptake into the cell wall, systems based on a differential swelling of cell wall layers, and systems that illustrate the capacity of water as a plant movement actuator.

### Acknowledgment

We would like to thank the following people and organisations for their support in publishing this book: The authors of the chapters for their contributions, The anonymous reviewers for the chapters for their insightful and helpful comments, J Machta, R Hallock, R Lilly and A Wootters in a long intermittent conversation that informed our understanding, and Institute of Geophysics and Planetary Physics and EES-17 at Los Alamos National Laboratory, the University of Nevada, Reno, USA and the University of Bath, UK.

## List of Contributors

### ***Laurent Brochard***

Université Paris-Est  
Laboratoire Navier (UMR 8205)  
CNRS, ENPC, IFSTTAR  
77420 Marne-la-Vallée  
France

### ***Ingo Burgert***

ETH Zurich - Swiss Federal  
Institute of Technology  
Institute for Building Materials  
(IfB)  
HIF E 23.2,  
Stefano-Franscini-Platz 3  
8093 Zurich  
Switzerland

*and*

Empa, Swiss Federal Laboratory  
for Materials Science and  
Technology  
Applied Wood Research  
Laboratory  
Ueberlandstrasse 129  
8600 Dubendorf  
Switzerland

### ***Jan Carmeliet***

ETH Zürich, Institute of  
Technology in Architecture  
Chair of Building Physics  
Stefano-Franscini-Platz 5  
8093 Zurich  
Switzerland

*and*

Empa, Swiss Federal Laboratory  
for Materials Science and  
Technology  
Laboratory of Building Science  
and Technology  
Ueberlandstrasse 129  
8600 Dubendorf  
Switzerland

### ***Patrick Dangla***

Université Paris-Est  
Laboratoire Navier (UMR 8205)  
CNRS, ENPC, IFSTTAR  
77420 Marne-la-Vallée  
France

***Timothy W. Darling***

Los Alamos National Laboratory  
Los Alamos, NM 87545  
USA

*and*

University of Nevada  
Physics Department  
1664 N. Virginia St.  
Reno, NV 89557-0220  
USA

***Dominique Derome***

Empa  
Swiss Federal Laboratory for  
Materials Science and  
Technology  
Laboratory of Building Science  
and Technology  
Uberlandstrasse 129  
8600 Dubendorf  
Switzerland

***Annie Grosman***

Institut des Nanosciences de  
Paris (INSP)  
Universite's Paris 6  
UMR-CNRS 75-88  
Campus Boucicaud  
140 rue de Lourmel  
75015 Paris  
France

***Robert A. Guyer***

Los Alamos National Laboratory  
Los Alamos, NM 87545  
USA

*and*

University of Nevada  
Department of Physics  
1664 N. Virginia Street  
Reno, NV 89557-0220  
USA

***H. Alicia Kim***

University of Bath  
Department of Mechanical  
Engineering  
Bath  
BA2 7AY  
UK

***Saeid Nikoosokhan***

Université Paris-Est  
Laboratoire Navier (UMR 8205)  
CNRS, ENPC, IFSTTAR  
77420 Marne-la-Vallée  
France

***Camille Ortega***

Institut des Nanosciences de  
Paris (INSP)  
Universite's Paris 6  
UMR-CNRS 75–88  
Campus Boucicaud  
140 rue de Lourmel  
75015 Paris  
France

***Alessandra Patera***

Empa  
Swiss Federal Laboratory for  
Materials Science and  
Technology  
Laboratory of Building Science  
and Technology  
Uberlandstrasse 129  
8600 Dubendorf  
Switzerland

*and*

Paul Scherrer Institute  
Swiss Light Source  
5232 Villigen  
Switzerland



**Ahmad Rafsanjani**

McGill University  
Mechanical Engineering  
Department  
817 Sherbrooke Street West  
Montreal Quebec H3A OC3  
Canada

**Khashayar Razghandi**

Max-Planck-Institute of Colloids  
and Interfaces  
Department of Biomaterials  
Am Mühlenberg 1  
14476 Potsdam  
Germany

**Mark W. Schraad**

Fluid Dynamics and Solid  
Mechanics Group (T-3)  
Theoretical Division  
Los Alamos National Laboratory  
Mail Stop B216, P.O. Box 1663  
Los Alamos, NM 87545  
USA

**James A. TenCate**

Los Alamos National Laboratory  
Los Alamos, NM 87545  
USA

**Sebastien Turcaud**

Max-Planck-Institute of Colloids  
and Interfaces  
Department of Biomaterials  
Am Mühlenberg 1  
14476 Potsdam  
Germany

**Matthieu Vandamme**

Université Paris-Est  
Laboratoire Navier (UMR 8205)  
CNRS, ENPC, IFSTTAR  
77455 Marne la Vallée  
France

**Sven C. Vogel**

Los Alamos National Laboratory  
Los Alamos, NM 87545  
USA



## 1

# Dynamic Pressure and Temperature Responses of Porous Sedimentary Rocks by Simultaneous Resonant Ultrasound Spectroscopy and Neutron Time-of-Flight Measurements

*James A. TenCate, Timothy W. Darling, and Sven C. Vogel*

## 1.1

## Introduction and Background

Rocks are everywhere, yet there are still surprising puzzles about their peculiar dynamic elastic properties, especially their hysteresis, non-Hookean response, and rate-dependent behavior. Since before recorded history, mankind has been making dwellings, hammering out monuments, and even constructing huge buildings out of rock, for example, the famous Strasbourg Cathedral built in the Middle Ages is made almost entirely from Vosges sandstone. Nowadays, one extracts oil and gas from rocks, explores ways to store excess CO<sub>2</sub> in them, and tries to mimic their resilience and durability with concrete. The imperfect way in which mineral grains end up cemented into rocks dictates how fluids move in oil or gas reservoirs or in aquifers. Indeed, these very fluids are often a key mechanism for that cementation. The diagenesis of rocks, their formation, and cementation history are of great geological interest as well. Hence, the dynamic elastic properties of rocks have been a topic of continuing scientific study for well over a century.

To narrow the focus of this chapter, the subject is primarily the behavior of rocks that have commercial interest. These rocks may contain oil and gas, or might be considered as a reservoir for CO<sub>2</sub> storage. These rocks are primarily sedimentary, and the focus of this chapter will sharpen even more, dealing exclusively with sandstones. A sandstone is an imperfectly cemented collection of quartz grains, which is porous and permeable to fluids (which often play a key role in the cementation) and may contain significant amounts of clays and other materials. In the experiments described here, the rocks studied will be extremely pure and clean sandstones, 99+% pure SiO<sub>2</sub> formed from quartz (prehistoric, 77 MYBP) Aeolian beach sand, known as Fontainebleau sandstone. Such rocks are simply composed of the grains and cementation.

How does one describe and examine such a sandstone and how is it different from man-made materials? A thin section examined under a polarizing microscope can show the crystallographic orientation and the nature of the grains, bonds, and cementation. A thin section of Fontainebleau sandstone is shown in

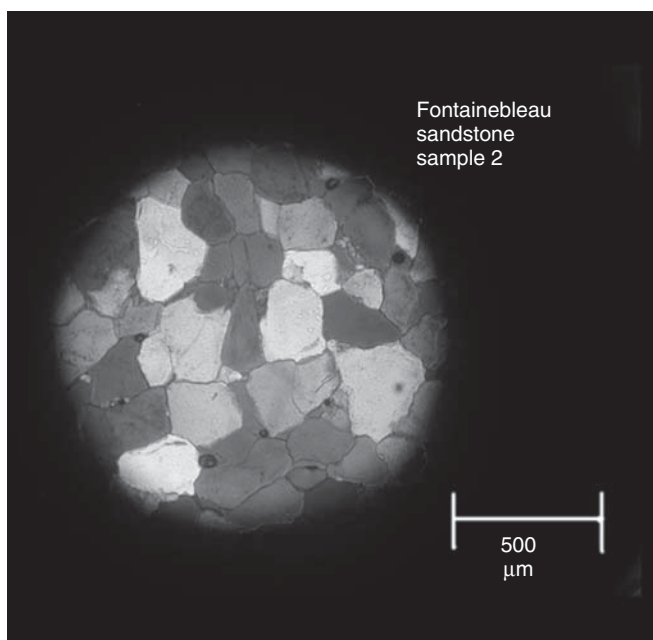


**Figure 1.1** An image of a thin section of Fontainebleau sandstone in a polarizing microscope. The largely single crystal grains are rounded (convex) while porosity, filled with epoxy, has more concave boundaries. The largest visible grains are taken as

characteristic of the grain size, about 200  $\mu\text{m}$  across. With very porous rocks, the possibility of grain movement during polishing must be considered, possibly distorting apparent boundaries.

Figure 1.1. All the grains are roughly of the same size (about 150–200  $\mu\text{m}$ ), and none of the material in the section shown here has any significant polycrystalline components and very little of it is amorphous or glassy (which shows up as black under crossed polarizers). However, the reality is that a thin slice of a rock really does not give a very good representation of the porosity and permeability or even of the cementation. Care must be taken in extracting distributions of pore and grain sizes from sections, and often the cementation at grain contacts is difficult to identify. Amorphous cement, for example, can easily be missed and more advanced petrographic techniques such as cathodoluminescence or electron backscatter diffraction in an SEM must be used [1]. Occasionally, pore casts – where an epoxy is spun into the pore space and the sand dissolved away with an acid – are made to study the three-dimensional network of pores [2]. X-ray micro-CT images on very small samples are made as well, originally to provide an input for modeling, but similar to thin sections, they contain no information on the mechanical properties of the system. The contact network of grains, the pore space they can rotate into, and the fluids that can move around in that pore space (e.g., water, oil, and gas) all couple to the dynamics of a rock; direct measurements on the scale of these features is extremely difficult.

So the cementation, porosity, and permeability are important for many reasons: what can be done to study and understand how a rock is put together in a laboratory setting? The following lists several possible applied external fields [3] that will guide the experimental discussion that follows:

- 1) Pressure/stress
- 2) Temperature
- 3) “Humidity” resulting in the movement of fluid in a rock
- 4) Electric or magnetic fields
- 5) Vibration or acoustic energy.

The first two parameters, pressure — and the associated stress-strain measurements — and temperature — and the associated sound speed versus temperature measurements, seem to have been motivated by oil and gas exploration at the turn of the last century. “Humidity” measurements came out of interest in ultra dry lunar/moon rocks in the 1970s. Interest in electric and magnetic fields came a bit later and the last, vibration and acoustic energy, came later still. Vibration as an applied field is a bit unusual and is distinct from the use of a low amplitude stress wave to measure sound speed. “Vibration” has to do with changing the internal arrangement of strain fields with an acoustic AC drive — dubbed slow dynamics by TenCate and Shankland [4] — in contrast with the other DC applied fields. Other experiments and external fields may be possible. However, in this chapter just pressure and temperature measurements will be considered. These measurements are rate dependent and show a nonreversible response normally thought of as “hysteresis.” These are all “macroscopic” measurements, done at sample scales of a few to tens of centimeters. Some discussion of each kind of measurement is appropriate at this point before we delve into the combined macroscopic and atomic (neutron) measurements reported in the bulk of the chapter.

## 1.2

### Macroscopic Measurements

#### 1.2.1

##### Stress-Strain Measurements

The hysteretic macroscopic strain response of rocks to uniaxial compressive stress (force/unit area) has been noted since the turn of the last century [5]: after being brought to a “state of ease” (conditioning) by application of high stresses, most rocks display a repeatable curved, stress–strain loop under cyclic loading, for example, [6, 7]. Fully recoverable hysteretic processes, driven by stress and dependent on the previous extreme stress values, produce multiple values of strain for stresses between the cycle and values. The details of these processes (which produce similar effects in many different kinds of rocks) are usually ascribed to grain contact and fluid effects.

The literature reports a number of models to describe this hysteretic behavior, such as the Hertz–Mindlin model [8] and the Preisach–Mayergoyz (P–M) space model [9–11]. In analogy with magnetic domains in a magnetic system, a hysteretic rock “domain” or unit in the P–M scheme opens at one stress and closes at another. While these models can reproduce qualitatively the observed responses, assignment of the model systems to real physical elements has some problems, such as requiring frictional surface slip at interfaces in sandstone, where we expect small-area, perhaps brittle, bonds of a solid silicate. The tensile and shear strength of rocks, however, suggest that macroscopic slip cannot occur at every contact.

Rate effects have been reported and are worth noting. Claytor *et al.* [12] discovered that the *rate* at which hysteresis loops are taken is important for certain rock samples, especially sandstones. Elastic aftereffect, in analogy with magnetic aftereffect, is a process whereby hysteretic elements do not stay “switched” but snap back to some “relaxed” state. Thus, if a hysteresis loop is taken slowly enough, the area between the loops vanishes and the stress–strain curve is merely nonlinear. Figure 1.2 shows two stress–strain hysteresis loops taken from Claytor’s data: one quickly, 0.38 s between stress increments; and the other very slowly, over a weekend with 60 s between stress increments. The area within the error bars (not shown) is essentially zero for the very long stress–strain experiment. What physics is responsible? Fluids coupling to the rock grain skeleton could be one answer, and there may be many other possible explanations. There is simply not enough data on enough rocks yet to model how fluids couple to rock grains and affect the dynamics of a rock. (Reference to chapter by Jan Carmeliet.)

## 1.2.2

### Temperature Variations

Macroscopic temperature measurements on rocks started to appear in the 1920s and 1930s. Although there are many measurements where sound speed (modulus) is measured as a function of temperature for a wide variety of crystal rocks, there are almost no reports of hysteresis in temperature measurements that we are aware of. Ide *et al.* [13] did some of the first measurements of temperature versus modulus/sound speed, dating back to the mid-1930s. His work was motivated by learning about the composition of the earth’s crust under combined high temperatures and pressures. Although Ide did reverse the temperature protocol several times during the course of his experiments, he was looking for permanent deformation and did not report any hysteresis in his temperature data. The research done by Ulrich and Darling [14], on the other hand, is one of the very few reported observations of large hysteresis temperature loops. Their work is interesting because the hysteresis loops were observed at very low temperatures that are typically found on planets other than the Earth (see also [15]).

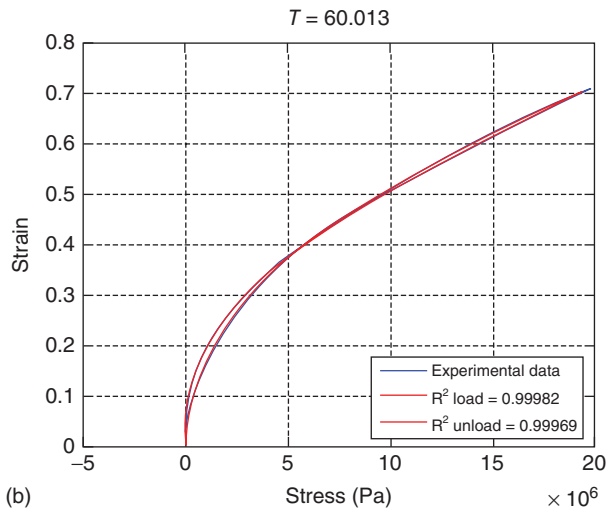
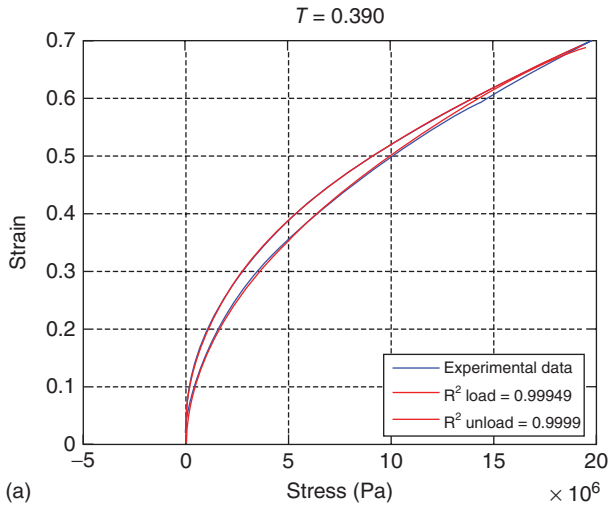


**Figure 1.2** Stress–strain characteristics for sandstone from unconstrained quasistatic, uniaxial stress measurements. (a) The higher strain rate shows a difference between the

loading and unloading curves; (b) in a low strain rate experiment this hysteresis is much less apparent.

### 1.2.3

#### Moisture Content Variations

For completeness, it should be noted that careful and extensive macroscopic varying “humidity” measurements [16] hint at hysteresis, and there is extensive literature on the hysteresis seen in capillary condensation in soils as well. The book by Guyer and Johnson [3] discusses saturation and fluid content as a way of altering

the thermodynamic state of a rock, just as varying temperature can be thought of that way. However, varying moisture content and carefully quantifying it is much more difficult than varying temperature. It is also not so amenable to neutron scattering measurements, and thus these measurements are outside of the selected scope of this chapter.

#### 1.2.4

##### Vibrational Excitation Variations

Finally, we mention an interesting applied field, introducing vibration as an applied field, resulting in a phenomenon called slow dynamics. In these experiments, the application of an external acoustic drive introduces a change of the sample's internal energy as manifested by a softening of its modulus. An experiment where the acoustic drive is repeatedly turned on and off and the conditioning and recovery is observed were reported in [17] for a wide variety of rocks and even concretes (see Figure 1.3). Conditioning and recovery of the sample back to its original elastic state and modulus is time dependent, similar to creep in that it has been shown to condition and recover as  $\log(t)$  where  $t$  is time [18]. What is interesting is that slow dynamics and rate effects are seen even in very dry rocks under ultra high vacuum (T.W. Darling, personal communication, 2011; also discussed in [18]). Very thin layers of water are not necessarily fluid-like in a very dry rock, but they may still play an important role and experiments are being carried out to continue to explore these aspects. Slow dynamics experiments are worth mentioning because the simultaneous neutron

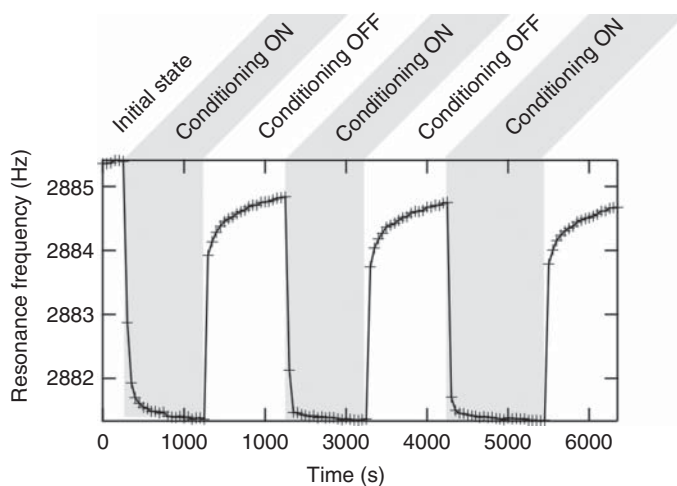


**Figure 1.3** “Slow dynamics” – an accumulated mechanical effect using a symmetrical alternating strain acoustic drive. The elasticity of the rock, related to the resonant

frequency, diminishes rapidly initially, and then gradually a high amplitude drive is applied. The elasticity recovers in a similar way when the drive is removed.



diffraction including the following temperature measurements will mirror the same protocol, applying cooling and heating instead of applying an acoustic drive.

### 1.3

#### Motivation for Neutron Scattering Measurements

To learn about the mechanisms responsible for the interesting dynamic behavior just discussed, one must be able to probe and measure at very small scales. Systems with magnetic hysteresis have domains that can actually be observed flipping on a microscopic scale. Unfortunately, it is very difficult to microscopically watch what is going on or to understand what is causing the hysteresis observed in elastic/macroscopic measurements. Hence, there is a need for a probe/experiment that operates at a different (and much smaller) scale than these experiments discussed previously. It is also essential to simultaneously measure the macroscopic scale behavior, for example, stress–strain loops, slow dynamics, temperature, or humidity changes while using this probe.

A beam of neutrons traversing a rock can probe a smaller scale, the atomic (crystalline) structures, and dynamics of ordered *and* disordered materials such as crystals, glasses, and combinations thereof (e.g., perfect for sandstones). Since neutrons have no charge and scatter only from atomic nuclei, they penetrate deeply into most materials. This is important; the grains and bonds at the surface of a rock behave differently from the interior grains. Because other grains do not completely surround them and they are exposed to air and humidity, these surface grains are not representative of the bulk conditions that dominate the macroscopic effects observed. To learn about what is going on with the components deep *within* the sample, neutrons are absolutely essential.

Now contrast neutron with X-ray diffraction techniques—these have also been used to probe the atomic/crystalline structure of rocks. X-ray diffraction on small samples of *powdered* rocks is an effective way to determine chemical composition; moreover, some X-ray sources are energetic enough to penetrate and do microtomography on small intact samples to learn about vesicle and pore space density. X-rays, however, do not scatter effectively from the lighter elements such as oxygen, silicon, aluminum, calcium, sodium, potassium, and magnesium. These elements make up about 95% of the Earth's crust; oxygen and silicon alone make up about three-fourth of the weight of rocks on the Earth's surface. Neutron scattering cross-sections do not suffer from this atomic number dependence. Neutrons are thus an ideal choice to probe larger samples of intact rock at an atomic/crystalline scale (nanometers).

Neutron diffraction measurements with large intact samples allow simultaneous probing of the crystalline structure together with macroscopic measurements. Such was the aim of two sets of experiments described in this chapter, altering the pressure (stress–strain) and altering the temperature (temperature modulus), both done while simultaneously probing the crystalline structure with neutron scattering. One set of experiments made it possible to alter the stress on a sample and make stress–strain measurements while simultaneously watching the

behavior of the bulk of the crystalline content (the grains) in the rock. Another experiment, using a beamline with a very high neutron flux, allowed us to alter another external field, the temperature, while simultaneously tracking the behavior at the atomic scale.

Both the SMARTS (Spectrometer for MAterials Research at Temperature and Stress) and HIPPO (high-pressure preferred orientation) neutron time-of-flight (TOF) diffractometers are part of the neutron instrument suite at the Los Alamos Neutron Science Center (LANSCE). At the core of LANSCE is a half-mile long 800 MeV proton accelerator, serving multiple facilities, among them is the spallation neutron source of the Manuel Lujan Neutron Scattering Center [19].

The high-energy protons eject (“spall”) neutrons from the heavy nuclei in the spallation target. This pulse of fast neutrons is moderated to room temperature or lower, where the neutron de Broglie wavelengths are comparable to atomic spacings in solids. These neutrons leave the moderator at nearly the same time ( $t=0$ ), but have a thermal distribution of energies (wavelengths). Shorter wavelength (faster) neutrons arrive first at the sample, followed by longer wavelengths. As these neutrons scatter from the sample, some wavelengths will fulfill the Bragg condition and produce a diffracted beam from a crystallite in the sample. The detected intensity of these diffracted beams as a function of time is also a function of wavelength, which provides the data for determining the atomic plane spacings within the crystallite. The random orientation and the large number of the crystallites fulfill the condition for *powder diffraction* where diffracted beams occur in a cone around the beam axis, so detectors intercepting any part of the cone will collect information on all the diffraction. We assume this condition to be true in our *intact* rock samples as well.

SMARTS is a third-generation neutron diffractometer optimized for the study of various engineering materials. It consists of an Instron load frame placed in such a way that simultaneous stress–strain and neutron diffraction measurements can be made under a variety of conditions. It was funded by DOE and constructed at the Lujan Center, coming online in the summer of 2001. SMARTS provides a range of capabilities for studying polycrystalline materials focusing on two areas: the measurement of deformation under stress (and extreme temperatures if desired), and the measurement of spatially resolved strain fields. SMARTS expands the application base of neutron diffraction to a wider range of engineering problems than previously possible, especially for the geomaterials (rocks) discussed in this chapter. With an extensive array of *in situ* capabilities for sample environments, it enables measurements on small to large ( $1\text{ mm}^3$  to  $1\text{ m}^3$ ) samples. Permanently mounted alignment theodolites provide a simple and efficient way to position samples or equipment within 0.01 mm. *In situ* uniaxial loading on samples up to 1 cm in diameter with stresses from a few megapascals up to 2 GPa is routine. Sets of neutron diffraction measurements made on a suite of rocks [20] were taken at room dry conditions with maximum stresses up to 80 MPa; a subset of that work, the sandstones reported here, can withstand stresses up to about 50 MPa.

HIPPO is another third-generation neutron diffractometer that came online in 2001 funded primarily with support from the University of California and the US

DOE. It is unique in that its sample chamber is positioned very close (9 m) to the spallation target. The incoming thermal neutron flux on the sample is about  $10^7 \text{ n}^{-1} \text{ cm}^{-2} \text{ s}^{-1}$  [21], delivered in pulses at a repetition rate of 20 Hz and typically collimated to a 10 mm diameter beam spot. The high count rate at HIPPO allows for dynamic measurements; atomic changes that occur on the order of minutes can be observed. We chose HIPPO to perform numerous step-temperature changes while simultaneously taking neutron diffraction measurements. Notable though is that in spite of high count rates at HIPPO, the low flux compared to the number of atoms in the irradiated volume (of the order of  $10^{22}$  from Avogadro's number) and the energy of the order of 10 meV of thermal neutrons make effects like sample heating (or radiation damage) negligible. At the time, HIPPO was the only beamline in the world capable of these experiments, tracking the atomic/crystalline scale behavior of the rock during step-temperature changes. A vacuum-tight sample chamber in the HIPPO beamline of  $\sim 1 \text{ m}^3$  accommodates a large variety of sample environments to expose vacuum dry samples to temperature [20], pressure [22], stress [23], magnetic fields, and combinations thereof as well as user-supplied sample environments. Our samples were mounted in a small helium-filled chamber (for heat transfer and, thus, were effective at room dry conditions). This inner sample chamber was then placed within the HIPPO sample chamber.

We now describe the results of *stress–strain measurements* on SMARTS [20] relevant to this chapter, and then follow that with a thorough discussion of the HIPPO experiment (unpublished), namely, *temperature modulus measurements* with simultaneous neutron diffraction data.

#### 1.4

##### SMARTS: Simultaneous Stress–Strain and Neutron Diffraction Measurements

We used the SMARTS beamline to examine the *lattice* strain response of rock samples to an external cyclic pressure (stress) while simultaneously measuring the *macroscopic* strain response. All samples were cylinders of 13.4 mm diameter and 26.0 mm length, with flat, parallel ends ground perpendicular to the axis. X-ray diffraction was used to identify the solid components of the porous rocks, and the porosity was determined by the ratio of rock to mineral density. The SMARTS geometry is shown in Figure 1.4. The sample can be seen held horizontally between the conical anvils. (The copper tubing seen wrapped around one anvil is maintaining the temperature of that anvil.) The macroscopic strain is measured by a 12 mm (black) extensometer strain gauge, with knife edges held against the sample by elastic bands and hanging below the sample as seen in the figure. Data from detector 2 is used to determine the spacing of lattice planes, and these are compressed by the applied external stress. Lattice strains are determined from changes in the lattice spacings relative to an initial value. Since the sample was initially subject to a holding stress of around 4 MPa, the strain gauge was zeroed at that point and

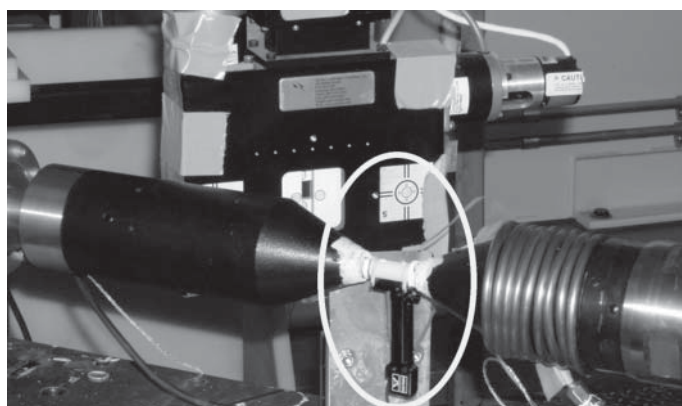
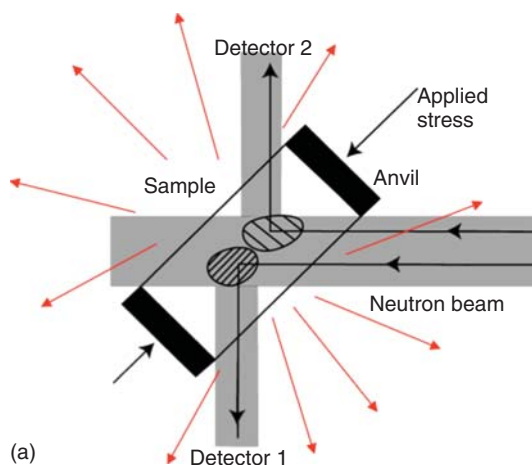


**Figure 1.4** (a) The diagram shows neutrons scattered from a stressed sample (red arrows). Neutrons that are Bragg diffracted from atomic planes compressed by the axial stress are collected by detector 2, while

planes that deform radially diffract beams to detector 1. (b) The actual experiment in SMARTS is shown. Note the extensometer strain gauge attached under the sample to avoid direct exposure to the neutron beam.

the initial lattice spacings were measured. Initial experiments determined breaking stresses, and then further cycles on another sample were then limited to 70% of these values. Measurements were carried out at room dry ambient conditions ( $24-28^{\circ}\text{C}$ ,  $24\% < \text{relative humidity} < 32\%$ ).

Macroscopic stress and strain values were recorded every 10 s throughout the experiment. The applied stress was changed between maximum and minimum values at  $3\text{ MPa min}^{-1}$ , in an approximately triangle wave protocol. Neutron TOF diffraction spectra were collected for 15 min while holding the stress constant at fixed values, resulting in a slightly stepped load variation from the ideal triangle protocol.

Two perpendicularly directed lattice parameters ( $a$ ,  $c$ ) are needed to describe the trigonal unit cells of quartz. Rietveld analysis of the TOF spectra provides the spacing, and, more accurately, the *changes* in spacing (strain) of lattice planes perpendicular and parallel to the applied stress. In this chapter, only the neutron data for the response of  $a$  and  $c$  lattice parameters under compression (detector 2) are shown and compared with the macroscopic compression data.

The macroscopic stress–strain curves measured during the *in situ* loading measurements are shown in Figure 1.5. Neutron diffraction patterns for the Fontainebleau sandstone sample were recorded at compressive stresses of 5, 10, 15, 20, and 25 MPa followed by unloading by the same load levels. The macroscopic curve exhibits the expected nonlinear, hysteretic relation between stress and macroscopic strain (measured by the extensometer) similar to that shown in earlier work. The  $a$  and  $c$  lattice parameters – measured for the quartz grains at the holding stresses – are shown on the left (dashed) and both appear to be linear (elastic) within the margin of error. The slopes for  $a$  and  $c$  lattice parameters are slightly different because of the elastic anisotropy of quartz. The diffraction elastic constants, derived from linear fit to the data points, agree within error bars. The difference between macroscopic and microscopic maximal strain is striking. Continuum mechanics dictate agreement between macroscopic and microscopic strains, which is also observed in *in situ* neutron diffraction loading

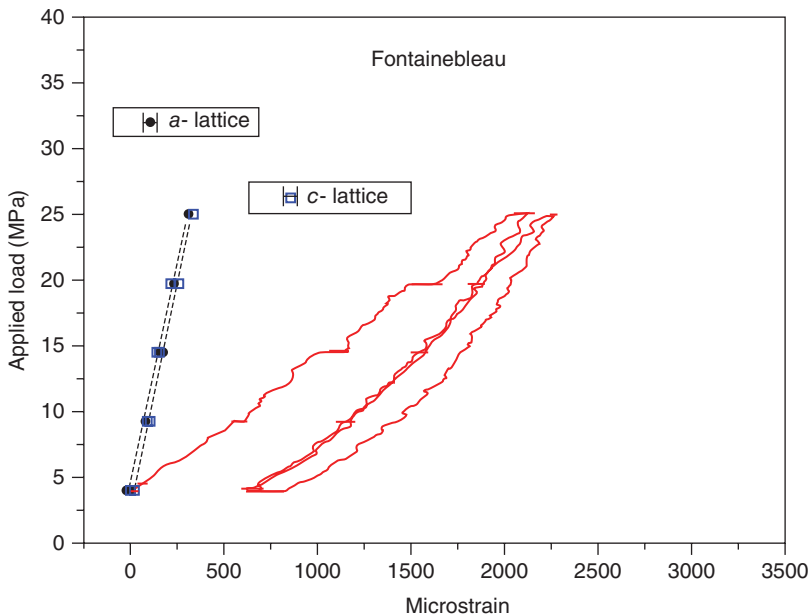


**Figure 1.5** SMARTS data from the Fontainebleau sample – the red curve shows the macroscopic stress–strain behavior with initial conditioning followed by a repeating

hysteretic loop. The lattice planes compressed axially (detector 2) show a linear nonhysteretic strain response to the applied stress.

measurements of other materials such as steel [25, 26]. While these findings do not explain the observed macroscopic peculiarities, they appear to exclude that their origin is within the bulk of the quartz crystals. The data strongly suggest that it is what is not bulk crystallinity, namely, the bond system, which is responsible for the hysteresis in this and other sandstone samples examined.

### 1.5

#### HIPPO: Simultaneous Step-Temperature Modulus/Sound Speed and Neutron Diffraction Measurements

Our experiment follows the elastic behavior of a sandstone sample at both bulk and atomic lattice scales as temperature is cycled. We need to measure elasticity, temperature, and lattice parameters, and to control and change the temperature and environment of the sample. Ideally, we strove to measure the response of the rock to a step function change in the temperature, as for an electrical circuit analog.

We use the resonant frequency of the sample to determine the qualitative behavior of the elastic constants of the sample. Piezoelectric disks (PZT-5A) bonded to the ends of a cylindrical core act as driver and receiver (Figure 1.6) in a typical low-amplitude swept-frequency resonant ultrasound spectroscopy (RUS) [27] measurement. Type E (chromel–constantan) thermocouple junctions made with 0.003" diameter wires are glued into small holes of 2 mm deep near the ends

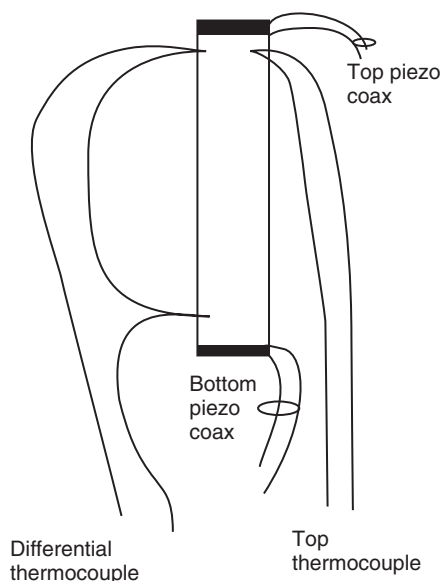


**Figure 1.6** A diagram of the HIPPO sample with thermocouple junctions and piezoelectric disks. The thermocouple wires are kept away from the incident neutron beam to avoid spurious diffraction peaks.

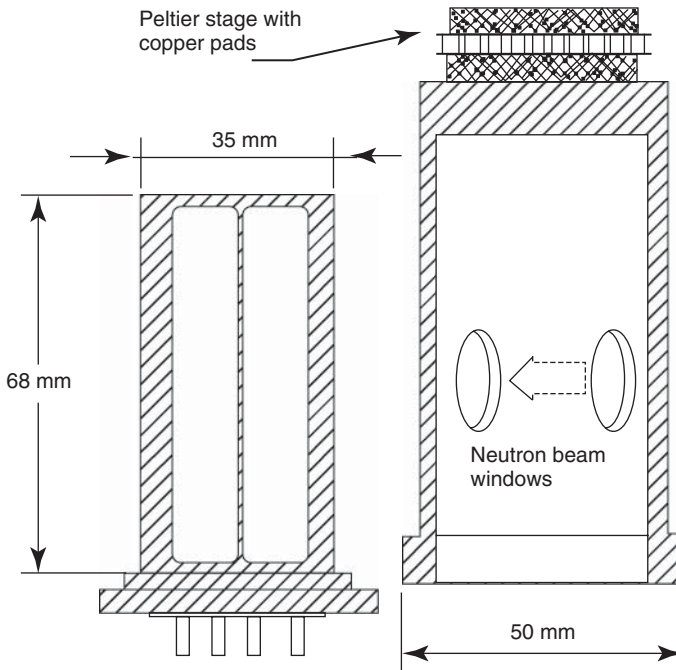


**Figure 1.7** A diagram of the HIPPO sample holder and can. The sample is supported by threads inside the frame. The assembled unit is sealed with an atmosphere of helium gas inside to provide heat transfer from can to sample.

of the rock. The top thermocouple is measured against the internal reference of a Lakeshore model 325 controller, and a differential measurement across the sample is made and recorded on an HP voltmeter. Wire lengths were made as long as possible to avoid heat conduction between the junctions and from the base feedthroughs.

As noted in [3], temperature control of porous rock samples is complicated by low thermal diffusivity that makes changing the temperature of the rock uniformly problematic. In initial experiments, we found that large temperature gradients persisted indefinitely when heating by direct contact at one end. Our final design heats and cools an aluminum shell and uses helium exchange gas at atmospheric pressure to heat and cool the rock (see Figures 1.7 and 1.8).

#### 1.5.1

##### Sample

The sample of interest is a 12.7 mm diameter core of Fontainebleau sandstone of length 55.6 mm. This is a relatively high porosity sample with  $\phi = 23\%$ . The grains are well rounded and in the size range 150–250  $\mu\text{m}$ . This sandstone is very clean, being  $>99.2\%$  quartz by XRD analysis. It also has one of the largest non-linear responses seen in acoustic tests [28], so making resonance measurements





**Figure 1.8** The HIPPO sample assembly – the neutron beam passes through Mylar windows in the can – which stretch under the helium pressure as the HIPPO well is evacuated, leaving wrinkles afterward.

at low amplitudes is essential. The sample is initially room dry, but the helium atmosphere for the measurements means water was being lost at a slow rate from the volume of the sample. Piezoelectric disks of PZT-5A material (in compression mode) are glued to each end with a thin copper foil for electrical connection at the junction. The glue used for the bonds is drawn in by capillary forces for a few millimeters into the sample at each end, as seen in Figure 1.8. This makes the sample a composite resonator of three components, dominated by the clean rock but with some glue-saturated rock and PZT elements at the ends. A finite element model (COMSOL) suggests that the observed resonances are consistent with a sound speed of approximately  $1600 \text{ m s}^{-1}$  in the clean rock. The gauge volume where the neutron beam probes the sample is in the central region of the clean rock.

### 1.5.2

#### Sample Cell

The sample cell provides the environment for the sample and must be able to operate inside the HIPPO experiment well. The cell is made up of two parts: each machined from a single piece of 6061 aluminum for maximum heat conductivity (see Figure 1.7). When assembled, the entire metal cell reaches a uniform



temperature in less than 100 s. An inner frame provides mounting space for the sample and its wire connections. Feedthroughs on the base of this frame pass electrical signals to the measurement apparatus. A standard Lakeshore curve-10 diode sensor is attached to the base of the frame to monitor the cell temperature. An outer can covers this frame and is sealed to it by an indium seal compressed by screws at the base. The top of the can has a single-stage Peltier unit, 1.5" square bolted to it with thick copper pads enabling us to solder the Peltier unit with low-temperature solder. The top of this Peltier assembly bolts to a 1.5" diameter aluminum rod that is both the mechanical support for the entire cell and the heat reservoir for the heating and cooling functions. The cell has windows – 15 mm diameter holes, sealed with aluminized 0.002" thick Mylar foil – placed so that the neutron beam can pass through the cell without hitting any of the solid aluminum parts. With the sample in place, the beam interacts with the central 1 cm of the sample. When the sample is mounted and all electrical connections have been made, the cell is assembled by displacing the air from the can with a flow of helium gas and inserting the frame and bolting the base to the can with the indium seal in place. The helium gas has a high conductivity and permeates the rock. This means heat transfer occurs not only through the gas from the can/frame to the outer surface of the rock but also through the He medium to the interior of the rock. This enhanced transfer enables us to approach a step function in temperature change, at least to timescales short compared to the nonlinear recovery times and to thermal diffusion times along the length of the sample. Although the HIPPO well is evacuated, we wrap the assembled cell in several layers of aluminized Mylar ("superinsulation") to provide radiation insulation against heat transfer with the well interior. The sample is supported inside the frame with dental floss thread, resting on a web below and with two tie points to keep the sample vertical. The frequency of vibration of the sample and this "springy" thread is below 200 Hz, so from the scale of the many kilohertz internal modes of the sample, it is essentially decoupled. A strain gradient possible due to gravity was shown to be negligible. Due to the pressure difference in the evacuated well, the windows suffer some stretching, leaving a corrugation when the cell is removed (Figure 1.8).

### 1.5.3

#### Procedure

LabVIEW® programs accumulate data from all the instruments. Measurements from the diode sensor on the can and the top thermocouple are recorded directly from the Lakeshore thermometers. The voltage across the differential thermocouples must be converted to a temperature difference using the known temperature of the nearby top thermocouple for one of the junctions, and so is post-processed. We have selected resonance modes near 26 kHz to monitor the elastic state of the sample. A DRS Inc. RUS system is used to sweep the drive and acquire the data. The swept-frequency data displays are also post-processed to extract the peak parameters by a Lorentzian profile-fitting procedure. The TOF diffraction

data are read as counts per neutron pulse and are stored and converted to  $S(Q)$  plots. A test that the neutron beam is not hitting the cell is that no lattice spacings corresponding to aluminum are seen in the data. In order to maintain a good signal-to-noise level, neutron counts were accumulated for runs of 5 or 10 min, although a test demonstrated that adequate statistics could be acquired in only a 10 s run because of the high neutron flux available to HIPPO. Temperature control is achieved by controlling the current to the Peltier stage. Since the heat flow is bidirectional according to current and the thermal reservoir is the same for each – room temperature connected by the thick aluminum rod – we expect to have approximately symmetrical behavior for temperature changes around room temperature. The parameters for PID controllers to make a step function when the time constants are relatively long and the heat paths are not very high conductivity are difficult to determine: given the duration we expect for the sample to reach equilibrium, we controlled the changes manually with a variable current supply.

#### 1.5.4

#### Results

Data were accumulated over a 17 h beam time run. The acoustic scan covered three compressional resonances corresponding to the second, third, and fourth modes (“Pochhammer” modes) at 22, 35, and 47 kHz approximately at room temperature. These modes are effectively driven by the large compression mode transducers. Scans were taken every minute at a drive amplitude as small as possible to avoid memory or slow dynamics effects – but large enough to be confident of the peak parameters. A sample scan is shown in Figure 1.9. The best-fit Lorentzian

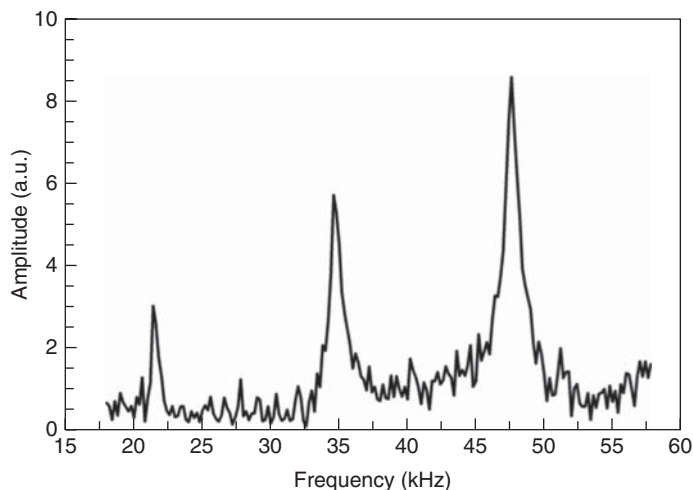


**Figure 1.9** The first three longitudinal vibration modes of the Fontainebleau sample. To avoid slow dynamical effects, we used the lowest amplitude drive that still gave a good signal-to-noise ratio.

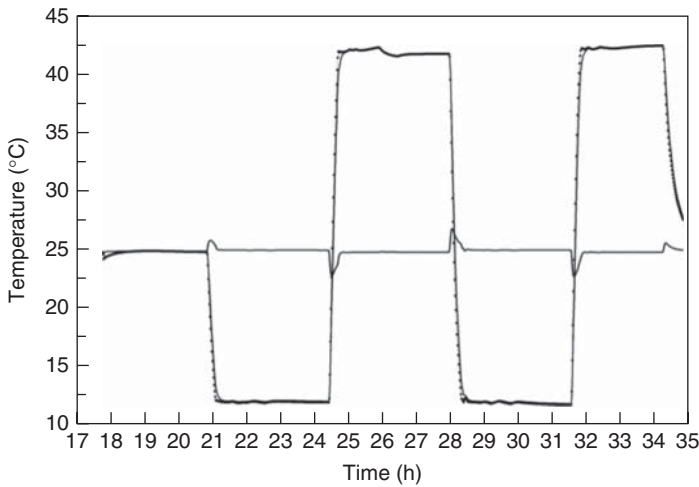


**Figure 1.10** The temperature protocol for the experiment. The top and bottom sample temperatures are shown (dotted and continuous) almost overlapping with a swing of about 30 K. The difference plot near the axis shows a small difference resolving to zero in about 15 min after each applied change. We avoided approaching the freezing point of water.

lineshape parameters show the effect on these peaks as temperature changes. The temperature of the sample cell was taken through two complete cycles where the temperature ranged from about 12 to 43 °C around a room temperature of 25 °C. The cell responds rapidly to the Peltier heat flow, but even with the He exchange gas the rock temperature and the gradient respond more slowly, taking 15–20 min to reach a steady state. The cell, rock, and differential (top to bottom) temperatures are shown in Figure 1.10. The temperature used in all the data plots corresponds to the temperature at the center of the sample, evaluated from the top and differential temperatures. This is quite accurately (within  $\pm 0.3$  °C) the temperature of the neutron gauge volume and is a good average for the overall acoustic response being within 1 °C in the 20 min after a temperature change and within 0.1 °C otherwise. Neutron scattering data were accumulated in 10 min runs for the first 13 runs and at 5 min runs thereafter to the end of the experiment. As can be seen from Figure 1.11, the circles representing the unit cell volume evaluated from the Rietveld lattice parameter refinement, scaled to the temperature swing, follow the rock average temperature curve accurately, albeit with a small spread of values. The absolute value of the unit cell volume is a little larger than standard values due to calibration deviations. These data confirm that the crystalline volume of the rock is responding essentially only to thermal expansion in an expected way with the temperature changes. As noted in the SMARTS data for uniaxial compression, this does not necessarily dictate the mechanical response of the entire sample.

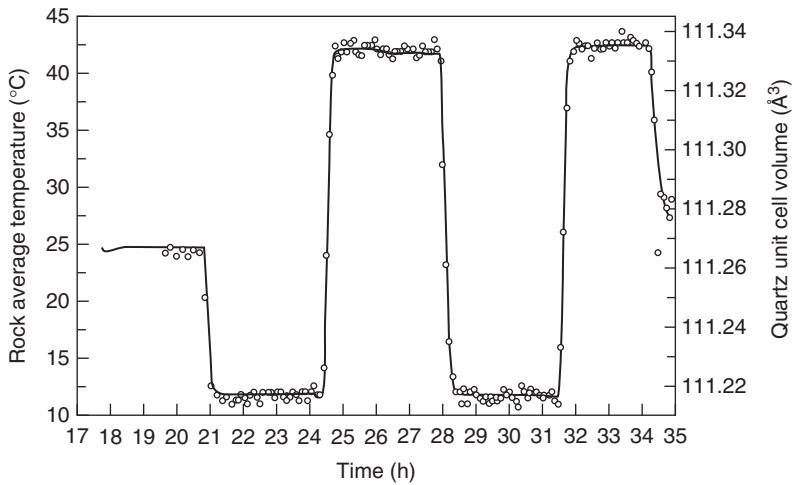


**Figure 1.11** The average (top + bottom)/2 temperature of the sample (continuous line) and the neutron diffraction derived atomic unit-cell volume (open circles) as a function of time. The lattice in the majority crystalline component in the grains changes essentially instantaneously to follow the temperature change.

The Lorentzian fitting program gives amplitude, center frequency, and width parameters for each peak. There is also phase information, but since the resonances do not overlap this information is not used. The quality factor “*Q*” of the sample resonance may be determined by dividing the center frequency by the width. Fits in general were good, given the signal to noise seen in Figure 1.9. Since these modes are of the same kind and the wavelengths are large compared to the microstructure of the sample, we expect the behavior of their parameters to be similar. It is shown in Figure 1.11 for the center frequency changes that this is indeed so, and is also true for the amplitude and width data. The highest frequency peak (mode 4) will be used to represent the behavior of all the peaks and the sample. Figure 1.12 displays the center frequency and the temperature variation for the sample. Several characteristics are worth noting: the initial cycle is different from the subsequent cycle, a “conditioning” behavior seen in many tests on rocks including standard stress–strain tests; the frequency is higher when the sample is colder, as expected, but an initial dip occurs for *both* temperature increases and decreases, followed by an increase; and the frequency lags considerably behind the temperature change. This last point represents the hysteretic response of the rock – the dry conditions and high permeability suggest that there is insufficient liquid to produce a viscous drag and the gas environment is too light and mobile to influence the mechanical response. The strain in the crystallites responds essentially instantaneously to temperature change, suggesting that the delay in the overall mechanical response of the sample is dominated by solid components that are not a large component of the coherent neutron scattering signal.

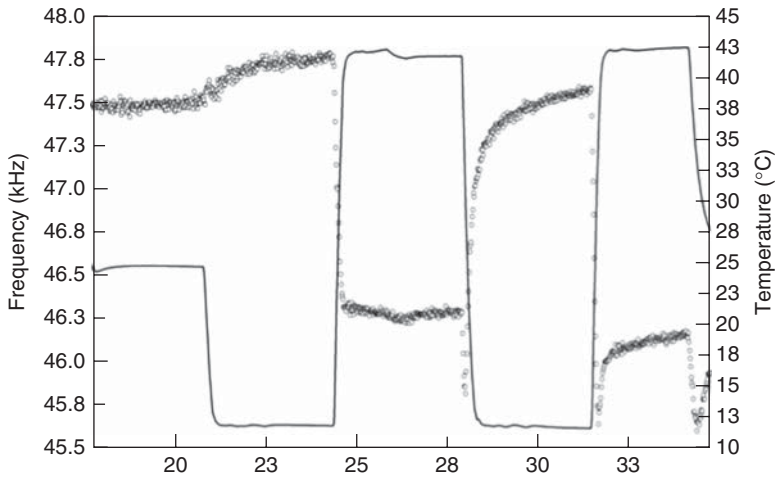


**Figure 1.12** The sample average temperature (continuous line) and the frequency of the third longitudinal mode (open circles) as a function of time. The overall change agrees with expected changes in the elasticity (higher  $T$  and lower modulus), but

the form does not follow the temperature, showing a gradual recovery after initial rapid change. Major differences with slow dynamics (Figure 1.3) are the downward dip at each temperature change and the “recovery-like” curve at both constant temperatures.

The width of mode 4 can be used to evaluate the change in  $Q$  of the sample with temperature, as shown in Figure 1.13. The  $Q$  of all three modes is between 20 and 50 over the entire temperature range.

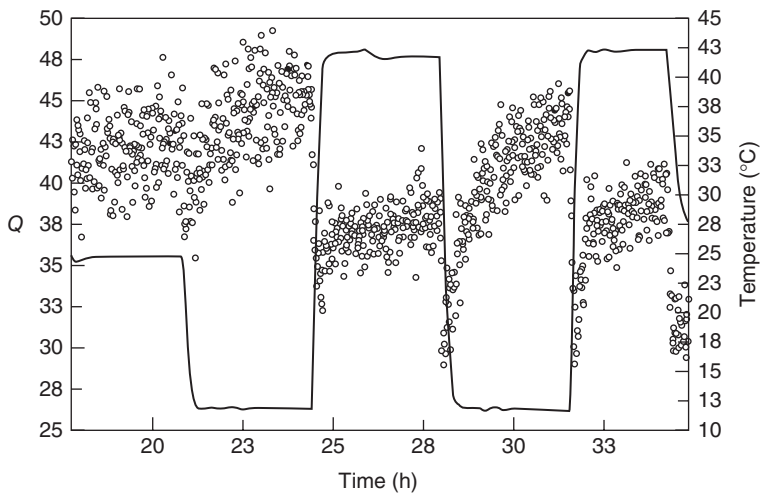
The  $Q$  is, in general, higher at lower temperatures but again the dip-and-recover characteristic can be seen – it is also in the width alone, demonstrating that there is a jump in the damping at each temperature change that diminishes with approximately the same time behavior as the center frequency.

Figure 1.14 shows center frequency plotted against temperature. This displays a typical hysteresis loop with two main features imposed on it. First, there is a conditioning effect – a removal of a transient property – that is not complete at the end of the experiment. This conditioning makes the loop decrease in frequency over time, but eventually leaves the sample in a state where the loop repeats – this experiment did not reach that state. Second, the dip-and-recover being similar at both signs of temperature change leads to the loop becoming a “bow-tie.” The crossing of these is seen at about 35 °C on the final cycle. This feature is not often observed in quasistatic tests, but is common in experiments where the excitation can be changed on shorter timescales than the recovery.

### 1.5.5

#### Comparison/Reference Measurements

A measurement on a known sample of the same size as these Fontainebleau samples – steel – was made to ensure that the results of the three-pronged (acoustic,



**Figure 1.13** The sample average temperature (continuous line) and the  $Q$  of the third longitudinal mode (open circles) as a function of time. Although there is more scatter in this data, the features noted for the center frequency (Figure 1.12) also appear in the  $Q$ .

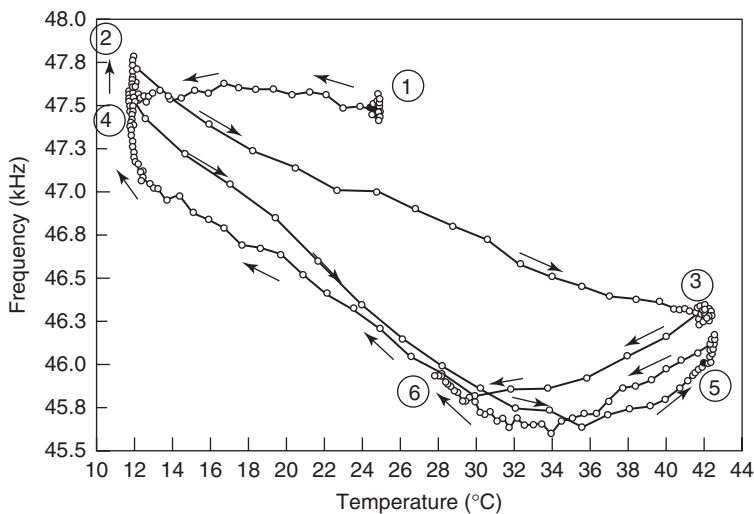


**Figure 1.14** Hysteresis loops in the temperature–frequency characteristic from Figure 1.12. The line merely joins the data points, to help follow the path, labeled 1–6.

After the first cycle, the loop changes toward a “bow-tie” shape, caused by the similar “recovery-like” response at both the high and low temperatures.

thermal, and neutron) approach made sense. Figure 1.15 shows the combined results for the center frequency of a compressional resonance, the fitted unit cell volume, and the applied temperature profile. The frequency plot has been inverted since we expect lowering the temperature to increase the frequency, and all are

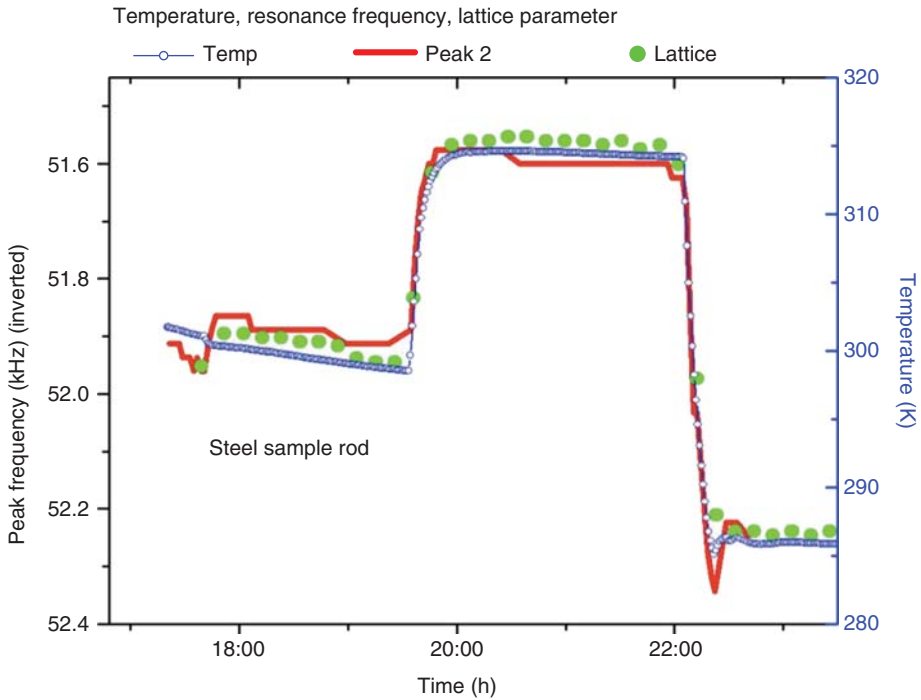


**Figure 1.15** A plot showing that in a known nonporous sample (steel), the temperature, the frequency of a resonant mode (inverted to correspond to the  $T$  change), and the atomic lattice spacing all correspond closely.

scaled to a common step height. For steel, with its high thermal diffusivity, the lattice and the whole body resonances respond identically to the temperature step. A later acoustic temperature measurement (no lattice information) was made on a sample of Novaculite, a very low porosity, pure dense quartzite. Figure 1.16 shows data plots matching those of Figures 1.12 and 1.14, respectively, for the Fontainebleau. Although the materials for both are  $>99\%$   $\text{SiO}_2$ , the porosity of the sandstone gives grains a room to displace and rotate, thus generating a highly nonuniform strain distribution. The high strains in the (also nonuniform) cementation drive the processes responsible for the mechanical hysteresis.

## 1.6

### Discussion and Conclusions

We have made a system that can make a relatively fast change in the temperature of a porous rock sample and then measure the time lag for the elastic properties to change. The longitudinal resonance frequency follows the change in the elasticity and can be measured with high accuracy, even in intrinsically low- $Q$  systems such as sandstones. We find that the speed of the temperature change is limited by three

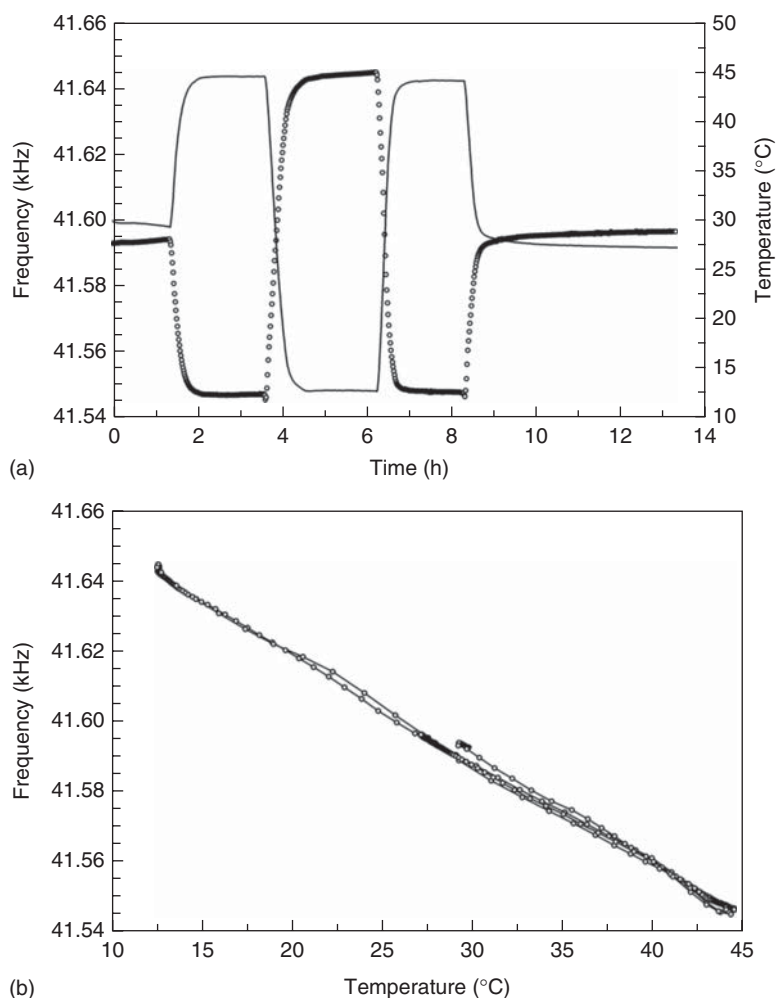


**Figure 1.16** The sample average temperature (continuous line) and the frequency of a longitudinal mode (open circles) as a function of time for a sample of Nova-culite (a) and the temperature–frequency characteristic (b). The temperature control was not as good as for the same experiment on Fontainebleau (Figures 1.12 and 1.14), but the behavior of this dense quartzite is clearly nonhysteretic.

factors: the power of the Peltier stage; the conductivity of the sample can and He exchange gas; and the thermal diffusivity of the sample. We believe that the helium gas permeates the rock and provides a high conductivity path to the interior of the rock, enabling it to reach thermal equilibrium more quickly than in vacuum. The rapidity with which the average lattice constant of the sample crystallites changes seems to bear this out; a large gradient would broaden the diffraction peaks. The aluminum can and frame are also of high conductivity, so it seems we might have made a more rapid step by increasing the power of the Peltier stage heat pump.



Observation shows that the time taken for the rock to attain elastic equilibrium after a given temperature step is several hours, so the temperature change over an interval of  $\sim 15$  min is relatively fast. Every element of material will be expanding or contracting according to the thermal expansion coefficients of quartz – the large crystallite volume matches this quickly, but other data [29] suggest that the overall expansion is close to 30% of the quartz (or dense quartzite) value implying that the grains expand or rotate into the pore space, placing large strains in the cementation. *We believe that the combined neutron diffraction results place the hysteretic behavior in the cementation*, a result similar to that reported for the SMARTS stress–strain data in [20].

The cement is generally a complex structure [1] – layered with possibly different morphologies, water content, and crystallinity in each layer – so a large number of potential strain-dependent energy structures might produce the microscopic hysteretic effects. Recent results with *very dry* Berea sandstone suggest that fluid water is not necessary for nonlinear or hysteretic effects, but monolayers of water within or on the cementation may still be active.

Finally, a note about the final external applied field was considered, applying an acoustic field to the rock while taking neutron diffraction data. While macroscopic measurements are relatively easy to track, the applied strain magnitudes are still small when compared with the strains produced in a stress–strain or change of temperature measurement. Nevertheless, an attempt was made to look for changes in the bulk crystalline structure of the rock by taking neutron TOF data during a few cycles of applied acoustic field and then turning that field off and repeating. No evidence of any changes was observed in the Rietveld analysis.

## Acknowledgments

We gratefully acknowledge the support of the US Department of Energy through the LANL/LDRD Program for this work. One of us (TWD) would additionally like to acknowledge the support from the DOE's Office of Basic Energy Sciences and Office of Geosciences under grant #DE-FG02-11ER16218 for some of this work.

## References

1. Haddad, S.C., Worden, R.H., Prior, D.J., and Smalley, P.C. (2006) Quartz cement in the Fontainebleau sandstone, Paris basin, France: crystallography and implications for mechanisms of cement growth. *J. Sediment. Res.*, **76**, 244–256.
2. Bourbie, T., Coussy, O., and Zinszner, B. (1987) *Acoustics of Porous Media*, *Institute Francais du Petrole Publications*, Editions Technip, Paris, (1986) (English translation).
3. Guyer, R.A. and Johnson, P.A. (2009) *Nonlinear Mesoscopic Elasticity*, Wiley-VCH Verlag GmbH, Print, ISBN: 9783527407033, Online ISBN: 9783527628261, doi: 10.1002/9783527628261.
4. TenCate, J.A. and Shankland, T.J. (1996) Slow dynamics in the nonlinear elastic

- response of Berea sandstone. *Geophys. Res. Lett.*, **23** (21), 3019–3022.
5. Adams, F.D. and Coker, E.G. (1906) *An Investigation into the Elastic Constants of Rocks, More Especially with Reference to Cubic Compressibility*, Carnegie Institute of Washington, Publication No. 46.
  6. Boitnott, G.N. (1993) Fundamental observations concerning hysteresis in the deformation of intact and jointed rock with applications to nonlinear attenuation in the near source region. Proceedings of the Numerical Modeling for Underground Nuclear Test Monitoring Symposium. Report LA-UR-93-3839, Los Alamos National Laboratory, p. 121.
  7. Hilbert, L.B. Jr., Hwang, T.K., Cook, N.G.W., Nihei, K.T., and Myer, L.R. (1994) in *Rock Mechanics Models and Measurements Challenges from Industry* (eds P.P. Nelson and S.E. Laubach), A. A. Balkema, Rotterdam, p. 497.
  8. Nihei, K.T., Hilbert, L.B. Jr., Cook, N.G.W., Nakagawa, S., and Myer, L.R. (2000) Frictional effects on the volumetric strain of sandstone. *Int. J. Rock Mech. Min. Sci.*, **37**, 121–132.
  9. Holcomb, D. (1981) Memory, relaxation, and microfracturing in dilatant rock. *J. Geophys. Res.*, **86** (B7), 6235–6248.
  10. McCall, K.R. and Guyer, R.A. (1994) Equation of state and wave propagation in hysteretic nonlinear elastic materials. *J. Geophys. Res.*, **99**, 23887.
  11. Guyer, R.A., McCall, K.R., Boitnott, G.N., Hilbert, L.B. Jr., and Plona, T.J. (1997) Quantitative implementation of Preisach-Mayergoyz space to find static and dynamic elastic moduli in rock. *J. Geophys. Res.*, **102**, 5281–5293.
  12. Claytor, K.E., Koby, J.R., and TenCate, J.A. (2009) Limitations of Preisach theory: elastic aftereffect, congruence, and end point memory. *Geophys. Res. Lett.*, **36**, L06304.
  13. Ide, J.M. (1937) The velocity of sound in rocks and glasses as a function of temperature. *J. Geol.*, **XLV**, October–November issue, 689–716.
  14. Ulrich, T.J. and Darling, T.W. (2001) Observation of anomalous elastic behavior in rock at low temperatures. *Geophys. Res. Lett.*, **28** (11), 2293–2296.
  15. Ulrich, T.J. (2005) Thesis. University of Nevada, Reno.
  16. Clark, V.A. (1980) Effect of volatiles on seismic attenuation and velocity in sedimentary rocks. PhD dissertation. Texas A&M, University Microfilms International, 8101583.
  17. TenCate, J.A., Smith, E., Byers, L.W., and Shankland, T.J. (2000) in *CP524, Nonlinear Acoustics at the Turn of the Millennium: ISNA 15* (eds W. Lauterborn and T. Kurz), American Institute of Physics, pp. 303–306.
  18. TenCate, J.A. (2011) in *Pure and Applied Geophysics, Special Issue on Brittle Deformation* (eds Y. Ben-Zion and C. Sammis), PAGEOPH Topical Volumes, Birkhauser, pp. 65–74.
  19. Lisowski, P.W. and Schoenberg, K.F. (2006) The Los Alamos Neutron Science Center. *Nucl. Instrum. Methods Phys. Res., Sect. A*, **562**, 910–914.
  20. Darling, T.W., TenCate, J.A., Brown, D.W., Clausen, B., and Vogel, S.C. (2004) Neutron diffraction study of the contribution of grain contacts to nonlinear stress-strain behavior. *Geophys. Res. Lett.*, **31**, L16604.
  21. Ino, T., Ooi, M., Kiyonagi, Y., Kasugai, Y., Maekawa, F., Takada, H., Muhrer, G., Pitcher, E.J., and Russell, G.J. (2004) Measurement of neutron beam characteristics at the Manuel Lujan Jr. neutron scattering center. *Nucl. Instrum. Methods Phys. Res., Sect. A*, **525**, 496–510.
  22. Zhao, Y., Zhang, J., Xu, H., Lokshin, K.A., He, D., Qian, J., Pantea, C., Daemen, L.L., Vogel, S.C., Ding, Y., and Xu, J. (2010) High-pressure neutron diffraction studies at LANSCE. *Appl. Phys. A*, **99**, 585–599.
  23. Hartig, C., Vogel, S.C., and Mecking, H. (2006) In-situ measurement of texture and elastic strains with HIPPO–CRATES. *Mater. Sci. Eng. A*, **437**, 145–150.
  24. Vogel, S.C. and Priesmeyer, H.-G. (2006) in *Neutron Scattering in Earth Sciences, Reviews in Mineralogy and Geochemistry*, vol. 63 (ed. H.-R. Wenk), pp. 27–57.
  25. Clausen, B., Lorentzen, T., and Leffers, T. (1998) Self-consistent modeling of the plastic deformation of FCC polycrystals

- and its implications for diffraction measurements of internal stresses. *Acta Mater.*, **46**, 3087.
26. Clausen, B., Lorentzen, T., Bourke, M.A.M., and Daymond, M.R. (1999) Lattice strain evolution during uniaxial tensile loading of stainless steel. *Mater. Sci. Eng.*, **A259**, 17.
  27. Migliori, A. and Sarrao, J.L. (1997) *Resonant Ultrasound Spectroscopy*, John Wiley & Sons, Inc.
  28. Johnson, P.A., Zinszner, B., and Rasolofosaon, P.N.J. (1996) Resonance and nonlinear elastic phenomena in rock. *J. Geophys. Res.*, **101** (B5), 11553–11564.
  29. Touloukian, Y.S., Judd, W.R., and Roy, R.F. (1981) *Physical Properties of Rocks and Minerals*, Thermophysical Data for High Porosity Sandstone, Purdue Research Foundation.

## 2

## Adsorption, Cavitation, and Elasticity in Mesoporous Materials

Annie Grosman and Camille Ortega

This chapter focuses on the role of the adsorption-induced strain in the adsorption process, in particular in the origin of the irreversibility of the process observed in mesoporous materials.

While the importance of stress and strain effects on surface physics has been extensively recognized, the elastic deformation of the solid is still ignored in the physics of adsorption in porous materials even though they have huge surface area compared to compact materials of the same volume.

Nevertheless, it is known for a long time that gas adsorption causes elastic deformation of the porous matrix. The reversible formation of an adsorbed film, which precedes capillary condensation, results in an extension of the porous material while, in the hysteresis region, the pores full of liquid are submitted to large negative pressures under the concave menisci that contract the porous matrix. The elastic deformation exhibits a hysteresis loop in the same pressure region as the adsorption phenomenon.

These deformations have been neglected in the overwhelming majority of adsorption studies. This default has two reasons. First, the deformations, typically in the range  $10^{-4}$  to  $10^{-3}$  in rigid porous solids that are the subject of study of this chapter, were (wrongly) considered to be small and were supposed to have small effects on the adsorption process; second, no experiment had contradicted the dominant models developed by Cohan [1] and Mason [2].

For more than 70 years, these models connect the origin and the shape of the hysteresis loop to the morphology of the porous solids. These are based on the idea that the emptying of a porous solid can be achieved only by the creation of a vapor path from the surface toward the interior of the solid via the propagation of receding concave menisci.

For disordered porous solids composed of cavities that are highly interconnected by constrictions, these models predicted that the cavities evaporate only after the emptying of these constrictions. Thus, the cavities do not empty independently of each other but via a percolation process, and the source of the interaction is the intersection. In the literature, this mechanism is referred to as pore-blocking/percolation mechanism. The shape of the hysteresis loop is then expected to be asymmetrical (type H2 in the IUPAC classification [3])

with a broad condensation branch rather characteristic of the large pore size distribution and a steeper evaporation branch, the slope of which is a complex function of the interconnection network.

Now, if the porous solid is composed of non-interconnected cylindrical pores, there is no obstacle to the evaporation which then occurs at thermodynamic equilibrium via the propagation of receding menisci. The pores empty independently of each other and the hysteresis loop should exhibit parallel branches (type H1 in the IUPAC classification), the slope of which reflects the pore size distribution. This is referred in the literature as Cohan's model.

These models were supported by experimental results obtained in porous glass and more recently in mesoporous silicas such as MCM-41 or SBA-15. Indeed, the hysteresis loop found in Vycor, a highly disordered porous glass, is asymmetrical. In the case of mesoporous silicas exhibiting a regular array of cylindrical pores, hysteresis loops of type H1 are observed.

New experiments have shown that collective effects occur during the evaporation from porous systems where the pores are not interconnected [4], leading to take into account a new parameter that couples the pores, namely, the adsorption-induced strain of the pore walls.

We report on experimental and theoretical arguments, which show that it is actually a key parameter in the physics of adsorption.

The following points are developed:

- 1) Experimental results obtained in porous silica SBA-15 and  $p^+$ -type porous silicon are shown which question the dominant models.
- 2) An elastic and thermodynamic approach of solid–fluid interface is presented, which shows the importance of surface elastic energy and surface stress in the porous solid–vapor and porous solid–liquid systems.
- 3) The influence on the adsorption process of an external stress exerted on the porous solid is shown by several experiments.
- 4) Experimental evidence is brought so that porous silicon empties via cavitation rather than via the propagation of menisci into the pores. Arguments in favor of the nucleation of gas bubbles on the pore wall surface (heterogeneous cavitation) rather than in the bulk fluid (homogeneous cavitation) are presented.

## 2.1

### Experimental Evidence of Collective Effects During Evaporation

#### 2.1.1

##### Porous Vycor Glass

Vycor is the prime example of disordered porous system. It is described as a 3D network of cavities of different sizes connected to one another by several constrictions.

Most of the cavities are located within the porous material and have no direct access to the gas reservoir but have indirect access through many constrictions and cavities. According to the pore-blocking/percolation model [2], if evaporation is commenced when the porous system is completely filled, a cavity cannot empty as long as a continuous vapor path is not created to the cavity from the vapor reservoir. But, as soon as the pressure is reduced to some critical value, the porous system begins to empty and many routes are created from the vapor reservoir to the buried pores that result in the emptying of the whole system in a cascade-like manner. Thus, the emptying of a disordered porous material is believed to take place through a percolation process. The boundary hysteresis loop (see Figure 2.1) is asymmetrical (type H2 in the IUPAC classification), with a broad condensation branch characteristic of the large pore size distribution and a steep evaporation branch that is the signature of collective effects during the emptying.

Now if the evaporation process is commenced when the porous system is not completely filled, a filled cavity can have a neighboring empty cavity, so that it can empty into this empty cavity, the desorbed material being carried by a series of condensation–evaporation steps to the bulk vapor. Therefore, the hysteretic behavior of a filled cavity depends on whether the adjacent cavities are filled or empty, and the shapes of the obtained primary descending scanning curves (PDSCs) are different from that of the boundary evaporation branch (see Figure 2.1).

Mason reproduced the asymmetrical boundary loop and the family of PDSCs obtained in Vycor with a number of interconnections per cavity equal to four on average [2]. Thus, it is believed that the observation of the hysteresis loop of type H2 and of the PDSCs represented in Figure 2.1 is the signature of the occurrence of a percolation process in disordered porous materials.

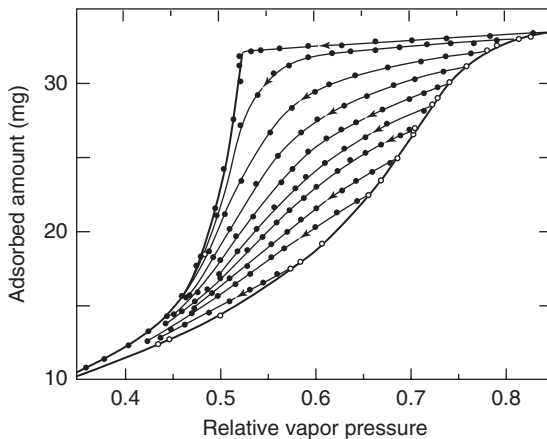


**Figure 2.1** Xenon adsorption isotherm and PDSCs measured at 151 K in porous Vycor glass. The sample weight is 61.60 mg. The solid lines are guide for eye. (Adapted from Ref. [2].)

## 2.1.2

**Porous Silicon**

This ordered porous system, formed on highly boron doped (1 0 0) Si substrate, is composed of straight tubular pores, perpendicular to the substrate, separated from each other by single-crystal Si walls of apparent constant thickness ( $\sim 5$  nm). The section of the pores by a plane parallel to the substrate is polygonal. The pore size distribution (PSD) is large, for example,  $13 \pm 6$  nm for a 50% porosity. The numerical treatment of transmission electronic microscopy plane views of the surface of the samples, a 2D image, yields the same porosity as that obtained by weighting that corresponds to the 3D morphology. These whole results suggest that, except the presence of different facets on the Si walls that yields to some roughness of which the amplitude is smaller than the wall thickness and *a fortiori* than the pore size, the pore section does not vary significantly along the pore axis (for more details, see Refs. [4] and [5]). Moreover, the pores are not interconnected [6] and their average direction is parallel to within  $0.1^\circ$  to the [100] crystal axis [7]. This system is hence very different from Vycor. However, the hysteretic behaviors represented in Figures 2.1 and 2.2 are very similar: the same asymmetrical hysteresis loop, the same PDSCs.

Moreover, the two subloops between the same pressure end points shown in Figure 2.3 are not superimposable. For independent domains, according to Preisach's model [8], they should be. We recall that in this model, adapted to capillary condensation in porous materials by Everett [9], a domain is defined by its condensation and evaporation pressures. Note that a correction must be brought to the subloops to account for the presence of an adsorbed film on the surface of the empty pores [4]. Indeed, this test can be rigorously applied only for systems composed of two state microsystems, which is not the case for adsorption in porous materials: a pore is not filled or empty but filled or empty

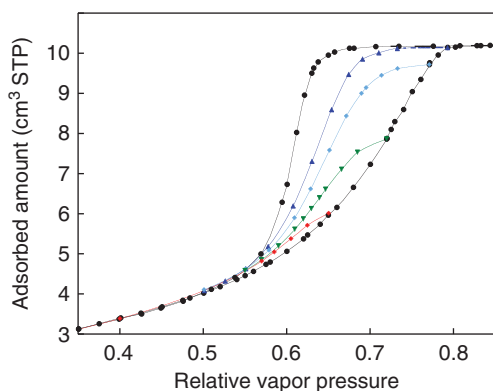


**Figure 2.2** Nitrogen adsorption isotherm at 77.4 K and PDSCs in a porous silicon layer of 50% porosity. The solid lines are guide for eye [4].

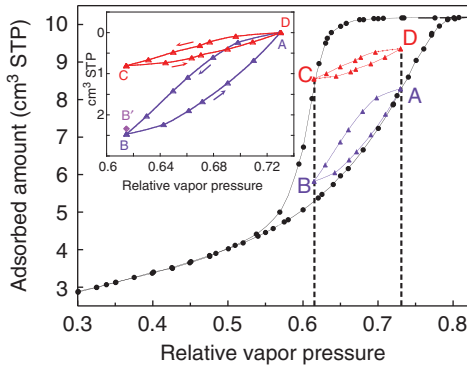


**Figure 2.3** Hysteresis loop shown in Figure 2.2 with two subloops measured between the same limiting pressures initiated on the primary filling (ABA) and draining (CDC) branches. The inset shows the two

subloops for which the right end points A and D are offset to overlap. The point B' accounts for the correction as described in the text. The solid lines are guide for eye [4].

with a film on the pore walls, the thickness of which depends on the pressure. In the inset of Figure 2.3, the point B' accounts for this correction.

We have then to explain collective effects during evaporation of an assembly of non-connected pores.

### 2.1.3

#### SBA-15 Silica

Similar observations have been made in other ordered porous systems such as SBA-15 [10] silica, which is a 2D hexagonal arrangement of cylindrical pores with narrow diameter distribution. Indeed, as shown in Figure 2.4, although a boundary hysteresis loop with two-step parallel branches (type H1 in the IUPAC

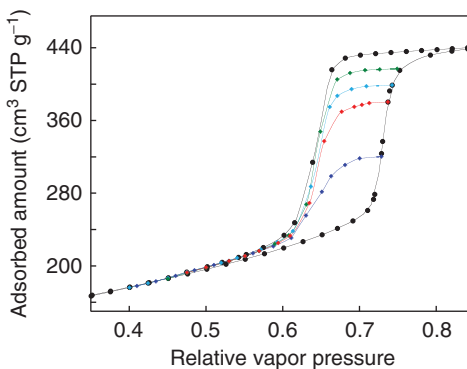


**Figure 2.4** Nitrogen adsorption isotherm at 77.4 K and PDSCs in SBA-15 silica. The solid lines are guide for eye [11].



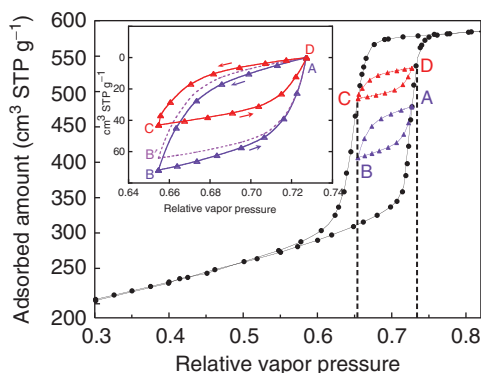


**Figure 2.5** Hysteresis loop shown in Figure 2.4 with two subloops measured between the same limiting pressures initiated on the primary filling (ABA) and draining (CDC) branches. The inset shows the two

subloops for which the right end points A and D are offset to overlap. The point B' accounts for the correction as described in the text. The solid lines are guide for eye [10].

classification) is obtained, which was considered as the signature of a model of independent pores [1], the PDSCs are qualitatively similar to those presented earlier and two subloops measured between the same pressure end points are not congruent (see Figure 2.5).

Note that the intrawall microporosity, which exists in such ordered tubular pores that open at both ends, does not play any role in the adsorption process in the mesopores in the sense that these micropores fill and empty in a pressure range far below the hysteresis loop.

The results presented in this section show that collective effects during the evaporation process occur in all ordered (SBA-15, porous Si) or disordered (Vycor) porous media, whether the pores are interconnected or not and whatever the shape of the hysteresis loop is.

Two approaches are proposed to explain the results obtained in the ordered porous solids SBA-15 and porous Si.

First, the pores are heterogeneous and can be divided into domains randomly distributed along the pore axis, which differ by the size and roughness or by the fluid–wall interaction [12–14]. They are not the pores but the domains inside each pore that interact, the evaporation of which is delayed by that of the narrowest (or most attractive) domains. This is reminiscent of a pore-blocking effect inside each pore.

Nevertheless, this approach fails to explain two major experimental results found in porous silicon, stress effects on the adsorption process developed in Section 2.4 and the absence of evaporation along the saturation plateau (see Figure 2.20). This is discussed in detail in Refs. [4, 5].

Moreover, to reproduce PDSCs similar to those found in porous silicon, it is necessary to introduce the calculations based on the pore-blocking/percolation model that has more than four connections per domain [2, 14] while, in this

approach, the material is assimilated to a 1D network of domains each of them being connected to two neighboring domains.

Second, we propose to find an explanation common to all the rigid porous solids in order to reproduce the whole results. For the purpose, on the basis of our morphological and adsorption studies, we have chosen to consider each pore in the ordered porous materials as a domain either filled or empty so that the previous results (Figures 2.3 and 2.5) show that the pores in SBA-15 and porous Si do not evaporate independently of each other. As these materials are weak or non-interconnected, we propose that the coupling parameter between pores could be the adsorption-induced strain of the pore walls, the thickness of which is typically some nanometers.

## 2.2

### Adsorption-Induced Strain

Adsorption and desorption of gas cause elastic deformations of the porous matrix. These deformations were studied in a number of systems such as Vycor, charcoal, silica aerogel, porous silicon, and more recently MCM-41 and SBA-15 mesoporous silicas (for references, see [15]). In disordered media, one measures the variation of the external dimensions of the material. In MCM-41 and SBA-15 silicas, which are hexagonal arrangements of cylindrical pores, the pore lattice can be measured by X-ray diffraction [16, 17]. In porous silicon, which is a single crystal, diffraction experiments allow to directly measure the interatomic distance. The magnitude of the deformation depends on the stiffness of the bulk material, on the porosity, and on the properties of the adsorbed molecules. For rigid porous materials, the relative deformations vary in the range  $10^{-4}$  to  $10^{-3}$ .

Despite the porous materials cited earlier have very different morphologies, the deformations during the condensation and evaporation of fluids present common features. Figure 2.6 represents schematically an adsorption isotherm of type H2 and typical adsorption-induced strains, which exhibit a hysteresis loop in the same pressure region as the adsorption phenomenon.

Along the reversible path OA preceding capillary condensation, the formation of an adsorbed film results in an extension of the porous material whose magnitude depends on the adsorbate–adsorbent couple. The 2D pressure exerted on the pore walls by the film is usually called spreading pressure. Between points A and B, where the condensation process takes place, a contraction is generally observed. During this step, the pores that sequentially fill from the smallest to the largest menisci are presumably formed at the top of the filled pores, and the thickness of the adsorbed film increases reversibly in the empty pores leading to a further extension of the porous material. Therefore, the net contraction generally observed during capillary condensation is attributed to the negative pressure created under the concave menisci. At point B, all the pores are filled. Along BC, a marked extension occurs, attributed to the vanishing of the negative pressure

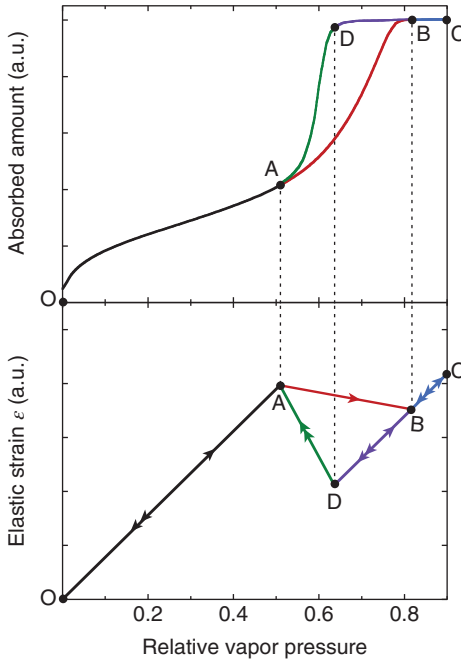


**Figure 2.6** Schematic representation of an adsorption isotherm presenting a hysteresis loop of type H2 and typical linear extension  $\varepsilon$  observed during the adsorption–desorption cycle.

within the fluid consequent upon the flattening of the concave menisci. Nevertheless, it is noteworthy that the final state C corresponds to an extension higher than that of the initial state O before adsorption, which suggests that the spreading pressure increases with the vapor pressure even when the pores are filled.

Conversely, along CD, a marked contraction occurs due to large negative fluid pressure generated by the formation of concave menisci. In the region BCD, named the saturation plateau, both adsorption and deformation data are reversible and no capillary empties.

Along DA, the pores evaporate and the deformation recovers the initial value at point A. From A to O, the path is the reverse of that along OA.

### 2.3

#### Thermodynamics of the Solid–Fluid Interface

In this section, we recall the elastic and thermodynamics properties of interfaces largely developed in publications devoted to surface and interface physics (see, e.g., [18, 19]). We extend this approach to the case of adsorption and capillary condensation in porous materials.

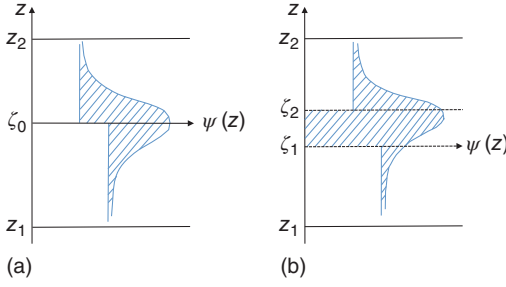


**Figure 2.7** Definition of the interfacial excess,  $\psi_s$  (shaded area), of a function  $\psi(z)$  with (a) a single dividing surface  $\zeta_0$  or (b) two dividing surfaces  $\zeta_1$  and  $\zeta_2$ .

We consider two homogeneous phases, one is the solid phase and the other is the fluid phase, separated by a planar interface perpendicular to the  $z$ -axis. There is no external force and no mass transfer between the two phases. To define the different interfacial excess quantities, we will use a single dividing Gibbs surface,  $\zeta_0$ , attached to the solid surface, which will prove to be the natural choice. The excess of an extensive function  $\psi(z)$ , shaded area in Figure 2.7(a), is defined by the equation:

$$\psi_s = \int_{z_1}^{z_2} \psi(z) dz - \psi_1[\zeta_0 - z_1] - \psi_2[z_2 - \zeta_0] \quad (2.1)$$

where  $\psi_1$  and  $\psi_2$  are the values of  $\psi(z)$  far from the interface.

Along the  $z$ -axis, the system is defined by two planes parallel to the interface initially at  $z_1, z_2$ . The interface area is  $A$ , and the volumes of the bulk phases are  $V_1 = A[\zeta_0 - z_1]$  and  $V_2 = A[z_2 - \zeta_0]$ . The fluid cannot induce shear in the solid, the strain and stress tensors,  $\epsilon_{ij}, \sigma_{ij}$ , are hence diagonal in both phases. Far from the interface, the strain and stress tensor elements are constant and depend only on  $z$  in the interfacial region. In the fluid, the stress tensor elements are all equal to  $-P$ , where  $P$  is the vapor pressure. The local mechanical condition  $\sum_j \frac{\partial \sigma_{ij}}{\partial x_j} = 0$  with  $x_1 = x, x_2 = y$ , and  $x_3 = z$ , leads to  $\sigma_{zz}$  constant in the whole system.

We assume that the interface remains plane during adsorption. It would be the case, for example, of a solid plate with the same fluid on both sides. The tangential strains,  $\epsilon_{xx}, \epsilon_{yy}$ , are thus necessarily independent of  $z$ .

To sum up:

- 1) The tangential strains,  $\epsilon_{xx}, \epsilon_{yy}$ , and the vertical stress,  $\sigma_{zz}$ , are the same on both sides of the interface.
- 2) The vertical strain  $\epsilon_{zz}$  and the horizontal stresses,  $\sigma_{xx}, \sigma_{yy}$ , vary in the interfacial region. They display surface excesses.

For simplicity, we consider 2D strains ( $\epsilon_{xx}, \epsilon_{zz}$ ). The displacements of the two planes parallel to the interface at  $z_1, z_2$  are  $u_{z,1}(z_1)$  and  $u_{z,2}(z_2)$ , and the variation of the surface area is  $\delta A = A \delta \epsilon_{xx}$ . The fluid can exchange molecules with the reservoir at constant temperature.

The change of the total elastic energy produced by infinitesimal deformations  $\delta\epsilon_{xx}$  and  $\delta\epsilon_{zz}$  is as follows:

$$\delta W = A \left[ \int_{z_1}^{z_2} (\sigma_{xx} \delta\epsilon_{xx} + \sigma_{zz} \delta\epsilon_{zz}) dz \right]. \quad (2.2)$$

As  $\delta\epsilon_{xx}$  and  $\delta\epsilon_{zz}$  are independent of  $z$ , Eq. 2.2 may be written

$$\delta W = A \left[ \delta\epsilon_{xx} \int_{z_1}^{z_2} \sigma_{xx} dz + \sigma_{zz} \int_{z_1}^{z_2} \delta\epsilon_{zz} dz \right]. \quad (2.3)$$

Far from the interface, the bulk stress  $\sigma_{xx}^b$  and strain  $\epsilon_{zz}^b$  are constant. The change in the interfacial elastic energy is defined as any other surface excess (see Figure 2.7(a)):

$$\delta W_s = A[\sigma_{xx,s} \delta\epsilon_{xx} + \sigma_{zz} \delta\epsilon_{zz,s}] \quad (2.4)$$

where the surface stress  $\sigma_{xx,s}$  is defined by

$$\sigma_{xx,s} = \int_{z_1}^{z_2} \sigma_{xx} dz - \sigma_{xx,1}^b [\zeta_0 - z_1] - \sigma_{xx,2}^b [z_2 - \zeta_0] \quad (2.5)$$

where  $\sigma_{xx,2}^b = -P$ , the vapor pressure.

The definition of the surface strain  $\epsilon_{zz,s}$  depends somewhat on whether we are in presence of a solid–solid or a solid–fluid interface.

For a solid–solid interface, we have

$$\epsilon_{zz,s} = \int_{z_1}^{z_2} \epsilon_{zz} dz - \epsilon_{zz,1}^b [\zeta_0 - z_1] - \epsilon_{zz,2}^b [z_2 - \zeta_0] \quad (2.6)$$

where  $\epsilon_{zz}$  is related to the component displacement  $u_z(z)$  attached to a given atom by  $\epsilon_{zz} = du_z/dz$ . Far from the interface,  $u_z$  varies linearly with  $z$  and may be written as follows:

$$u_{z,i}^b(z) = \epsilon_{zz,i}^b [z - \zeta_0] + u_{z,i}^b(\zeta_0) \quad (i = 1, 2) \quad (2.7)$$

From Eq. 2.6, we obtain  $\epsilon_{zz,s} = u_{z,2}^b(\zeta_0) - u_{z,1}^b(\zeta_0)$ , which is the difference between the extrapolated values of the two bulk displacement components at  $\zeta_0$ .

For a solid–fluid interface, a difficulty appears since the notion of displacement attached to a given atom does not make any sense in the fluid. The variation of  $\epsilon_{zz}$  with  $z$ , induced by the presence of the surface, occurs in the solid and  $\epsilon_{zz,s}$  is defined by

$$\epsilon_{zz,s} = \int_{z_1}^{\zeta_0} \epsilon_{zz} dz - \epsilon_{zz,1}^b [\zeta_0 - z_1] = u_{z,1}(\zeta_0) - u_{z,1}^b(\zeta_0) \quad (2.8)$$

where  $u_{z,1}(\zeta_0)$  is the actual displacement component attached to the atoms at  $\zeta_0$ . The surface strain  $\epsilon_{zz,s}$  is now the difference between the actual position of the surface atoms and the ideal position, which they would have without the influence of the surface.

To determine the change in the interfacial free energy,  $\delta F_s$ , we must take into account the change in the chemical surface free energy:

$$\delta F_s = \delta W_s + \mu_1 \delta N_{s,1} + \mu_2 \delta N_{s,2} \quad (2.9)$$

where  $\mu_1$  and  $\mu_2$  are the solid and fluid chemical potentials, and  $N_{s,1}$  and  $N_{s,2}$  are the surface excesses of the number of the solid and fluid atoms.

As regards the solid, when increasing the volume and the surface area, one cannot bring new matter to fill the new volume and the new surface. If we define the interface by two fixed Gibbs surfaces,  $\zeta_1$  in the solid and  $\zeta_2$  in the fluid (see Figure 2.7(b)), the change in the number of the interfacial solid atoms is equal to the number of atoms which cross  $\zeta_1$ , that is,

$$\delta N_{s,1} = A \rho_1 \delta u_{z,1}(\zeta_1) \quad (2.10)$$

where  $u_{z,1}(\zeta_1)$  is the component displacement of the atoms at  $\zeta_1$  and  $\rho_1$  is the number of solid atoms per unit volume. If  $\zeta_1$  is attached to the solid atoms, then  $\delta N_{s,1} = 0$ .

The choice of a single Gibbs surface  $\zeta_0$  attached to the surface appears as the best choice when studying adsorption on solid surface: the embarrassing variable  $\delta N_{s,1}$  disappears and  $\epsilon_{zz,s}$  has a simple physical interpretation; it is the additional displacement of the surface atoms induced by the presence of the surface (see Eq. 2.8).

As regards the fluid, it is necessary to distinguish the region preceding capillary condensation from the hysteresis loop region. In the first case, we are in presence of a solid–vapor interface and the number of fluid molecules displays a surface excess,  $N_{s,2}$ , which is practically equal to the number of adsorbed molecules currently determined in porous materials by volumetric or gravimetric measurements. In the second case, we are in presence of a solid–liquid interface, we will neglect the variation of the liquid density, and consequently the surface number of fluid molecules  $N_{s,2} \simeq 0$ .

### 2.3.1

#### The Solid–Vapor Interface

The change in the surface free energy is as follows:

$$\delta F_s = A \left[ \sigma_{xx,s} \delta \epsilon_{xx} + \sigma_{zz} \delta \epsilon_{zz,s} + \mu \frac{\delta N_s}{A} \right] \quad (2.11)$$

where we have put  $N_{s,2} = N_s$  and  $\mu_2 = \mu$ , the chemical potential of the vapor.

Equation 2.11 means that the variation of the surface free energy is due to the following parameters:

- 1) the work of surface stress  $\sigma_{xx,s}$  upon a change of bulk strain  $\delta \epsilon_{xx}$ ;
- 2) the work of bulk stress  $\sigma_{zz}$  upon a change of surface strain  $\delta \epsilon_{zz,s}$ ;
- 3) adsorption onto the surface of some fluid molecules (last term).

The surface free energy is the sum of two terms: a term of surface elastic energy proportional to  $A$ ; and a term of surface chemical energy proportional to  $N_s$ :

$$F_s = \gamma A + \mu N_s \quad (2.12)$$

Its differential is

$$dF_s = \gamma dA + A d\gamma + \mu dN_s + N_s d\mu \quad (2.13)$$

Equating Eqs. 2.11 and 2.13, one finds the Gibbs–Duhem equation

$$d\gamma = (\sigma_{xx,s} - \gamma) \delta \epsilon_{xx} + \sigma_{zz} \delta \epsilon_{zz,s} - \frac{N_s}{A} d\mu \quad (2.14)$$

from which we obtain the Shuttleworth's equation

$$\sigma_{xx,s} = \gamma + \left[ \frac{\partial \gamma}{\partial \epsilon_{xx}} \right]_{\mu, \epsilon_{zz,s}} \quad (2.15)$$

and the Gibbs adsorption isotherm

$$\frac{N_s}{A} = - \left[ \frac{\partial \gamma}{\partial \mu} \right]_{\epsilon_{xx}, \epsilon_{zz,s}} \quad (2.16)$$

Using Eq. 2.16,  $\Delta \gamma$  can be determined from adsorption data  $N_s(\mu)$ :

$$A \Delta \gamma = - \int N_s d\mu = - \int N_s k_B T \frac{dP}{P} \quad (2.17)$$

where  $k_B$  is Boltzmann's constant.

There are very few experiments in which both the adsorption and induced deformation are measured. The most complete study dates from 1950s. Figure 2.8 shows the isotherm adsorption of water in a porous glass rod and the variation of the length rod measured by Amberg and McIntosh [20].

In the region of reversible adsorption preceding capillary condensation, we observe a marked extension  $\epsilon$  of the rod length. As shown in Figure 2.9,  $\epsilon$  varies linearly with  $\int N_s k_B T dP/P$ :

$$A[\gamma(\epsilon) - \gamma(0)] = - \int_0^P N_s k_B T \frac{dP}{P} = -k \epsilon \quad (k > 0) \quad (2.18)$$

The Shuttleworth's relation (Eq. 2.15) tells us that if  $\gamma$  varies linearly with  $\epsilon$ , the same goes for the surface stress:

$$\sigma_{xx,s}(\epsilon) - \sigma_{xx,s}(0) = \gamma(\epsilon) - \gamma(0) = -\frac{k}{A} \epsilon \quad (k > 0) \quad (2.19)$$

In the physics of adsorption, the changes of the surface elastic energy and surface stress (also called spreading pressure) are equal and vary linearly with the strain.

Let us determine now the relationship between the proportionality factor  $k$  and the elastic constants of the solid. We have seen earlier that the mechanical equilibrium along the  $z$ -axis is realized by the condition  $\sigma_{zz}$  constant. It remains to find the condition that satisfies the mechanical equilibrium along the  $x$ -axis. The

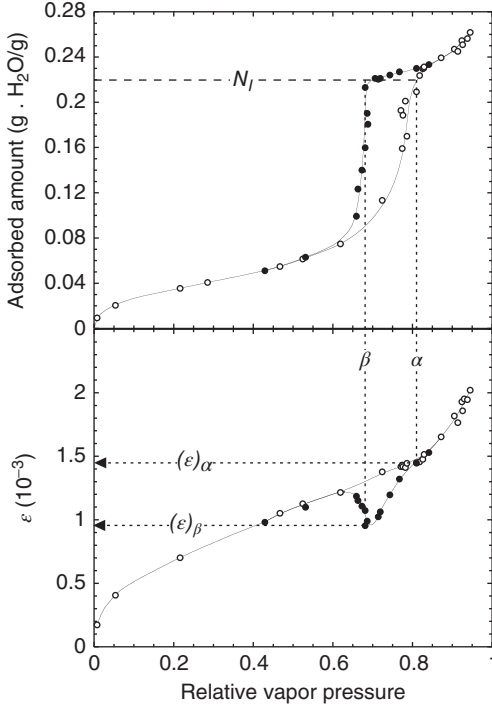


**Figure 2.8** Adsorption isotherm of water at 18.75°C ( $P_0 = 16.22$  mmHg) in a porous glass rod and the corresponding rod extension  $\epsilon$ . (Adapted from Ref. [20].) For a given adsorbed amount, equal to

0.22 g.H<sub>2</sub>O/g.porous glass, we have represented the two corresponding states of the system,  $\alpha$  [ $P_\alpha/P_0 = 0.81$ ,  $(\epsilon)_\alpha = 0.145 \times 10^{-2}$ ] and  $\beta$  [ $P_\beta/P_0 = 0.68$ ,  $(\epsilon)_\beta = 0.096 \times 10^{-2}$ ].

change in the total elastic energy, including the surface, the bulk of the fluid and that of the solid, is as follows:

$$\delta W = -P\delta V_2 + V_1 \sum_{ii} \sigma_{ii,1}^b \delta \epsilon_{ii,1}^b + \delta W_s \quad (i = x, z) \quad (2.20)$$

where  $\delta V_2 = V_2 \delta \epsilon_{xx} + A \delta(z_2 - \zeta_0)$ .

The mechanical equilibrium condition along the  $x$ -axis,  $\partial W / \partial \epsilon_{xx} = 0$ , leads to

$$-PV_2 + A\sigma_{xx,s} + V_1 \sigma_{xx,1}^b = 0 \quad (2.21)$$

Using again the data of Ref. [20], we can show that the first term  $-PV_2$  is very small with regard to the second term. In the relative pressure gap  $[0 - 0.6]$ , one finds  $PV_2 = 2.86 \times 10^{-4} \text{ J g}^{-1}$  while  $A\Delta\gamma = A\Delta\sigma_{xx,s} = -16.7 \text{ J g}^{-1}$ .

The mechanical equilibrium becomes

$$A \sigma_{xx,s} \simeq -V_1 \sigma_{xx,1}^b \simeq -V_1 C(E, \nu) \epsilon_{xx} \quad (2.22)$$

where  $C(E, \nu)$  is a function of the Young modulus  $E$  and the Poisson ratio  $\nu$ .



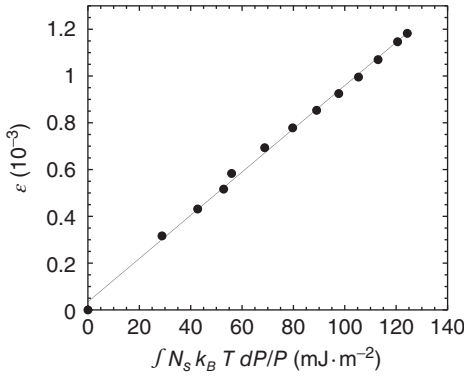


**Figure 2.9** Linear extension  $\epsilon$  of a porous glass rod during water adsorption at 18.75°C as a function of  $\int_0^P N_s k_B T dP/P$  (see Eq. 2.17). The surface area equals 129 m<sup>2</sup> g<sup>-1</sup> and the regression coefficient of the linear fit is 0.999. (Adapted from Ref. [20].)

Equations 2.18, 2.19, and 2.22 show that the bulk stress can be calculated quite simply from adsorption data. Equation 2.22 shows also that the factor  $k$  defined by Eq. 2.18 is only a function of the elastic constants of the bulk solid.

In the case of real porous materials that cannot be assimilated to an assembly of planes, the surface stress cannot be defined by Eq. 2.5 but rather by

$$\Delta\sigma_s = \frac{(\partial\gamma A)}{\partial A} \quad (2.23)$$

However, the mechanical equilibrium still leads to a linear relationship between the surface stress and the strain [15]. For instance, for isotropic materials such as porous Vycor glass where the extension of the material is the same in any direction,

$$A[\sigma_s(\epsilon) - \sigma_s(0)] = A[\gamma(\epsilon) - \gamma(0)] = -k \epsilon \simeq -V_1 C(E, \nu)\epsilon \quad (2.24)$$

where the proportionality factor  $C(E, \nu)$  is of course different from that introduced in Eq. 2.22.

### 2.3.2

#### The Solid–Liquid Interface

We consider the same system as above but with a liquid phase in contact with the solid. From a practical point of view, this can be realized with a slit pore made up of two parallel flat walls: as the vapor pressure is increased from  $P = 0$ , the adsorbed film thickness increases on both sides and reaches a critical value from which liquid bridges can be formed between the two walls and capillary condensation occurs.

As already noted, we will neglect the variation with  $z$  in the liquid density, so that  $N_s \simeq 0$ . The variation in the surface free energy is thus only of elastic origin.

Equation 2.11 becomes

$$\delta F_s = A[\sigma_{xx,s} \delta \epsilon_{xx} + \sigma_{zz} \delta \epsilon_{zz,s}] \quad (2.25)$$

and the surface free energy is simply

$$F_s = \gamma A. \quad (2.26)$$

The variation  $\Delta \gamma$  can be only determined by measuring the strains and using the mechanical equilibrium condition 2.21:

$$-P_1 V_2 + A \sigma_{xx,s} + V_1 \sigma_{xx,1}^b = 0. \quad (2.27)$$

$P_1$  is the liquid pressure given by Laplace–Kelvin equation

$$P_1 = P + \frac{RT}{v_1} \ln \frac{P}{P_0} \quad (2.28)$$

where  $v_1$  is the molar volume of the liquid.

The term  $-P_1 V_2$  cannot be neglected any more as the term  $-PV_2$  was it above. For water at 18.75°C, in the relative pressure gap [0.7 – 1],  $\Delta P_1 \simeq 48$  MPa which is four orders of magnitude higher than the variation  $\Delta P \simeq 1.3$  kPa of the vapor pressure in the relative pressure gap [0 – 0.6].

Equation 2.27 means that the bulk stress originates in the surface stress, as in Eq. 2.22, and also in the liquid pressure.

The following analyses of the results obtained with water at 18.75°C already shown in Figure 2.8 and with butane at –6.2°C [20, 21] support this prediction. In Figure 2.10,  $\epsilon$  and  $P_1$  are represented as a function of  $\ln p$  between  $p = 0.7$  and  $p = 0.95$ .

The slope of  $P_1$  versus  $\ln p$  is 5.9 times higher for water than for butane while the slope of  $\epsilon$  versus  $\ln p$  is only 1.9 times higher. In other words, as noted by the authors, the compressibility of porous glass measured with butane is three times higher than that measured with water. In those days, this embarrassing result was discussed at length without finding solution. Actually, the above results show that the deformation does not depend only on the liquid pressure but also on the variation of the surface stress according to the equilibrium Eq. 2.27. Quinn and McIntosh [21] were fully aware of the variation of  $\gamma$  since they included it in the variation of the total free energy on the saturation plateau, but they perhaps did not make the link between surface energy and surface stress.

As shown in Figure 2.10, the relation  $\epsilon$  versus  $P_1$  is practically linear. Putting

$$P_1 \simeq \frac{RT}{v_1} \ln \frac{P}{P_0} = C_1 (\epsilon - \epsilon_0) \quad (C_1 > 0) \quad (2.29)$$

where  $\epsilon_0$  is the extension of the rod at  $P_0$ , Eq. 2.27 may be rewritten for isotropic porous solids such as Vycor as

$$\begin{aligned} A[\sigma_s(\epsilon) - \sigma_s(\epsilon_0)] &= A[\gamma(\epsilon) - \gamma(\epsilon_0)] \\ &= -[V_1 C(E, v) - V_2 C_1](\epsilon - \epsilon_0). \end{aligned} \quad (2.30)$$

This equation means that when the pores are full of liquid, the surface energy varies linearly with the strain but the linearity factor depends not only on the

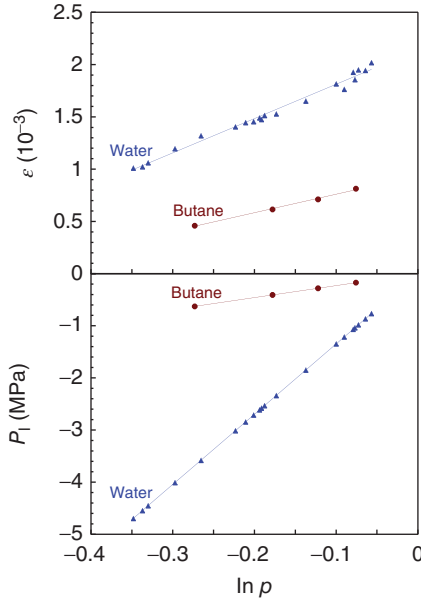


**Figure 2.10** Linear extension of a porous glass rod induced by adsorption of water at 18.75°C and of butane at -6.2°C as a function of  $\ln (P/P_0)$ . We have also

represented the liquid pressure  $P_l$  calculated using Eq. 2.28 as a function of  $\ln (P/P_0)$  on the saturation plateau. (From data of Refs. [20, 21].)

solid elastic constant  $C(E, \nu)$  as in the region preceding capillary condensation (see Eq. 2.24) but also on the nature of the fluid and on the temperature. This coefficient, which is the difference between two positive terms, may be *a priori* positive, negative, or null. In the experiments illustrated in Figure 2.10,  $V_2 C_1$  equals  $\sim 0.88 \times 10^4 \text{ J.g}^{-1}$  for water and  $\sim 0.29 \times 10^4 \text{ J.g}^{-1}$  for butane, values that have to be compared to  $V_1 C(E, \nu) \simeq 1.39 \times 10^4 \text{ J.g}^{-1}$ .

This shows that the term  $V_2 C_1$  is of the same order of magnitude than the term  $V_1 C(E, \nu)$  and varies significantly with the nature of the fluid. We will come back to this question in Section 2.5.3.2.

Another important question in the physics of adsorption is the variation of the total free energy on the saturation plateau between two states ( $\alpha, \beta$ ) on the condensation and evaporation branches of the hysteresis loop (see Figure 2.8).

The total free energy including the surface and the bulks of the fluid and solid is as follows:

$$F = -P_l V_2 + \mu N_l + \gamma A + W_1 \quad (2.31)$$

where  $N_l$  is the number of liquid atoms and  $W_1$  is the elastic energy of the bulk solid.  $W_1$  varies quadratically with  $\varepsilon$  and can be neglected with regard to  $\gamma A$ .

The Gibbs–Duhem equation corresponding to the free energy of the bulk fluid (the first two terms) is

$$-V_2 dP_1 + N_1 d\mu = 0 \quad (2.32)$$

As  $V_2$  and  $N_1$  are practically constant, the variation of the free energy of the bulk fluid is null. It is important to note that making the assumption  $N_s \simeq 0$  means that  $P_1$  varies according to the Laplace–Kelvin equation 2.28.

The variation of the total free energy is hence given by

$$F(\beta) - F(\alpha) \simeq A[\gamma(\epsilon_\beta) - \gamma(\epsilon_\alpha)] = -[V_1 C(E, v) - V_2 C_1](\epsilon_\beta - \epsilon_\alpha) \quad (2.33)$$

For water we found  $F(\beta) - F(\alpha) \simeq +2.5 \text{ J g}^{-1}$ , whereas the corresponding variation of the chemical potential of the fluid equals  $-5.14 \text{ J g}^{-1}$ .

These results show that

- 1) the evaporation branch represents states of higher energy than that of the condensation branch;
- 2) the surface energy is an important parameter in the physics of adsorption;
- 3) the change in the total free energy of the solid–liquid system on the saturation plateau is essentially due to the variation of the surface elastic energy, a parameter that is still ignored in the overwhelming majority of studies!

## 2.4

### Stress Effect on the Adsorption Process

We have seen in Section 2.2 that gas adsorption causes elastic deformation of porous solids. In this section, we are interested in the reciprocal effect, predicted by the third Newton's law, of an external stress exerted on the porous matrix on the adsorption process itself.

For the purpose, we report on two experiments [22] made with porous silicon layers with which it is possible (i) to prepare identical porous layers either supported by or detached from the Si substrate in which they are formed and (ii) to change the pore length.

In these experiments, the Si substrate plays the role of an external stress exerted on the porous matrix we can monitor, from zero (free standing porous layers), by varying the pore length over substrate thickness ratio.

#### 2.4.1

##### Supported and Free Standing Porous Si Layers

Porous silicon layers are prepared by anodic dissolution of highly boron-doped (1 0 0) Si single crystal in hydrofluoric acid/ethanol (HF/EtOH) solutions. We thus obtain samples with a porous part supported by a silicon substrate. Once the desired pore length is obtained, the current density can be increased up to a value corresponding to the electropolishing regime during which the Si walls are

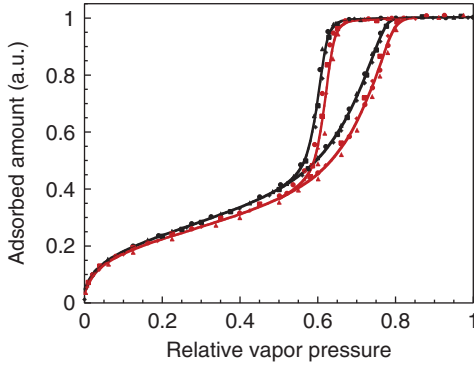


**Figure 2.11** Nitrogen adsorption isotherms at 77.4 K for several porous silicon layers, 20  $\mu\text{m}$  thick, either supported by (black symbols) or detached from (red symbols) the silicon substrate. The solid lines are interpolations of the mean values. The porosity is 50%.

dissolved at the bottom of the pores. The free standing porous Si layer (membrane) thus obtained is identical to the corresponding supported layer.

The isotherms for a supported porous layer and its corresponding membrane are distinct (see Figure 2.11). In the region of reversible adsorption, the adsorbed amount is lower for the membrane than for the supported layer, and the capillary condensation occurs at higher pressure in a concomitant way.

These results can be explained by the different elastic strain undergone by the two layers on account of the stress exerted by the substrate which prevents a deformation parallel to the substrate. According to the classical elasticity theory, for a given vapor pressure, this leads to an additional expansion along the pore axis such as

$$\epsilon_s = \beta \epsilon_m \text{ with } \beta > 1 \quad (2.34)$$

the indices  $s$  and  $m$  referring to the supported layer and membrane. According to the data found in Ref. [23],  $\beta \simeq 1.2$ .

In the region preceding capillary condensation, the surface energy varies linearly with the strain as  $A\Delta\gamma = -k\Delta\epsilon$  where  $k$  is a proportionality factor depending not only on the elastic constants of the porous solid (see Eq. 2.19 in Section 2.3.1) but also obviously on the external stress exerted on the porous layer. We have hence two relationships:

$$\begin{aligned} A\Delta\gamma_s &= -k_s\Delta\epsilon_s \\ A\Delta\gamma_m &= -k_m\Delta\epsilon_m \end{aligned} \quad (2.35)$$

From adsorption data presented in Figure 2.11 and using the Gibbs adsorption Eq. 2.16, we find  $A\Delta\gamma_s = 1.11 \times A\Delta\gamma_m$ . Using Eqs. 2.34 and 2.35, one finds  $k_s = (1.11/\beta)k_m \simeq 0.925 \times k_m$ . If in a coarse approach, we suppose that porous silicon behaves like an isotropic body,  $k_s/k_m = (1 - \nu)/(1 + \nu) \leq 1$ , which is in qualitative agreement with the experimental value. Now, in order to explain quantitatively the

difference between the two isotherms, it will be necessary to measure the induced deformation in both layers and to model these anisotropic geometries.

#### 2.4.2

##### Monitoring of the External Stress

The stress exerted by the substrate on the porous matrix can be partly relaxed by making thicker porous Si layers.

This effect is illustrated in Figure 2.12, which shows the nitrogen adsorption isotherms for supported porous Si layers of increasing thickness. Up to a thickness of 30  $\mu\text{m}$ , the isotherms are superimposed and then they shift toward that of the membrane, and for the 100  $\mu\text{m}$  thick supported layer, the isotherm is superimposed on that of the membrane. Simultaneously to the shift of the hysteresis loop, the adsorbed amount at low pressure decreases continuously (see inset of Figure 2.12).

These results can be explained by the breaking of Si–Si bonds under the effect of the stresses at the porous layer–substrate interface. The formation of a porous layer in a Si wafer produces an elastic bending of the wafer that becomes convex (see Figure 2.13). This shows that the supported porous layer behaves like an

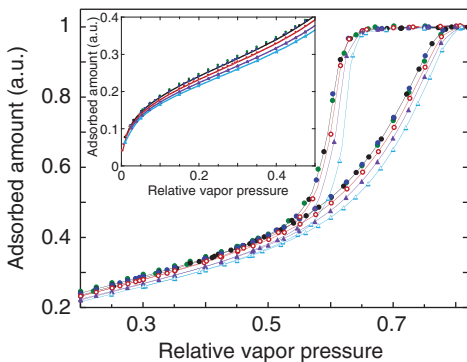


**Figure 2.12** Nitrogen adsorption isotherms at 77.4 K for 10  $\mu\text{m}$ , 20  $\mu\text{m}$ , 30  $\mu\text{m}$ , 40  $\mu\text{m}$ , 50  $\mu\text{m}$ , and 100  $\mu\text{m}$  thick supported porous silicon layers. The inset shows the corresponding amounts reversibly adsorbed

before capillary condensation. The isotherms for layers 10  $\mu\text{m}$ , 20  $\mu\text{m}$ , and 30  $\mu\text{m}$  (symbols:●) thick are superimposed in the whole pressure range. The lines are guides for eye.

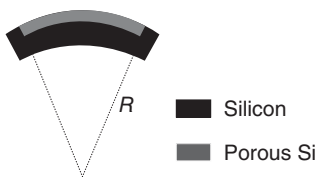


**Figure 2.13** The stress at the porous layer–silicon substrate interface produces an elastic bending of the substrate, which becomes convex with a radius of curvature  $R$ .

epitaxial layer over silicon, which would have a positive lattice mismatch parallel to the interface,  $(\Delta a/a)_{//}$ . The curvature radius is given by the classical theory of elasticity as

$$R = C_1 \frac{1}{(\Delta a/a)_{//}} \frac{t^2}{t_p} \quad (2.36)$$

where  $C_1$  is a function of elastic constants of the porous layer and substrate,  $t$  is the thickness of the substrate, and  $t_p$  is the thickness of the porous layer.

Moreover, the stress at the interface between porous layer and substrate is given by

$$\sigma = C_2 \frac{t^2}{R} \quad (2.37)$$

where  $C_2$  is a function of elastic constants of the substrate.

From Eqs. 2.36 and 2.37, we get

$$\sigma = \frac{C_2}{C_1} (\Delta a/a)_{//} t_p \quad (2.38)$$

As the porous layer thickness is increased, the stress at the porous layer–substrate interface increases and the radius of curvature decreases as expected by the classical theory of elasticity but for layers thicker than 30  $\mu\text{m}$  it deviates more and more, in relative terms, from the theoretical values as shown in Figure 2.14. This phenomenon is even more visible in the inset of Figure 2.14, which shows the relationship  $(t^2/R)$  versus  $t_p$ .

This shows that an increasing number of Si–Si bonds break when increasing the thickness from 30 to 100  $\mu\text{m}$ . The stress exerted by the substrate is thus partly

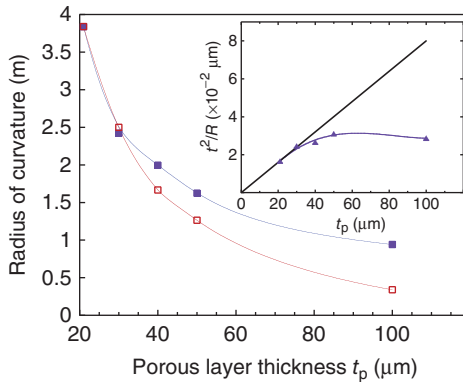


**Figure 2.14** Radius of curvature  $R$  measured from Newton's rings ( $\blacksquare$ ) and calculated from Eq. 2.36 ( $\square$ ), as a function of the porous layer thickness,  $t_p$ . The  $R$  values correspond to several measurements with a deviation of  $\sim 2\%$ . The inset shows the experimental values of  $t^2/R$  as a function of  $t_p$  where  $t$  is the substrate thickness ( $\blacktriangle$ ). The straight line that passes by the origin and the first two experimental points is calculated from Eq. 2.36. The porosity is 50%.

relaxed by the formation of dislocations, which results in the shift of the isotherms toward that of the membrane when the porous layer thickness is increased from 30 to 100  $\mu\text{m}$ .

A third experiment presented in Section 2.5 supports these earlier results and confirms the significant influence of an external stress exerted to the porous matrix on the adsorption process.

## 2.5

### Cavitation in Metastable Fluids Confined to Linear Mesopores

In Section 2.1, we have seen that collective effects occur during the evaporation process in ordered or disordered porous materials even if the pores are not interconnected as it is the case for porous silicon. Moreover, we have shown in Section 2.3 that the surface energy is a key parameter in the physics of adsorption.

To precise how the surface energy could couple the pores during the evaporation process, we need to understand the desorption mechanism itself.

Question then arises whether the fundamental concept of receding meniscus according to which the emptying of a porous solid can be done only by the creation of a vapor path from the surface toward the interior of the solid, which is the base of the Cohan's model and of the pore-blocking/percolation mechanism, is still valid if we take into account the elastic strain of the solid?

To answer this question, we checked the validity of pore-blocking effect by reproducing artificially the so-called ink-bottle geometry and making superimposed porous Si layers named Si/B/A and Si/A/B duplex porous layers where the pore diameters of layer A are narrower on average than those of layer B [5]. The method consists of first making a porous layer with chosen porosity and then changing the formation conditions, that is, the HF/EtOH solution and/or the current density value to make a second porous layer of different porosity underlying the first porous layer. The formation of the second porous layer does not affect the morphology of the first porous layer.

Elemental nitrogen adsorption isotherms in layers A and B either supported by or detached from the silicon substrate are measured and used to analyze those performed at 77.4 K in both Si/B/A and Si/A/B configurations.

#### 2.5.1

##### The Elemental Isotherms

Figure 2.15 shows the nitrogen adsorption isotherms at 77.4 K for layers  $A_s$  and  $B_s$  supported by the substrate and for the corresponding membranes  $A_m$  and  $B_m$ . The two pore size distributions (PSDs) determined by numerical treatment of transmission electron microscopy (TEM) plane views are presented in the inset [4].



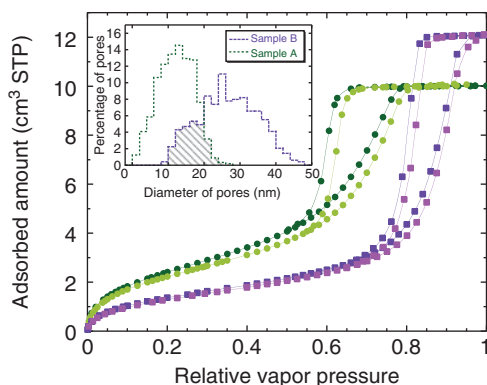


**Figure 2.15** Nitrogen adsorption isotherms at 77.4 K for supported porous silicon layers  $A_s$  (●) and  $B_s$  (■) and their corresponding free-standing layers, named membranes  $A_m$  (●) and  $B_m$  (■). The inset shows the two PSDs,

$13 \pm 6$  nm and  $26 \pm 14$  nm, for samples A and B of 50% and 70% porosity, respectively. The hatched region represents the overlap of the two PSDs. The lines are guides for eye.

## 2.5.2

### Si/A/B and Si/B/A Configurations

Figure 2.16 shows the nitrogen adsorption isotherms at 77.4 K measured in the duplex porous layers Si/B/A and Si/A/B.

Since the pore density is greater for sample A ( $3.7 \times 10^{11} \text{ cm}^{-2}$ ) than for sample B ( $1.2 \times 10^{11} \text{ cm}^{-2}$ ), layer A has inevitably dangling walls at the interface between the two layers in the Si/B/A configuration. The inset of Figure 2.16 schematically represents the two configurations.

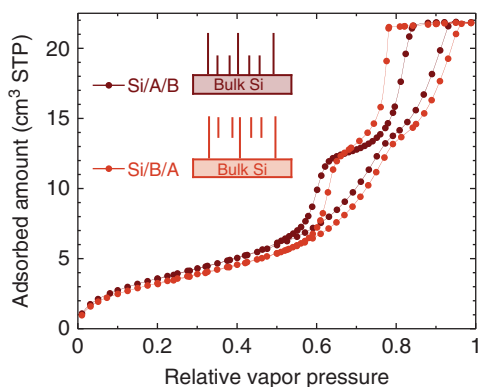


**Figure 2.16** Nitrogen adsorption isotherms at 77.4 K for Si/A/B (●) and Si/B/A (●) duplex porous layers, schematically represented in the inset. The lines are guides for eye.

### 2.5.2.1 Si/A/B Configuration

Let us analyze the isotherm shown in Figure 2.16 measured in the duplex layer Si/A/B.

During the adsorption process, the pores of layer A, which are smaller than those of layer B, first fill, the end of the filling of layer A being indicated by the presence of a tipping point on the condensation branch at a relative pressure  $p \simeq 0.8$ , then layer B fills in its turn. For the emptying, the sequence is inverted, layer B empties first followed by layer A.

As shown in Figure 2.17, this isotherm is superimposed perfectly on the solid line (blue curve), which corresponds to the addition of the isotherms measured separately in the two supported layers  $A_s$  and  $B_s$  shown in Figure 2.15. Hence, layers A and B in the duplex layer fill and empty in a sequential way exactly as if they were alone on their respective substrate in direct contact with the gas reservoir. For layer A, this is not surprising because it is in direct contact with the substrate. For layer B, this is less evident since the contact with the substrate is through layer A. This shows that most of the pore walls of B are in contact with the substrate, that is, are common to both layers from the top to the bottom of the duplex layer. This suggests that the pores of A are dug inside the pores of B, three pores of A in each pore of B, on average, as indicated by the pore density ratio value 3.7/1.2.

These results also show that the adsorption strains are not longitudinally transmitted from one layer to the other as expected. Indeed, to compress or stretch, a part of a spring does not change the state of compression or dilatation of the rest of the spring!

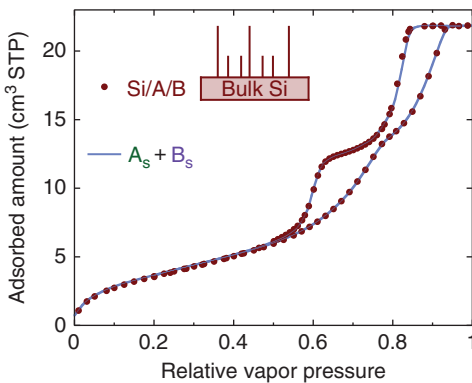


**Figure 2.17** Nitrogen adsorption isotherm at 77.4 K shown in Figure 2.16 for Si/A/B porous duplex layer (•). The solid line (—) is the sum of the isotherms measured in samples  $A_s$  and  $B_s$ , shown in Figure 2.15.

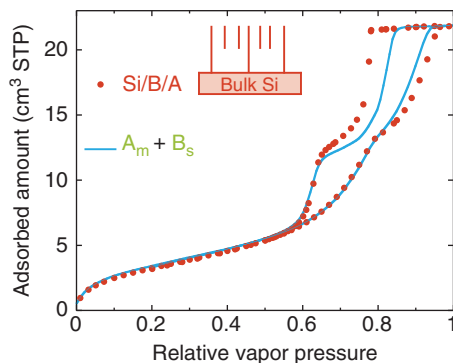


**Figure 2.18** Nitrogen adsorption isotherm at 77.4 K shown in Figure 2.16 for Si/B/A porous duplex layer (•). The solid line (—) is the sum of the isotherms measured in samples  $A_m$  and  $B_s$ , shown in Figure 2.15.

### 2.5.2.2 Si/B/A Configuration

We consider now the results concerning the duplex layer Si/B/A, the so-called ink-bottle geometry.

In Figure 2.18, the solid line (blue curve) results from the addition of the elemental isotherms measured in the membrane,  $A_m$ , and in the supported layer  $B_s$  shown in Figure 2.15. This curve reproduces perfectly the amount reversibly adsorbed at low pressure on the walls of both layers and the filling and emptying of layer A.

This means that layer A fills and empties like a membrane ( $A_m$ ). This has to be related to the fact that layer A in this configuration has dangling walls so that the stress exerted by the substrate on layer A is partly relaxed as clearly seen in Figure 2.16. Indeed, we recover the shift between the isotherms of the supported layer and membrane. This is an additional proof of the influence of an external stress on the adsorption process (see Section 2.4).

Layer B empties while layer A remains filled. This shows that there is no pore-blocking effect, but nucleation of gas bubbles that occurs in layer B under the effect of the negative liquid pressure created under the concave menisci at the top of layer A, according to Kelvin–Laplace equation, equals  $-4.5$  MPa. Since layer A remains filled, this shows that the liquid fracture pressure is as high (in absolute value) as the pore size is low.

Note that the filling and emptying of pores of layer B through the filled ones of layer A are slightly delayed toward higher pressures for the filling and toward lower pressures for the emptying with regard to the condensation–evaporation process of layer B in direct contact with the gas reservoir. For the moment, there is no explanation of these results.

Nitrogen and argon adsorption isotherms were measured in the same duplex porous Si layers at temperatures below the melting points [5]. The isotherms shown in Figure 2.19 exhibit essentially the same features as those obtained with nitrogen at 77.4 K. As in the case of liquid nitrogen, there is no pore-blocking

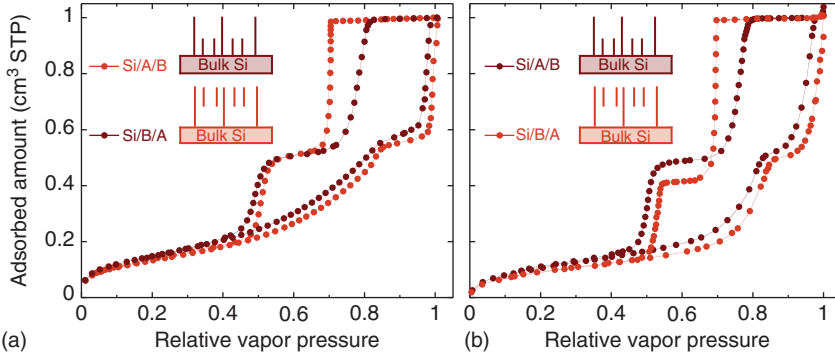


**Figure 2.19** Nitrogen (a) and argon (b) adsorption isotherms at 51.3 K and 60 K, respectively, for Si/A/B (•) and Si/B/A (•) duplex porous silicon layers, schematically

represented in the inset. The saturation vapor pressures are  $P_0 = 5.3$  mmHg for nitrogen and  $P_0 = 6.1$  mmHg for argon. The lines are guides for eye.

in the ink-bottle configuration but nucleation of gas bubbles with, however, a notable difference: the transition is now practically vertical.

For solid argon in the Si/B/A configuration, the emptying of a fraction of pores of layer A is triggered by the transfer of argon atoms from B to A as shown by the decrease in the saturation plateau of layer A (see Figure 2.19(b)). This is the first direct observation of metastable states of a dense phase confined to mesopores.

These whole experiments constitute the first experimental proof of cavitation phenomenon of confined fluids and van der Waals solids in mesoporous materials.

### 2.5.3

#### Nature of the Nucleation Process

Now, the question arises about the nature of this cavitation phenomenon. Recent experiments and simulations [24] point to the possibility that evaporation could occur via homogeneous cavitation. In this paper, however, the cavitation hypothesis is only supported by the value of the relative vapor pressure at which evaporation takes place from 0.4 to 0.5 for nitrogen, which is supposed to correspond to the limit of stress stability in the metastable condensed liquid.

In duplex porous layer, for  $N_2$  at 77.4 K, cavitation occurs in layer B at a relative vapor pressure  $\sim 0.78$  corresponding to a negative liquid pressure  $-4.5$  MPa. Does this fracture pressure of the liquid correspond to homogeneous nucleation?

#### 2.5.3.1 Homogeneous Nucleation

According to the classical theory of homogeneous nucleation (for references, see Ref. [5]), the number  $N$  of bubbles per unit time and per unit volume is related exponentially to the energy barrier  $\Delta F_{\max}$  required to form the bubble:

$$N = N_0 \exp \left[ - \frac{\Delta F_{\max}}{k_B T} \right] \quad (2.39)$$

where

$$\Delta F_{\max} = \frac{16\pi\gamma_{\text{lv}}^3}{3(\delta P)^2} \quad (2.40)$$

with  $k_B$  being Boltzmann's constant,  $\gamma_{\text{lv}}$  the surface energy per unit area of the liquid–vapor interface, and  $\delta P = P_v - P_l$ .

This energy barrier corresponds to a critical nucleus of radius

$$R^* = \frac{2\gamma_{\text{lv}}}{\delta P} \quad (2.41)$$

The number of bubbles with critical size  $R^*$  in a pore of volume  $v$  in a time  $\tau$  is thus  $Nv\tau$ . The prefactor  $N_0$  can be considered as an attempt frequency per unit time multiplied by the number of sites per unit volume where nucleation can take place. The attempt frequency is generally taken to be  $k_B T/h$  where  $h$  is the Plank's constant. Taking for the number of sites per unit volume, the inverse of the molecular volume of liquid nitrogen,  $1/v_l = \rho \mathcal{N}_A / M$ , where  $M$  is the molar mass,  $\mathcal{N}_A$  is Avogadro's number, and  $\rho$  is the density, we find  $N_0 = k_B T/hv_l = 2.8 \times 10^{40} \text{ m}^{-3} \text{ s}^{-1}$ .

The number  $Nv\tau$  equals 1 if

$$\Delta F_{\max} = k_B T \ln(N_0 v \tau) \quad (2.42)$$

Note that the prefactor value does not significantly change that of  $\Delta F_{\max}$  due to the logarithm dependence.

For layer B, the total pore volume, measured from adsorption data, is  $18.7 \times 10^{-3} \text{ cm}^3$  and the total number of pores,  $18.24 \times 10^{11} \text{ cm}^2$ . Taking for  $v$  the mean value of the volume of a pore,  $v \sim 10^{-20} \text{ m}^3$ , and  $\tau = 1 \text{ s}$ , we find

$$\Delta F_{\max} = 47 k_B T \quad (2.43)$$

From Eqs. 2.40 and 2.43, we deduce the negative liquid pressure at which cavitation can occur in the bulk fluid

$$P_l^{\text{cav, bulk}} - P_v = - \left[ \frac{16\pi}{3} \frac{\gamma_{\text{lv}}^3}{47k_B T} \right]^{1/2} \simeq P_l^{\text{cav, bulk}} \quad (2.44)$$

For  $\text{N}_2$  at 77.4 K, we find  $P_l^{\text{cav, bulk}} \simeq -15.4 \text{ MPa}$  and  $R^* = 1.2 \text{ nm}$ .

We have seen earlier that, for layer B,  $P_l^{\text{cav}} \sim -4.5 \text{ MPa}$ , that is, three times lower in absolute value than that of the bulk liquid. This suggests that in the linear pores of porous silicon, cavitation does not occur in the bulk fluid but on the surface of the pore walls. This so-called heterogeneous nucleation is actually generally observed at negative liquid pressure much lower, in absolute value, than that of the bulk.

### 2.5.3.2 Heterogeneous Nucleation and Elastic Strain

The problem of heterogeneous nucleation is complex. It depends on the geometry of the material that is itself complex in the case of porous materials. Even if we assimilate the actual pores to cylinders, the nucleation path does not preserve

necessarily this symmetry, and the problem has no analytical solution and must be solved numerically. At the moment we can only have a qualitative discussion on the relationship between heterogeneous nucleation and elastic strain.

If we consider, for instance, the simple case of a vapor bubble on a plane surface and if we assume that the bubble is a fraction of a sphere, the relation between the liquid pressures for fracture in the bulk liquid and on the pore surface is

$$P_1^{\text{cav, surface}} \simeq P_1^{\text{cav, bulk}} \times [\phi(m)]^{1/2} \quad (2.45)$$

where  $\phi(m) = \frac{1}{4}(2+m)(1-m)^2$  and

$$m = \cos(\pi - \theta) = \frac{(\gamma_{\text{sl}} - \gamma_{\text{sv}})}{\gamma_{\text{lv}}} \quad (2.46)$$

$\gamma_{\text{sl}}$ ,  $\gamma_{\text{sv}}$ , and  $\gamma_{\text{lv}}$  are the surface energies per unit area at the three interfaces solid–liquid, solid–vapor, and liquid–vapor.  $\theta$  is the contact angle between the vapor–liquid interface and the solid surface at the three phase line. For layer B,  $[\phi(m)]^{1/2} \simeq 1/3$ , which corresponds to  $\theta \simeq 130^\circ$ , that is,  $(\gamma_{\text{sl}} - \gamma_{\text{sv}}) > 0$ . We have seen in Section 2.3 that the surface energy varies linearly with strains, and that the linearity factor depends on the nature of the solid–vapor or liquid–vapor interface. This indicates that, for the porous silicon–nitrogen system, the structure of the solid–liquid and solid–vapor interfaces, that is, the elastic strains, is such that  $\gamma_{\text{sl}} - \gamma_{\text{sv}} > 0$ .

At this stage, it is important to distinguish between the two following situations: a meniscus *at the pore end* and a meniscus *inside a pore*.

When a porous material is filled at  $p = 1$ , desorption is initiated by decreasing the vapor pressure and a concave meniscus is formed (reversibly) at the pore end. The equilibrium of the concave meniscus and vapor is achieved by the equality of the chemical potentials of the vapor and liquid and by the Laplace equation. The liquid pressure, that is, the curvature radius, is then given by Kelvin–Laplace equation.

Once the curvature radius reaches a minimum value, it is generally admitted that it enters the pore and may be eventually blocked by geometric constrictions or less attractive sections of the pores. The contact angle corresponding to a meniscus inside a pore is obtained by a supplementary condition, the extremalization of the grand potential, and is also given by Eq. 2.46.

A receding meniscus with a contact angle lower than  $\pi/2$  ( $\gamma_{\text{sl}} - \gamma_{\text{sv}} < 0$ ) *inside* a pore and a gas bubble with a contact angle higher than  $\pi/2$  ( $\gamma_{\text{sl}} - \gamma_{\text{sv}} > 0$ ) are thus mutually exclusive. Our experimental result which suggest that cavitation is heterogeneous indicates that a concave meniscus cannot enter a pore. This is supported by two experimental facts.

- 1) Krypton adsorption isotherms at 77.4 K was measured for a porous silicon layer 1  $\mu\text{m}$  thick (see Figure 2.20). The amount of matter desorbed along the saturation plateau corresponds to 0.005  $\text{cm}^3\text{STP}$ , that is,  $1.35 \times 10^{17}$  atoms. The volume of menisci formed at the top of pores is equal to  $\sim 0.4 \times 10^{17}$  atoms by assuming hemispherical menisci. The amount reversibly adsorbed

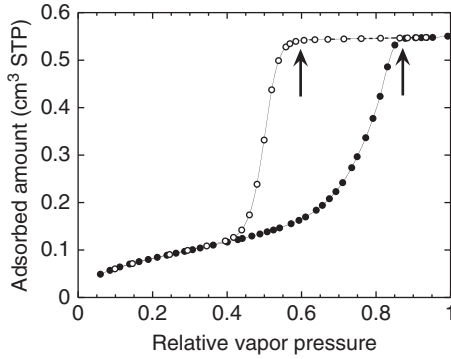


**Figure 2.20** Krypton adsorption isotherms at 77.4 K in a porous silicon layer, 1  $\mu\text{m}$  thick. The arrows indicate the two end points of the saturation plateau. The lines are guides for eye.

on the nonporous surfaces (analysis cell and external surface of the sample) corresponds to  $1.1 \times 10^{17}$  atoms. Thus, the Kr atoms desorbed along the plateau originate in the desorption from nonporous surfaces and in the formation of menisci [4]. These results show that no capillary empties, and that the menisci are pinned at the pore entrance. Note that the same observation has been done for porous glass: the adsorption along the plateau is reversible which also suggests that no capillary empties [20].

- 2) Duan *et al.* [25] report on evaporation-induced cavitation in water-filled hydrophilic nanochannels and visualize the pinning of the menisci at the entrance of nanochannels while vapor bubbles form and expand inside.

The cavitation liquid pressure is hence controlled by the curvature radius of the meniscus pinned at the pore end.

The results presented in this chapter suggest that the emptying process is closely related to the state of the deformation of the solid–vapor interface ( $\epsilon_{sv}$  inside the bubble) and of the solid–liquid interface ( $\epsilon_{sl}$  outside the bubble). Let us recall that the linear relationships between the surface energy and the strain depend on whether we are in presence of a solid–vapor (sv) or a solid–liquid (sl) interface. These relations can be schematically written as  $\Delta\gamma_{sv} = -k_{sv}[\epsilon_{sv}(p) - \epsilon(0)]$  and  $\Delta\gamma_{sl} = -k_{sl}[\epsilon_{sl}(p) - \epsilon(1)]$ , where  $p = P/P_0$ . Also remember that  $k_{sv}$  depends only on the elastic constant of the solid while  $k_{sl}$  depends on the nature of the fluid and the temperature through the liquid pressure value. Thus,  $(\gamma_{sl} - \gamma_{sv})$  is a function of all these parameters.

To study the evaporation process for a given solid–fluid couple, it is hence necessary to measure the adsorption isotherm together with the induced strain.

The consequences on the characterization of porous solids from adsorption data are considerable. The quantitative analysis methods that proposed to estimate the pore size from the desorption branch (supposed to occur via receding menisci) must be seriously questioned. The condensation pressure that depends not only

on the pore size but also on the elastic strain is not a good criterion. The IUPAC classification based on models in which the surface elastic energy, a function of the adsorbed induced strain, is disregarded although it is an important parameter of the total free energy must be reconsidered. In particular, hysteresis loops of types H1 and H2 could be the simple characteristics of a narrow and large pore size distributions, respectively.

## References

1. Cohan, L.H. (1938) Sorption hysteresis and the vapor pressure of concave surfaces. *J. Am. Chem. Soc.*, **60**, 433–435.
2. Mason, J. (1983) A model of adsorption-desorption hysteresis in which hysteresis is primarily developed by the interconnections in a network of pores. *Proc. R. Soc. London, Ser. A*, **A390**, 47–72.
3. Sing, K.S.W., Everett, D.H., Haul, R.A., Moscou, L., Pierotti, R.A., Rouquerol, J., and Siemieniewska, T. (1985) Reporting physisorption data for gas/solid systems. *Pure Appl. Chem.*, **57**, 603–619.
4. Grosman, A. and Ortega, C. (2008) Capillary condensation in porous materials. Hysteresis and interaction mechanism without pore blocking/percolation process. *Langmuir*, **24**, 3977–3986.
5. Grosman, A. and Ortega, C. (2011) Cavitation in metastable fluids confined to linear mesopores. *Langmuir*, **27**, 2364–2374.
6. Coasne, B., Grosman, A., Ortega, C., and Simon, M. (2002) Adsorption in noninterconnected pores open at one or at both ends: a reconsideration of the origin of the hysteresis phenomenon. *Phys. Rev. Lett.*, **88**, 256102–256104.
7. Amsel, G., d'Artemare, E., Battistig, G., Morazzani, V., and Ortega, C. (1997) A characterization of the morphology of porous silicon films by proton energy loss fluctuation measurements with a narrow resonance in the  $N^{15}(p,\alpha\gamma)C^{12}$  reaction. *Nucl. Instrum. Methods Phys. Res., Sect. B*, **122**, 99–112.
8. Preisach, F. (1935) About the magnetic aftereffect. *Z. Phys.*, **94**, 277–302.
9. Everett, D.H. (1967), Adsorption hysteresis, in *The Solid Gas Interface*, Vol. 2, Chapter 36 (ed. E.A. Flood), Marcel Dekker, New York, pp. 1055–1113.
10. Grosman, A. and Ortega, C. (2005) Nature of capillary condensation and evaporation processes in ordered porous materials. *Langmuir*, **21**, 10515–10521.
11. Grosman, A. and Ortega, C. (2010) Influence of elastic strains on the adsorption process in porous materials. Thermodynamics and experiment. *Appl. Surf. Sci.*, **256**, 5210–5215.
12. Puibasset, J. (2009) Monte-Carlo multiscale simulation study of argon adsorption/ desorption hysteresis in mesoporous heterogeneous tubular pores like MCM-41 or oxidized porous silicon. *Langmuir*, **25**, 903–911.
13. Naumov, S., Khokhlov, A., Kärger, J., and Monson, P. (2009) Understanding adsorption and desorption processes in mesoporous materials with independent disordered channels. *Phys. Rev. E*, **80**, 031607-1–9.
14. Cimino, R., Cychosz, K.A., Thommes, M., and Neimark, A.V. (2009) Experimental and theoretical studies of scanning adsorption-desorption isotherms. *Colloids Surf., A*, **437**, 76–89.
15. Grosman, A. and Ortega, C. (2008) Influence of elastic deformation of porous materials in adsorption-desorption process: a thermodynamic approach. *Phys. Rev. B*, **78**, 085433–085412.
16. Günther, G., Prass, J., Paris, O., and Schoen, M. (2009) Novel insights into nanopore deformation caused by capillary condensation. *Phys. Rev. Lett.*, **101**, 086104–086104.
17. Prass, J., Mütter, D., Fratzl, P., and Paris, O. (2009) Capillarity-driven deformation of ordered nanoporous silica. *Appl. Phys. Lett.*, **95**, 083121–083123.
18. Nozières, P. (1992) Shape and growth of crystals, in *Solids Far from Equilibrium*



- (ed. G. Godreche), Cambridge University Press, pp. 1–154.
19. Müller, P. and Saúl, A. (2004) Elastic effects on surface physics. *Surf. Sci. Rep.*, **54**, 157–258.
  20. Amberg, C.H. and McIntosh, R. (1952) A study of adsorption hysteresis by means of length changes of a rod of porous glass. *Can. J. Chem.*, **30**, 1012–1032.
  21. Quinn, H.W. and McIntosh, R. (1957) The hysteresis loop in adsorption isotherms of porous vycor glass and associated dimensional changes of the adsorbent. *Can. J. Chem.*, **35**, 745–756.
  22. Grosman, A. and Ortega, C. (2009) Influence of elastic strains on the adsorption process in porous materials. An experimental approach. *Langmuir*, **25**, 8083–8093.
  23. Barla, K., Herino, R., Bomchil, G., Pfister, J.C., and Freund, A. (1984) Determination of lattice parameter and elastic properties of porous silicon by X-ray diffraction. *J. Cryst. Growth*, **68**, 727–732.
  24. Rasmussen, C.J., Vishnyakov, A., Thommes, M., Smarsly, B.M., Kleitz, F., and Neimark, A.V. (2010) Cavitation in metastable liquid nitrogen confined to nanoscale pores. *Langmuir*, **26**, 10147–10157.
  25. Duan, C., Karnik, R., Lu, M.C., and Majumdar, A. (2012) Evaporation-induced cavitation in nanofluidic channels. *Proc. Natl. Acad. Sci. U.S.A.*, **109**, 3688–3693.

### 3

## Theoretical Modeling of Fluid–Solid Coupling in Porous Materials

*Robert Alan Guyer and Hyunsun Alicia Kim*

### 3.1

#### Introduction

A plethora of solid systems, natural and man-made, interact importantly with fluids, for example, array of solid grains amidst pores with fluids that are more or less connected (e.g., rock), a cellular solid [1] having fluids contained within the solid, and so on. The solid geometry may be irregular (e.g., foam [2], wood [3], keel of an ice plant [4]) or regular (e.g., MCM-41) [5]. Many of these systems exhibit mechanical hysteresis and anisotropy, the precise physics of which is not necessarily well understood. Certainly, the coupling of fluid to solid plays an important role in this mechanics. A case in point is the moisture-induced seed dispersal of pine cones [6, 7]. In this contribution, we develop a theoretical model of coupled fluid–solid systems that provides a foundation for understanding mechanical behavior.

### 3.2

#### Systems and Models

The primary interest here is a material system constituted of (a) a linear elastic solid, (b) a fluid that may (or may not) be self-bound, and (c) a coupling between solid and fluid. We develop a theoretical model that describes the behavior of these three elements and implement it in a finite element discretization of a 2D continuum (plane stress) [8], for example, constant strain triangular elements that have nodes at their vertices. Consequently, we use the elements and associated nodes as the basic units of description. The strain field and fluid density are associated with the elements, index  $i$ . The displacement is computed at the nodes of these elements, indexed with  $\alpha$ , Figure 3.1. The mechanical structure of the solid is called the skeleton and the nominally empty space is called the pore space. Figure 3.2 shows an example of a honeycomb cellular solid.

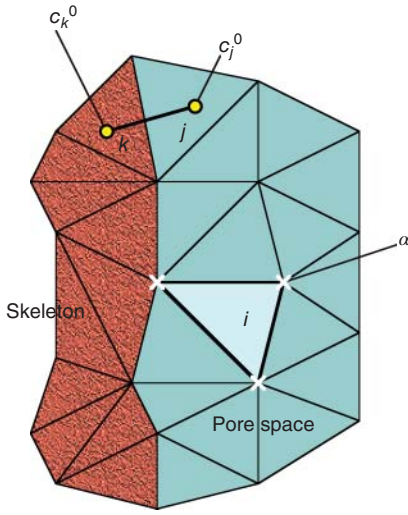


**Figure 3.1** Representation of system. The area elements,  $i$ , can be fluid bearing (blue) or solid (brown). The fluid exerts forces (that appear on the nodes of an element,  $\{i, \alpha\}$ , and are proportional to the fluid density on

the element,  $\rho_i$ ) that try to expand (contract) the element. The forces  $V$  in Eq. 3.3 are proportional to the distance between element centroids,  $|c_k^0 - c_j^0|$ .

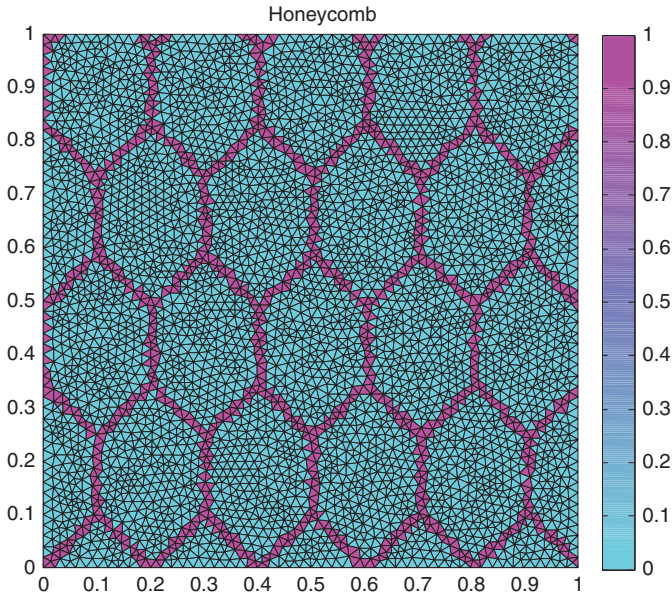


**Figure 3.2** Honeycomb system. A honeycomb frame is dressed by associating elements within a specified distance of the frame with the skeleton, the elastic system. The skeleton is quite coarse in this high porosity example,  $\phi \approx 85\%$ .

We construct an energy with three terms. The *energy for the fluid* is familiar from Kierlik *et al.* [9].

$$\mathcal{E}_F = -\frac{1}{\beta} \sum_i [\rho_i \ln \rho_i + (1 - \rho_i) \ln (1 - \rho_i)] + \sum_i \sum_j J_{ij} \rho_i \rho_j - \mu \sum_i \rho_i \quad (3.1)$$

where  $\beta = 1/k_B T$ ,  $\rho_i$  is the average fluid density in element  $i$ ,  $J_{ij} > 0$  is the attractive fluid–fluid interaction, and  $\mu$  is the chemical potential. The *energy for the solid*, elastically linear, is written schematically

$$\mathcal{E}_S = \frac{1}{2} \sum_i K_i \varepsilon_i^2 + \sum_i \sigma_i \varepsilon_i, \quad (3.2)$$

where  $(\sigma_i, \varepsilon_i)$  is the (applied stress, strain) associated with element  $i$ .

There are several choices for the *coupling of the fluid to the solid* according to the details of the physical situation. We need to consider two cases.

For the first case, we consider fluid *adsorbed on an interface* and residing in the adjacent pore space, Figure 3.1. When the fluid is near the interface between pore space and solid, it sees a potential energy that is a function of the distance from the interface. We model this with a potential energy as a function of the distance between the centroid of the element on which the fluid sits and the centroid of the element of the solid. For the fluid element  $i$  and the solid element  $j$ , we take the energy of interaction to be

$$\mathcal{E}_{FS} = \sum_{ij} V(|\mathbf{c}_i - \mathbf{c}_j|) \rho_i = \sum_{ij} \left\{ V(|\mathbf{c}_i^0 - \mathbf{c}_j^0|) \rho_i + V'(|\mathbf{c}_i^0 - \mathbf{c}_j^0|) (\mathbf{e}_{ij} \cdot \Delta \mathbf{u}_{ij}) \rho_i \right\}, \quad (3.3)$$

where  $V'(x) = \partial V(x)/\partial x$ ,  $\mathbf{c}_i^0$  is the centroid of element  $i$ ,  $\mathbf{e}_{ij}$  is the unit vector between the centroid of element  $i$  and the centroid of element  $j$ ,  $\Delta \mathbf{u}_{ij}$  is the location of the centroid of element  $i$  relative to the centroid of element  $j$ ,

$$\Delta \mathbf{u}_{ij} = \sum_{\alpha} \mathbf{u}_{\alpha}^i - \sum_{\alpha} \mathbf{u}_{\alpha}^j, \quad (3.4)$$

and  $\mathbf{u}_{\alpha}^i$  is the displacement of node  $\alpha$  of element  $i$ . There are various possibilities for the function  $V$ . Its influence is typically over a short distance. Thus, the static term, the first term on the RHS of Eq. 3.3, is understood as a wetting energy. The second term on the RHS of Eq. 3.3 is a coupling that causes deformation of the solid/rearrangement of the fluid to minimize the system energy.

For the second case, we consider *fluid absorbed into the skeleton*. For this case, we propose the coupling

$$\mathcal{E}_{FS} = \frac{1}{2} \sum_i \{ U_i \rho_i + W_i (\nabla \cdot \mathbf{u})_i (2\rho_i - 1) \}, \quad U_i \leq 0, \quad W_i \leq 0, \quad (3.5)$$

where  $U_i$  and  $W_i$  are fields that are associated with the elements. The first term in this coupling [9] is present on elements either adjacent to the skeleton or within the skeleton, cf. Eq. 3.3. For  $U_i \leq 0$ , fluid is drawn to element  $i$ . The

second term in this coupling describes an elastic energy that is changed by the presence of fluid. This term captures the notion that at  $\rho_i = 0$ , the strain  $(\nabla \cdot \mathbf{u})_i$  is driven negative by forces reducing the area available to the fluid [10]. At  $\rho_i = 1$ , the strain  $(\nabla \cdot \mathbf{u})_i$  is driven positive by forces increasing the area available to the fluid. Thus, fluid within a skeleton causes forces to work to accommodate more fluid.

The equations of equilibrium are found upon varying the total energy,  $\mathcal{E} = \mathcal{E}_F + \mathcal{E}_S + \mathcal{E}_{FS}$ , with respect to  $\rho_i$  and  $\varepsilon_\alpha^i$ . For illustrative purposes, we use the second case from above, Eq. 3.5. From  $\delta\mathcal{E}/\delta\rho_i$ , we find

$$\rho_i = \frac{1}{e^{\beta(\mu_i^c - \mu)} + 1}, \quad \mu_i^c = U_i + W_i(\nabla \cdot \mathbf{u})_i - \sum_j J_{ij}\rho_j, \quad (3.6)$$

where  $\mu_i^c$  is a critical value of  $\mu$  that controls the fluid state of element  $i$ .

From  $\delta\mathcal{E}/\delta\varepsilon_\alpha^i$ , we find the equation for the displacement field. We express this using the finite element method [8]. The equation for the displacement of node  $u_\alpha$  takes the form

$$\sum_\gamma \mathcal{K}_{\alpha\gamma} u_\gamma = \frac{1}{2} \sum_j e_{\alpha j} W_j (2\rho_j - 1), \quad (3.7)$$

where  $\mathcal{K}_{\alpha\gamma}$  are the elements of the stiffness matrix and  $e_{\alpha j}$  is the  $\alpha$  component of a unit vector from the centroid of element  $j$  to node  $\alpha$  of element  $j$ . The sum of the forces deployed by an element on its nodes is zero,  $\sum_\alpha e_{\alpha j} = 0$ .

We work at temperature such that  $\rho_i \approx 0$  for  $\mu_i^c - \mu > 0$  and  $\rho_i \approx 1$  for  $\mu_i^c - \mu < 0$ , Eq. 3.6. Consequently, the fluid state of element  $i$  is controlled by the relationship of  $\mu$  to the critical value  $\mu_i^c$ . Since  $\mu_i^c < 0$  at  $\mu \rightarrow -\infty$ , the forces on the elements try to compress the elements, the average strain is  $< 0$ . As  $\mu \rightarrow 0$ ,  $\mu > \mu_i^c$  and the forces on the elements try to expand the elements. The strains produced by the fluid feed back to the fluid through  $\mu_i^c$ . Consequently, Eqs. 3.6 and 3.7 must be solved self-consistently.

### 3.3

#### Problems

The formalism above can be applied to a series of cellular solid problems. We describe three such problems (see Figure 3.3). Two of these problems are developed extensively here while the third problem is included for completeness.

- 1) A cellular solid with initially empty pore space, for example, MCM-41 [5, 11]. The vapor of a fluid that is controlled by the chemical potential  $\mu$  is introduced into the pore space. There is an attractive interaction between solid and fluid that causes the fluid to wet the solid surface, form a liquid there, and couple to the displacement of the surface. This is the circumstance for an adsorption isotherm. We do not develop this problem here [12–15]. See chapter GO.

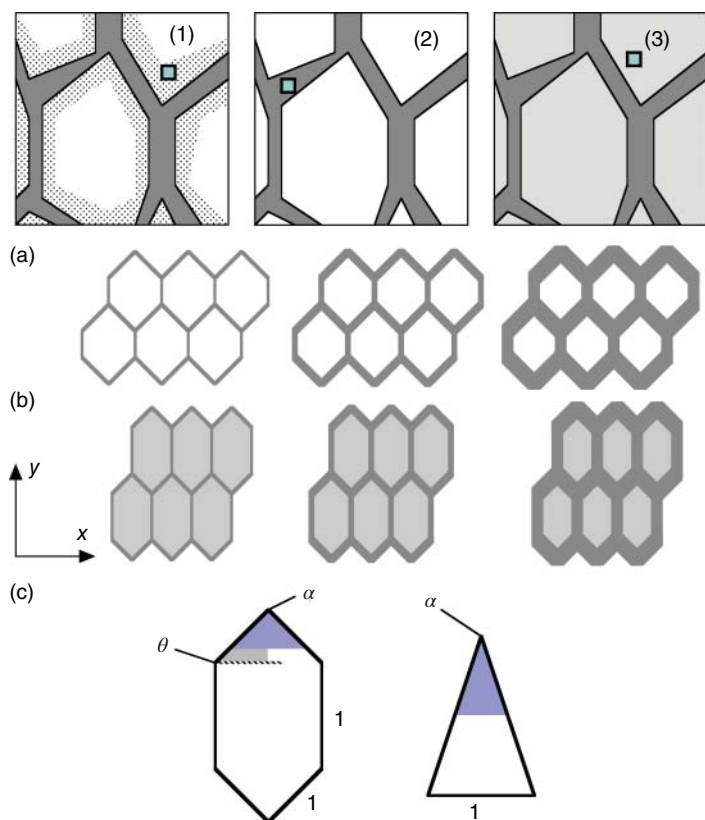


**Figure 3.3** Cellular solid geometry. (a) Example of three cases of interest; (1) fluid clings to the pore walls, (2) fluid resides in the skeleton, and (3) fluid resides in the fill of the pore space. (b) A solid skeleton is formed by dressing the frame to various

thicknesses by associating elements with the frame. (c) A frame (honeycomb or hexagonal) is made anisotropic by varying the angle  $\alpha$ . The angle  $\alpha$  is related to the angle  $\theta$ , see Gibson and Ashby [1].

- 2) A cellular solid for which wood [3] might be an example. The vapor of a fluid that is controlled by the chemical potential  $\mu$  is introduced into the pore space. The atoms/molecules of the vapor enter into the skeleton, bind to sites in the skeleton, and through the coupling cause forces that promote the further wetting of the skeleton, that is, the adsorption of more molecules into the skeleton [16, 17]. The fluid–fluid coupling is taken to be unimportant in this circumstance as the fluid is not imagined to be pooled as bulk liquid.
- 3) A cellular solid for which the ice plant [4] is an example. Instead of being empty, the pore space is filled with an elastically soft material. The vapor of a fluid that is controlled by the chemical potential  $\mu$  is adsorbed into

the pore filling. The atoms/molecules of the vapor enter the pore filling, bind to sites in the filling, and through the coupling cause forces that promote the further wetting of the filling, that is, the adsorption of more molecule into the filling. Similar to problem 2, the fluid–fluid coupling is taken to be unimportant as the fluid is not imagined to be pooled as bulk liquid.

For problems 2 and 3, the fluid enters material of the cellular solid. This entry would be molecule by molecule into sites that lie in the material (the skeleton or the filling) and are separated from one another by a distance larger than that over which the interaction  $J$  works. For these problems, we put  $J = 0$ , Eq. 3.6. Our primary concern is with the effect of the presence of fluid in the systems. However, these systems have important mechanical properties, independent of the presence of fluids. These properties establish the stage on which the fluids work. We will proceed by forming a variety of cellular solid systems without fluid and we will subject these systems to numerical testing to determine their elastic response. We will then put fluids into these systems and examine the resulting behavior.

### 3.3.1

#### Systems of Interest

The study of a sequence of cellular solids that are built from simple frames as illustrated in Figure 3.3 is presented. Consider the sequence of honeycombs in Figure 3.3b. On the left is an isotropic honeycomb skeleton with six interior angles of  $60^\circ$ , having porosity  $\phi \rightarrow 1$ . Solids of decreasing porosity are formed by increasing thickness of the skeleton, for example, from left to right in the figure. At porosity  $\phi = 0$ , the honeycomb cellular solid is reduced to a piece of uniform isotropic material as the skeleton invades the original pore space. The geometrical anisotropy of the honeycomb skeleton is characterized by the angle  $\alpha$  in Figure 3.3c, and  $\alpha$  is changed with the fixed side lengths. The pore spaces may be empty or may contain elastically different isotropic material, problem 3. In addition to cellular honeycomb solids, triangular and random geometry cellular solids are studied. The geometrical anisotropy of the triangular frame is characterized by the angle  $\alpha$ , (see Figure 3.3c), which is changed at fixed base. For the random geometry, only an approximately isotropic cellular geometry is studied.

### 3.3.2

#### Quantities of Interest

We begin by performing numerical tests to determine the elastic properties of each cellular solid. These tests are (a) a uniaxial stress in  $y$  test (and  $x$ ), (b) a uniaxial strain in  $y$  test (and  $x$ ), and (c) a shear stress test. Due to the complex structure of the cellular solid along the boundaries, these tests are

conducted by setting the surface displacements of the skeleton and determining the forces in very stiff springs that enforce these displacements. From these numerical tests, the elastic tensor of the cellular solid can be determined, the results are reported in Section 3.4. We then turn to the mechanical response of the cellular solid to fluids that are free of applied stresses, have an empty pore space, and are driven by fluid that resides in the skeleton (Section 3.5). In Section 3.6, we discuss the study of the mechanical response of cellular solids that are free of applied stresses, have a pore space that is filled with elastically isotropic material, and are driven by fluid that resides in the pore filling.

### 3.4

#### Mechanical Response to Applied External Forces

This subject is well established with the book by Gibson and Ashby [1] providing a complete description. We examine two types of mechanical testing: (i) the extension ratio and (ii) the swelling ratio.

(1) *The extension ratio.* The extension ratio, denoted  $R_E$ , is the ratio of the modulus of extension in the  $y$ -direction,  $E_y$ , to the modulus of extension in the  $x$ -direction,  $E_x$ ,  $R_E = E_y/E_x$ . The Hooke's law in  $x$ -direction can be written as

$$\epsilon_x = \frac{1}{E_x} \sigma_x, \quad (3.8)$$

where  $\epsilon_x$  is the strain response to stress  $\sigma_x$  applied along  $x$ . In relating  $E_x$  to the elastic constants, the requirement  $\sigma_y = 0$  implies that

$$\sigma_y = C_{yy}\epsilon_y + C_{yx}\epsilon_x = 0, \quad (3.9)$$

or

$$\epsilon_y = -\frac{C_{yx}}{C_{yy}}, \quad \epsilon_x = -\nu_{xy}\epsilon_x, \quad (3.10)$$

where  $\nu_{yx}$  is the Poisson's ratio. A similar Poisson's ratio is defined in forming  $E_y$ . The extension moduli are

$$E_x = C_{xx} - C_{xy}\nu_{xy}, \quad E_y = C_{yy} - C_{yx}\nu_{yx} \quad (3.11)$$

and the ratio  $R_E$  is

$$R_E = \frac{E_y}{E_x} = \frac{C_{yy}}{C_{xx}}. \quad (3.12)$$

The extension ratio, involving the diagonal components of the modulus tensor, is independent of the Poisson's ratios. The diagonal components of the modulus tensor control uniaxial strain and the longitudinal and transverse sound speeds.



The Poisson's ratios characterize the off-diagonal couplings. Since  $C_{yx} = C_{xy}$ , generally

$$E_x \nu_{yx} = E_y \nu_{xy}. \quad (3.13)$$

(2) *The swelling ratio.* The swelling ratio,  $R_S$ , is defined to be the ratio of the  $x$ -strain to the  $y$ -strain when the system is subject to a uniform stress, that is,  $\sigma_x = \sigma_y = \sigma$ . From

$$\sigma_x = \sigma = C_{xx}\epsilon_x + C_{xy}\epsilon_y, \quad (3.14)$$

$$\sigma_y = \sigma = C_{yx}\epsilon_x + C_{yy}\epsilon_y \quad (3.15)$$

find

$$R_S = \frac{\epsilon_x}{\epsilon_y} = \frac{C_{yy} - C_{xy}}{C_{xx} - C_{yx}} = R_E \frac{1 - \nu_{yx}}{1 - \nu_{xy}}. \quad (3.16)$$

For anisotropic systems, the Poisson's ratio can change sign and possibly cross through 1 [18].

We look at the extension ratio and swelling ratio for honeycomb cellular solids and for hexagonal cellular solids (Figure 3.3). Figure 3.4 shows the value of  $R_E$  as a function of the angle  $\alpha$  for a wide range of honeycomb cellular solids with a varying porosity via thickness of the skeleton. The extension ratio for the fixed  $\alpha$  and varying porosity appears as a vertical string of points in Figure 3.4. As the thickness varies from small ( $\phi \rightarrow 1$ ) to large ( $\phi \rightarrow 0$ ), the points move away from the solid line to  $R_E = 1$  ( $\log_{10}(R_E) = 0$ ), that is, isotropic. At  $\alpha = 120^\circ$ , the solid is near isotropic for all thicknesses. The solid line, the  $\phi \rightarrow 1$  extension ratio, from Gibson and Ashby [1], is

$$R_E = \left[ \frac{(1 + \sin \theta) \sin \theta}{\cos^2 \theta} \right]^2, \quad (3.17)$$

where  $\theta = (\pi - \alpha)/2$  and the angle  $\theta$  is defined in Figure 3.3. This limiting ratio corresponds to a skeleton built of isotropic material of infinitesimal thickness. In a finite element calculation, the cellular solids look approximately similar to Figure 3.2, an example with  $\alpha = 120^\circ$  and  $\phi = 0.87$ . In the numerical work, for a fixed cellular solid geometry, we vary the mesh density to be assured that a qualitative property reported is not an artifact of mesh size, and to illustrate the range of results the natural coarseness of cellular solids might confer. As seen in Figure 3.2, the solids of concern are not mathematically perfect. The two distorted honeycombs in Figure 3.4 are intended to give a sense of the skeleton geometry away from isotropy,  $\alpha = 120^\circ$ . The honeycomb geometry is stiff in the  $x$ -direction as  $\alpha \rightarrow \pi$  and stiff in the  $y$ -direction as  $\alpha \rightarrow 0$ .

In Figure 3.5, we show the extension ratio for hexagonal solids of varying anisotropy and porosity. The  $\phi = 1$  limiting curve is given by

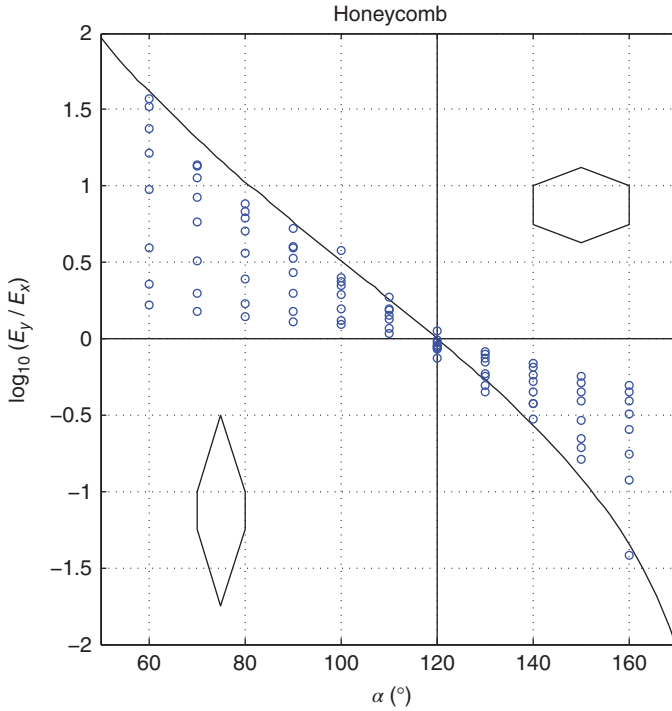


**Figure 3.4** HCRE Extension ratio, honeycomb. The extension ratio for honeycomb solids built by dressing frames for various angles  $\alpha$ ,  $60^\circ < \alpha < 160^\circ$ . At each angle, the porosity varies from near zero, where the extension ratio is near 1 ( $\log_{10}(E_y/E_x) \approx 0$ )

to near 1. The heavy solid line is the  $\phi = 1$  limit for  $E_y/E_x$  from Gibson and Ashby [1]. Skeletons built from a frame with  $\alpha = 120^\circ$  are isotropic,  $E_y/E_x = 1$ . The extension ratio is  $> 1$  ( $< 1$ ) for  $\alpha > (<) 120^\circ$ .

$$R_E = \frac{\cos^4 \beta}{\sin \beta (1 + \sin^3 \beta)}, \quad (3.18)$$

where  $\beta = \alpha/2$ . The extension ratio of the hexagonal system, basically a cross-braced honeycomb, is much less sensitive to anisotropy. The vertical scale in Figure 3.5 is linear in contrast to the logarithmic vertical scale in Figure 3.4.

The swelling ratio is much more sensitive to the geometry of the solid than the extension ratio. This is at least suggested by the appearance of the factors involving the Poisson's ratio in Eq. 3.16. Figure 3.6 exhibits the swelling ratio and extension ratio for a series of honeycomb cellular solids of fixed skeleton thickness and varying  $\alpha$ . We note that the swelling ratio is always outside of the extension ratio, that is,  $R_S > R_E$  for  $\alpha < 120^\circ$  ( $R_E > 1$ ) and  $R_S < R_E$  for  $\alpha > 120^\circ$  ( $R_E < 1$ ). The bump near  $\alpha \approx 70^\circ$  in Figure 3.6 is a symptom of the near vanishing of  $\epsilon_y$ , Eq. 3.16. Figure 3.7 shows the swelling ratio and extension ratio for a

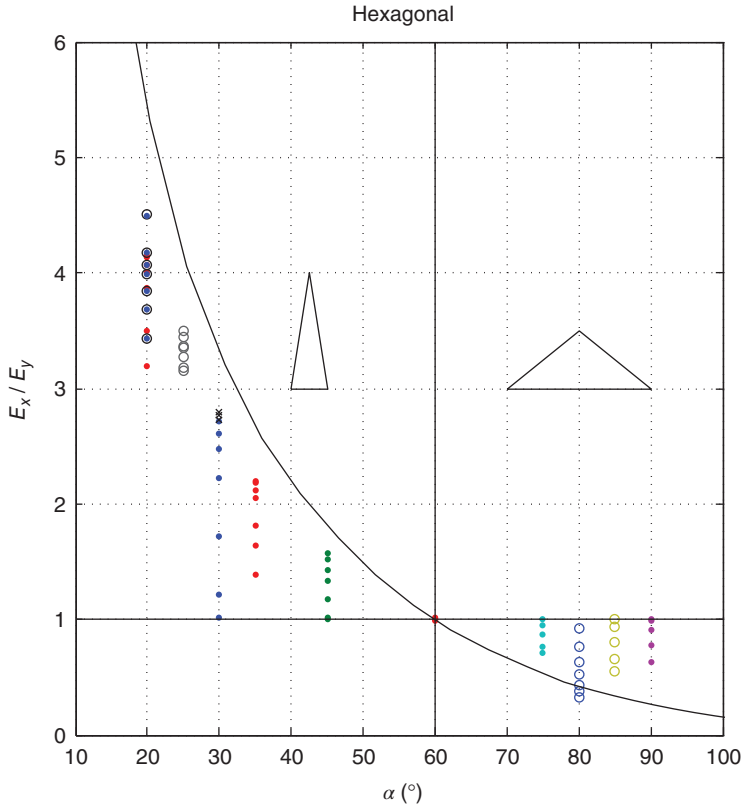


**Figure 3.5** hexRE Extension ratio, hexagonal. The extension ratio for hexagonal solids built by dressing frames for various angles  $\alpha$ ,  $20^{\circ} < \alpha < 90^{\circ}$ . At each angle the porosity varies from near zero, where the extension

ratio is near 1, to near 1. The heavy solid line is the  $\phi = 1$  limit for  $E_y/E_x$  from Eq. 3.18. Skeletons built from a frame with  $\alpha = 60^{\circ}$  are isotropic,  $E_y/E_x = 1$ . The extension ratio is  $> 1$  ( $< 1$ ) for  $\alpha >$  ( $<$ )  $60^{\circ}$ .

series of hexagonal cellular solids of fixed skeleton thickness and varying  $\alpha$ , representing a second example of the relationship of the swelling ratio to the extension ratio. The difference between these ratios for the hexagonal solids is much weaker as expected.

### 3.5

#### Fluid in the Skeleton

We now turn to the response of cellular solids to internal forces produced by fluids. The  $1 \times 1$  solids are fixed at their center,  $(x, y) = (0.5, 0.5)$ , and subject to neither applied forces nor displacements. We adopt Eq. 3.5 for the description

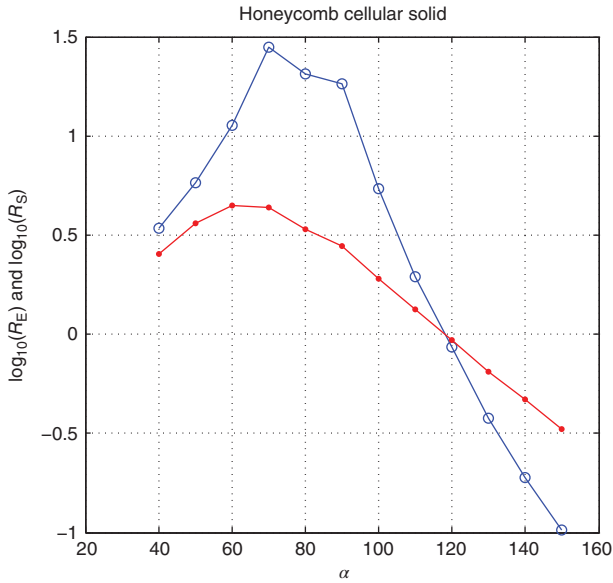


**Figure 3.6** RSHC Swelling ratio, honeycomb. The swelling ratio for honeycomb solids with fixed skeleton thickness and various angles  $\alpha$  (open circles). The extension ratio of the same solids (closed circles). In general,  $R_S > (<) R_E$  for  $\alpha < (>) 120^\circ$ .

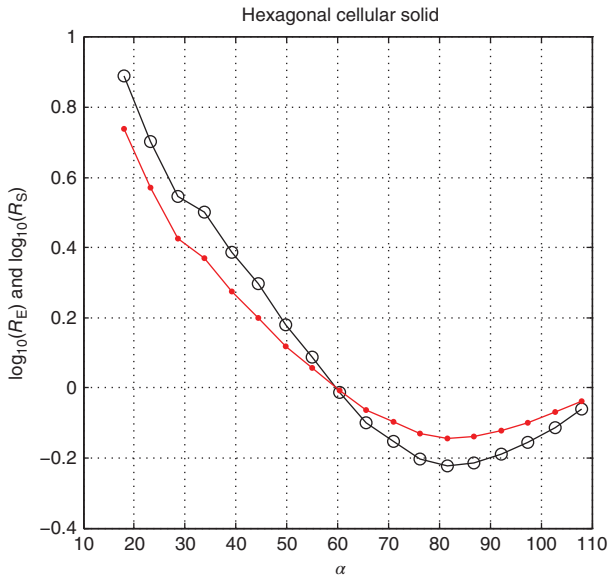


**Figure 3.7** RShex Swelling ratio, hexagonal. The swelling ratio for hexagonal solids with fixed skeleton thickness and various angles,  $\alpha$ , (open circles). The extension ratio

of the same solids (closed circles). In general  $R_S > (<) R_E$  for  $\alpha < (>) 60^\circ$ . Compared to Figure 3.6, the hexagonal solids are less volatile than the honeycomb solids.

of the fluid–solid coupling, and to emphasize the role of this coupling we work exclusively at  $J_{ij} = 0$ . Deformation of the solids results from the internal forces induced by the fluid. The fluid configurations are controlled by the chemical potential. For convenience we take the values of  $\mu_c$ , Eq. 3.6, to be normally distributed about  $\mu = 0$  with width 1. We employ an *isotherm* chemical potential protocol, a loop from  $\mu = -5$  (dry) to  $\mu = +5$  (saturated) and back to  $\mu = -5$  (dry) [5, 11]. The system of internal forces from the fluids exerts neither a net force nor a net torque as they comprise a system of force dipoles. We monitor

the moisture content

$$m = \frac{\sum_{i=1}^{N_e} A_i \rho_i}{\sum_{i=1}^{N_e} A_i}, \quad (3.19)$$

where  $A_i$  is the area of element  $i$ ,  $N_e$  is the total number of elements in the system, and  $\rho_i = 0, 1$ ;

the  $x$ -strain

$$\epsilon_x = \frac{U_x(x=1) - U_x(x=0)}{1}, \quad (3.20)$$

where  $U_x(x=1)$  is the average  $x$ -displacement of the right side and  $U_x(x=0)$  is the average  $x$ -displacement of the left side of the system;

the  $y$ -strain

$$\epsilon_y = \frac{U_y(y=1) - U_y(y=0)}{1}, \quad (3.21)$$

where  $U_y(y=1)$  is the average  $y$ -displacement of the upper edge and  $U_y(y=0)$  is the average  $y$ -displacement of the lower edge of the system.

We begin with a honeycomb cellular solid with  $\alpha = 75^\circ$  ( $35\% \leq \phi \leq 80\%$ ) for which the coupling constant  $W$ , which is nonzero in Eq. 3.7, is set to zero in Eq. 3.6. Consequently, the internal forces are deployed by the fluid but the resulting strains do not influence the behavior of the fluid, that is,  $\mu_i^c$  is independent of strain. As seen in Figure 3.8, the important evolution of  $m$ ,  $\epsilon_x$ , and  $\epsilon_y$  occurs as  $\mu$  crosses  $\mu \approx 0$ . In each panel there are six curves, which closely overlay one another, corresponding to six values of the porosity,  $35\% \leq \phi \leq 80\%$ , with the curve corresponding to  $\phi \approx 80\%$  indicated by the solid dots. The moisture content, panel (a), is normed to 1 for each  $\phi$ , Eq. 3.19. The strains, panels (b) and (c), are independent of  $\phi$  and  $\epsilon_x \approx \epsilon_y$  (thus, the curves overlay one another). In Figure 3.9, we show  $\epsilon_x$  as a function of  $m$ . Again there are six curves corresponding to six values of  $\phi$ . The strain is proportional to  $m$  as implied by Eq. 3.7.

We now turn on the coupling constant  $W$ , that is,  $W \neq 0$  in Eq. 3.7. We repeat the calculations reported earlier (Figures 3.8 and 3.9), with  $\alpha = 75^\circ$  and  $\phi \approx 80\%$ . The results are shown in Figures 3.10 and 3.16. In Figure 3.10, we see that  $m$ ,  $\epsilon_x$ , and  $\epsilon_y$  are the hysteretic functions of  $\mu$ , and that  $\epsilon_x$  and  $\epsilon_y$  are similar to

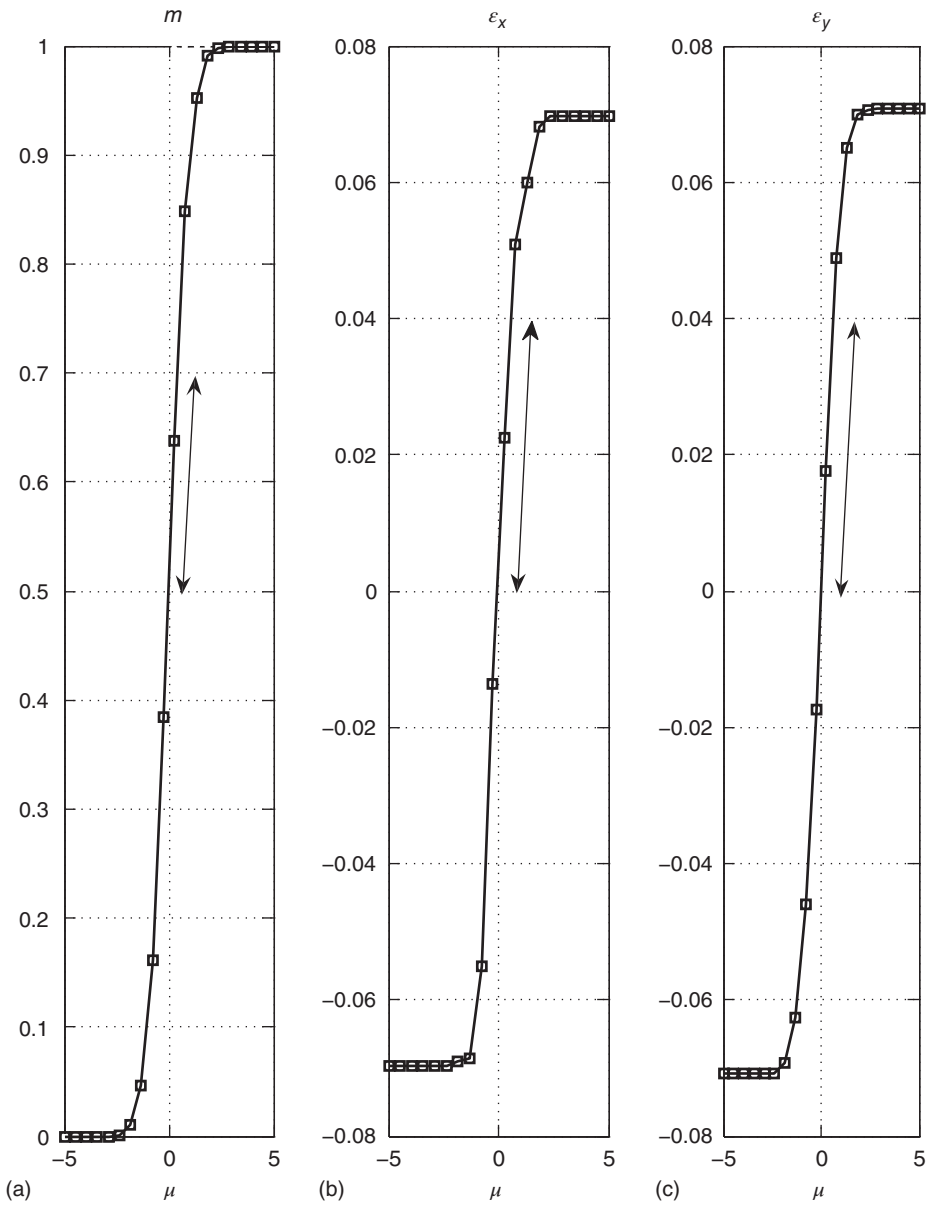


**Figure 3.8 caseb1** Fluid response of honeycomb solids,  $W = 0$ , fluid in skeleton. Results for a cellular solid with  $\alpha = 75^\circ$  and  $\phi \approx 80\%$ . (a) The moisture content (normed so that  $m(\mu = +5) = 1$ ) as a function of  $\mu$ . (b) The

x-strain,  $\epsilon_x$ , as a function of  $\mu$ . (c) The y-strain,  $\epsilon_y$ , as a function of  $\mu$ . The behavior shown is independent of  $\phi$  ( $35\% \leq \phi \leq 80\%$ ) as  $\mu$  protocol varies  $-5 \rightarrow +5 \rightarrow -5$ .

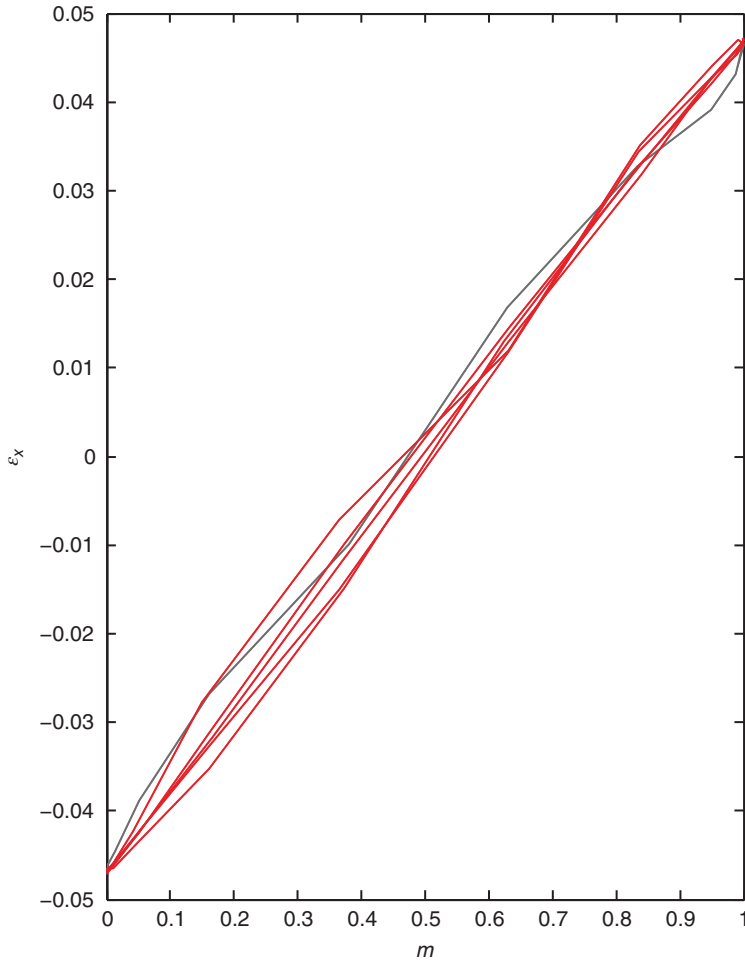


**Figure 3.9** exu Fluid response of honeycomb solids,  $\epsilon_x - m$ ,  $W = 0$ , fluid in skeleton. The  $x$ -strain,  $\epsilon_x$ , as a function of fluid content,  $m$ , for six cellular solids with  $\alpha = 75^\circ$  and  $35\% \leq \phi \leq 80\%$ . A plot of  $\epsilon_x - \mu$  would overlay one another in Figure 3.8, so would the  $y$ -strain.

one another. The middle curve with squares in each panel is a reminder of the behavior seen when the interaction in Eq. 3.7 is turned off (Figure 3.8). The strains, which are a hysteretic function of  $\mu$ , are at most a very weak hysteretic function of the moisture content, (Figure 3.16), the loops are almost closed (see also Figure 3.17).

The hysteresis seen in the response to a chemical potential protocol is emergent, that is, while there is no local hysteresis at the microscopic level, there is hysteresis at the macroscopic system. This hysteresis arises from the strain response of the

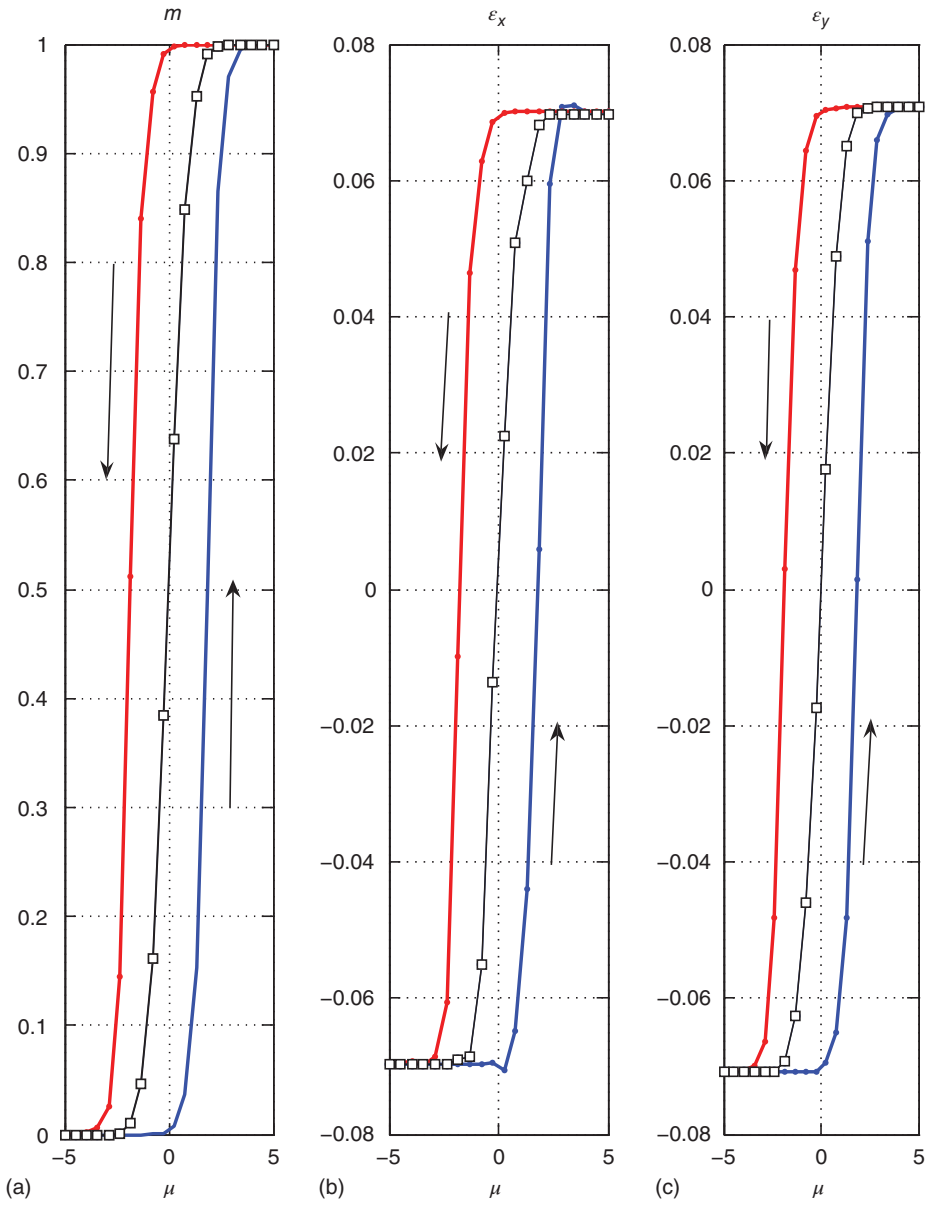


**Figure 3.10 caseb2** Fluid response of honeycomb solids,  $W \neq 0$ , fluid in skeleton. Results for a cellular solid with  $\alpha = 75^\circ$  and  $\phi \approx 80\%$ . (a) The moisture content (normed so that  $m(\mu = +5) = 1$ ) as a function of  $\mu$ . (b) The x-strain,  $\epsilon_x$ , as a function of  $\mu$ . (c) The

y-strain,  $\epsilon_y$ , as a function of  $\mu$ . All curves are traced as indicated by the arrows as the  $\mu$  protocol varies  $-5 \rightarrow +5 \rightarrow -5$ . The middle curve is the reversible curve for  $W = 0$  from Figure 3.8.



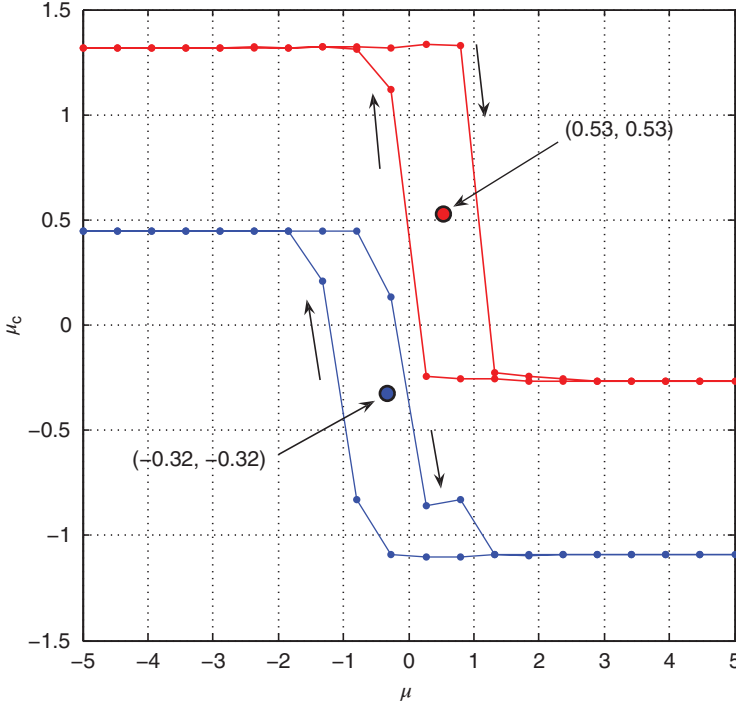


**Figure 3.11**  $\mu_c$  Behavior of  $\mu_c$ . The value of  $\mu_c^i$  for two elastic elements in the skeleton, one with  $U_i = -0.32$  and the other with  $U_i = 0.53$ , as the chemical potential is swept  $-5 \rightarrow +5 \rightarrow -5$ . For  $W = 0$ , the values of  $\mu_c^i$  are equal to  $U_i$  independent of  $\mu$ .

critical chemical potentials, Eq. 3.7, for example,

$$\mu_i^c = U_i + W_i \quad (\nabla \cdot \mathbf{u})_i \quad (3.22)$$

where  $(\nabla \cdot \mathbf{u})_i$  is the strain on element  $i$ . In Figure 3.11,  $\mu_c^i$  of two arbitrary elements is followed as a function of  $\mu$ . For large negative  $\mu$ , the internal forces are compressive,  $(\nabla \cdot \mathbf{u})_i < 0$ , and the effective chemical potential is greater than the *bare* value ( $U$ ), for example,  $U_i = +0.53$  and  $-0.32$ , as shown in the figure (recall  $W_i \leq 0$ ). Thus, on  $\mu$  increase,  $\mu$  must go to  $\mu > U_i$  in order for  $\rho_i$  to make the transition from  $\rho_i = 0$  to  $\rho_i = 1$ . As the chemical potential increases to allow fluid into the system, the internal forces evolve from compression-like to tension-like ( $(\nabla \cdot \mathbf{u})_i > 0$ ) and the critical chemical potentials evolve as shown. So, as  $\mu$  decreases,  $\mu$  must go to  $\mu < U_i$  in order for  $\rho_i$  to make the transition from  $\rho_i = 1$  to  $\rho_i = 0$ . The hysteresis arises from a fluid–fluid interaction that is mediated by the elastic system, that is, the fluid is coupled to the solid, which in turn is coupled back to the fluid, Eq. 3.7 ( $\rho \rightarrow \mathbf{u}$ ) and Eq. 3.6 ( $\mathbf{u} \rightarrow \rho$ ).

The results of the study of a variety of cellular solids with varying porosity and structural anisotropy are shown in Figure 3.17, where  $d\epsilon_y/d\epsilon_x$  is plotted as a function of extension ratio,  $E_y/E_x$ . The asymmetry of the  $x$  and  $y$  responses to applied forces, seen in Figures 3.4 and 3.5, makes no appearance in  $d\epsilon_y/d\epsilon_x$  even as  $R_E$  varies over *two* orders of magnitude. The strain response to the internal forces is point-wise in an elastically isotropic material, that is, it is the same everywhere. Thus, the material shrinks and expands uniformly.

### 3.6

#### Fluid in the Pore Space

We have so far established the elastic properties of the cellular solids in response to applied external forces and in response to internal forces that live in the skeleton. We now turn to the response of cellular solids to internal forces produced by fluids that reside in a filled *pore space*, case 3 in Figure 3.3. The solids, which occupy a  $1 \times 1$  square, are fixed at their center,  $(x, y) = (0.5, 0.5)$ , subject to neither applied forces nor imposed displacements. In addition, there were no internal forces on or in the skeleton. Deformation of the solids results only from the internal forces caused by fluid in the filled pore space. The pore space is elastically isotropic and soft, having elastic constants that are 1% those of the skeleton. Our interest is in the way in which the skeleton responds to forces on it. As earlier, we make the initial study where  $W = 0$  in Eq. 3.6.

We report results analogous to those reported in Figures 3.8–3.10. In Figure 3.12, we show  $m$ ,  $\epsilon_x$ , and  $\epsilon_y$  as a function of  $\mu$  for  $\alpha = 75^\circ$  and  $35\% \leq \phi \leq 80\%$ , with solid dots on the  $\phi \approx 80\%$  curve. For each  $\phi$ , the moisture content is normed to  $m_{\max} = 1$ . Most notable, in contrast to the case of fluid only in the skeleton, the  $x$  and  $y$  strains differ from one another (i.e., the system is anisotropic) and depend importantly on  $\phi$ . At  $\phi \approx 80\%$ ,  $|\epsilon_x| \approx 20|\epsilon_y|$  at  $m = 0$  and  $m = 1$ . As seen in Figure 3.13, the  $x$  and  $y$  strains scale with  $m$  but differently for each  $\phi$ . Therefore, the slope  $d\epsilon_y/d\epsilon_x$  is a function of  $\phi$  (Figure 3.14).

The contrast between what we see here and what was observed in Figures 3.8 and 3.10 arises because of the way in which the forces are delivered by the fluid. The forces in the filled pores push on the skeleton uniformly from all directions, canceling in the interior of the system and resulting in an approximately uniform stress on the system surface. The responses to this surface stress are, thus, similar to the response to a uniform applied stress. So the swelling ratio,  $R_S$ , discussed in Section 3.4, is the controlling elastic property.

Let us turn on the coupling  $W$  in Eq. 3.6 to see how hysteresis influences these results. In Figures 3.15 and 3.16, we show results analogous to those in Figures 3.12 and 3.13. Because of the complications made by the hysteresis, for clarity we show the results for only two porosities, the largest ( $\approx 80\%$ ) and the smallest ( $\approx 35\%$ ). The  $x$  and  $y$  strains are hysteretic functions of  $\mu$  that straddle the  $W = 0$  curves. They are weakly hysteretic functions of  $m$  as illustrated in Figure 3.16, a plot of  $\epsilon_x$  as a function of  $m$ , for  $\phi \approx 60^\circ$ .

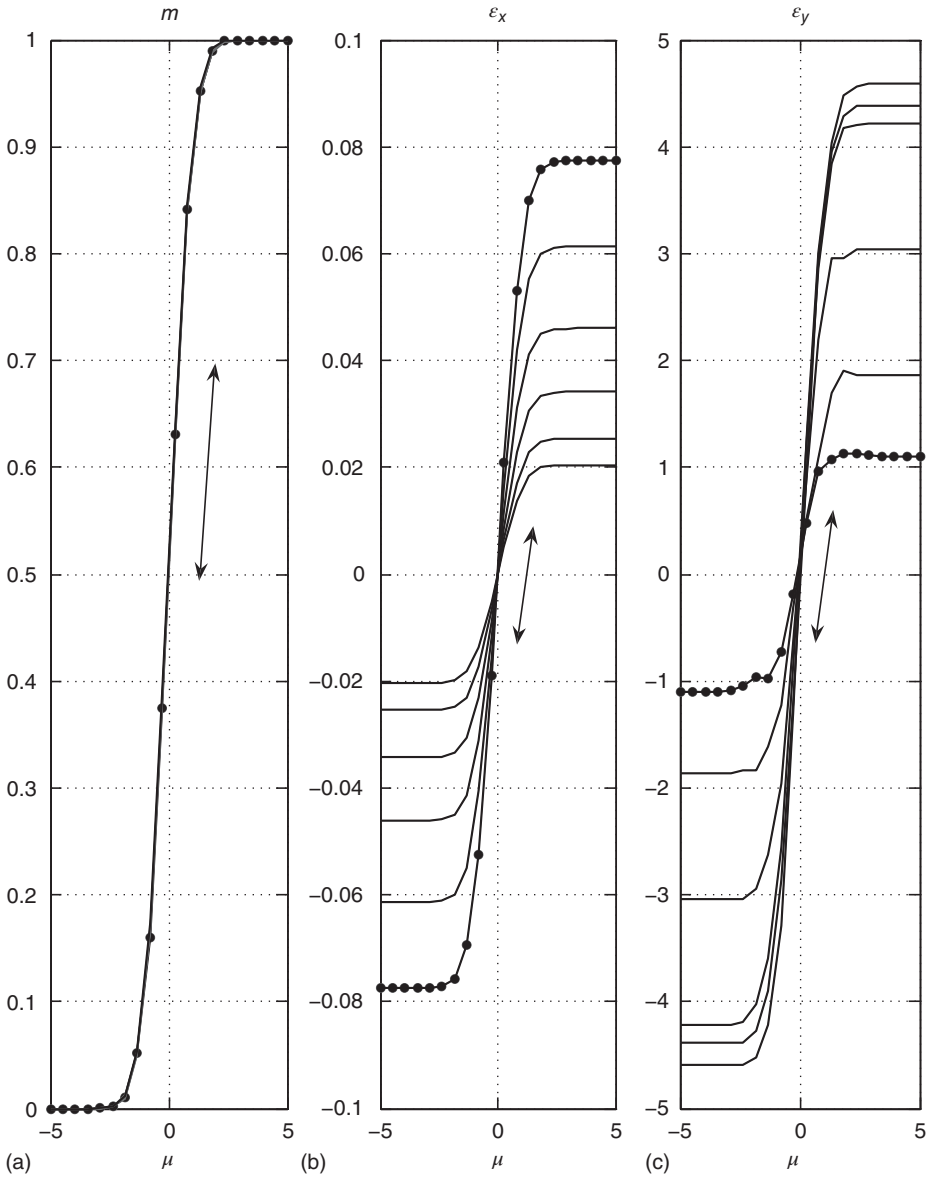


**Figure 3.12** v03 Fluid response of honeycomb solids,  $W = 0$ , fluid in pore filler. Results for six cellular solids with  $\alpha = 75^\circ$  and  $35^\circ \leq \phi \leq 80\%$ . (a) The moisture content (normed so that  $m(\mu = +5) = 1$ ) as a function of  $\mu$ . (b) The x-strain,  $\epsilon_x$ , as a function of  $\mu$ . (c) The y-strain,  $\epsilon_y$ , as a function of

$\mu$ . The behavior depends on  $\phi$ , compare to Figure 3.8. The curve for  $\phi \approx 80\%$  has closed circles. As the  $\mu$  protocol varies  $-5 \rightarrow +5 \rightarrow -5$ , each curve is traced reversibly. Note the evolution of the x-strain (y-strain) as  $\phi$  varies.

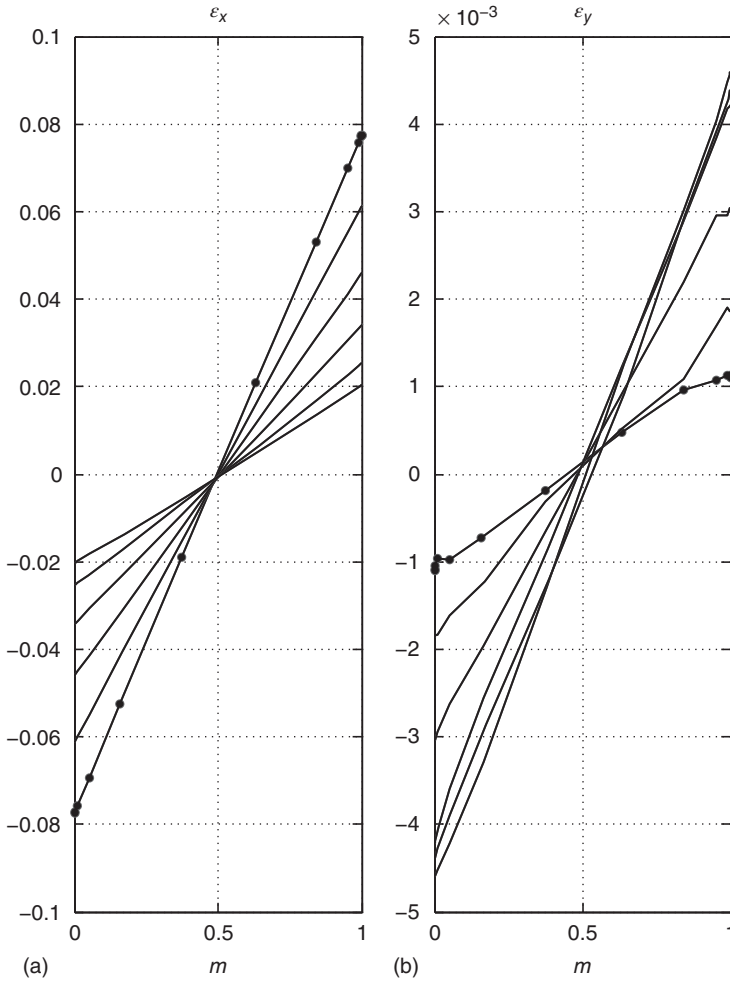


**Figure 3.13** *vexueyu* Fluid response of honeycomb solids,  $W = 0$ , fluid in pore filler, strain versus fluid content. Results for six cellular solids with  $\alpha = 75^\circ$  and  $35^\circ \leq \phi \leq 80\%$  in the form  $\epsilon - m$ : (a)  $\epsilon_x - m$  and (b)  $\epsilon_y - m$ . The curve for  $\phi \approx 80\%$  has closed circles. As the  $\mu$  protocol varies  $-5 \rightarrow +5 \rightarrow -5$ , each curve is traced reversibly. Note the evolution of the x-strain (y-strain) as  $\phi$  varies.

In Figure 3.17, we show  $d\epsilon_y/d\epsilon_x$  as a function of  $R_s$  for approximately 100 examples of cellular solids with different frame geometries, anisotropies, and porosities when the fluid is in the filled pore space. In this figure, we also show  $d\epsilon_y/d\epsilon_x$  as a function of  $R_E$  for approximately 100 examples of cellular solids with different frame geometries, anisotropies, and porosities when the fluid is only in the skeleton. The contrast is striking. When the fluid is in the skeleton there is no

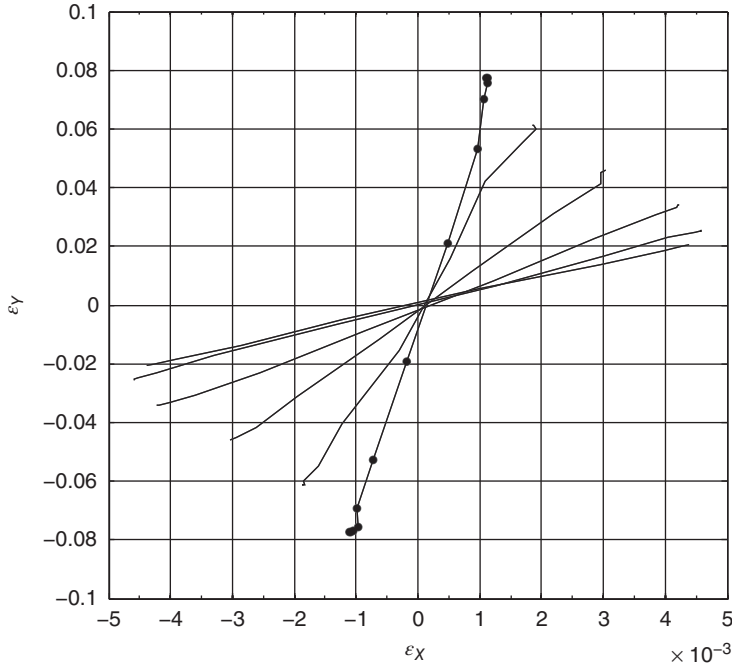


**Figure 3.14** **vexey** Fluid response of honeycomb solids,  $W = 0$ , fluid in pore filler,  $x$ -strain versus  $y$ -strain. Results for six cellular solids with  $\alpha = 75^\circ$  and  $35^\circ \leq \phi \leq 80\%$  in the form  $\varepsilon_x - \varepsilon_y$ . The curve for  $\phi \approx 80\%$

has closed circles. As the  $\mu$  protocol varies  $-5 \rightarrow +5 \rightarrow -5$ , each curve is traced reversibly. Note  $d\varepsilon_y/d\varepsilon_x$  varies importantly with  $\phi$ .

unusual behavior,  $d\varepsilon_y/d\varepsilon_x = 1$ . When the fluid is in the filled pore space,  $d\varepsilon_y/d\varepsilon_x$  approximately follows  $R_S$  and can be highly anisotropic,  $d\varepsilon_y/d\varepsilon_x \neq 1$ .

### 3.7

#### Summary and Conclusion

In this chapter, we presented a unifying theoretical model for describing fluid–solid coupling in porous materials. We applied this model to investigate the response of cellular solids to the presence of fluids. Through the fluid–solid coupling, Eq. 3.5, the fluids in the structural features of the solid promote the presence of more fluid in these features. Thus, the fluid interacts with itself and responds hysteretically to a chemical potential protocol. Two cases were studied in detail: (i) that in which the fluid entered the skeleton and (ii) that in which the fluid entered the pore filling. The response in these two cases, while qualitatively similar, was quantitatively very different. The difference in response

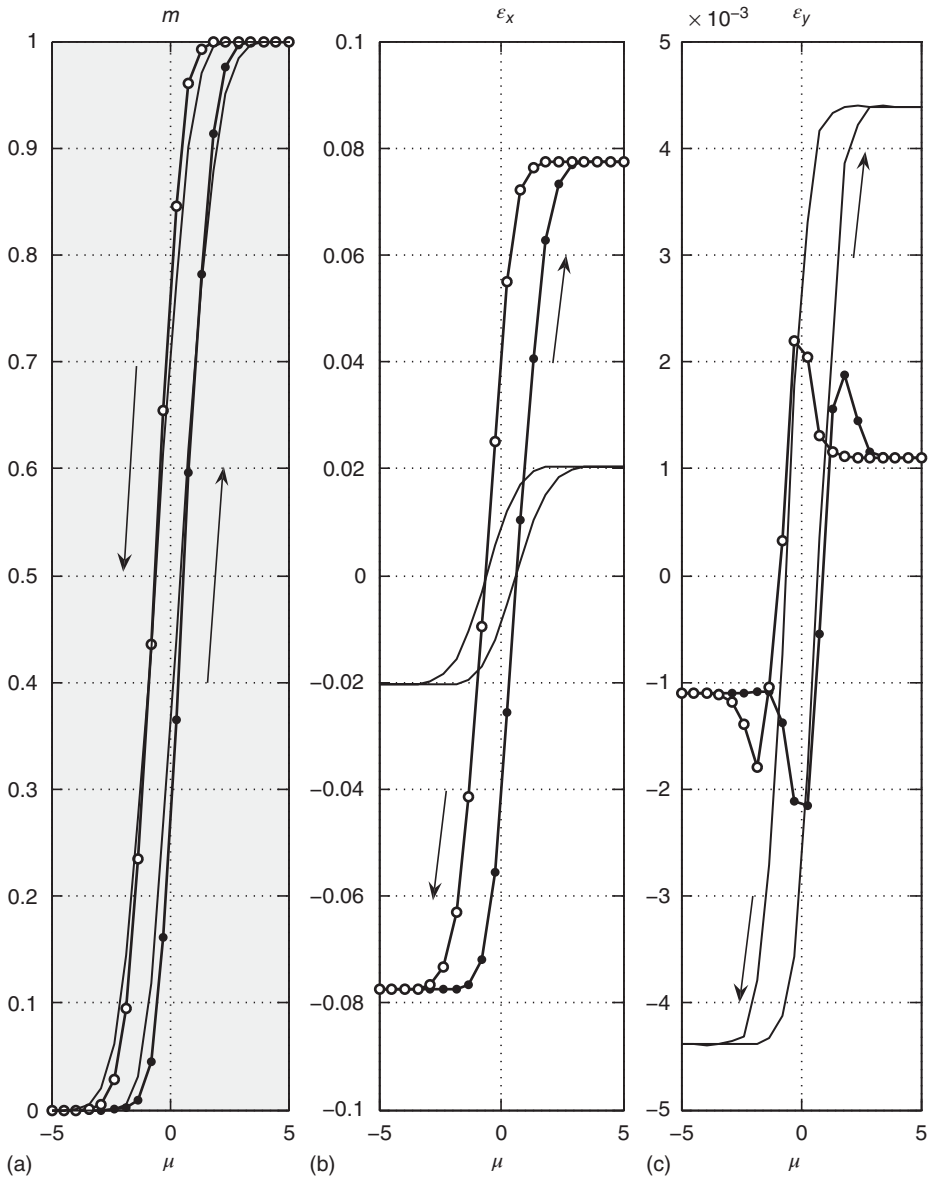


**Figure 3.15** vLam3 Fluid response of honeycomb solids,  $W \neq 0$ , fluid in pore filler. Results for two cellular solids with  $\alpha = 75^\circ$  and  $\phi \approx 35^\circ$  and  $\phi \approx 80\%$  (closed circles). (a) The moisture content (normed so that  $m(\mu = +5) = 1$ ) as a function of  $\mu$ . (b) The

x-strain,  $\epsilon_x$ , as a function of  $\mu$ . (c) The y-strain,  $\epsilon_y$ , as a function of  $\mu$ . The behavior is hysteretic and depends on  $\phi$  compared to Figure 3.12. As the  $\mu$  protocol varies  $-5 \rightarrow +5 \rightarrow -5$ , each curve is traced as indicated by the arrows.

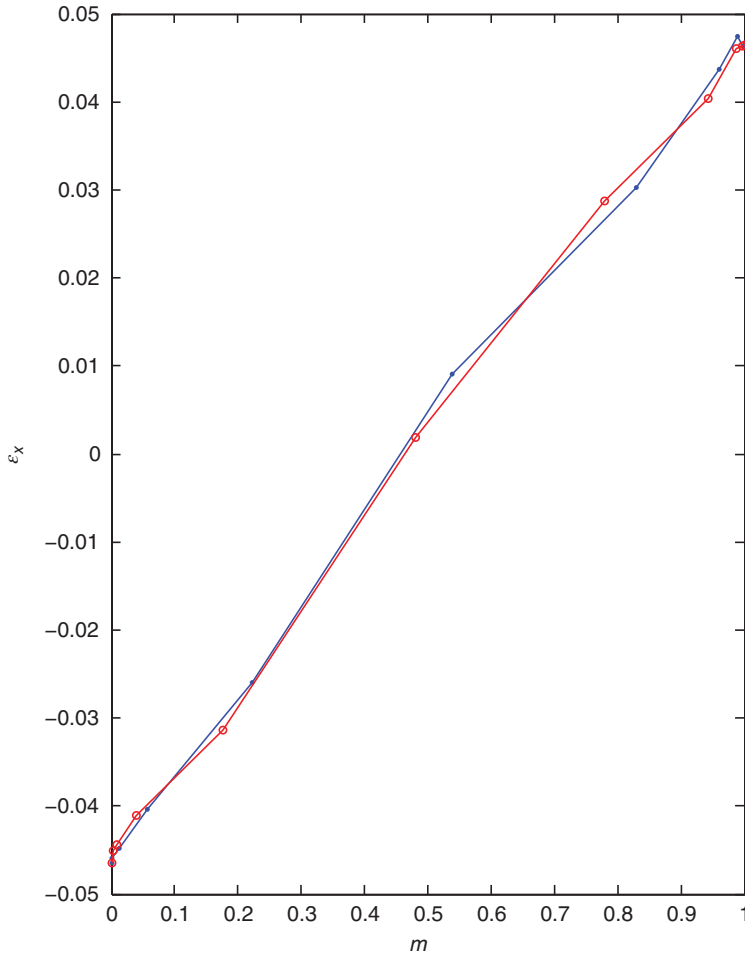


**Figure 3.16** *exuLam* Fluid response of honeycomb solids,  $W \neq 0$ , fluid in pore filler,  $\alpha = 75^\circ$  and  $\phi \approx 60\%$ . The strain is a possibly weak hysteretic function of  $m$  compared to strain versus  $m$ . The x-strain,  $\epsilon_x$ , as a function of fluid content,  $m$ , for a cellular solids with Figure 3.15.

arises because different fluid configurations, through the fluid–solid coupling, push differently on the mechanical structure, the skeleton. These different pushes probe different aspects of the cellular solids elastic response.

The theoretical model exhibited here can be generalized to study the case of conventional adsorption isotherms [5, 11] as well as the complementary bricks and mortar geometry in which the mechanically stiff material is embedded in a soft material [12–14].

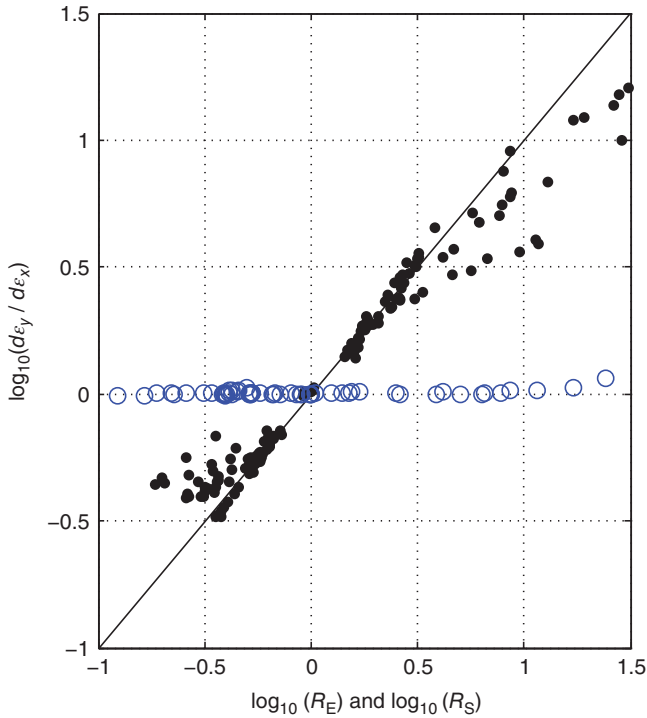


**Figure 3.17 composite67** Strain response to fluid in skeleton/filler. Open circles, the derivative  $d\epsilon_y/d\epsilon_x$  as a function of the extension ratio,  $R_E$ , for many cellular solids, a variety of geometries (honeycomb, hexagonal, rectangular), porosities ( $30\% < \phi < 85\%$ ), and anisotropies when the fluid is in

the skeleton. Closed circles, the derivative  $d\epsilon_y/d\epsilon_x$  as a function of the extension ratio,  $R_S$ , for many filled cellular solids, a variety of geometries (honeycomb, hexagonal, rectangular), porosities ( $30\% < \phi < 85\%$ ), and anisotropies when the fluid is in the pore filler.

## References

1. Gibson, L.J. and Ashby, M.F. ((2000) *Cellular Solids*, 2nd edn, Cambridge University Press, Cambridge.
2. Schraad, M.W. and Harlow, F.H. (2006) *Int. J. Mech. Sci.*, **48**, 85.
3. Dinwoodie, J.M. (2000) *Timber, Its Nature and Behaviour*, 2nd edn, Van Nostrand Reinhold Co. Ltd., London.
4. Harrington, M.J., Razghandi, K., Ditsch, F., Guiducci, L., Rueggerberg, M., Dunlop, J.W.C., Fratzl, P., Nienhuis, C., and Burgert, I. (2011) *Nat. Commun.*, **2**, 337.
5. Grosman, A. and Ortega, C. (2009) *Langmuir*, **25**, 8083.
6. Dawson, J., Vincent, J.F.V., and Rocca, A.M. (1997) *Nature*, **390**, 668.
7. Elbaum, R., Zaltman, L., Burgert, I., and Fratzl, P. (2007) *Science*, **316**, 884.
8. Hughes, T.J.R. (1987) *The Finite Element Method*, Prentice-Hall, Edgewood Cliffs, NJ.
9. Kierlik, E., Monson, P.A., Rosinberg, M.L., Sarkisov, L., and Tarjus, G. (2001) *Phys. Rev. Lett.*, **87**, 055701.



10. Guyer, R.A. (2006) in *The Science of Hysteresis III* (eds G. Bertotti and I. Mayergoyz), Elsevier, Cambridge, MA.
11. Lilly, M.P., Finley, P.T., and Hallock, R.B. (1993) *Phys. Rev. Lett.*, **71**, 4186.
12. Biot, M.A. (1962) *J. Appl. Phys.*, **33**, 1482.
13. Coussy, O. (2010) *Mechanics and Physics of Porous Solids*, John Wiley and Son, Ltd, Chichester.
14. Vandamme, M., Bouchard, L., LeCampion, B., and Coussy, O. (2010) *J. Mech. Phys. Solids*, **58**, 1489.
15. Gor, G.Y. and Neimark, A.V. (2011) *Langmuir*, **27**, 6926.
16. Schultz, E.P., Alarcon, L.M., and Appignanesi, G.A. (2011) *Eur. Phys. J. E*, **34**, 114.
17. Bergenstrahle, M. (2008) *Crystalline cellulose in bulk and at interfaces*. thesis, KTH.
18. Ting, T.C.T. and Chen, T. (2005) *Int. J. Mech. Appl. Math.*, **58**, 73.

## 4

## Influence of Damage and Moisture on the Nonlinear Hysteretic Behavior of Quasi-Brittle Materials

*Jan Carmeliet*

## 4.1

### Nonlinear, Hysteretic, and Damage Behavior of Quasi-Brittle Materials

In many environmental and engineering applications materials such as rocks, natural stones, and artificial materials such as mortar and concrete are loaded in cyclic quasistatic conditions at different moisture conditions. The cyclic loading may initiate a damage process showing an evolution from microcrack initiation and growth, toward a coalescence of microcracks into macrocracks, which further develop in major cracks leading finally to the failure of the material or structure. Figure 4.1 shows as an example the damage in an oolitic limestone resulting from the cyclic wetting with a salt solution and drying accompanied with crystallization damage [1]. The cracks show a complex pattern, following partly the internal material structure, influenced by the presence of initial damage or weak interfaces between the different components of the material. We observe multiple cracks running parallel to each other bridged by undamaged material regions in between. Due to the crack bridging phenomenon, mechanical forces can still be transmitted in the damaged material, meaning the material shows a remaining load-bearing capacity although damaged. With increasing damage level, the remaining load-bearing capacity or residual material strength further reduces. Materials showing this kind of damage behavior characterized by a gradual reduction of material strength are commonly called quasi-brittle materials. Figure 4.2 shows the typical load-deformation behavior of a quasi-brittle material (in this case concrete) in cyclic uniaxial loading. We distinguish two loading cases: cyclic loading in the tensile regime only [2] and cyclic loading in a combined tensile and compressive regime [3]. In the stress–strain curves, we can typically distinguish two regions. In the first region before reaching maximal loading, the so-called pre-peak region, a nonlinear stress–strain curve is observed. In this stage, the nonlinearity is due to loading of initial damage zones or due to the development of diffuse microcracks, which leads to a more than linear increase in strain at increasing stress. In the second region after reaching the maximal stress, we reach the so-called post-peak region, where a strain softening of the material occurs, that is, the load-carrying capacity reduces with increasing deformation, resulting in a descending post-peak

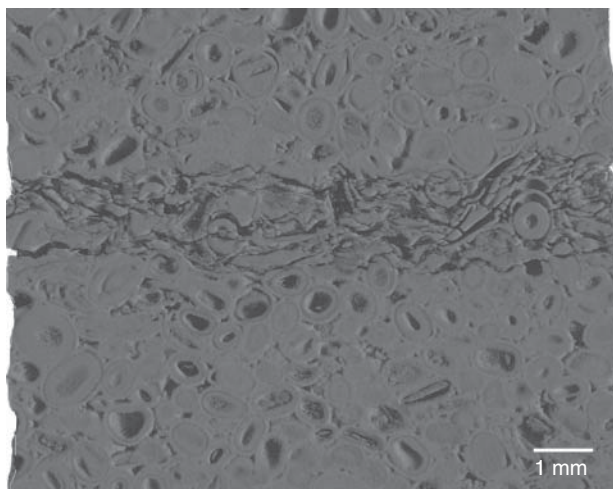


**Figure 4.1** Example of cracking pattern in an oolitic limestone (Savonieres) after four wetting–drying cycles with a 1.4 m  $\text{Na}_2\text{SO}_4$  salt solution [1].

stress–strain curve. The increasing deformations are due to a localization of deformation in limited damage regions in the material in the form of a single crack or multiple cracks. In a continuum description, the descending stress–strain curve is commonly called the strain-softening curve. We further see in Figure 4.2a that when we unload from the strain-softening curve, an unloading stress–strain curve is followed showing a reduction in material stiffness. This stiffness reduction is attributed to the presence of cracks or damage. When we reach zero tensile stress upon further unloading, we observe permanent strains that are due to the geometric misfit between opposite crack faces of closing cracks. When loading the damaged material further in compression (Figure 4.2b), the stiffness increases again, referred to as stiffness recovery, which is attributed to the closure of cracks at high compressive load. The crack-closure results in an increase in the material area sustaining load or a recovery of the initial stiffness of the material. When we again decrease the compressive load and continue loading again into the tensile domain, hysteretic loops are formed between unloading and reloading. Figure 4.2c shows that the shape of the tensile-compressive hysteretic loops changes markedly when we unload from the strain-softening curve at higher strain or damage levels. This means that the level of damage has an important influence on the hysteretic behavior under cyclic loading.

In summary, we observe nonlinear hysteretic loops in cyclic loading, a reduction of the stiffness with damage, permanent strains on unloading, and a stiffness recovery in compression; on damage evolution a strain-softening curve is followed; the shape of the hysteretic loops depends strongly on the damage level and on the stress, tensile, or compressive.

To further understand the particular behavior of quasi-brittle materials, we have to understand the mechanical behavior of the different components of these

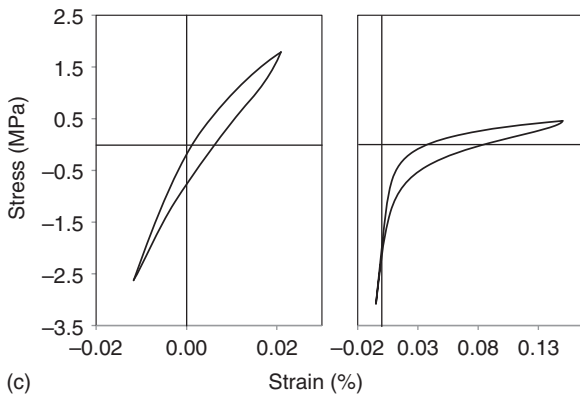
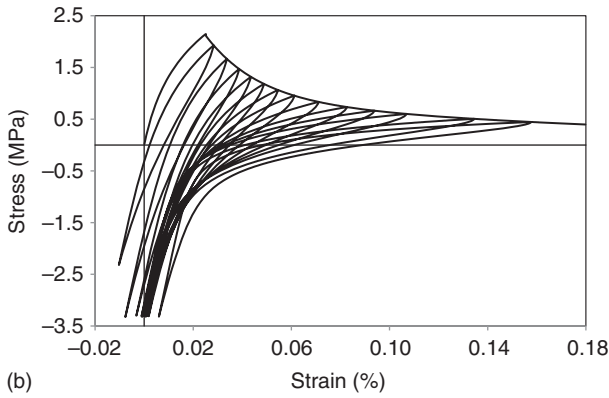
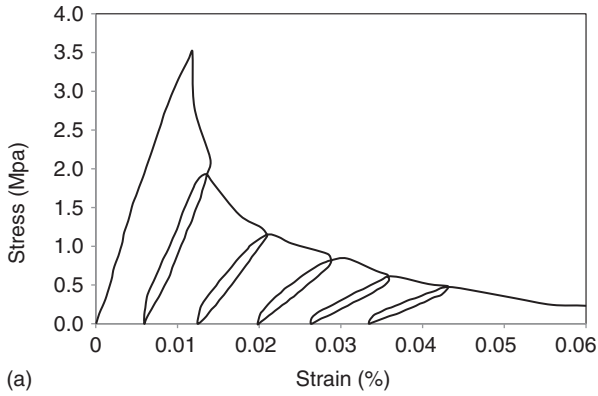


**Figure 4.2** (a) Stress-strain curve of concrete in cyclic tensile loading. (After [2].) (b) Stress-strain curve of concrete in tensile-compressive cyclic loading. (After [3].) (c)

Hysteretic loops at damage level 0.18 (left) and 0.9 (right) in tensile-compressive cyclic loading (After [3].).

materials and their interaction at the mesoscale. Consider quasi-brittle materials composed of granulates or grains that interface one another through a bond system, having both macroporosity and microporosity. Examples are sandstones and concrete. Darling *et al.* [4] demonstrated that the bond system between the aggregates in natural stones is responsible for the macroscopic, nonlinear elastic and hysteretic behavior, while the granulates show an elastic behavior. Quasistatic compressive tests on sandstones and limestones in combination with neutron diffraction experiments allowed to separate the strain of the bond system and strain in the bulk of the grain system. It was shown that the grains behave purely linear elastically, while the macroscopic strain is nonlinear and hysteretic. The nonlinear and hysteretic behavior of the material in the pre-peak region can, thus, be attributed to the behavior of the bond system. In concrete, the mortar bond system between the aggregates is rich of microcracks and a weaker (microcracked) zone at the interface of the aggregates, which develop due to a misfit between mortar and aggregates when the mortar is drying and shrinking. This microcracked bond system in concrete is at the origin of the nonlinear hysteretic behavior at the macroscale.

In continuum modeling, the strain-softening behavior, including stiffness reduction and permanent deformations, is often modeled by means of combined damage – plasticity models, which are enriched by higher order formulations (nonlocal or gradient [5, 6]) in order to adequately capture the strain localization phenomenon into cracks in a continuum sense. Rageneau *et al.* [7] proposed a damage plasticity model, where the stiffness reduction is modeled by damage and the hysteresis phenomenon by a plasticity model. Other approaches modeling mechanical hysteresis include a spring-slider model [8] and an interface cyclic model based on plasticity theory [9]. On the other hand, Gylltoft [10], Reinhardt *et al.* [11], Yankelevsky and Reinhardt [12], and Hordijk [13] proposed semi-empirical relations for describing the cyclic behavior of concrete. These models are macroscopic models in which the underlying heterogeneous structure of the material at lower levels is homogenized towards the macroscale. These models are not able to capture all observed nonlinear hysteretic and damage phenomena in a coupled way. One of the reasons is that a continuum (homogenized) description even enriched with higher order formulations, or semi-empirical models does not account explicitly for the lower scale phenomena, such as crack bridging and crack closure, which are at the origin of the observed nonlinear and hysteretic phenomena at the macroscale. In this chapter, we propose a two-scale model in which lower scale phenomena, such as crack opening and closure, are modeled at the microscale and mesoscale in a phenomenological way, and then the resulting constitutive properties, such as a stiffness or inelastic strain, are coupled to a continuum damage model at the macroscale. The proposed model is bidirectional, meaning that the damage evolution predicted at macroscale by the damage model is transferred back to the lower scales influencing the nonlinear and hysteretic phenomena.

In this paper, we model the nonlinear elastic hysteretic behavior of quasi-brittle materials at mesoscale and lower scales by a Preisach–Mayergoyz space model

(PM model). Preisach [14] described ferromagnetic hysteresis as a superposition of several bistable elements. The original description accounts for nonlinearity and losses under cyclic magnetization. This model has been further developed by Mayergoyz [15–17], hence the name Preisach–Mayergoyz model (PM model). The PM model has been applied to magnetic hysteresis as well as to nonlinear elastic behavior of materials (e.g., [18–21]), where Guyer and McCall applied the PM model to describe the quasistatic nonlinear stress–strain behavior of rocks. The proposed PM model is based on the observation that the nonlinear, hysteretic response is caused by the presence of defects in the material, for example, local contacts in microcracks and macrocracks, contacts between grains loaded in normal (adhesion) and shear modes. The number and nature of these contacts depend on the amount and characteristics of the cracks or defects present in the material and, therefore, also depend on the evolving damage process. Therefore, in this research, we link the PM model that describes the nonlinear elastic behavior at a given damage level, with a macroscopic damage model that is able to describe the damage evolution during a loading history [22]. The PM model also provides insight into the nature of material behavior at lower scales and at different degrees of damage, by studying the change of the PM parameters with evolving damage.

## 4.2

### Macroscopic Damage Model for Quasi-Brittle Materials

In this section, we develop a macroscopic damage model that describes the behavior of a damaged material, the conditions for damage growth, and the evolution of damage. A uniaxial scalar formulation is used for simplicity. Figure 4.3 gives a typical stress–strain curve in uniaxial tensile loading for a quasi-brittle material. An initial linear elastic curve with stiffness  $E_0$  is followed by a nonlinear pre-peak curve, reaching a maximum at the tensile strength  $f_t$ . The post-peak curve shows strain-softening behavior, that is, a decrease in residual strength with increasing strain. When unloading (and reloading) from a given point on the softening curve at a residual strength  $f_r$ , a hysteretic curve is followed. The total strain  $\varepsilon$  for a point on the hysteretic loop can be decomposed into an elastic strain  $\varepsilon_e$  and an inelastic strain  $\varepsilon_{in}$ . The inelastic strain covers inelastic phenomena such as nonlinear elasticity, residual deformations, and stiffness reduction, as well as stiffness recovery in compressive loading. Using the strain decomposition principle and using a scalar notation

$$\varepsilon = \varepsilon_e + \varepsilon_{in}. \quad (4.1)$$

For describing damage in the material, we introduce the damage variable  $d$ . According to the theory of continuum damage mechanics (see e.g., [23]), the damage parameter  $d$  is defined as the ratio of damaged versus initial undamaged material area. Assuming the damage to be isotropic, the damage variable has the same value in all directions and is a scalar. The damage variable describes also the reduction in stiffness or in strength during the damage process. The damage variable is

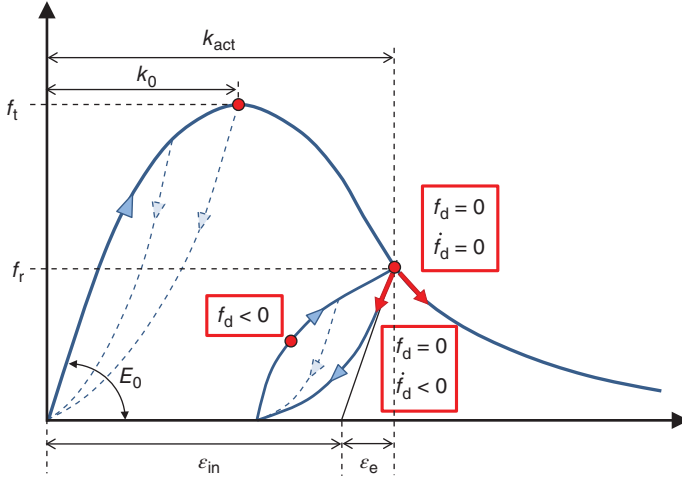


**Figure 4.3** Typical strain-softening curve in tensile loading for quasi-brittle materials. Pre-peak curve with unloading loops and post-peak curve with a hysteretic loop. Illustration of the loading conditions.

then defined as

$$d = 1 - \frac{f_r}{f_t} = 1 - \frac{E}{E_0} \quad (4.2)$$

with  $f_r$  being the residual strength of the material during the damage process,  $f_t$  the initial tensile strength,  $E$  the stiffness of the damaged material, and  $E_0$  the initial stiffness. Recalling the observations by Darling *et al.* [4], the elastic strain can be attributed to the elastic behavior of the aggregate (grain) system described by Hooke's law

$$\varepsilon_e = \frac{\sigma}{E_0} \quad (4.3)$$

with  $E_0$  the initial stiffness for the undamaged material and  $\sigma$  the stress. According to Eqs. (4.1) and (4.3), the total strain  $\varepsilon$  associated with the stress  $\sigma$  equals

$$\varepsilon = \frac{\sigma}{E_0} + \varepsilon_{in} \quad (4.4)$$

Equation (4.4) written in rate form becomes

$$\dot{\varepsilon} = \frac{\dot{\sigma}}{E_0} + h\dot{\sigma} = \frac{\dot{\sigma}}{E_T} \quad (4.5)$$

where the dot represent the time derivative. In Eq. (4.5),  $E_T$  is the tangential stiffness and  $h$  is the inelastic tangential compliance given by

$$h = \frac{\partial \varepsilon_{in}}{\partial \sigma}, \quad \frac{1}{E_T} = \frac{1}{E_0} + h. \quad (4.6)$$

In the next section, we will use the PM approach to determine the compliance  $h$ .

Figure 4.3 illustrates also how the nonlinear behavior is described in the pre-peak and post-peak regions during unloading and reloading. We assume that the hysteretic loops are closed after an unloading–loading cycle. In the pre-peak regime, no residual deformations are present, so we assume that the damage does not develop in the pre-peak regime and the material behaves nonlinear elastic without damage development. After reaching the peak strength, damage evolves and strain softening occurs, and upon unloading/reloading a hysteretic loop is formed, while permanent deformations are present at stress  $\sigma = 0$ . We assume that, in the hysteretic loop during unloading/reloading from the strain softening, damage does not develop and that the damaged material behaves nonlinearly. However, the nonlinear elastic behavior differs from that of the pre-peak region, since damage and stiffness reduction occur. Thus, we assume that damage evolution only occurs when the strain-softening curve is followed, the material behaves nonlinear elastic when unloading/reloading in the pre-peak regime or starting from the softening curve.

To model damage following the strain-softening curve, we assume that damage develops when an equivalent strain reaches a damage threshold. This condition is expressed by satisfying a damage threshold criterion  $f_d = 0$ . The function  $f_d$  is called the damage loading function, defining a damage surface in the equivalent strain space. For mode I type of damage, that is, tensile cracking, a Rankine type of damage loading function is often used

$$f_d = \varepsilon_{eq} - k_{act} \quad (4.7)$$

where  $\varepsilon_{eq}$  is the equivalent strain and  $k_{act}$  is the actual damage threshold. For mode I damage, we use the equivalent strain  $\varepsilon_{eq}$  as defined by Mazars [24] and Mazars and Pijaudier-Cabot [25]

$$\varepsilon_{eq} = \sqrt{\sum_i \langle \varepsilon_i \rangle^2} \quad (4.8)$$

In Eq. (4.8),  $\langle \varepsilon_i \rangle = \varepsilon_i$  if  $\varepsilon_i \geq 0$  and  $\langle \varepsilon_i \rangle = 0$  if  $\varepsilon_i < 0$ , with  $\varepsilon_i$  being the principal strain values. The actual damage threshold  $k_{act}$  in Eq. (4.8) equals the largest value of  $\varepsilon_{eq}$  ever reached during the damage process. The initial damage threshold is  $k_0$  and equals the strain at peak strength  $f_t$ .

We have to consider different possible loading conditions, as illustrated in Figure 4.3. The different loading conditions can be defined as follows:

- 1) If the equivalent strain is located within the damage surface or  $f_d < 0$ , then no damage evolution occurs ( $\dot{d} = 0$ ) and the material behaves nonlinear elastic.
- 2) If the equivalent strain is located on the damage surface or  $f_d = 0$ , two states can be distinguished:
  - a) If  $\dot{f}_d < 0$ , then no damage evolution takes place and the material behaves nonlinear elastic (unloading).
  - b) If  $\dot{f}_d = 0$ , then the damage grows and  $\dot{d} = F_d(\varepsilon_{eq})$  where  $F_d$  is the damage evolution equation.



The two arrows starting from a point on the softening branch show the different paths that can be followed: unloading or damage development. For simplicity, the damage evolution law  $F_d$  is often defined in an integrated way. We use the following integral damage evolution:

$$d = \alpha_1(1 - \exp(-\alpha_2(k_{\text{act}} - k_0))) + (1 - \alpha_1)(1 - \exp(-\alpha_3(k_{\text{act}} - k_0))) - \alpha_4(k_{\text{act}} - k_0) \quad (4.9)$$

with  $\alpha_i$  being the parameters to be determined from experiments. The parameters used can be found in Mertens [22].

In the next section, a PM model is presented to determine the inelastic strain, which describes nonlinear elastic phenomena such as stiffness reduction, residual deformations, hysteresis during unloading and reloading, and stiffness recovery in the compressive region.

### 4.3

#### Preisach–Mayergoyz (PM) Model for Nonlinear Hysteretic Elastic Behavior

The inelastic strain  $\varepsilon_{\text{in}}$  and the compliance  $h$ , as defined in Eqs. (4.1) and (4.6), are modeled using a PM approach. In the PM model, the behavior of the bond system is modeled by an ensemble of bistable elements (see Figure 4.4a), also called non-classical units (NCU)s. An NCU can only be in one of the two states, open (o) or closed (c). The behavior of a single hysteretic element is such that it is, for example, originally closed having a length  $L_c$ . When the tensile stress  $\sigma$  increases to  $\sigma_o$ , it will open to a length  $L_o$  and then remain open as the tensile stress continues to increase. When the applied stress  $\sigma$  again decreases, the element will close to its original length  $L_c$  at a closing stress  $\sigma_c$ , which can be different from the opening stress  $\sigma_o$ , thereby creating hysteresis at the NCU scale. The corresponding strain of an NCU equals  $\gamma = (L_o - L_c)/L_o$ . NCUs behave either in a reversible or in a hysteretic manner. An NCU is reversible when  $\sigma_o = \sigma_c$ , or when it opens and closes at the same stress (see Figure 4.4a).

It is assumed that a large number of NCU elements with different values for  $\gamma$ ,  $\sigma_o$ , and  $\sigma_c$  describe the global behavior of the bond system. The nonlinear strain  $\varepsilon_{\text{in}}$  is the outcome of the behavior of all these NCUs during a given stress protocol. The NCUs are mapped onto a stress space, where the values for  $\sigma_o$  and  $\sigma_c$  are used as coordinates (see Figure 4.4b). This space, called the PM space, is half-filled, since  $\sigma_o > \sigma_c$ . Reversible nonhysteretic NCUs reside on the diagonal, while hysteretic NCUs are located away from the diagonal. The NCUs are distributed over the PM space according to a PM density distribution  $\rho(\sigma_o, \sigma_c)$  (see Figure 4.4b). The integral over the domain  $\Omega_o$  of all open NCUs at a given stress state gives then the inelastic strain

$$\varepsilon_{\text{in}} = \int_{\Omega_o} \gamma(\sigma_o, \sigma_c) \rho(\sigma_o, \sigma_c) d\sigma_o d\sigma_c \quad (4.10)$$

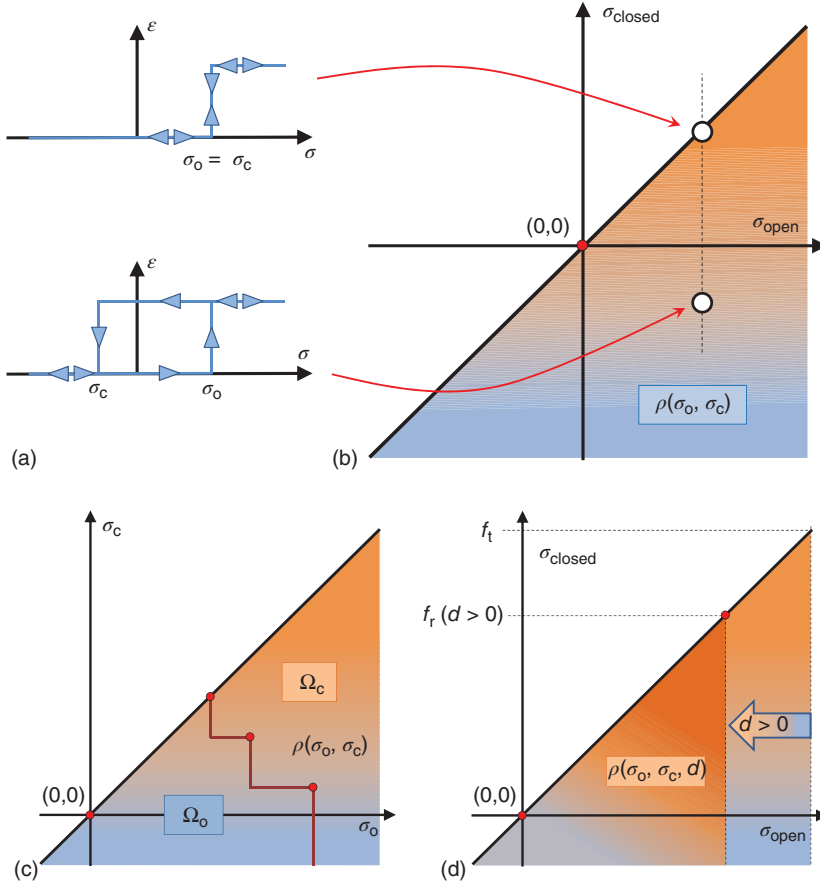


**Figure 4.4** (a) Nonhysteretic and hysteretic NCU units. (b) Mapping of the NCUs on the PM space, described by a PM distribution  $\rho(\sigma_o, \sigma_c)$ . (c) The domain of open and closed

elements in the PM space is divided by a staircase line after a certain loading history. (d) Due to damage development, the PM space shrinks at the right-hand side.

Following Carmeliet and Van Den Abeele [26], the NCU strain  $\gamma$  can be incorporated into the functional parameters of the PM density function. Therefore,  $\gamma$  is assumed to be equal to 1. During a stress protocol, NCUs will be opened and closed. During loading the stress follows the horizontal axis characterizing the opening stress  $\sigma_o$ , while during unloading the stress follows the vertical axis characterizing the closing stress  $\sigma_c$ . After a given stress protocol, the total PM domain is divided into a domain  $\Omega_o$  of open NCUs and a domain  $\Omega_c$  of closed NCUs. The two domains are always separated by a staircase line. The staircase line is characterized by vertices that correspond to extremes in the stress loading history (see Figure 4.4c). The compliance  $h$  in Eq. (4.6) is defined as the partial derivative of the inelastic strain, with respect to the closing stress for decreasing loading and the opening stress for increasing loading. Considering the definition of inelastic strain

in a PM formulation (Eq. (4.10)), the partial derivative equals the line integral over the horizontal lines in the staircase with  $\sigma = \sigma_c$  for decreasing loading, while for increasing loading it equals the line integral over the vertical lines of the staircase with  $\sigma = \sigma_o$ . In general, we may write

$$h = \frac{\partial \varepsilon_{in}}{\partial \sigma} = \int_{\sigma} \rho(\sigma_o, \sigma_c) d\sigma \quad (4.11)$$

Following Carmeliet and Van Den Abeele [26], the PM distribution is described by a sum of exponential functions

$$\rho(\sigma_o, \sigma_c) = \sum_{i=1}^n a_i \exp(b_i \sigma_m) \exp(-\kappa_i \sigma_d) \quad (4.12)$$

where  $\sigma_m$  is the mean stress located on the diagonal defined as  $\sigma_m = (\sigma_o + \sigma_c)/2$  and  $\sigma_d$  the distance normal to the diagonal in the PM space, or  $\sigma_m = (\sigma_o - \sigma_c)/2$ . The first term in Eq. (4.12) described by an exponential function depends on  $\sigma_m$  and describes the diagonal of the PM distribution. The parameter  $a_i$  is the PM value at zero stress of the  $i$ th exponential function and  $b_i$  describes the increase in the PM diagonal with  $\sigma_m$ . The second exponential function describes the decay of the PM value from the diagonal with  $\kappa_i$  the decay parameter. A decay parameter  $\kappa_i = 0$  means that the PM distribution is uniform starting from the diagonal showing a lot of hysteretic NCUs.

As stated earlier, the inelastic strain is a function of the damage. Therefore, the PM distribution and the parameters describing the PM distribution are also function of the damage. It is important to notice that when damage develops, the residual strength  $f_r$  decreases. The residual strength is the maximal tensile stress that can be applied on a damaged material and thus equals the maximum opening stress  $\sigma_o$ , which can be applied to the NCUs. Consequently, the NCUs are mapped with increasing damage in smaller regions of the PM space, or the populated PM space shrinks at the right border as damage increases (Figure 4.4d). The obtained model is referred to as the damage-dependent PM model.

The number of exponential functions  $n$  and the parameters  $a_i$ ,  $b_i$ , and  $\kappa_i$  are determined by inverse identification, minimizing the difference between experimental inelastic strain in a hysteretic loop and inelastic strain determined by the PM model. In Figure 4.5, a comparison of the experimental and the PM results is shown for tensile and tensile-compressive hysteretic loops. A good agreement is observed, meaning the present PM model is able to describe the hysteretic loops at different damage levels. It is found that the PM distribution for the cyclic tensile behavior can be described by one exponential function. For tensile-compressive behavior two exponential functions are needed, indicating the existence of two different NCU populations. The evolution of the PM parameters as a function of the damage is presented in Figure 4.6a–c, both for cyclic tensile and tensile-compressive behavior. The parameters  $a_i$  and  $b_i$  are plotted in semilogarithmic scale, while  $\kappa_i$  is plotted in linear scale.

For all loading cases the parameters  $a_1$  and  $b_1$  increase with damage, meaning the diagonal of the PM distribution becomes more populated with NCUs when

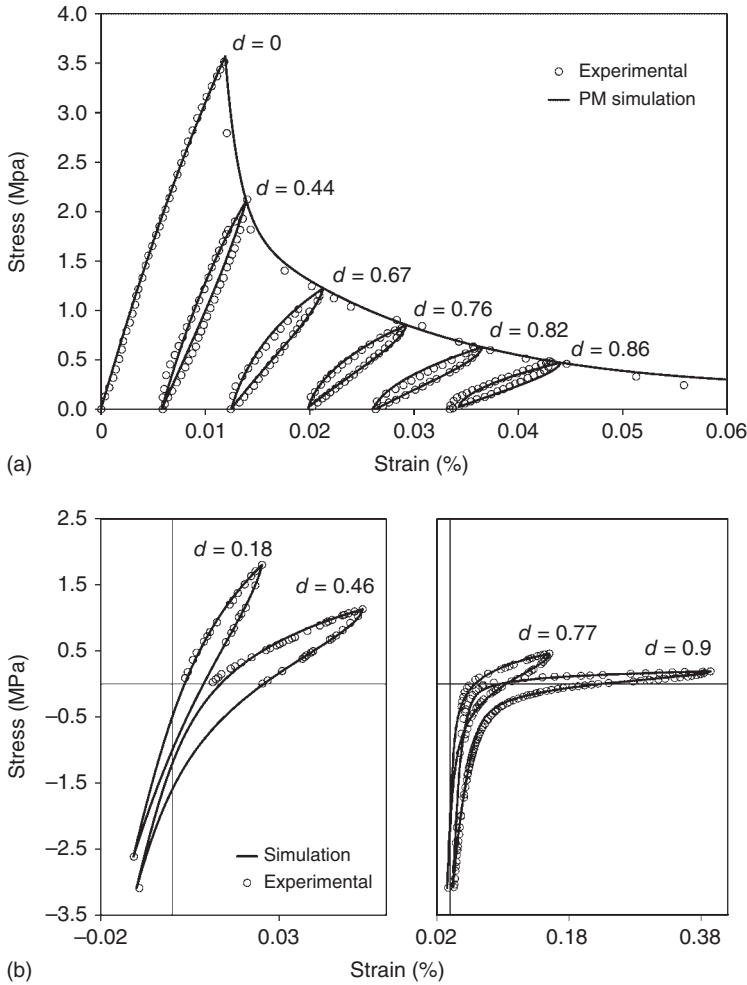


**Figure 4.5** Comparison of the experimental and the simulation results for tensile (a) and tensile-compressive (b) hysteresis loops at different levels of damage  $d$ .

damage is increasing. For cyclic tensile loading, the decay parameter  $\kappa_1$  increases with damage indicating that the NCUs become more closely populated near the diagonal, which means they behave less and less hysteretic. We see the same evolution for the decay parameter  $\kappa_1$  in tensile-compressive loading. However, for the tensile-compressive case at higher damage levels  $d \geq 0.8$ , the parameter  $\kappa_1$  of the first population decreases again to zero. At these damage values, macrocracks are present in the material. The decrease in  $\kappa_1$  indicates a shift of the NCUs again away from the diagonal, meaning they become more hysteretic. At the same time at these higher damage levels  $d \geq 0.8$ , we observe that a second NCU population develops and becomes active. The parameter  $a_2$  of the second population becomes only significant at higher damage levels (Figure 4.6a). The decay parameter  $\kappa_2$

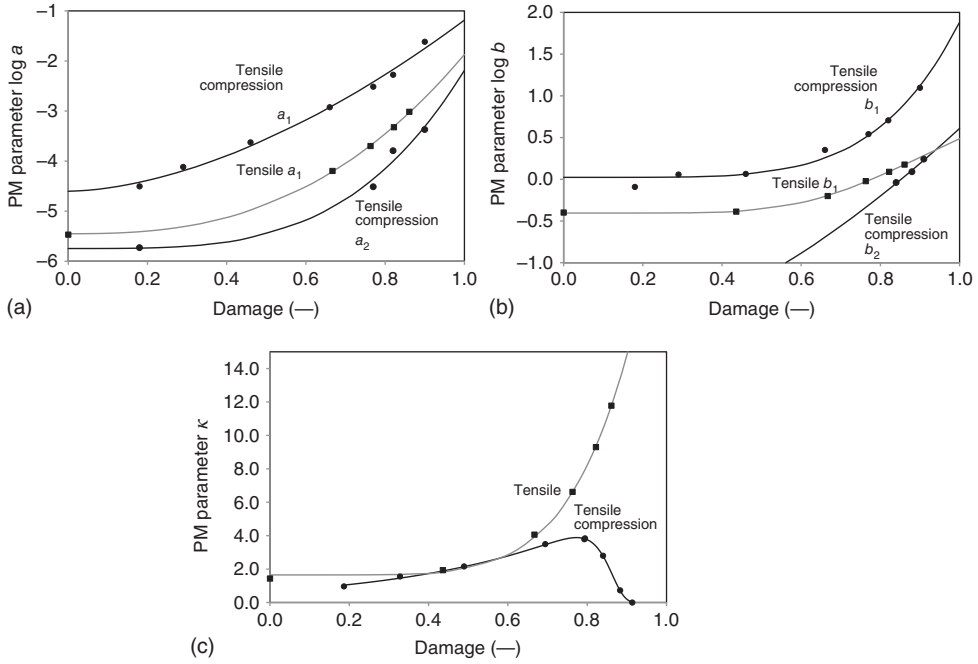


**Figure 4.6** PM parameters as function of damage for cyclic tensile and tensile-compression case. (a) Parameter  $a_i$ , (b) parameter  $b_i$ , and (c) parameter  $\kappa$ .

of this second population equals zero, or the second NCU population shows a uniform distribution starting from the diagonal, meaning all NCUs are behaving hysteretic. So for the tensile-compressive case, both the first and second NCU population behave quite hysteretic at high damage levels. This hysteretic nature of both NCU distributions at high damage level captures especially the very convex characteristic of the hysteretic loops at high damage levels.

The evolution of the PM parameters both for tensile and tensile-compressive loading indicates a change in number of NCUs and in hysteretic response of NCUs. This allows to understand in more detail the underlying lower scale phenomena when damage evolves. The increase in the NCUs with increasing damage level may be correlated with the increasing level of microcracking. We observed that the NCUs behave less hysteretic when further damage increases. During damage development, the microcracks start to coalesce in more continuous cracks. We may hypothesize that more continuous cracks behave less hysteretic than a large number of distributed microcracks. If this hypothesis applies, the process of crack coalescence may explain the change in nature of the NCUs to a less hysteretic behavior, or an increase in the  $\kappa$  value with damage. This increase in  $\kappa$  value is seen for the tensile and tensile-compression case for the lower damage levels. In pure tensile loading, the number of NCUs continues to increase and become less hysteretic (increasing  $\kappa$ -value) at very high damage levels. In tensile-compressive loading, the same evolution is observed up to

a damage level of 0.8. This behavior is thus also explained by the increase in microcracks with damage and also by the coalescence of microcracks into more continuous cracks, which behave less hysteretic. After a damage of 0.8, the two loading cases clearly differ. In the tensile loading case the NCUs continue to be less hysteretic, while for the tensile-compressive loading case the NCUs become more and more hysteretic. This difference between the two loading cases is attributed to the effect of compressive loading on the nature of damage in the material. At high damage levels, the cracks are evolved into macrocracks. When these macrocracks are closed at high compressive stress, the misfit between the crack surfaces spawns highly hysteretic contacts. The effect of the misfit of closing cracks on hysteresis has been shown by Aleshin and Van Den Abeele [27]. They showed that rough crack surfaces loaded in shear generate a stick-slip behavior, which shows PM characteristics and can thus be modeled by a PM approach. This explains the decrease in the  $\kappa$ -value for the first distribution and the zero  $\kappa$ -value of the second population in the tensile-compressive case.

In this section, we developed a PM model able to describe the hysteretic loops in tensile and tensile-compression loading at different damage levels. We also showed that the evolution of the PM parameters offers the possibility to more closely interpret the hysteretic behavior of damaged materials. In the next section, we will couple the macroscopic damage model with the damage-dependent PM model, allowing to upscale information from PM level to macrolevel and downscaling damage information from macroscale to PM scale.

#### 4.4

##### **Coupling the Macroscopic Damage Model and Damage-Dependent PM Model: Algorithmic Aspects**

The macroscopic damage model and the microscopic damage-dependent PM model are now coupled to predict the behavior of quasi-brittle materials in cyclic tensile and tensile-compression loading. In computational modeling, there exist two ways to apply external loading: a mechanical load can be imposed or we can prescribe a displacement at the boundary. These two approaches are commonly referred to as load (stress) and displacement (strain) control. For strain-softening materials, applying a stress control is not so straightforward since the stress increases in the pre-peak regime and decreases again in the post-peak regime. This means that the stress has to be tracked, since it cannot be imposed as a monotonically increasing load. Applying a displacement (strain) is therefore more favorable since the strain monotonically increases during the pre-peak and post-peak curves. In load control, the tangent stiffness is used to track the stress increase/decrease and also close to the maximum. At peak load the tangent stiffness becomes zero, which numerically is unfavorable. Therefore, for modeling strain softening, displacement (strain) control is mostly preferred. In displacement (strain) control, a strain increment  $\Delta\epsilon$  is applied at the beginning

of a loading step  $n$

$${}^n\varepsilon = {}^{n-1}\varepsilon + \Delta\varepsilon. \quad (4.13)$$

Knowing the new imposed strain value  ${}^n\varepsilon$ , we can evaluate if damage occurs and update the damage value (using Eqs. (4.7)–(4.9)). Knowing the new values for the strain and damage, the new stress value is determined. Using a trial stress value  ${}^n\sigma^i$ , the corresponding linear elastic strain  ${}^n\varepsilon_e^i$  is determined using Eq. (4.3). The superscript  $i$  refers to the iteration number, while the superscript  $n$  refers to the incremental step number. Then using the damage-dependent PM model, the inelastic strain  ${}^n\varepsilon_{in}^i$  using Eq. (4.10) and compliance  ${}^nh_i$  using Eq. (4.11) are determined. The strain residue  $R_\varepsilon$  at iteration  $i$  is then determined using the equation  $R_\varepsilon = {}^n\varepsilon - {}^n\varepsilon_e^i - {}^n\varepsilon_{in}^i$ . When the residue  $R_\varepsilon$  is below a chosen convergence limit, the converged stress value  ${}^n\sigma$  is obtained. If the residue  $R_\varepsilon$  is larger than the convergence limit, the stress  ${}^n\sigma^i$  is iteratively updated using a Newton–Raphson scheme

$${}^n\sigma^{i+1} = {}^n\sigma^i + \frac{R_\varepsilon}{E_0^{-1} + {}^nh^i} = {}^n\sigma^i + {}^nE^i R_\varepsilon \quad (4.14)$$

where  ${}^nE_i$  is the tangent stiffness at iteration  $i$ . With the updated stress  ${}^n\sigma^{i+1}$ , the elastic and inelastic strains and compliance  $h$  are again updated, and these steps are repeated until convergence.

To show the applicability of the coupling of macroscopic damage model and damage-dependent PM model, the quasi-brittle material behavior in cyclic tensile and tensile-compression loading is modeled. Figure 4.5a and b, for example, compares the experimental and modeled curves, including damage evolution. We observe a good agreement between experimental and modeling results for the strain-softening curve as well as for the hysteretic loops.

#### 4.5

##### Moisture Dependence of Hysteretic and Damage Behavior of Quasi-Brittle Materials

Many quasi-brittle materials are porous showing a macroporous system composed of air spaces between the granulates/grains and a microporous systems in the bond system. For many materials, the microporous system shows a huge hydrophilic internal surface area, promoting the sorption of in the fluid molecules.

Porous media can be classified into macroporous, mesoporous, and microporous media, depending on their pore size. Typically, the diameter of a macropore is greater than 50 nm (i.e., much larger than the characteristic range of intermolecular forces), that of a micropore is smaller than 2 nm (which is in the order of the characteristic range of intermolecular forces), and that of a mesopore is in between. In a macropore, when a liquid is adsorbed, surface effects can be neglected, and all fluid molecules in the macropore are in their bulk state. Here, the material behavior depends only on the bulk pressure of the fluid phase. In mesoporous media, a fraction of the molecules is not in the bulk state but adsorbed on the solid surfaces. An additional term intervenes in the energy

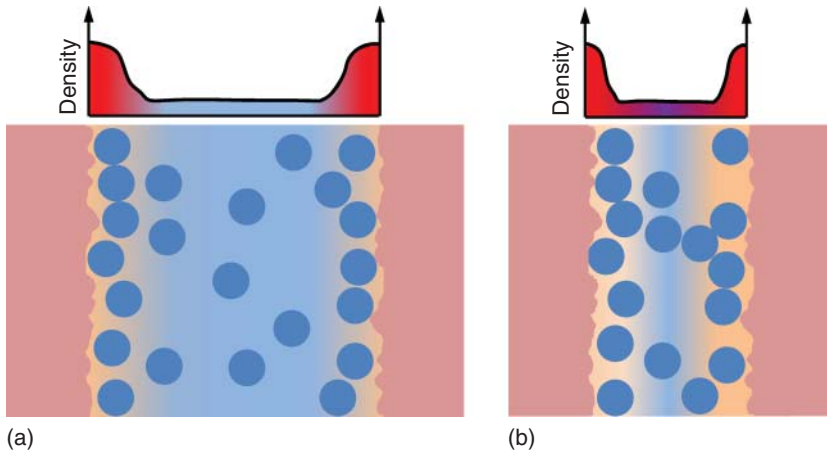


**Figure 4.7** (a) Sketch of the layers of water molecules adsorbed at two pore surfaces and their density profile. (b) Sketch when the two parallel fluid–solid interfaces are separated by a distance that is smaller than the range of molecular interactions [figure adapted from 29].

balance of the system, which accounts for the energy stored at the fluid–solid interface. The mechanical effect of surface adsorption is the appearance of a surface mechanical stress that acts in the plane of the fluid–solid interface, leading to straining of the fluid–solid interface and/or adding of new molecules to the interface [28]. An analysis of the order of magnitude shows that surface effects are significant only for mesoporous media whose specific surface is large and whose material stiffness is low [29]. In a pore of nanometer size, fluid molecules are no longer in their bulk state since they interact strongly with the atoms of the solid. When the size of the pores is in the order of range of the molecular interactions (microporous or nanoporous materials), a mechanical pressure arises orthogonal to the interface: for slit pores with parallel pore surfaces, such a pressure is called the disjoining pressure. This occurs when the inhomogeneous layers of adsorbed fluid overlap (Figure 4.7b, [29]) or, stated differently, when the two parallel fluid–solid interfaces are separated by a distance that is smaller than the range of molecular interactions.

With increasing chemical potential (or relative humidity), the thickness of the adsorbed layers increases finally leading to capillary condensation. Capillary condensation occurs when the molecular adsorbed water layers abruptly alter to a more stable energy arrangement forming menisci between the liquid water and the gas phase. The equilibrium of a water meniscus in a tubular pore is described by the Young–Laplace equation, introducing a capillary pressure, defined as the difference between gas and liquid pressure across the meniscus. The above description shows that in a porous material, which shows a broad pore size range, different kinds of fluid–solid interactions are at play. All these fluid-induced interactions exert mechanical forces on the solid phase. The fluid–solid interaction forces show generally a tendency to develop high internal compressive stresses (or low tensile stresses depending on the choice of the reference stress)



at lower degrees of saturation. Upon increasing fluid saturation, the compressive internal stresses lower or the internal tensile stresses increase. A well-known example of the impact of these fluid-induced forces is the swelling of in the materials, when the material goes from compressive to more tensile forces upon increasing degree of saturation. As a result, the material experiences an extension or swelling. Since the nature and magnitude of the fluid–solid interactions may change with degree of saturation, the magnitude of the fluid-induced mechanical forces also depends strongly on the fluid saturation of the porous material.

In this study on moisture dependence of nonlinear hysteretic damage behavior, we focus on water as liquid and sandstone/concrete as porous material. In unsaturated conditions, the pore space is filled with liquid water, dry air, and water vapor forming the gas phase. Granular rocks consist of grains embedded in a bond system that is highly disordered, showing microscopic features such as asperities and microcracks. The bond system for rocks such as Berea sandstone is also rich in moisture-sensitive mineral clays. The microporous bond system is, therefore, sensitive to water sorption introducing disjoining pressures and capillary forces, and as such important fluid–solid interaction forces or moisture-induced microstresses exist in the porous bond system [30]. Due to the moisture sensitivity of the soft bond system, the material shows an important moisture-dependent mechanical behavior at the macroscale. When homogenizing the random internal moisture-induced stresses to the macroscopic scale, it is commonly assumed that the deviatoric components of these internal stresses balance out and vanish. This is a correct assumption for isotropic materials, where only a hydrostatic mechanical stress or pressure arises. Analogously in the homogenization of the fluid pore pressures, we obtain a macroscopic hydrostatic fluid pore pressure. In poromechanics [31, 32], the macroscale hydrostatic mechanical pressure obtained from homogenization is linked to the homogenized hydrostatic liquid pore pressure introducing a coupling coefficient, also known as the Biot coefficient.

Following poromechanics, we also introduce in our modeling approach a fluid–solid interaction pressure  $\pi(S)$  depending on the degree of saturation  $S$ . This pressure represents the mechanical effect of all the fluid–solid interactions appearing in the considered porous material. In the framework of the PM model, changes in the fluid–solid interaction pressure will induce changes when NCUs are opened or closed on changing the degree of saturation.

#### 4.5.1

##### Moisture-Dependent Mechanical Experiments

Carmeliet and Van Den Abeele [33] performed compressive cyclic experiments on Berea sandstone cylinders at different degrees of saturation. Cyclic loading was performed with a maximum compressive stress of 20 MPa, which is below the damage limit. The nonlinear and hysteretic behavior at different saturation levels  $S$  is shown in Figure 4.8. The stiffness increases with increasing compressive stress, which is attributed to the closing of defects and microcracks in the bond system of

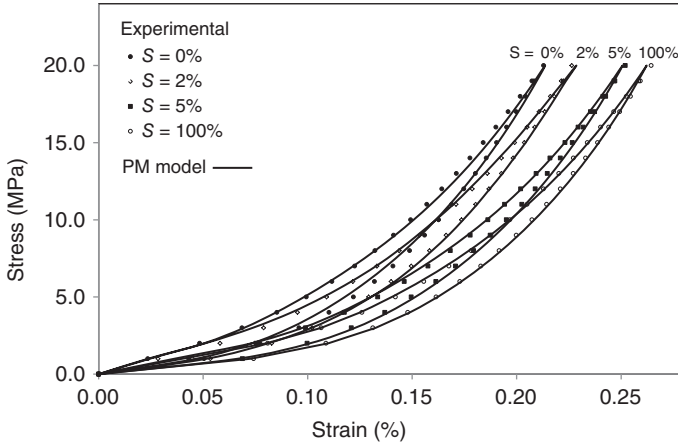


**Figure 4.8** Uniaxial compressive tests on Berea sandstone at different degrees of saturation [experimental data from 33]. Comparison of experimental and simulation results.

the material. At a given stress level, the stiffness decreases with increasing degree of saturation, showing the softening of the wet material.

A second set of experiments are the monotonic tensile experiments on yellow Felser sandstone performed by Visser [34]. The load–displacement curves at two degrees of saturation (nearly dry and saturated) are given in Figure 4.9. In the pre-peak region, the behavior is nonlinear elastic and the stiffness and tensile strength decrease with increasing degree of saturation.

As explained earlier, the material experiences an increasing internal stress  $\pi(S)$  with increasing the degree of saturation. This internal tensile stress exhausts the

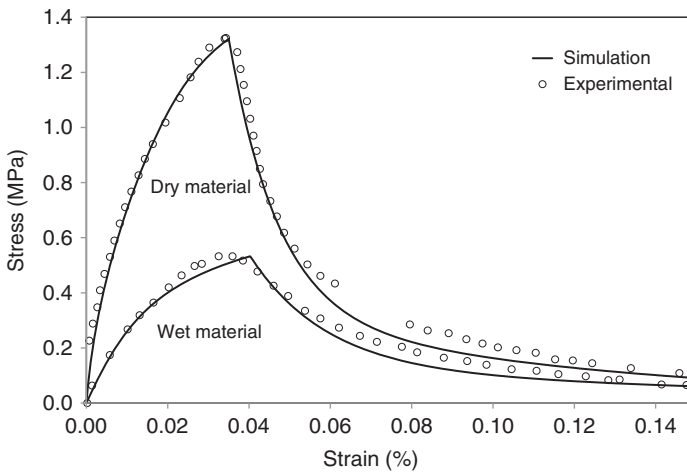


**Figure 4.9** Tensile test on dry and saturated specimen of Felser sandstone [experimental data from 34]. Comparison of experimental and simulation results.

tensile strength, meaning it lowers the maximal external stress the material can experience. The tensile strength of the material thus apparently lowers at higher degree of saturation

$$f_{t,S} = f_{t,S=0} - \pi(S) \quad (4.15)$$

with  $f_{t,S=0}$  the tensile strength of the dry material. In Figure 4.9, we also observe that the post-peak curve, or softening curve, shows a less brittle response or becomes more ductile with increasing the degree of saturation. The surface under the softening branch is referred to as the fracture energy. This fracture energy  $G_f$  depends on the degree of saturation, and is commonly divided into different parts:

$$G_f(S) = \sum_i \alpha_i G_{f,i}(S) \quad (4.16)$$

with  $G_{f,i}$  being the  $i$ th part of fracture energy and  $\alpha_i$  being the weighing factors independent of the degree of saturation. Following Bazant and Pratt [35], the moisture dependence of the  $i$ th part of the fracture energy is expressed with an exponential function:

$$G_{f,i}(S) = G_{f,i,S=0} e^{\gamma_i S} \quad (4.17)$$

with  $G_{f,i,S=0}$  being the  $i$ th part of fracture energy of the dry material and  $\gamma_i$  being a material parameter. For reasons, becoming clear in the next section, where we define a moisture-dependent damage evolution function, we introduce the normalized fracture energy with respect to the tensile strength  $g_f(S) = G_f(S)/f_t(S)$ . Using Eq. (4.16), we get

$$g_f(S) = \frac{\sum_i \alpha_i G_{f,i}(S)}{f_t(S)} = \sum_i \alpha_i \frac{G_{f,i}(S)}{f_t(S)} = \sum_i \alpha_i g_{f,i}(S) \quad (4.18)$$

where  $g_{f,i}(S)$  is the  $i$ th part of normalized fracture energy, which is using Eq. (4.17) equal to

$$g_{f,i}(S) = G_{f,i,S=0} \frac{e^{-\gamma_i S}}{f_t(S)} \quad (4.19)$$

From Eqs. (4.18) and (4.19), we observe that the moisture-dependent normalized fracture energy depends on the fracture energy of the dry material, the moisture-dependent tensile strength (given by Eq. (4.15)), and the parameters  $\alpha_i$  and  $\gamma_i$ . In the following section,  $g_{f,i}(S)$  will be used to define a moisture-dependent damage evolution function.

To summarize, the moisture dependence of the material consists of a decrease in stiffness and tensile strength with increasing degree of saturation, hysteretic loops showing more softening (or higher strain levels), and a more ductile post-peak softening behavior. A last moisture-dependent phenomenon, not documented in the experiments, is the well-known swelling of these materials with increasing degree of saturation.

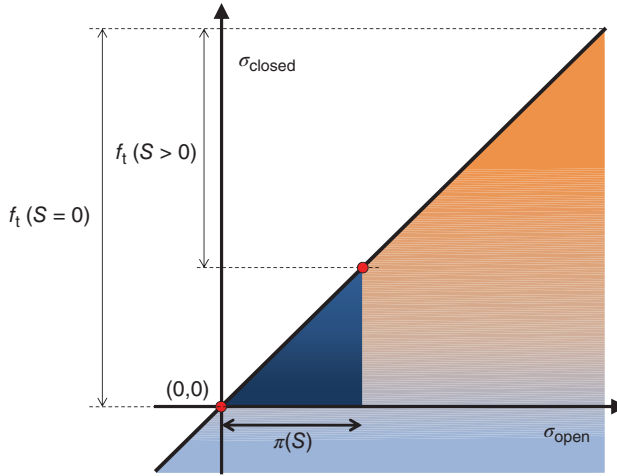


**Figure 4.10** Moisture-dependent PM space. A fluid–solid interaction pressure  $\pi(S)$  results in an opening of NCUs producing a swelling strain when the degree of saturation is increased.

#### 4.5.2

#### Moisture-Dependent Damage and PM Model

Referring to Eq. (4.3), the elastic part is described by Hooke's law. The initial stiffness  $E_0$  reflects the elastic behavior of the solid grains and is not dependent on the degree of saturation, since the nonporous grains are assumed to not adsorb moisture (solid part). The inelastic strain covers the nonlinear elastic phenomena as well as the moisture dependence of the material behavior and is described by a moisture-dependent PM model. Following Carmeliet and Van Den Abeele [26, 33], moisture is considered to generate an internal stress that acts as an activator of NCUs. The mechanical activation is modeled in the PM space by the fluid–solid interaction pressure  $\pi(S)$  as introduced earlier. In Figure 4.10, the moisture-dependent PM space is explained. We consider the material initially dry and stress free at point  $(0, 0)$ . We then increase the saturation, generating a fluid–solid interaction pressure  $\pi(S)$ . This results in the opening of the NCUs in the triangle  $(0, 0) - (\pi, 0) - (\pi, \pi)$ . The strain resulting from the opening of these NCUs is the swelling strain. Then we load the material with an external tensile stress  $\sigma$ , opening new NCUs in the PM space. Decreasing again the external stress, we obtain a hysteretic loop that depends on the degree of saturation. Repeating this experiment, but changing the level of saturation, we obtain a swelling curve (swelling strain versus degree of saturation) and different hysteretic loops as in the experiments of Carmeliet and Van Den Abeele [26, 33].

In this study, the fluid–solid interaction pressure is modeled by a sum of exponential functions

$$\pi(S) = \sum_{i=1}^m \zeta_i (1 - e^{-\xi_i S}) \quad (4.20)$$

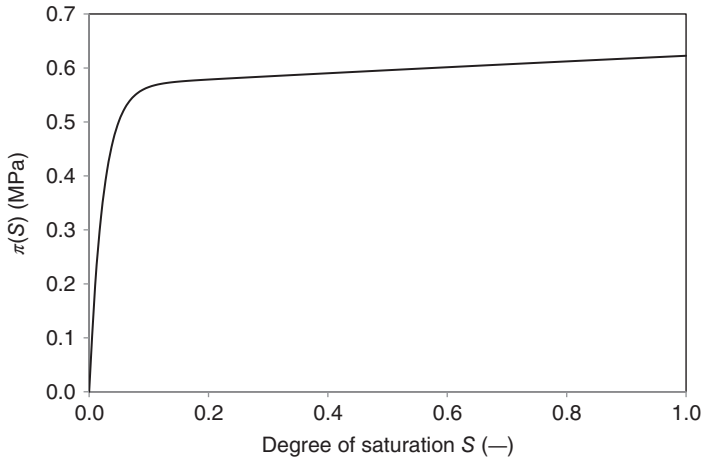


**Figure 4.11** The fluid–solid interaction pressure as a function of the degree of saturation.

with  $m$  being the number of functions. The PM distribution is described using Eq. (4.12). The parameters of the PM distribution and the fluid–solid interaction pressure are determined from the experiments using an inverse identification technique. The parameters used can be found in Mertens [22]. The comparison of the cyclic compression tests at different degrees of saturation with PM results is given in Figure 4.8. We observe a good agreement between experiments and PM model simulations, showing that the moisture-dependent PM model is capable to describe the influence of moisture on stiffness and hysteretic loops. The fluid–solid interaction pressure  $\pi(S)$  is modeled by a sum of two exponential functions and is given in Figure 4.11 as a function of the degree of saturation. We observe an important increase in  $\pi(S)$  from 0% to 10% degree of saturation. At higher degrees of saturation, the fluid–solid interaction pressure becomes more or less constant. The important increase in fluid–solid interaction pressure at lower degree of saturation is attributed to fluid–solid interaction forces induced by phenomena related to sorption and capillary condensation, while at higher degrees of saturation, the added fluid is in its bulk state and, thus, exerts no additional mechanical forces on the porous material.

The PM model is also used to model the monotonic tensile behavior at different degrees of saturation (Figure 4.9, Visser [34]). The number and parameters describing the PM distribution, as well as the parameters describing the fluid–solid interaction pressure, are determined by inverse estimation using the pre-peak data curve. The parameters used can be found in Mertens [22].

For modeling the post-peak region, the isotropic damage model is adapted to take into account the moisture dependence of the tensile strength and fracture energy. The moisture dependence of the tensile strength is modeled by the fluid–solid interaction pressure  $\pi(S)$  using Eqs. (4.15) and (4.20). The moisture-dependent tensile strength is incorporated in the Rankine damage criterion. The moisture dependency of the fracture energy as described by Eq. (4.19) allows

to define a moisture-dependent damage evolution equation  $F(d, S)$ . The damage evolution is modeled by a sum of exponential functions

$$F(d, S) = \sum_i^r \alpha_i (1 - e^{-\beta_i(S)(k-k_i)}) \quad (4.21)$$

where the parameters  $\alpha_i$  are the same as the parameters in Eq. (4.16). Considering Eq. (4.19) for  $g_{f,i}(S)$  and following Bazant and Pratt [35],  $\beta_i(S)$  in Eq. (4.21) can be identified as

$$\beta_i(S) = \frac{1}{g_{f,i}(S)} = \frac{f_t(S)}{f_{t,S=0}} \frac{1}{g_{f,i,S=0} e^{-\gamma_i S}} = \frac{f_t(S)}{f_{t,S=0}} \frac{\beta_{i,S=0}}{e^{-\gamma_i S}} \quad (4.22)$$

where the moisture-dependent tensile strength  $f_t(S)$  is given by Eq. (4.15). The parameters  $\alpha_i$ ,  $\beta_{i,S=0}$ , and  $\gamma_i$  describing the moisture-dependent damage evolution function by Eqs. (4.21) and (4.22) can be determined from the strain-softening curves at different degrees of saturation, as given in Figure 4.9. For the present case, we assume that the  $\gamma_i$  values are all equal. The parameters used can be found in Mertens [22]. The experimental and modeled stress–strain curves for the dry and wet materials are compared in Figure 4.9. We observe that the moisture-dependent mechanical behavior is accurately captured by the coupled moisture-dependent isotropic damage and PM model. In the pre-peak region, the reduction of the tensile strength and stiffness with increasing moisture content, as well as the nonlinear behavior, are well described. In the post-peak regime, a good agreement is also observed.

We now describe in a more detailed way how the curves in Figure 4.9 are obtained. We start with the dry material assuming it in the stress-free state, or in the PM space the initial material state is located at the origin (0, 0). We load the material mechanically until failure and obtain the stress–strain curve for the dry material (Figure 4.12a). Then we take a second specimen of the same material in the initial dry state. Now we first wet the material in a stress-free state.

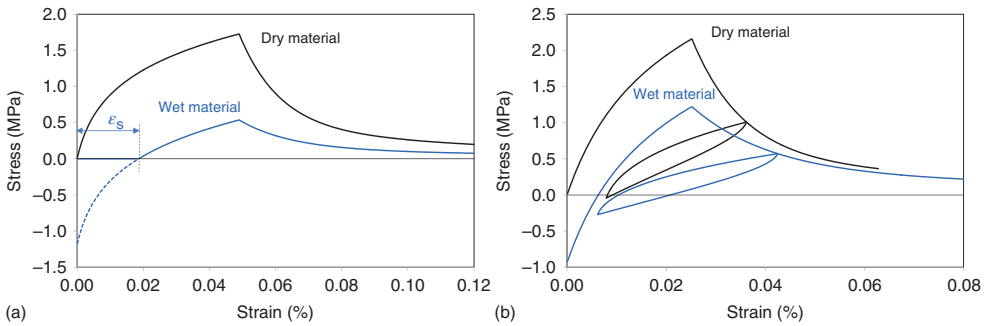


**Figure 4.12** (a) Simulated stress–strain curve for dry and wet material including damage. Wetting results in a swelling strain  $\epsilon_s$ . The dashed line is obtained by compressing the initial wet material to a strain equal

to zero to compensate for the swelling strain. (b) Simulated stress–strain curve for dry and wet material subjected to damage and cyclic loading.

The material will swell and experience a swelling strain equal to  $\epsilon_s$  (Figure 4.12a). Subsequently, the material is mechanically loaded. A lower strength is observed. The dashed line in Figure 4.12a is obtained by compressing the material to a strain equal to zero to compensate for the swelling strain. To compare the wet and dry results, such as in Figure 4.9, the curve for the wet material is shifted to the origin.

In Figure 4.12b, the model is used to predict the behavior for a fully saturated and dry concrete specimen subjected to a cyclic loading. We observe that the model is able to predict the damage behavior including hysteresis for different degree of saturation. The presented coupled moisture-dependent isotropic damage and PM model is thus capable of predicting the mechanical behavior of the material, subjected to a loading protocol situated in the phase space of mechanical stress and degree of saturation, including loading and unloading conditions as well as damage evolution.

### Acknowledgment

We acknowledge the important contribution of the PhD work of Stijn Mertens to this paper. His PhD was possible by the financial support by the Institute for the Promotion of Innovation by Science and Technology in Flanders (IWT-Vlaanderen) under the Grant No. SBO-IWT-03175. We also acknowledge the financial support of the Swiss National Science Foundation 420 (SNF) under Grant No. 125184.

### References

- Derluyn, H. (2012) Salt transport and crystallization in porous limestone: neutron – X-ray imaging and poromechanical modeling. Dissertation. ETH No. 20673, ETH Zurich, Switzerland.
- Gopalaratnan, V.S. and Shah, S.P. (1985) Softening response of plain concrete in direct tension. *ACI J.*, **82**, 310–323.
- Reinhardt, H.W. and Cornelissen, H.A.W., 1984 Post-peak cyclic behaviour of concrete in uniaxial tensile and alternating tensile and compressive loading. *Cement and concrete research*, **14** (2), 263–270.
- Darling, T.W., TenCate, J.A., Brown, D.W., Clausen, B., and Vogel, S.C. (2004) Neutron diffraction study of the contribution of the grain contacts to nonlinear stress-strain behaviour. *Geophys. Res. Lett.*, **31**, L16604.
- Pijaudier-Cabot, G. and Bazant, Z.P. (1987) Nonlocal damage theory. *J. Eng. Mech.*, **113**, 1512–1533.
- de Borst, R., Pamin, J., Peerlings, R.H., and Sluys, L.J. (1995) On gradient-enhanced damage and plasticity models for failure in quasi-brittle and frictional materials. *Comput. Mech.*, **17** (1-2), 130–141.
- Rageneau, F., La Borderie, C., and Mazars, J. (2000) Damage model for concrete-like materials coupling cracking and friction, contribution to structural damping: first uniaxial applications. *Mech. Cohesive Mater.*, **5**, 607–625.
- Duda, H. (1991) *Bruchmechanisches Verhalten von Beton unter monotoner und zyklischer zugbeanspruchung*, Deutscher ausschuss für stahlbeton, heft 419, Beuth verlag GmbH.
- Oliveira, D.V. (2002) Experimental and numerical analysis of blocky masonry structures under cyclic loading. PhD-report, Universidade do Minho, Portugal.
- Gylltoft, K. (1984) Fracture mechanics model for fatigue in concrete. *Mater. Struct.*, **17** (97), 55–58.

11. Reinhardt, H.W., Cornelissen, H.W., and Hordijk, D.A. (1986) Tensile tests and failure analysis of concrete. *J. Struct. Eng.*, **112** (11), 2462–2477.
12. Yankelevsky, D.Z. and Reinhardt, H.W. (1989) Uniaxial behavior of concrete in cyclic tension. *ASCE J. Struct. Eng.*, **115** (1), 166–182.
13. Hordijk, D.A. (1991) local approach to fatigue of concrete. PhD-report, Technische Universiteit Delft, The Netherlands.
14. Preisach, F. (1935) über die magnetische nachwirkung. *Z. Phys.*, **94**, 277–302.
15. Mayergoyz, I.D. (1985) Hysteresis models from the mathematical and control points of view. *J. Appl. Phys.*, **57**, 3803–3805.
16. Mayergoyz, I.D. (1986a) Mathematical models of hysteresis. *Phys. Rev. Lett.*, **56** (15), 1518–1521.
17. Mayergoyz, I.D. (1986b) Mathematical models of hysteresis (invited). *IEEE Trans. Magn.*, **22** (5), 603–608.
18. Ortin, J. (1992) Preisach modelling of hysteresis for a pseudoelastic Cu-Zn-Al single crystal. *J. Appl. Phys.*, **94**, 277–302.
19. Guyer, R.A., McCall, K.R., and Boitnott, G.N. (1994) Hysteresis, discrete memory and nonlinear wave propagation in rock. *Phys. Rev. Lett.*, **74**, 3491–3494.
20. Guyer, R.A., McCall, K.R., Boitnott, G.N., Hibert, G.N., and Plona, T.J. (1997) Quantitative implementation of Preisach-Mayergoyz space to find static and dynamic elastic moduli in rock. *J. Geophys. Res.*, **102** (B3), 5281–5293.
21. McCall, K.R. and Guyer, R.A. (1996) A new theoretical paradigm to describe hysteresis, discrete memory and nonlinear elastic wave propagation in rock. *Nonlinear Processes Geophys.*, **3**, 89–101, 3113–3124.
22. Mertens, S. (2009) Hysteresis, damage and moisture effects in quasi-brittle porous materials. PhD-report. Katholieke Universiteit Leuven, Belgium.
23. Lemaitre, J. and Chaboche, J.L. (1994) *Mechanics of Solid Materials*, Cambridge University Press.
24. Mazars, J. (1984) Application de la mécanique de l'endommagement au comportement non-linéaire et à la rupture de béton de structure. PhD-report. Université Paris 6.
25. Mazars, J. and Pijaudier-Cabot, G. (1989) Continuum damage theory – application to concrete. *J. Eng. Mech.*, **115**, 345–365.
26. Carmeliet, J. and Van Den Abeele, K.E.A. (2002) Application of the Preisach-Mayergoyz space model to analyze moisture effects on the nonlinear elastic response of rock. *Geophys. Res. Lett.*, **29**, 7.
27. Aleshin, V. and Van Den Abeele, K. (2006) Friction in unconforming grain contacts as a mechanism for tensorial stress strain hysteresis. *J. Mech. Phys. Solids*, **55** (4), 765–787.
28. Vandamme, M., Brochard, L., Lecampion, B., and Coussy, O. (2010) Adsorption and strain: the CO<sub>2</sub>-induced swelling of coal. *J. Mech. Phys. Solids*, **58** (10), 1489–1505.
29. Brochard, L. (2011) Poromécanique et adsorption: application au gonflement du charbon lors du stockage géologique du carbone. These de doctorat. L'université Paris-Est.
30. Van Den Abeele, K.E.A., Carmeliet, J., Johnson, P., and Zinszner, B. (2002) Influence of water saturation on the mesoscopic response in Earth materials and the implications to the mechanisms of nonlinearity. *J. Geophys. Res.*, **107**, 6.
31. Coussy, O. (1995) *Poromechanics*, John Wiley & Sons Ltd, Chichester.
32. Coussy, O. (2004) *Poromechanics*, John Wiley & Sons Ltd, Chichester.
33. Carmeliet, J. and Van Den Abeele, K. (2004) Poromechanical approach describing the moisture influence on the non-linear quasi-static and dynamic behaviour of porous materials. *Mater. Struct./Concr. Sci. Eng.*, **37**, 271–280.
34. Visser, J.H.M. (1998) Extensile hydraulic fracturing of (saturated) porous materials. PhD thesis. Delft University of Technology, The Netherlands.
35. Bazant, Z.P. and Pratt, P.C. (1988) Effect of temperature and humidity on fracture energy of concrete. *ACI Mater. J.*, **4**, 262–271.



## 5

## Modeling the Poromechanical Behavior of Microporous and Mesoporous Solids: Application to Coal

*Matthieu Vandamme, Patrick Dangla, Saeid Nikoosokhan, and Laurent Brochard*

This chapter focuses on poromechanical modeling of porous solids, that is, of solids for which the mechanical behavior is significantly impacted by the presence of a fluid in its pore network. The size of the pores of such materials can vary on several orders of magnitude, as is observed in Figure 5.1 for a loess. Other examples are that of cement pastes, coal, wood, soils, among other natural materials, for which pores can range from a millimeter size down to a sub-nanometer size.

According to their size, pores can be divided into subcategories: macropores (the diameter of which is above 50 nm), mesopores (the diameter of which is between 2 and 50 nm), and micropores (the diameter of which is below 2 nm). This subdivision can be explained by the fact that the characteristic range of intermolecular forces is on the order of the nanometer in most cases, except when charged particles are involved (e.g., ions, colloids) [2]. Therefore, in a macroporous medium, almost all molecules of fluid are in a bulk state, that is, behave as if they were surrounded by an infinite volume of fluid: only a negligible fraction of the molecules of fluid in the macroporous medium are in intermolecular interaction with the atoms of the solid. In contrast, micropores are so small that almost all molecules of fluid interact with the atoms of the solid skeleton, so that those molecules no more behave as if they were in a bulk state. Between those two extremes, one finds the mesopores, in which both a significant fraction of molecules of fluid in a bulk state and a significant fraction of molecules of fluid in intermolecular interaction with the atoms of the solid skeleton are present. Those latter molecules of fluid are located close to the walls of the mesopores, so that in this case we come back to the classical definition of adsorption, which, according to the International Union of Pure and Applied Chemistry, is a surface phenomenon and, more precisely, ‘an increase in the concentration of a dissolved substance at the interface of a condensed and a liquid phase due to the operation of surface forces’ [3]. By extension, we consider adsorbed molecules to be those that are in intermolecular interactions with the atoms of the solid skeleton. Therefore, we will also refer to molecules of fluid in a microporous medium—which are in intermolecular interaction with the atoms

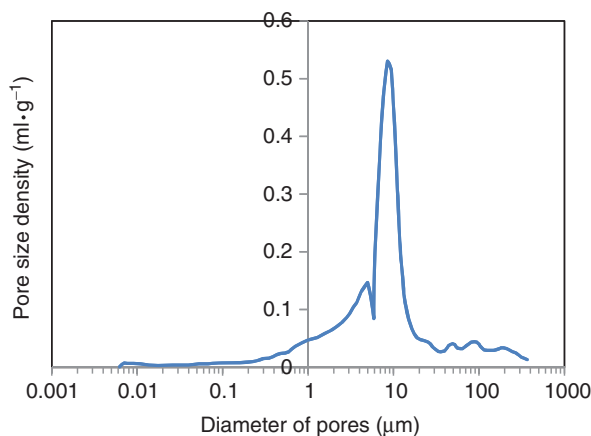


**Figure 5.1** Pore size distribution of a loess, measured by mercury intrusion porosimetry (Adapted from Ref. [1]).

of the solid skeleton—as being “adsorbed,” in spite of the fact that in such a case adsorption is not a surface phenomenon, but occurs more by pore filling.

This chapter is dedicated to describe how the mechanical behavior of such macroporous, mesoporous, or microporous media can be modeled in presence of fluids. For each type of medium, we will discuss its specificities and the simplifications that can be made. The modeling will be restricted to the case of porous media saturated with a pure fluid, that is, to media for which the pore space is occupied by one pure fluid. The modeling here presented should, therefore, be extended if one aims at studying the behavior of partially saturated media, such as a chunk of soil upon drying, for which part of the pore space is occupied by air (at atmospheric pressure) and part of the pore space is occupied by liquid water at a pressure lower than the atmospheric pressure because of capillary effects. For those interested in the modeling of the mechanical behavior of partially saturated materials, we refer to the large amount of work available, both on porous solids in general [4, 5] and on specific porous media such as unsaturated soils for instance [6].

As an application, we will consider the case of underground coal seams. Accurately modeling the behavior of such seams is of prime importance for energy production, since those seams naturally contain methane that can be produced. In addition, coal seams are one of the types of reservoirs identified by the International Panel on Climate Change as potential sites for the underground storage of carbon dioxide [7]. Again, performing such a storage at an industrial level would require an accurate modeling of the behavior of the seam. But the pore network of such seams is complex and extends from macroporous cleats down to the micropores of the coal matrix. How to tackle the modeling of such material will be described and we will show how the derived equations can be used for reservoir simulations.

## 5.1

**Modeling of Saturated Porous Media**

Porous media being solids, their mechanical behavior can be well studied and modeled with the help of regular solid mechanics. For nonporous media, the aim of the modeling at the material level is to derive the constitutive equation that links the stresses  $\underline{\underline{\sigma}}$  that can be applied to a small homogeneous volume of material with the resulting strains  $\underline{\underline{\varepsilon}}$  of this small volume. In contrast to nonporous media, porous media can also be injected with one or several fluids. In this chapter, we consider only the case of a porous medium saturated with a pure fluid: in addition to a stress or a strain, a given pressure  $p$  of the pore fluid (or a given molar chemical potential  $\mu$ ) can be applied or the number  $N_v$  of moles of pore fluid (per unit volume of undeformed medium) can be controlled. For such porous media, the aim of the modeling at the material level is to determine the constitutive equations that link stresses  $\underline{\underline{\sigma}}$ , strains  $\underline{\underline{\varepsilon}}$ , pressure  $p$  of the pore fluid (or molar chemical potential  $\mu$ ), and number  $N_v$  of moles of pore fluid (per unit volume of undeformed medium).

One must note that the stresses  $\underline{\underline{\sigma}}$  that can be applied to the medium can be independently controlled from the pressure  $p$  of the fluid. In many applications in civil engineering, those two parameters are indeed independent: for a piece of soil in the underground, the pressure of the water in its pores is governed by the height of the water table, while the vertical stress is basically due to the weight of the soil layers above. That is why, in geotechnical applications, the mechanical behavior of a sample must be characterized in function of both the pressure of the pore fluid and the stresses applied to the sample. Those stresses are usually called “confining” stresses. An apparatus that enables to do so is the triaxial cell (see Figure 5.2), which enables to control not only the pressure of the pore fluid but also both the axial stress and the radial stress applied to the sample. In summary, for a porous medium, stresses and fluid pressure are parameters that are truly independent. A specific case is that of a porous sample immersed in a fluid at a given pressure  $p$ . This pressure  $p$  is the pressure of the fluid in the pore network of the sample and also applies a stress on the boundaries of the sample: in such a very specific case, pressure  $p$  of the fluid and stresses  $\underline{\underline{\sigma}}$  acting on the boundary of the sample are no more independent.

In order to derive the constitutive equations for the various porous media considered, we will use thermodynamics. Quantities defined per unit volume will be referred to with the subscript  $v$ . The volume considered for those quantities will be that of the undeformed system: all quantities defined per unit volume in this chapter will be Lagrangian ones. The thermodynamic system considered is the porous medium of interest. We note  $F_v$  its Helmholtz free energy, thus per unit volume of undeformed porous medium. Work can be provided to the sample by straining it with stresses or, since it is an open system, by adding fluid molecules to it. Making use of the first two laws of thermodynamics yields

$$dF_v \leq \underline{\underline{\sigma}} : d\underline{\underline{\varepsilon}} + \mu dN_v - S_v dT, \quad (5.1)$$

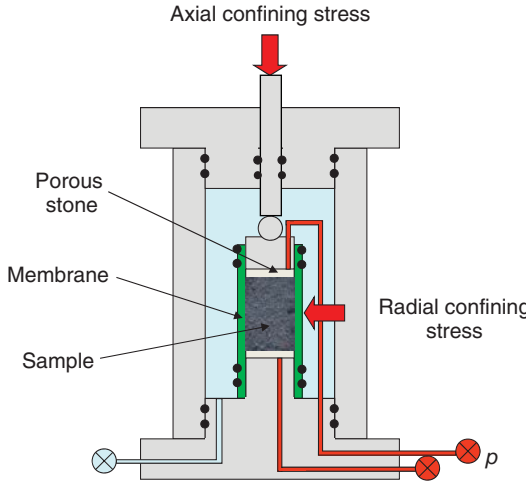


**Figure 5.2** Triaxial cell used classically in soil or in rock mechanics. (Courtesy of D. N. Espinoza.)

where  $\mu$  is the molar chemical potential of the fluid in the system,  $N_v$  is the number of moles of fluid in the system (still per unit volume of undeformed porous medium),  $S_v$  is the entropy of the system (again per unit volume of undeformed porous medium), and  $T$  is the temperature. Under the assumption of isothermal reversible evolutions, this equation can be rewritten as

$$d\Omega_v = d(F_v - N_v\mu) = \sigma d\varepsilon - N_v d\mu + s_{ij} de_{ij} \quad (5.2)$$

where  $\Omega_v = F_v - N_v\mu$  is the grand potential of the system and where the stress tensor  $\underline{\underline{\sigma}}$  and the strain tensor  $\underline{\underline{\varepsilon}}$  have been decomposed into their volumetric and deviatoric part, that is,  $\underline{\underline{\sigma}} = \sigma \underline{\underline{1}} + \underline{\underline{s}}$  and  $\underline{\underline{\varepsilon}} = \frac{1}{3}\varepsilon \underline{\underline{1}} + \underline{\underline{e}}$ .  $\sigma = \frac{1}{3}\text{tr}(\underline{\underline{\sigma}})$  is the mean confining stress (also called volumetric confining stress) and  $\varepsilon = \text{tr}(\underline{\underline{\varepsilon}})$  is the volumetric strain.  $\underline{\underline{s}}$  and  $\underline{\underline{e}}$  are the shear stresses and the shear strains, respectively. This energy balance will be at the heart of the subsequent derivations.

### 5.1.1

#### Macroporous Media

The first case we consider is that of a medium that contains macropores only. Starting from the energy balance 5.2, one can use the Gibbs–Duhem relation for the fluid phase, which, under isothermal evolutions reads:  $d\mu - V_b dp = 0$ , where  $V_b$  is the bulk molar volume of the fluid, so that Eq. 5.2 reads

$$d\Omega_v = \sigma d\varepsilon - N_v V_b dp + s_{ij} de_{ij} \quad (5.3)$$

In a macroporous medium, the Lagrangian porosity  $\Phi$  (i.e., the actual volume of the pores divided by the volume of the undeformed system) is well identified and

the pore space is filled by a fluid in a bulk state, so that  $\Phi = N_v V_b$ . The above energy balance can, therefore, be rewritten as

$$d\Omega_v = \sigma d\varepsilon - \Phi dp + s_{ij} de_{ij} \quad (5.4)$$

From this energy balance, one concludes that small increments  $d\sigma$  of volumetric confining stress,  $d\Phi$  of porosity, and  $ds_{ij}$  of shear stresses are linked to small increments  $d\varepsilon$  of volumetric strain,  $dp$  of pressure of pore fluid, and  $de_{ij}$  of shear strain. In addition, under the assumptions of isotropy of the medium and of uncoupled volumetric and deviatoric behavior,  $d\sigma$  and  $d\Phi$  do not depend on a small increment  $de_{ij}$  of shear strain, while a small increment  $ds_{ij}$  only depends on this latter. Therefore, one can write

$$\begin{aligned} d\sigma &= A_1 d\varepsilon + A_2 dp \\ d\Phi &= A_3 d\varepsilon + A_4 dp \\ ds_{ij} &= A_5 de_{ij} \end{aligned} \quad (5.5)$$

for which, in addition, the Maxwell relation  $\partial^2 \Omega_v / \partial \varepsilon \partial p|_{e_{ij}} = \partial^2 \Omega_v / \partial p \partial \varepsilon|_{e_{ij}} \Rightarrow \partial \sigma / \partial p|_{\varepsilon, e_{ij}} = -\partial \Phi / \partial \varepsilon|_{p, e_{ij}}$  imposes  $A_2 = -A_3$ . In the general case of a nonlinear poroelastic medium, the coefficients  $A_i$  depend on the state variables  $\varepsilon$ ,  $p$ , and  $e_{ij}$ . However, in the simplest case of linear poroelasticity, one considers that all those coefficients are constant, so that the above set of equations can readily be integrated:

$$\begin{aligned} \sigma &= K\varepsilon - bp \\ \Phi - \Phi_0 &= b\varepsilon + p/N \\ s_{ij} &= 2Ge_{ij} \end{aligned} \quad (5.6)$$

where  $\Phi_0$  is the porosity in the undeformed state of reference. This set of equations is the set of classical poroelastic constitutive equations for a linear elastic isotropic porous medium. The different poroelastic parameters are the bulk modulus  $K$ , the shear modulus  $G$ , the Biot coefficient  $b$ , and the Biot modulus  $N$ . The bulk modulus  $K$  and the shear modulus  $G$  can be identified on a dry medium, while the Biot coefficient  $b$  and the Biot modulus  $N$  are specific to the presence of the porous network. Micromechanical relations exist, which enable to express those coefficient and modulus in terms of the bulk modulus  $K_s$  of the solid skeleton [4]:

$$\begin{aligned} b &= 1 - K/K_s \\ 1/N &= (b - \Phi_0)/K_s \end{aligned} \quad (5.7)$$

Therefore, for a regular porous medium, the Biot coefficient  $b$  must verify  $\Phi_0 \leq b \leq 1$ , the Biot modulus  $N$  must verify  $N \geq K_s/(1 - \Phi_0)$ , and the bulk modulus  $K$  must verify  $K \leq (1 - \Phi_0)K_s$ .

## 5.1.2

**Generic (and Potentially Microporous) Media**

We now consider a medium with a generic pore size distribution. Potentially, this medium could contain micropores that are so small that their volume is ill-defined, in the sense that trying to measure their volume by filling the micropores with a fluid will lead different values, depending on whether the molecule is small enough in order to penetrate within the micropore or not. The modeling of such a material should, therefore, restrain to refer to a pore volume. Moreover, the apparent density of adsorbed fluid is likely to differ from that of the bulk fluid. It is therefore no more possible to assert, as was done in the previous section for a macroporous medium, that the fluid occupies the whole porosity: the relationship  $\Phi = N_v V_b$  no more holds. Therefore, in the previous derivations, the energy balance 5.4 is no more valid. In contrast, the energy balances 5.2 and 5.3 still hold. We therefore start from this former equation, which, with the help of Maxwell relations and under the assumptions of isotropy and of uncoupled volumetric and deviatoric behaviors, leads to the following constitutive equations in an incremental form:

$$\begin{aligned} d\sigma &= B_1 d\varepsilon + B_2 d\mu \\ dN_v &= -B_2 d\varepsilon + B_3 d\mu \\ ds_{ij} &= B_4 de_{ij} \end{aligned} \quad (5.8)$$

where the amount  $N_v$  of fluid in the system can be identified as the adsorption isotherm of the fluid considered on the porous medium of interest. In the general case, for an isotropic medium this adsorption isotherm can depend on both the molar chemical potential  $\mu$  and the volumetric strain  $\varepsilon$ :  $N_v = N_v(\varepsilon, \mu)$ . Considering that this adsorption isotherm amount  $N_v = N_v(\varepsilon, \mu)$  is known as a function of both its state variables, the first of these constitutive equations can be rewritten as

$$d\sigma = B_1 d\varepsilon - \left. \frac{\partial N_v}{\partial \varepsilon} \right|_{\mu} d\mu \quad (5.9)$$

Similar to Section 5.1.1, the functions  $B_1$  and  $B_4$  can then be identified as being the tangent bulk modulus  $K(\varepsilon, \mu)$  and twice the shear modulus  $G$ , respectively. Maxwell relations show that the shear modulus  $G$  depends neither on the volumetric strain  $\varepsilon$  nor on the molar chemical potential  $\mu$  of the fluid and is therefore constant. Note that if one assumes that the tangent bulk modulus  $K(\varepsilon, \mu)$  does not depend on the molar chemical potential of the pore fluid, that is, if one assumes  $\partial B_1 / \partial \mu|_{\varepsilon} = 0$ , the Maxwell relation  $\partial B_1 / \partial \mu|_{\varepsilon} = \partial B_2 / \partial \varepsilon|_{\mu}$  inferred from Eq. 5.8 imposes that, at constant molar chemical potential, the adsorption isotherm  $N_v(\varepsilon, \mu)$  must depend linearly on the volumetric strain. In the general case, an integration of the same Maxwell relation enables to express the tangent bulk modulus  $K(\varepsilon, \mu)$  as

$$K(\varepsilon, \mu) = K_0 - \int_{-\infty}^{\mu} \left. \frac{\partial^2 N_v}{\partial \varepsilon^2} \right|_{\tilde{\mu}} d\tilde{\mu} \quad (5.10)$$

where  $K_0(\epsilon)$  is the bulk modulus of the dry medium, that is,  $K_0(\epsilon) = K(\epsilon, \mu \rightarrow -\infty)$ .

We now assume that, when the molar chemical potential of the pore fluid (and thus its pressure) is kept constant, the porous medium behaves linearly with respect to stresses. Under such an assumption, the set of incremental equations 5.8 can be integrated in order to yield the constitutive equations of a porous medium with a generic pore size distribution:

$$\begin{aligned}\sigma &= K_0 \epsilon - \int_{-\infty}^{\mu} \frac{\partial N_v}{\partial \epsilon} \bigg|_{\tilde{\mu}} (\epsilon, \tilde{\mu}) d\tilde{\mu} \\ N_v &= N_v(\epsilon, \mu) \\ s_{ij} &= 2G e_{ij}\end{aligned}\tag{5.11}$$

Those equations can be rewritten as a function of the bulk pressure  $p$  of the fluid, which is linked to the molar chemical potential  $\mu$  of the fluid through the above-mentioned Gibbs–Duhem relationship:

$$\sigma = K_0 \epsilon - \int_0^p \frac{\partial N_v}{\partial \epsilon} \bigg|_{\tilde{p}} V_b d\tilde{p} = K_0 \epsilon - \int_0^p b(\epsilon, \tilde{p}) d\tilde{p}\tag{5.12}$$

The pressure  $p$  that intervenes in this equation, also obtained by Coudert *et al.* [8] and Gor and Neimark [9], is the thermodynamic pressure of the fluid, that is, the pressure of the fluid in a bulk reservoir in thermodynamic equilibrium with the system. In the general case, this pressure differs from the mechanical pressure that the fluid can apply on the walls of the pores. Thermodynamic and mechanical pressures are only equal in macroporous media.

One observes that the constitutive equation 5.12 can be written in terms of a tangent Biot coefficient  $b = -\partial\sigma/\partial p|_{\epsilon} = \partial N_v/\partial \epsilon|_p V_b$ . In the general case, this tangent Biot coefficient depends on both the thermodynamic pressure  $p$  of the fluid and the volumetric strain  $\epsilon$  of the medium, that is,  $b = b(\epsilon, p)$ . For linear elastic isotropic macroporous media, however, this coefficient is constant, so that the macroporous constitutive equations 5.6 are recovered. For a generic (and potentially microporous medium), the dependence of the tangent Biot coefficient  $b$  on both  $\epsilon$  and  $p$  must be characterized. Indeed, as explained in details in [10] with the help of molecular simulation, for crystalline microporous media this tangent Biot coefficient  $b$  can significantly be dependent on those two state variables. For more disordered media, however, that is, for media with a more spread pore size distribution, it seems that the adsorption isotherm  $N_v$  can be well approximated by a first-order expansion in terms of the volumetric strain  $\epsilon$  of the medium, so that the tangent Biot coefficient depends no more on the strain:  $b = b(p)$ . With the above-mentioned Maxwell relation  $\partial B_1/\partial \mu|_{\epsilon} = \partial B_2/\partial \epsilon|_{\mu}$ , one concludes that the tangent bulk modulus  $K$  no more depends on the molar chemical potential  $\mu$  of the fluid. Under such a simplification, the tangent Biot coefficient  $b$  can be calibrated on an experiment in which the swelling of a sample upon an immersion in a fluid would be measured, or in which one would measure the swelling pressure that a sample would exert in an isochoric cell (i.e., a cell that keeps the volume of the sample constant) upon an increase in pressure of the pore fluid.

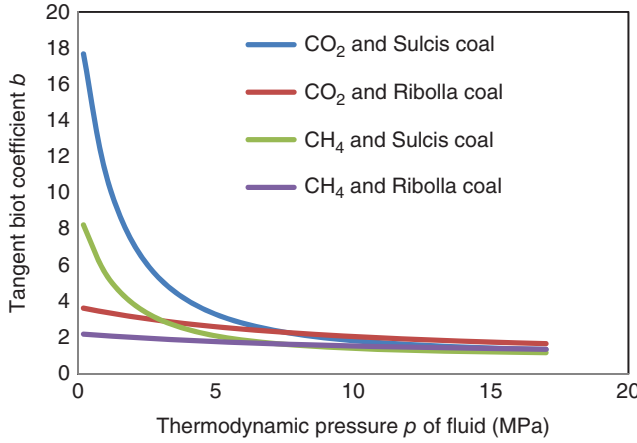


**Figure 5.3** Tangent Biot coefficients for two types of coals (Ribolla and Sulcis coals, both from Italy) immersed in methane or in carbon dioxide. (Adapted from Ref. [12].) The calibration was performed on swellings measured upon immersion of coal samples in the fluids of interest [11].

Such a calibration can be performed on coal. For instance, we display in Figure 5.3 the tangent Biot coefficients of Ribolla and Sulcis coal samples in the presence of methane and carbon dioxide. The calibration was performed by using experimental data gathered by Pini [11], who measured the swellings of coal samples upon immersion in the fluids of interest. One observes that this tangent Biot coefficient indeed depends significantly on the pressure of the fluid. Moreover, especially at low pressure, this coefficient can be greater than unity, while this latter value is an upper bound for macroporous media. Physically, a tangent Biot coefficient  $b$  greater than unity means that, for a sample kept at constant volume, a small increment  $\Delta p$  of pressure of fluid leads to an increase  $b\Delta p$  of confining stress (in absolute value), which can be much greater than the small increment  $\Delta p$  of pressure of fluid. Such an unexpected behavior is a direct consequence of the microporous feature of coal.

### 5.1.3

#### Mesoporous Media

We now aim at deriving the constitutive equations that govern the mechanical behavior of a mesoporous medium. In such a medium, the pore volume  $\Phi$  is well identified, as is the surface area  $A_{v0}$  of the pore walls in the state of reference per unit volume of material. In contrast to what is observed for a macroporous medium, in a mesoporous medium energy can be stored at the interfaces, so that the grand potential of the porous medium is the sum of the grand potential of the solid skeleton, of the bulk fluid in the pores, and of the interfaces. In the energy balance 5.3 derived for a macroporous medium, the grand potential  $\Omega_v$  was only that of the bulk fluid in the pores and of the solid skeleton, since a negligible amount



of fluid could be adsorbed on the pore walls and thus no energy could be stored at interfaces. To avoid any confusion, we will now refer to this grand potential of the macroporous medium as to  $\Omega_{v,macro}$ . Therefore, in order to adapt the energy balance for macroporous media to the case of a mesoporous medium, to the grand potential  $\Omega_{v,macro}$  must be added the grand potential of interfaces, which by definition is  $\gamma A_{v0}$ , where  $\gamma$  is the surface energy (also called commonly surface tension), here defined in a Lagrangian manner, that is, with respect to the surface area  $A_{v0}$  in the state of reference. Thus, the grand potential of the mesoporous medium is equal to  $\Omega_{v,macro} + \gamma A_{v0}$ . Therefore, the energy balance 5.3 must be adapted as

$$d(\Omega_{v,macro} + \gamma A_{v0}) = \sigma d\epsilon - N_v V_b dp + s_{ij} de_{ij} \quad (5.13)$$

where  $\Omega_{v,macro}$  is the grand potential of the solid skeleton and of the bulk fluid only, that is, the grand potential of a macroporous medium.

The amount  $N_v$  of fluid in the system can be divided into fluid molecules that are in a bulk state and fill the whole pore space at their bulk molar volume  $V_b$  and into molecules adsorbed at the surface of the pores. The amount of adsorbed molecules per unit volume is  $\Gamma A_{v0}$ , where  $\Gamma$  is the Lagrangian amount of adsorbed molecules per unit area of the undeformed pore walls. Therefore, the energy balance can be rewritten as

$$d(\Omega_{v,macro} + \gamma A_{v0}) = \sigma d\epsilon - (\Phi + \Gamma A_{v0} V_b) dp + s_{ij} de_{ij} \quad (5.14)$$

so that

$$d\Omega_{v,macro} = \left( \sigma - A_{v0} \frac{\partial \gamma}{\partial \epsilon} \bigg|_p \right) d\epsilon - \left( \Phi + A_{v0} \Gamma V_b + A_{v0} \frac{\partial \gamma}{\partial p} \bigg|_\epsilon \right) dp + s_{ij} de_{ij} \quad (5.15)$$

In the system considered here, energy can be stored at the surface of the pores, in a very similar manner to how energy can be stored in a stretched membrane by elastic deformation. Therefore, similar to a membrane force, there exists a force that opposes an elastic deformation of the surface of the pores: we call this force the surface stress  $\tilde{\sigma}^s$ . How such a surface stress  $\tilde{\sigma}^s$  can be related to the surface energy  $\gamma$  and to adsorption effects is explained by Gibbs [13] and Shuttleworth [14]. The Shuttleworth equation [14] governs how the surface stress  $\tilde{\sigma}^s$  evolves with the surface energy  $\gamma$ :

$$\tilde{\sigma}^s = A_{v0} \frac{\partial \gamma}{\partial A_v} \bigg|_p \quad (5.16)$$

where  $A_v$  is the surface area of the pore walls per unit volume of undeformed material, while the Gibbs adsorption isotherm [13] governs how the surface energy  $\gamma$  evolves with the amount  $\Gamma$  of fluid adsorbed at the surface of the pores:

$$\Gamma = - \frac{\partial \gamma}{\partial \mu} \bigg|_{A_v} = - \frac{1}{V_b} \frac{\partial \gamma}{\partial p} \bigg|_{A_v} \quad (5.17)$$

In both the Shuttleworth equation and the Gibbs adsorption isotherm, the surface energy  $\gamma$  is a function of the surface area  $A_v$  and of the pressure  $p$  of the fluid. However, for the mesoporous medium considered here, the state variables of interest

are the volumetric strain  $\varepsilon$  and the pressure  $p$  of the fluid. With respect to this latter set of state variables, the energy balance 5.15 can be rewritten as follows:

$$d\Omega_{v,macro} = \left( \sigma - \tilde{\sigma}^s \frac{\partial A_v}{\partial \varepsilon} \bigg|_p \right) d\varepsilon - \left( \Phi + \tilde{\sigma}^s \frac{\partial A_v}{\partial p} \bigg|_\varepsilon \right) dp + s_{ij} de_{ij} \quad (5.18)$$

in which the partial derivatives of the surface energy  $\gamma$  combine as follows:  $\partial\gamma/\partial p|_\varepsilon = (\tilde{\sigma}^s/A_{v0})(\partial A_v/\partial p|_\varepsilon) + \partial\gamma/\partial p|_{A_v}$ .

In the energy balance 5.18 for mesoporous media and in the energy balance 5.4 for macroporous media, the grand potentials  $\Omega_v$  or  $\Omega_{v,macro}$  are the sum of the grand potential of the solid skeleton with that of the bulk fluid. In those two energy balances, those grand potentials  $\Omega_v$  and  $\Omega_{v,macro}$  must therefore be identical, and so must be their first derivatives. Consequently, by comparison with the constitutive equations 5.6 for macroporous media, we can readily obtain the constitutive equations of an isotropic linear elastic mesoporous medium:

$$\begin{aligned} \sigma - \tilde{\sigma}^s \frac{\partial A_v}{\partial \varepsilon} \bigg|_p &= K\varepsilon - bp \\ \Phi - \Phi_0 + \tilde{\sigma}^s \frac{\partial A_v}{\partial p} \bigg|_\varepsilon &= b\varepsilon + p/N \\ s_{ij} &= 2Ge_{ij} \end{aligned} \quad (5.19)$$

where the evolutions of the surface stress  $\tilde{\sigma}^s$  with adsorption are governed by a combination of the Gibbs adsorption isotherm 5.17 with the Shuttleworth equation 5.16. The coefficients  $\partial A_v/\partial \varepsilon|_p$  and  $\partial A_v/\partial p|_\varepsilon$  that weigh the effect of the surface stress are material properties with a physical meaning: the former is determined by how the surface area  $A_v$  evolves with the volumetric strain  $\varepsilon$  of the medium at fixed pressure  $p$  of the fluid, while the latter is determined by how the surface area  $A_v$  evolves with the pressure  $p$  of the fluid at fixed volumetric strain  $\varepsilon$  of the medium. Those coefficients can be related to microstructural features for specific microstructures [15].

## 5.2

### Application to Coal Seams

This part is dedicated to applying the framework presented in Part 5.1 to coal seams. Indeed, coal seams are complex natural porous materials with pores, the size of which is less than the nanometer. Because of its microporosity, the coal of which those seams are made exhibits a very peculiar poromechanical behavior. In particular, when immersed in methane or in carbon dioxide, a swelling of the coal sample is observed with an increasing pressure of the pore fluid (see Figure 5.4), while poromechanical equations for macroporous media 5.6 predict that, in the saturated case, the coal sample should shrink with an increase in the pressure of the fluid. This swelling is a consequence of adsorption in the micropores of the coal.

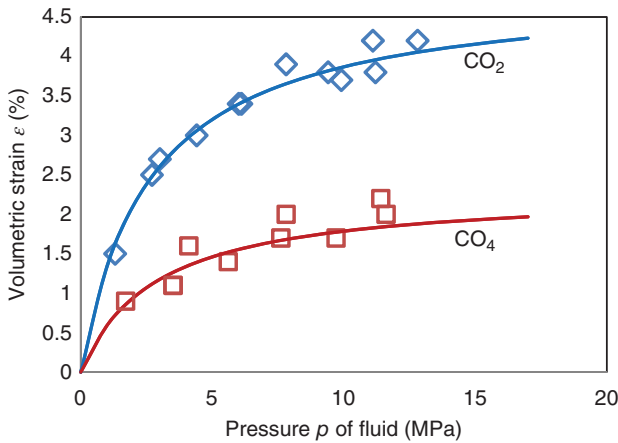


**Figure 5.4** Volumetric strain of a coal sample immersed in methane or in carbon dioxide. (Adapted from Ref. [11].)

Being able to accurately model those variations of volume is of prime interest for reservoir engineers. Indeed, coal seams naturally contain methane that can be extracted for energy production. This process is known as coal bed methane (CBM) production. In order to increase the economic viability of the process, one wants to enhance the amount of methane that can be produced in a given period of time. To do so, an injection well can be used, through which carbon dioxide is injected (see Figure 5.5: carbon dioxide occupies the pore space and is being adsorbed in the coal preferentially to methane, so that more methane can eventually be recovered. This process is known as CO<sub>2</sub>-enhanced coal bed methane recovery (CO<sub>2</sub>-ECBM). Moreover, given the actual concerns regarding global warming, injecting carbon dioxide into underground formations to have it stored over hundreds or thousands of years might be paid for in the future.

However, large-scale pilot projects of injection of carbon dioxide in coal seams around the world have shown an unexpectedly fast decrease in permeability of the seam close to the injection well, which hinders further injection. The reasons for this decrease in permeability are the following: coal seams are naturally fractured, and their permeability is mostly governed by their set of small natural fractures (called cleats), which are spaced by a few centimeters from each other. Upon injection, the diffusion of carbon dioxide from the cleats to the coal matrix makes the coal matrix swell, which, in the confined conditions that prevail in the underground, leads to a closure of the cleats and thus to a decrease in permeability. In order to estimate the economic viability of CO<sub>2</sub>-ECBM projects, accurately modeling the poromechanical behavior of the seam and how adsorption leads to a decrease in permeability is required. In addition, modeling is a first step toward remediation.

The coal seams that are deemed viable for ECBM applications are generally located at depths between 300 and 2000 m. The pressures of fluid of interest are, therefore, in the range of 3–20 MPa. The confining stresses, which result from the

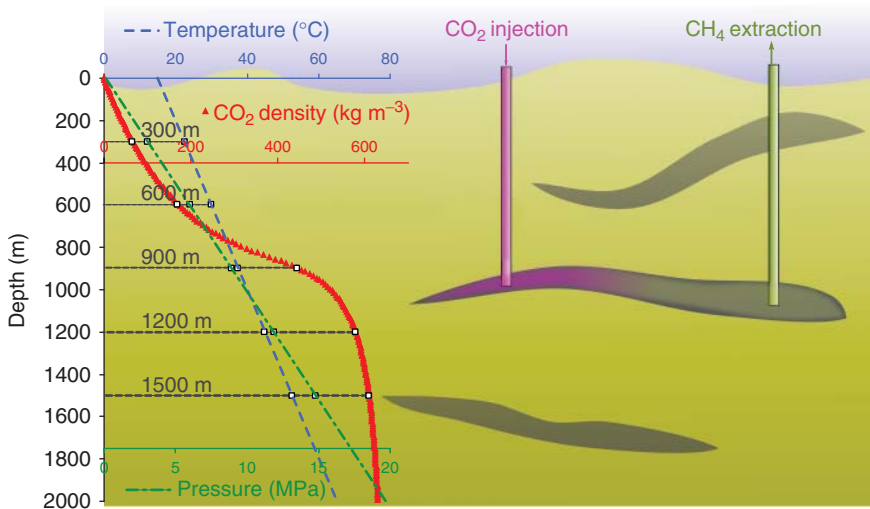


**Figure 5.5** CO<sub>2</sub>-enhanced coal bed methane recovery process (ECBM).

weight of the geological layers above, are of about half a dozen of megapascals up to a few dozens of megapascals. At depths larger than 2000 m, the permeability of the seam is too low because of the high confining stresses resulting from the geological layers above.

The goal of Section 5.2.1 is to model the behavior of a small chunk of fractured coal. The derived constitutive equations will be used in Section 5.2.3 in order to simulate an injection of carbon dioxide into a coal seam. The constitutive equations of the fractured coal will be derived by following the same approach as the one presented in Section 5.1 for various porous media. We will however take into account that the pore network of fractured coal is made of two very distinct types of pores, that is, the cleats and the pores of the coal matrix: the derived model will, therefore, be a dual-porosity model. We will show in Section 5.2.2 that the presence of those two types of porosity can be a source of hysteresis.

### 5.2.1

#### Modeling of a Representative Elementary Volume of a Coal Seam

A coal seam is considered to be the juxtaposition of a large number of small representative volumes of fractured coal, to which we will refer as to “representative elementary volumes” (see Figure 5.6). The aim of the modeling at the material scale is, therefore, to derive the constitutive equations that govern the behavior of such representative elementary volumes. The simulation of a whole coal seam will be performed by juxtaposing numerically a large number of those representative elementary volumes of fractured coal. To each representative elementary volume is associated one set of state variables, considered to be homogeneous in the volume.

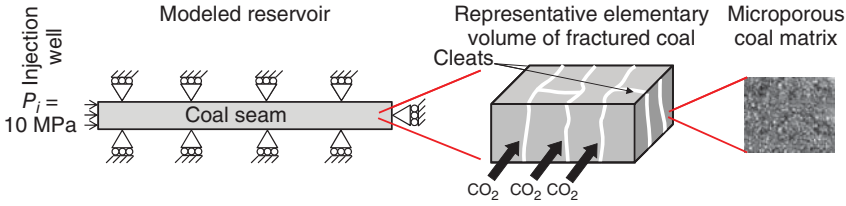


**Figure 5.6** Various scales involved in the problem of an injection of carbon dioxide into a coal seam.

Here, we consider a representative elementary volume of fractured coal, which is a representative of a small part extracted from the seam (see the center part of Figure 5.6). Given the centimeter spacing between cleats, the characteristic size of a representative elementary volume would be on the order of a dozen of centimeters. In this volume, we consider that the pressure  $p_c$  of the fluid in the cleats, the thermodynamic pressure  $p_m$  in the coal matrix, the volumetric confining stress  $\sigma$ , and all other state variables are homogeneous. The pore network of fractured coal can be divided into two distinct types of pores: the pores of the coal matrix and the cleat system. Given their size, cleats are considered as macropores, which occupy a well-defined porosity  $\Phi_c$ . In those cleats, fluid is therefore considered to be in a bulk state. In contrast, no assumption is made on the pore size distribution of the coal matrix: the coal matrix is considered as a generic porous medium. Therefore, adsorption may take place in the coal matrix, but not in the cleats. The coal matrix and the cleats are permanently exchanging fluid molecules and, accordingly, at thermodynamic equilibrium, the chemical potential of the fluid must be the same in both types of porosity. But the transfer of fluid in the coal matrix takes some time, so that, in practice, fluid molecules in the cleats and in the coal matrix may not be in thermodynamic equilibrium. Therefore, from a modeling point of view, we consider the thermodynamic pressure  $p_m$  of the fluid in the coal matrix and the pressure  $p_c$  of the fluid in the cleats to be independent state variables.

Our modeling starts from Eq. 5.2, and by recognizing that the amount  $N_v$  of fluid in a small representative elementary volume of fractured coal can be divided into the amount  $N_{v,c}$  of fluid in the cleats (at a molar chemical potential  $\mu_c$ ) and the amount  $N_{v,m}$  of fluid in the coal matrix (at a molar chemical potential  $\mu_m$ ):

$$d\Omega_v = \sigma d\epsilon - N_{v,c} d\mu_c - N_{v,m} d\mu_m + s_{ij} de_{ij} \quad (5.20)$$

As stated earlier, cleats are considered as macropores that occupy a well-defined porosity  $\Phi_c$  filled by bulk fluid (i.e.,  $\Phi_c = N_{v,c} V_b$ ), so that the above energy balance can be rewritten as

$$d(\Omega_v + p_c \Phi_c) = \sigma d\epsilon + s_{ij} de_{ij} + p_c d\Phi_c - N_{v,m} d\mu_m \quad (5.21)$$

From this equation, again by assuming that the material is isotropic, we end up with the constitutive equations of the fractured coal in an incremental form:

$$\begin{aligned} d\sigma &= C_1 d\epsilon + C_2 d\Phi_c - C_3 d\mu_m \\ dp_c &= -C_2 d\epsilon + C_4 d\Phi_c - C_5 d\mu_m \\ dN_{v,m} &= C_3 d\epsilon - C_5 d\Phi_c + C_6 d\mu_m \\ ds_{ij} &= C_7 de_{ij} \end{aligned} \quad (5.22)$$

The amount  $N_{v,m}$  of fluid in the coal matrix must depend only on state variables at the scale of the coal matrix: those variables can be for instance the volumetric strain  $\epsilon_m$  of the matrix and the chemical potential  $\mu_m$  of the fluid in the coal matrix, that is,  $N_{v,m}(\epsilon, \Phi_c, \mu_m) = N_{v,m}(\epsilon_m, \mu_m)$ . This volumetric strain  $\epsilon_m$  is related to state variables at the scale of a representative elementary volume of coal seam through the relation [5]:

$$\epsilon_m = \frac{\epsilon - \Phi_c + \Phi_{c0}}{1 - \Phi_{c0}} \quad (5.23)$$

so that we readily find out that  $C_3 = C_5$ .

For coal, which is amorphous, Brochard *et al.* [10] identified that the amount of methane adsorbed in the coal matrix depends linearly on the volumetric strain of the matrix. Considering that this first-order expansion remains valid for any fluid, the amount  $N_{v,m}$  of fluid adsorbed in the matrix can be expressed as

$$N_{v,m} = C_3(\mu_m)(\epsilon - (\Phi_c - \Phi_{c0})) + N_{v,m}^0(\mu_m) \quad (5.24)$$

where  $N_{v,m}^0(\mu_m)$  is the adsorbed amount of fluid in the coal matrix when the coal matrix is kept at constant volume. Under the assumption of validity of such a first-order expansion, the coefficient  $C_3$  depends on the molar chemical potential  $\mu$  of the fluid, so that  $\partial C_3 / \partial \epsilon|_{\mu_m, \Phi_c} = 0$ . By making use of the Maxwell relation  $\partial C_1 / \partial \mu_m|_{\epsilon, \Phi_c} = -\partial C_3 / \partial \epsilon|_{\mu_m, \Phi_c}$  related to the first constitutive equation of the set of equations 5.22, we infer that the coefficient  $C_1$  is independent of the molar chemical potential  $\mu_m$  and thus of the thermodynamic pressure  $p_m$  of the fluid in the coal matrix. Likewise, one shows that the coefficients  $C_2$  and  $C_4$  do not depend on the molar chemical potential  $\mu_m$  of the fluid in the coal matrix.

If we assume that the relationships between the state variables  $(\sigma, p_c, s_{ij})$  and  $(\epsilon, \Phi_c, e_{ij})$  are linear, we end up with the following state equations:

$$\begin{aligned} \sigma &= C_1 \epsilon + C_2(\Phi_c - \Phi_{c0}) - p^a \\ p_c &= -C_2 \epsilon + C_4(\Phi_c - \Phi_{c0}) + p^a \\ N_{v,m} &= N_{v,m}(\epsilon_m, \mu_m) \\ s_{ij} &= C_7 e_{ij} \end{aligned} \quad (5.25)$$

or equivalently

$$\begin{aligned}
 \sigma &= K\varepsilon - b_c(p_c - p^a) - p^a \\
 \Phi_c - \Phi_{c0} &= b_c\varepsilon + (p_c - p^a)/N_c \\
 N_{v,m} &= N_{v,m}(\varepsilon_m, \mu_m) \\
 s_{ij} &= 2Ge_{ij}
 \end{aligned} \tag{5.26}$$

where the volumetric strain  $\varepsilon_m$  of the coal matrix is given by Eq. 5.23, and where the adsorption stress  $p^a(\mu_m) = p^a(p_m)$  satisfies

$$dp^a = \left. \frac{\partial N_{v,m}}{\partial \varepsilon} \right|_{\Phi_c, \mu_m} d\mu_m = (1 - \Phi_{c0}) \left. \frac{\partial N_{v,m}}{\partial \varepsilon_m} \right|_{\mu_m} V_b dp_m \tag{5.27}$$

This equation leads to the following expression for the adsorption stress:

$$p^a = \int_0^{p_m} b_m d\tilde{p}_m = \int_0^{p_m} (1 - \Phi_{c0}) \left. \frac{\partial N_{v,m}}{\partial \varepsilon_m} \right|_{\mu_m} V_b d\tilde{p}_m \tag{5.28}$$

In this expression, the quantity  $(1 - \Phi_{c0})N_{v,m}$  is the amount of fluid in the coal matrix per unit volume of undeformed coal matrix.

We now have a set of constitutive equations to model the poromechanical behavior of a representative elementary volume of fractured coal, seen as dual-porosity medium: a set of cleats considered as macropores that occupies a well-defined porosity  $\Phi_c$ , and a microporous coal matrix with an ill-defined porosity and subjected to adsorption phenomena. We can now make use of this set of equations in order to tackle various processes. Before considering the scale of a whole coal seam and simulating an injection of carbon dioxide in the seam (see Section 5.2.3), we will first consider the scale of a representative elementary volume of fractured coal and bring to light one possible source of hysteresis for this system in the following section.

### 5.2.2

#### A Source of Hysteresis: The Kinetics of Transfer Between Cleats and Coal Matrix

In the set of constitutive equations for a representative elementary volume of fractured coal derived in the previous section, the pressure  $p_c$  of the fluid in the cleats is considered to be a state variable that is independent of the thermodynamic pressure  $p_m$  of the fluid in the coal matrix. Indeed, but at thermodynamic equilibrium, those two pressures have no reason to be equal to each other. In practice, upon an injection of fluid in the seam, for instance, what can be directly controlled is the pressure  $p_c$  of the fluid in the cleats. The thermodynamic pressure  $p_m$  of the fluid in the coal matrix evolves over time, mainly governed by the transfer of fluid from the cleats to the coal matrix and vice versa.

We can derive a simple model to govern the kinetics of this transfer based on Darcy's law, from which follows that the molar amount transferred from the cleat

system to the coal matrix per unit time is directly proportional to the difference of pressures, that is,

$$-\frac{\partial N_{v,c}}{\partial t} = \frac{\partial N_{v,m}}{\partial t} = \frac{k_m}{V_b \eta l^2} (p_c - p_m) \quad (5.29)$$

where  $k_m$  is the intrinsic permeability of the coal matrix,  $\eta$  is the viscosity of the fluid, and  $l$  is the characteristic spacing between cleats (here, chosen equal to  $l = 1$  cm). Dimensional analysis provides a characteristic time  $\tau_d$  for the transfer of fluid between cleats and coal matrix:

$$\tau_d = \frac{\eta l^2}{p_f k_m} \quad (5.30)$$

where  $p_f$  is a characteristic pressure of the fluid, chosen equal to  $p_f = 1$  MPa.

We now consider a representative elementary volume of fractured coal, confined so that its volume cannot vary (therefore,  $\varepsilon = 0$ ). This volume will be exposed to carbon dioxide. The poromechanical behavior of this representative elementary volume is governed by the set of constitutive equations 5.26 derived in Section 5.2.1, while the kinetics of transfer of fluid between cleats and coal matrix is governed by Eq. 5.29. The coal sample is considered to be made of Sulcis coal, characterized by Pini [11] experimentally and with the results of which we can calibrate the different parameters of the model, among which the tangent Biot coefficient  $b_m$  (see Figure 5.3) and the amount  $N_{v,m}^0$  of fluid are adsorbed by the undeformed coal matrix. The bulk modulus of the sample is considered to be  $K = 0.78$  GPa, its shear modulus is  $G = 0.44$  GPa, its Biot coefficient is  $b_c = 0.25$ , its Biot modulus is  $N = 4.77$  GPa, and the initial porosity associated with the cleats is  $\Phi_{c0} = 3.2\%$ . The viscosity of the fluid is chosen equal to  $\eta = 1.79 \times 10^{-5}$  Pa.s, which is the viscosity of carbon dioxide at a temperature  $T = 318$  K and a pressure  $p = 6$  MPa.

The pressures  $p_c$  of the fluid in the cleats and  $p_m$  of the fluid in the coal matrix are initially equal to zero. The pressure of the fluid in the cleats is increased linearly with time from 0 up to 17 MPa in a duration  $\tau_l$  and decreased linearly with time back to 0 MPa in the same duration  $\tau_l$ . The response of the system is, therefore, going to be governed by the dimensionless ratio  $\tau_d/\tau_l$  of the characteristic time  $\tau_d$  of transfer between cleats and coal matrix to the characteristic time  $\tau_l$  of loading. For various dimensionless ratios  $\tau_d/\tau_l$ , the constitutive equations are solved numerically.

The results of the calculations performed on this representative elementary volume are displayed in Figure 5.7. We observe two limit cases. The first limit case corresponds to a ratio  $\tau_d/\tau_l$  that tends toward zero, that is, to a case for which the transfer of fluid between cleats and coal matrix is much faster than the imposed variations of pressure  $p_c$  of fluid in the cleats. At any time during the process, cleats and coal matrix are in thermodynamic equilibrium, so that, as is observed in Figure 5.7b, at any time  $p_c = p_m$ . The increase in thermodynamic pressure  $p_m$  that accompanies the increase in pressure  $p_c$  in the cleats translates into a swelling of the coal matrix and into a decrease in the porosity  $\Phi_c$  associated with the cleat system (see Figure 5.7a) since the volume of the system is constrained. The second



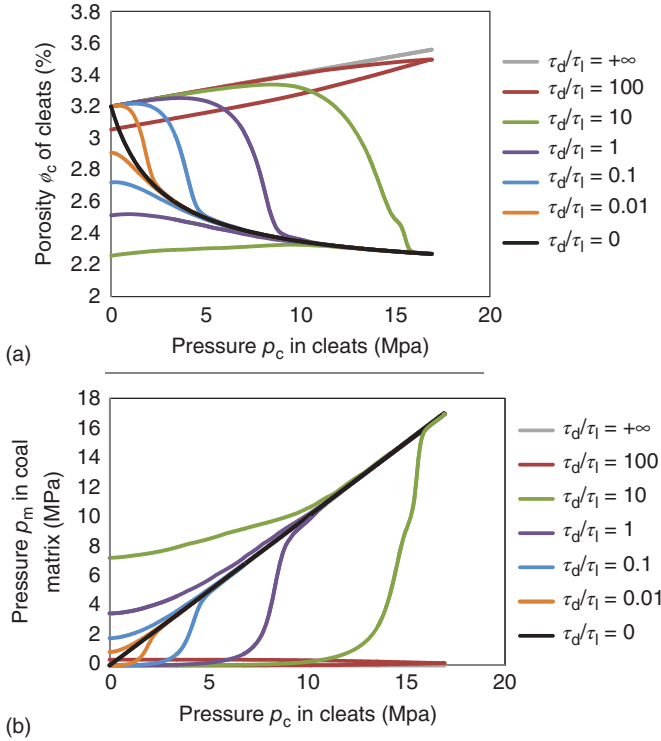


**Figure 5.7** Representative elementary volume confined to a constant volume and for which the pressure  $p_c$  in the cleats is increased linearly with time up to a maximal value and decreased back to zero: (a) porosity  $\Phi_c$  of the cleats and (b) pressure  $p_m$  in the coal matrix.

limit case corresponds to a ratio  $\tau_d/\tau_l$  that tends toward infinity, that is, to a case for which the transfer of fluid between cleats and coal matrix is much slower than the imposed variations of pressure  $p_c$  of the fluid in the cleats. In such a case, the thermodynamic pressure  $p_m$  of the fluid in the coal matrix remains equal to zero at any time during the process (see Figure 5.7b): fluid has no time to penetrate into the matrix. Consequently, the representative elementary volume behaves like a linear elastic macroporous medium: the porosity  $\Phi_c$  increases linearly with the pressure  $p_c$  of the pore fluid, as can be observed in Figure 5.7a.

Between those two limit cases, the process was simulated for ratios  $\tau_d/\tau_l$  that ranged between  $10^{-2}$  and  $10^2$ . For those intermediate cases, we observe that, while the pressure  $p_c$  of the fluid in the cleats is increased, the thermodynamic pressure  $p_m$  of the fluid in the cleats increases as well but remains lower than  $p_c$ . In contrast, when the pressure  $p_c$  of the fluid in the cleats is decreased, the thermodynamic pressure  $p_m$  of the fluid in the cleats decreases as well but remains larger than  $p_c$ . Those delayed variations of  $p_m$  lead to complex variations of the porosity  $\Phi_c$  associated with the cleat system (see Figure 5.7b). Since the permeability of

fractured coal is mostly governed by the cleat system, we would therefore expect that, consequently, the permeability would evolve over time in a complex manner.

On all intermediate cases simulated, a hysteresis is observed. In contrast, no hysteresis is observed for the two limit cases. This difference is due to the fact that, in the simulated process on this representative elementary volume, the only potential dissipation is associated with the transfer of fluid between cleats and coal matrix. For the limit case  $\tau_d/\tau_l \rightarrow \infty$ , no fluid is transferred to the coal matrix, so that no dissipation and thus no hysteresis is observed. In contrast, for the limit case  $\tau_d/\tau_l \rightarrow 0$ , the variations of pressure  $p_c$  in the cleats are so slow that cleats and coal matrix are in thermodynamic equilibrium at all times: transfer of fluid occurs, but so slowly that no dissipation is associated with this transfer; therefore, for this limit case also, no hysteresis is observed.

### 5.2.3

#### Simulating an Injection of Carbon dioxide in a Coal Seam

In this last section, we aim at performing simulations at the scale of a whole coal seam (see the left part of Figure 5.6). To do so, we discretized the seam and used the finite element method to solve the equilibrium equation,  $\sigma_{ij,j} = 0$ , and the two mass balance equations associated with the  $\text{CO}_2$  gas of the cleats (at the pressure  $p_c$ ) and that of the matrix coal (at the pressure  $p_m$ ). These mass balance equations include, as source term, the rate of transferred mass given by Eq. 5.29. The other set of constitutive equations was derived in Section 5.2.1 and given in Eqs. 5.26. In addition, the transport of gas, which occurs only in the cleats, is governed by Darcy's law. After discretization, the system of nonlinear algebraic equations is solved by using an implicit time discretization and Newton iterative method until a convergence criterion is met under the form

$$\frac{u^{n+1} - u^n}{\Delta u_{\text{obj}}} < \varepsilon \quad (5.31)$$

where  $u_{\text{obj}}$  is a given objective variation of the unknown  $u$  (as a displacement or pressure) and  $\varepsilon$  is a positive number small compared to unity, typically  $10^{-4}$ . Practically, this model was implemented in the open-source software “Bil” developed at Laboratoire Navier.<sup>1)</sup>

The case considered is that of a coal seam from which all methane initially present in the seam would have been produced, thanks to a former injection of carbon dioxide. At the beginning of the simulation, some carbon dioxide is, therefore, already present in the seam and the simulated injection is performed into a saturated medium. This case is hypothetical but can be treated with the constitutive equations derived here, which are only valid in the saturated case.

The coal seam is considered to be axisymmetric with a radius of 500 m. In the center of the seam is located the injection well, the radius of which is 10 cm. The performed simulations are axisymmetric plane-strain one-dimensional

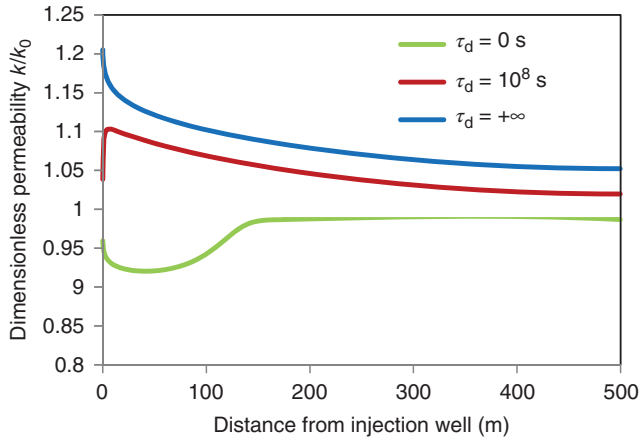
1) Software and documentation available at <http://perso.lcpc.fr/dangla.patrick/bil>

(see the left part of Figure 5.6). We impose no displacement of the edge of the reservoir and no flow through the edge of the reservoir. The initial pressure of carbon dioxide in the system is considered to be equal to 1 MPa, and the pressure  $P_i$  of injection is kept constant and equal to  $P_i = 10$  MPa for a year. The seam is considered to be made of Sulcis coal, the parameters of which have already been given in the previous section.

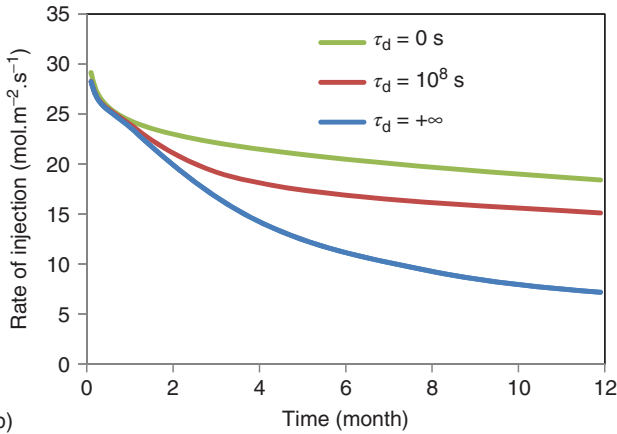
In addition to the constitutive equations, the equation that governs the transport of fluid must be given. We consider that this transport occurs mostly through the cleats and that it is governed by Darcy's law:  $\underline{q} = -(k/\eta) \underline{\nabla} p_c$ , where  $\underline{q}$  is the volume flow vector of the fluid and  $\eta$  is its viscosity, here equal to  $\eta = 1.79 \times 10^{-5}$  Pa.s. The intrinsic permeability  $k$  of a small representative elementary volume of fractured coal is assumed to be governed by the porosity  $\Phi_c$  associated with the cleat system only: this intrinsic permeability is considered to depend on this porosity  $\Phi_c$  through the Kozeny–Carman relation  $k \propto \Phi_c^3/(1 - \Phi_c^2)$ . In the state of reference, the intrinsic permeability of the medium is considered to be equal to 10 mD. Simulations are performed by considering various kinetics of transfer of fluid between cleats and coal matrix: the characteristic time  $\tau_d$  of transfer introduced in the previous section is assumed to be equal to zero,  $10^8$  s, and tend toward infinity.

The results of the simulation are displayed in Figure 5.8. Figure 5.8a shows non-monotonic variations of the permeability of the seam for the various cases. Such phenomenon is due to two competing effects: on the one hand, the increase in the pressure of fluid in the cleats increases the permeability; on the other hand, the increase in the thermodynamic pressure of fluid in the coal matrix leads to a swelling and to a decrease in permeability (see Figure 5.7). We show in Figure 5.8b the variations of injectivity (i.e., the ability of an injection well to receive injected fluid, here characterized by the rate of injection) over a year for the various characteristic times  $\tau_d$  of transfer of fluid between cleats and coal matrix. The greater this characteristic time, the more pronounced the loss of injectivity (i.e., the decrease in rate of injection) in the reservoir. Those variations of rate of injection also result from a competition: on the one hand, for smaller values of  $\tau_d$ , swelling happens faster and the permeability of the reservoir is smaller (see Figure 5.8a), which tends to lower the rate of injection; on the other hand, smaller values of  $\tau_d$  lead to faster adsorption in the coal matrix, which provides additional accessible pore volume and tends to increase the amount of fluid that is injected in a given period of time.

The simulations here performed were repeated for a characteristic time  $\tau_d$  of diffusion equal to  $\tau_d = 4.11 \times 10^3$  s, which corresponds to a realistic intrinsic permeability  $k_m = 4.34 \times 10^{-4}$  mD for the coal matrix. Results obtained with such a value for  $\tau_d$  coincide with results obtained with  $\tau_d = 0$ , that is, when assuming thermodynamic equilibrium between cleats and coal matrix. Therefore, for the reservoir and the profile of injection of interest, it appears that assuming an infinitely fast transfer of fluid between cleats and coal matrix is a very reasonable assumption.



(a)



(b)

**Figure 5.8** Results of finite-element simulations of a methane-free coal seam injected with carbon dioxide, for various characteristic times  $\tau_d$  of transfer of fluid between cleats

and coal matrix: (a) dimensionless permeability along the reservoir after a month of injection and (b) rate injection over a year of injection.

### 5.3

#### Conclusions and Perspectives

This chapter focused on poromechanical modeling of porous solids, that is, of solids for which the mechanical behavior is significantly impacted by the presence of a fluid in its pore network. We considered various types of porous solids: macroporous, mesoporous, and microporous solids. For each type of porous solid, we detailed what simplifications could be made and derived specific constitutive equations. The derivations were rigorously based on thermodynamic principles.

We then showed that, based on the same approach, we could tackle more complex problems, such as the one of a representative elementary volume of coal seam: this porous solid is a dual-porosity one, made of macroporous cracks (i.e., cleats) and of the micropores of the coal matrix. For this coal, we derived constitutive equations that take into account the fact that the thermodynamic pressures in the cleats and in the micropores could be different. Choosing a law of transfer between the two pore spaces, we then studied hysteretic effects at the material scale induced by the application of a cycle of the pressure of fluid in the cleats. At a scale above, we showed that the derived constitutive equations can be implemented in a finite-element/finite-volume software, in order to treat numerically the problem of an injection of carbon dioxide in a coal seam.

We identify three limitations of the approach that would require further work. The first limitation is that, here, constitutive equations were derived in the saturated case, that is, when the pore space is occupied by only one type of fluid. In practice, such formulation needs to be extended to the partially saturated case, that is, to the case where the pore space is occupied by several fluids. The second limitation is that, here, constitutive equations were derived in the reversible case. Therefore, those equations are not suited to capture irreversible processes such as creep or fracture, although it is known that such processes are modified by adsorption. The last limitation is that the generic constitutive equations derived in Section 5.1.2 do not allow, in their present form, to make use of any knowledge regarding the pore size distribution (also called PSD). This PSD is somewhat hidden in how the amount of fluid in the system depends on its chemical potential and on the strain of the solid (see the second equation in the set of equations 5.11). However, we saw that we could take advantage of more information on this PSD in order to obtain more simple or more relevant constitutive equations: for instance, in Section 5.1.1, we obtained simple constitutive equations valid for macroporous solids only, the pores of which are only occupied by the bulk fluid. Also, any explicit use of information on the PSD could be of value for the study of transport properties, which are often mostly governed by the largest pores. Therefore, noting that many natural geomaterials contain micropores, mesopores, and macropores simultaneously (see Figure 5.1), deriving constitutive equations that make use of as much information as possible on the wide pore size distributions encountered in natural geomaterials remains a challenge.

## References

1. Muñoz Castelblanco, J.A., Pereira, J.M., Cui, Y.J., and Delage, P. (2012) The water retention properties of a natural unsaturated loess from northern France. *Géotechnique*, **62** (2), 95–106, doi: 10.1680/geot.9.P.084.
2. Israelachvili, J.N. (2011) *Intermolecular and Surface Forces*, 3rd edn, Academic Press, Inc.
3. IUPAC (1987) *Orange Book: IUPAC Compendium of Analytical Nomenclature*, 2nd edn, Blackwell Scientific Publications, Oxford.
4. Coussy, O. (2004) *Poromechanics*, John Wiley & Sons, Inc., Hoboken, NJ.
5. Coussy, O. (2010) *Mechanics and Physics of Porous Solids*, John Wiley & Sons, Ltd.

6. Lu, N. and Likos, W.J. (2004) *Unsaturated Soil Mechanics*, John Wiley & Sons, Inc.
7. IPCC (2005) *IPCC Special Report on Carbon Dioxide Capture and Storage*, Cambridge University Press, Cambridge and New York.
8. Coudert, F.X., Jeffroy, M., Fuchs, A.H., Boutin, A., and Mellot-Draznieks, C. (2008) Thermodynamics of guest-induced structural transitions in hybrid organic-inorganic frameworks. *J. Am. Chem. Soc.*, **130** (43), 14294–14302, doi: 10.1021/ja805129c.
9. Gor, G.Y. and Neimark, A.V. (2010) Adsorption-induced deformation of mesoporous solids. *Langmuir*, **26** (16), 13021–13027, doi: 10.1021/la1019247.
10. Brochard, L., Vandamme, M., and Pellenq, R.J.M. (2012) Poromechanics of microporous media. *J. Mech. Phys. Solids*, **60** (4), 606–622, doi: 10.1016/j.jmps.2012.01.001.
11. Pini, R. (2009) Enhanced coal bed Methane Recovery Finalized to Carbon Dioxide Storage. PhD thesis, ETH Zürich.
12. Nikoosokhan, S. (2012) Geological storage of carbon dioxide in coal beds: from material to reservoir. PhD thesis, École des Ponts ParisTech.
13. Gibbs, J.W. (1876) On the equilibrium of heterogeneous substances - first part. *Transactions of the Connecticut Academy of Arts and Sciences*, **111**, 108–248.
14. Shuttleworth, R. (1950) The surface tension of solids. *Proc. Phys. Soc. London, Sect. A*, **63**, 444–457.
15. Vandamme, M., Brochard, L., Lecampion, B., and Coussy, O. (2010) Adsorption and strain: the CO<sub>2</sub>-induced swelling of coal. *J. Mech. Phys. Solids*, **58** (10), 1489–1505, doi: 10.1016/j.jmps.2010.07.014.

## 6

# A Theoretical Approach to the Coupled Fluid–Solid Physical Response of Porous and Cellular Materials: Dynamics

Mark W. Schraad

## 6.1

### Introduction

Many materials studied for general scientific purposes or designed for engineering applications are porous in nature and possess underlying cellular structures. Examples include porous rock; many natural and biological materials and tissues such as wood, sponge, cartilage, and, bone; and synthetic cellular materials used as cushions as well as used for thermal and sound insulation. Each of these materials contain interstitial fluids that permeate and flow through the underlying solid structures, for example, oil, gas, and water in porous rock; biological fluid in hydrated soft tissues; and air in most synthetic cellular materials. These materials, therefore, can be viewed as coupled fluid–solid systems, and a proper accounting of the mechanical response may need to include a formal coupling between the interstitial fluid and the porous or cellular solid fields.

Decades of both theoretical and experimental research suggest that the continuum-scale mechanical response of porous and cellular materials is complicated by a characteristic, highly nonlinear, mechanical response of the structured solid, which is a result of competing deformation mechanisms occurring at the pore or cellular scale. The interested reader need look no further than Gibson and Ashby [1] for a comprehensive discussion concerning historic model development, supporting experimental data, and investigations into the structure and properties of cellular solids. Related research (see, for example, [2–8]), however, also demonstrates that fluid transport at the pore or cellular scale, coupled to the response of the deforming solid matrix, can significantly influence the continuum-scale mechanical response of these multimaterial systems. Both fluid pressure and fluid flow contribute to the load-carrying capacity of these materials; affect rate dependence, signal propagation speeds, and hysteresis; and influence the material's susceptibility to failure. Therefore, any modeling approach developed for porous or cellular materials should provide a suitable representation of the pressure evolution and flow behavior of the fluids present in these systems.

Applications involving this class of materials are myriad and varied, as are the associated technical problems and questions regarding the associated physical response. For example, the energy and environmental industries require a detailed knowledge of how oil, gas, and water are transported through porous rock. Bioengineers and medical researchers continue to search for appropriate synthetic surrogates for bone and cartilage implants. And mechanical engineers study the suitability of certain synthetic cellular materials to serve as car seat cushions and crash mitigation systems for the automobile industry. Obviously, understanding how these materials respond to loading can be critically important to many fields of science and engineering, but surprisingly, the research required to model, with fidelity, the associated physical behavior remains incomplete.

### 6.1.1

#### Traditional Modeling Approaches

Traditional modeling efforts either have restricted attention to the response of the porous and cellular solids, essentially ignoring the influence of the fluids permeating the underlying structures, or have focused on the two-phase (i.e., multi-material or multifield) aspect of these materials, but in a manner that treats the coupled system as a homogenized mixture, neglecting the underlying structures and deformation mechanisms occurring at the porous and cellular length scales, and unable to account for those physical mechanisms associated with differences in velocities between the fluid and solid fields.

Prior development in multifield theory most relevant to the present investigation is, perhaps, the research conducted by Biot [2, 9–12], whose contributions include a substantial volume of work concerning consolidation and wave propagation in porous geological materials. Early research in geomechanics (see [13]), and a significant body of research since (see, for example, [14, 15]), has focused on the Darcy law approximation to the formal multifield conservation equations, or on similar simplified representations, in their study of porous geological materials. The most recent textbook by Wang [8] summarizes the state of the art in that field, however, the work of Biot [2] is widely considered to be the foundation of the field of poroelasticity. The materials of interest to these investigations are much denser than typical biological or synthetic cellular materials, and the applications of interest involve smaller deformations and lower strain rates than those considered here. In spite of the obvious differences in material characteristics and applications, however, the use of poroelasticity theory to describe these geological materials points to the applicability of multifield theory to the dynamics of the lower density and much more compliant, but still porous, biological and synthetic cellular materials.

Modeling approaches developed in the biomechanics community include efforts based on mixture or biphasic theory (see [3]). Mow *et al.* [16] applied these theories to soft tissue, suggesting that the rheological behavior of some biological materials depends on the intrinsic interaction between the deforming solid matrix and the relative motion of the interstitial fluid. Furthermore, the



pressure evolution and flow behavior of the interstitial fluid may, in some circumstances, dominate the mechanical behavior of the tissue. As a result, binary mixture theory represents the minimum required to describe the behavior of such material systems, and, indeed, a significant volume of literature on this subject has followed after the pioneering work of Mow and his colleagues (see, for example, [7] for advanced work in this field). However, it should be noted that, although the formulations may be different, the poroelastic approach introduced by Biot and the biphasic mixture approach of Mow and coworkers can provide equivalent results (see, for example, [6]). The interested reader should refer to the reviews of [17, 18] and the bibliographies contained therein for a list of references covering these and related topics in biomechanics.

In the development of biphasic modeling approaches, it is customary to ignore the porous or cellular nature of the matrix material and simply model the mixture using conventional elastic or viscoelastic constitutive models (see [5, 19, 20]). The properties and highly nonlinear mechanical response exhibited by these materials at the continuum scale, however, are directly related to the mechanisms of deformation occurring in the structure found at the level of an individual pore or cell. Nonlinear effects associated with deformation mechanisms occurring at these structural scales lead to the characteristic nonlinear response exhibited at the continuum scale. For fidelity, therefore, a model that spans the two length scales is required. Furthermore, a more general multifield approach has not been used to extend the results of biphasic theory, as is required for complex 3D loading states or highly dynamic regimes of behavior, under which the velocities of the cellular solid and interstitial fluid fields may be distinctly different from the average velocity of the mixture.

For synthetic cellular materials, the earliest modeling efforts (see, for example, [21]) focused on using single-cell mechanics to develop continuum-scale constitutive models for cellular solids. Even these early investigators, however, understood that closed-cell foams stiffen with the increasing fluid pressure that accompanies compressive deformations and that open-cell foams dissipate energy through viscous mechanisms as the interstitial fluid flows, or is restricted from flowing, through the complex cellular structure. Subsequent efforts to model the mechanical response of cellular materials, however, mostly neglect the behavior of the fluids permeating these material systems. Such efforts include cellular-scale modeling approaches based on the simplified mechanics of single idealized cells and modeling approaches based on finite-element discretizations of realistic representative cellular structures. Many researchers have devoted themselves to understanding the physical mechanisms occurring at the level of an individual cell and relating this cellular-scale behavior to the continuum-scale response of these materials (see, for example, [22–29]). The most often referenced work in the fields of cellular-scale mechanics and modeling is the classic text of Gibson and Ashby [1], which provides examples of the current state of the art for developing single-cell mechanical response descriptions for cellular solids.

Usually, each of these modeling approaches has advantages associated with its use. The simple mechanical descriptions offered by a single-cell approach provide

a convenient means of incorporating cellular-scale physics into continuum-scale models. Despite being more physically based, however, this single-cell view is overly simplistic and can lead to inaccurate predictions of stress levels for given levels of strain [30]. Furthermore, these cellular-scale and numerical modeling approaches have not been used to construct a fully 3D constitutive model for the materials of interest. Perhaps most importantly, the basic failing in both cellular-scale modeling approaches and numerical modeling approaches is in the complete lack of attention given to the interstitial fluids present in these systems and the effects of these fluids on the overall response of the materials of interest.

The geomechanics, biomechanics, and mechanical engineering communities have evolved distinct methods and models for treating porous and cellular materials and their applications. And certainly, these methods and models have served tremendous purpose. As will be shown, however, the representation of relevant physical process for these coupled multimaterial systems remains incomplete. Fortunately, for the materials and applications of interest, there are tremendous overlaps in the underlying physical processes, and these overlaps point to the utility of a unifying theoretical approach to modeling the coupled fluid–solid mechanical response of porous and cellular materials.

### 6.1.2

#### **A Unifying Theoretical Approach**

The primary objective of this work is to outline a new approach to modeling the coupled fluid–solid mechanical response of porous and cellular materials – an approach that integrates advanced constitutive models for the solid matrix materials with the coupled physical response of the interstitial fluids comprising such systems in a comprehensive continuum-scale mechanical response description. The goal is to quantify the influence of the interstitial fluid on the response of the porous or cellular solid, and to distinguish between those physical mechanisms and material response characteristics that are due to solid material response, and those that are due to the physical behavior of the fluid. The purpose of these investigations is to highlight the distinct roles of the cellular solid matrix and the interstitial fluids in the overall physical response of coupled fluid–solid material systems, to provide evidence that suggests previous attempts to model these materials that neglected relevant physical behavior, and to provide an improved approach to modeling these materials.

The modeling approach presented here couples the mechanical response of porous and cellular solids with the physical behavior of the fluids permeating these materials through a formal multifield description of the governing equations of motion. Multifield theory is applicable when the average motion of one material in a multimaterial system is distinctly different from that of the other materials. Examples of systems for which a multifield formulation has been used to describe dynamic behavior include gas bubbles in water, fuel spray particles in air, and the motion of fluidized beds of sand or other particle-laden flows. It is well beyond the scope of this presentation to provide a detailed review of the research in all

of these fields; however, the classic text by Ishii [31], the more recent assessment of the subject provided by Drew and Passman [32], and the papers of Zhang and Prosperetti [33, 34], along with the substantial bibliographies contained therein, provide excellent starting points for the interested reader.

The multifield formulation begins with the seemingly obvious assumption that such materials comprise two separate, but interacting, material fields, namely, the porous or cellular solid and the interstitial fluid. In general, the motion of the two material fields is not identical, but is coupled through the relative motion of the two fields. The response of each material, therefore, is characterized by its own distinct velocity field, while the response of the coupled fluid–solid system is governed by a set of coupled conservation equations.

Equations governing the conservation of mass and momentum are derived in multifield form through the use of an appropriate ensemble-averaging technique. For loading rates well below the sonic threshold, temperature and energy effects are neglected, and thus, the energy equation does not appear in the present formulation. The derivation of multifield conservation equations is straightforward; however, governing equations derived in this manner necessarily include additional momentum source terms arising through the averaging process. Consideration is given, therefore, to closing this set of coupled, multifield equations through the development of appropriate constitutive models for the resulting source terms.

Solution of the equations of motion requires implementation in an appropriate computational test bed. The most suitable numerical approach for treating the multifield equations is offered by a conventional finite-volume technique. The formulation is fully three dimensional; however, initial implementation is made in a 1D setting, in which the numerical issues associated with differencing schemes, advection terms, stability, and so on are addressed most easily.

The multifield approach is used to simulate the finite-strain uniaxial compression of two different materials under dynamic loading conditions. A synthetic cellular material and a natural biological material are examined, and the influence of various interstitial fluids along with the effects of microstructure and loading rate on the dynamic response of these materials are investigated. Consistent with recent experimental data, results demonstrate that the interstitial fluid can play a major role in the general response of porous and cellular materials, point to the usefulness of the multifield formulation, and provide theoretical evidence to suggest that any modeling approach developed for porous or cellular materials provide a proper accounting of the pressure evolution and flow behavior of the interstitial fluids present in these coupled fluid–solid systems.

## 6.2

### Theoretical Approach

Consider any natural or synthetic material, such as those shown in Figure 6.1. Each of these materials is porous, with an underlying cellular solid matrix and an interstitial fluid permeating the cellular structure. Traditional approaches for modeling

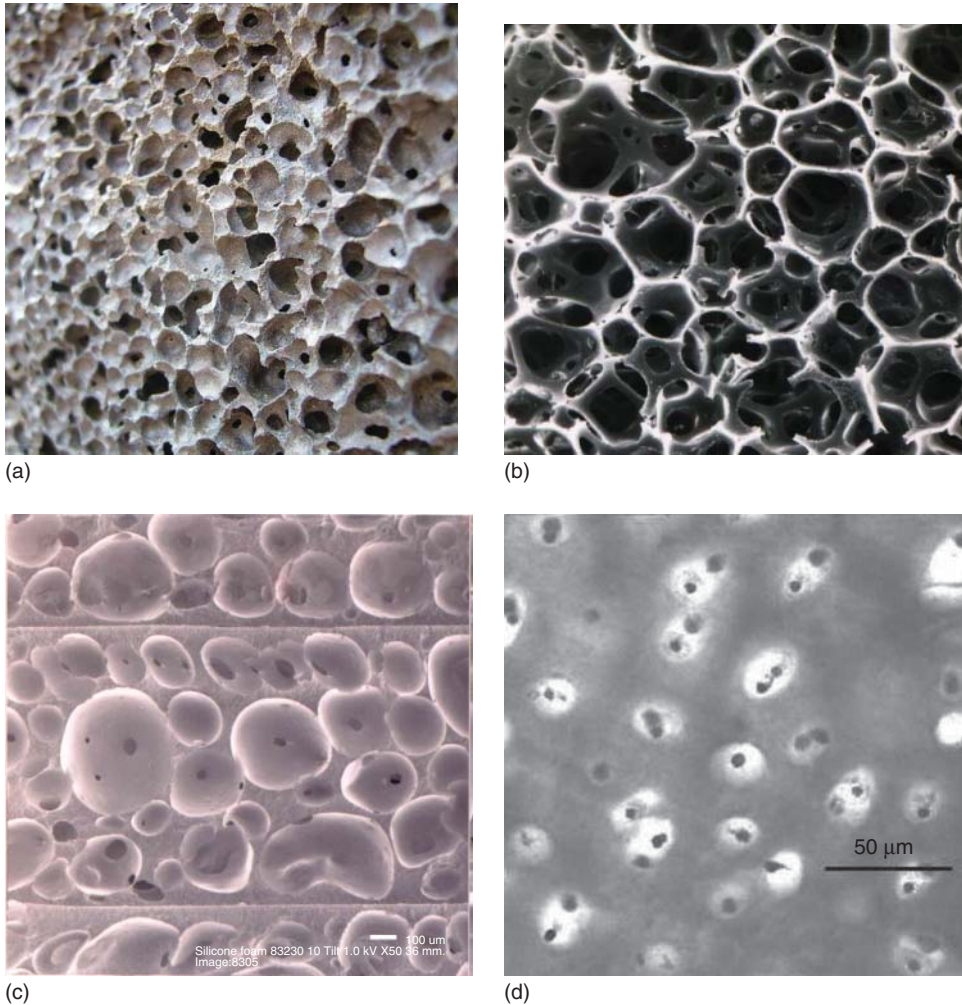


**Figure 6.1** Examples of natural and synthetic porous and cellular material systems including (a) porous rock, (b) polyurethane foam, (c) silicone foam, and (d) articular cartilage.

the mechanical response of such materials have focused almost exclusively on the mechanics of the deforming cellular solid or on a homogenized mixture representation of the coupled system, either neglecting the coupled pressure and flow behavior of the interstitial fluid, or the detailed mechanics occurring at the structural scale. To account for this coupled behavior, a new approach for modeling the mechanical response of these types of coupled fluid–solid systems is required. To a large extent, the approach offered here is based on the derivation of conservation equations in multifield form.

The theory of multifield systems, which can include multicomponent chemical mixtures, multiphase flows, and multimaterial systems, is well established. It is

not the intent here to reproduce theoretical derivations presented elsewhere in the literature; however, for reasons of completeness, the salient features of a multifield derivation are presented. Therefore, equations governing the conservation of mass and momentum are derived in multifield form through the use of an appropriate ensemble-averaging technique. This derivation is straightforward; however, governing equations derived in this manner necessarily include additional momentum source terms arising through the averaging process. Consideration is given, therefore, to closing this set of coupled, multifield equations through the development of appropriate constitutive models for the resulting source terms. The uniqueness in this approach comes about through the integration of advanced constitutive models for the porous and cellular solids into the formal multifield formulation.

### 6.2.1

#### Single-Field Equations and the Ensemble Averaging Process

For a single field, equations governing the conservation of mass and conservation of momentum are given, respectively, by

$$\frac{\partial \rho}{\partial t} + \frac{\partial \rho u_i}{\partial x_j} = 0, \quad (6.1)$$

and

$$\frac{\partial \rho u_i}{\partial t} + \frac{\partial \rho u_i u_j}{\partial x_j} = \rho b_i + \frac{\partial \sigma_{ij}}{\partial x_j}, \quad (6.2)$$

in which  $\rho$  is the material density,  $u_i$  are the components of the material velocity vector,  $b_i$  are the components of the body force vector,  $\sigma_{ij}$  are the components of the Cauchy stress tensor,  $x_i$  are the components of the spatial position vector, and  $t$  is time. The usual indicial notation is used here and throughout the remainder of this presentation, in which, unless noted otherwise, subscripted indices range from 1 to 3 and repeated indices imply summation.

The single-field conservation equations describe the dynamics of any material field at a point in space,  $x_i$ , and an instant in time,  $t$ , in a single-field system or multifield system. For a multifield system contained in a volume,  $V$ , each field,  $k$ , is contained in a subvolume,  $V^k$ , in which  $V = V^1 \cup V^2 \cup \dots \cup V^n$  and  $n$  is the total number of material fields. To provide a unique material identifier, the following function is defined:

$$A^k(x_i, t) = \begin{cases} 1, & x_i \in V^k, \\ 0, & \text{otherwise,} \end{cases} \quad (6.3)$$

which is subject to

$$\frac{DA^k}{Dt} \equiv \frac{\partial A^k}{\partial t} + u_i \frac{\partial A^k}{\partial x_i} = 0. \quad (6.4)$$

The function,  $A^k$ , is referred to as the field function, and Eq. (6.4) asserts that a point originally associated with material field,  $k$ , is always associated with material field  $k$ , and that the field function,  $A^k$ , is a Lagrangian invariant.

Multifield conservation equations are obtained by taking an ensemble average of the product of the field function,  $A^k$ , and the single-field equations. For the conservation of mass, the averaging process leads to

$$\frac{\partial \overline{A^k \rho}}{\partial t} + \frac{\partial \overline{A^k \rho u_j}}{\partial x_j} = 0, \quad (6.5)$$

and for the conservation of momentum, the averaging process leads to

$$\frac{\partial \overline{A^k \rho u_i}}{\partial t} + \frac{\partial \overline{A^k \rho u_i u_j}}{\partial x_j} = \overline{A^k \rho b_i} + \frac{\partial \overline{A^k \sigma_{ij}}}{\partial x_j}. \quad (6.6)$$

### 6.2.2

#### Multifield Equations

In the averaged mass and momentum conservation equations defined above, a line over any quantity denotes that quantity's properly weighted ensemble average. For example, in the averaged mass conservation equation, the field-weighted average density is defined by

$$\bar{\rho}^k \equiv \frac{\overline{A^k \rho}}{\overline{A^k}} \Rightarrow \overline{A^k \rho} = \overline{A^k} \bar{\rho}^k, \quad (6.7)$$

and the mass-weighted average velocity is defined by

$$\bar{u}_i^k \equiv \frac{\overline{A^k \rho u_i}}{\overline{A^k \rho}} \Rightarrow \overline{A^k \rho u_i} = \overline{A^k} \bar{\rho}^k \bar{u}_i^k, \quad (6.8)$$

in which the volume fraction of component  $k$ ,  $\phi^k$ , is defined by the ensemble average of the field function

$$\phi^k = \overline{A^k}. \quad (6.9)$$

The ensemble-averaged conservation of mass equation then can be rewritten as

$$\frac{\partial \phi^k \bar{\rho}^k}{\partial t} + \frac{\partial \phi^k \bar{\rho}^k \bar{u}_j^k}{\partial x_j} = 0. \quad (6.10)$$

In the averaged momentum conservation equation, the advective momentum flux term,  $\partial \overline{A^k \rho u_i u_j} / \partial x_j$ , can be written in a more convenient form by considering the decomposition of the velocity field into mean and fluctuating parts

$$u_i = \bar{u}_i^k + u_i^{k'}. \quad (6.11)$$

The quantities,  $u_i^{k'}$ , are the fluctuations in the components of the velocity vector for material field  $k$ . This decomposition provides

$$\overline{A^k \rho u_i u_j} = \phi^k \bar{\rho}^k \bar{u}_i^k \bar{u}_j^k + \overline{A^k \rho u_i^{k'} u_j^{k'}}. \quad (6.12)$$



If the field-weighted average Reynold's stress is defined by

$$\overline{R_{ij}^k} \equiv -\frac{\overline{A^k \rho u_i^{k'} u_j^{k'}}}{\overline{A^k}} \Rightarrow \overline{A^k \rho u_i^{k'} u_j^{k'}} = \phi^k \overline{R_{ij}^k}, \quad (6.13)$$

then the advective momentum flux term can be rewritten as

$$\frac{\partial \overline{A^k \rho u_i u_j}}{\partial x_j} = \frac{\partial \phi^k \overline{\rho^k u_i^k u_j^k}}{\partial x_j} - \frac{\partial \phi^k \overline{R_{ij}^k}}{\partial x_j}. \quad (6.14)$$

Also, if the mass-weighted average body force is defined by

$$\overline{b_i^k} \equiv \frac{\overline{A^k \rho b_i}}{\overline{A^k \rho}} \Rightarrow \overline{A^k \rho b_i} = \phi^k \overline{\rho^k b_i^k}, \quad (6.15)$$

then the ensemble-averaged conservation of momentum equation can be rewritten as

$$\frac{\partial \phi^k \overline{\rho^k u_i^k}}{\partial t} + \frac{\partial \phi^k \overline{\rho^k u_i^k u_j^k}}{\partial x_j} = \frac{\partial \phi^k \overline{R_{ij}^k}}{\partial x_j} + \phi^k \overline{\rho^k b_i^k} + \overline{A^k \frac{\partial \sigma_{ij}}{\partial x_j}}. \quad (6.16)$$

Equations (6.10) and (6.16) represent the ensemble-averaged conservation of mass and conservation of momentum equations, respectively, for a multifield system. The mass equation is fully determined as a result of using the mass-weighted ensemble average. In the derivation of the momentum equation, however, source terms due to spatial gradients in the average Reynold's stress, average body forces, and average material stress gradients emerge and require additional attention. Consideration must be given to closing this set of coupled multifield equations through the development of appropriate constitutive models for the resulting source terms.

### 6.3

#### Closure Models

The derivation presented thus far applies, in general, to any coupled fluid–solid system. To fully close the set of governing equations represented by Eqs. (6.10) and (6.16), the three terms on the right-hand side of the momentum equation require modeling. Modeling the momentum source terms requires more specific attention to the materials and applications of interest and may depend on specific details related to microstructure, fluid properties, and loading conditions. Therefore, the remainder of this derivation will be carried out specifically with two surprisingly similar materials in mind: namely, the silicone foam and the articular cartilage, shown in Figure 6.1c and d, respectively.

## 6.3.1

**Reynold's Stress and Body Forces**

The first term on the right-hand side of Eq. (6.16) represents a momentum source due to gradients in the average Reynold's stress,  $\overline{R}_{ij}$ . The average Reynold's stress is related to velocity fluctuations, which are negligible in the solid matrix, but substantial and important for determining viscous drag contributions associated with the interstitial fluid, especially for circumstances involving turbulent flow. For slow flow through a porous or cellular structure, the Reynold's stress is dominated by viscous mechanisms, but the corresponding contributions to the overall momentum source can be considered within a model for the momentum exchange, which will be described in Section 6.3.2.1. Therefore, it is assumed that

$$\overline{R}_{ij}^k = 0. \quad (6.17)$$

In addition, body forces, such as those due to gravity, are neglected, and thus

$$\overline{b}_i^k = 0. \quad (6.18)$$

This leaves the momentum source due to average gradients in the material stress,  $\sigma_{ij}$ .

## 6.3.2

**Material Stress Gradients**

The average material stress gradients can be decomposed into terms associated with permeating fluid stresses, stresses in the cellular solid, and momentum-exchange sources resulting from relative motion of the two fields at material interfaces. For this purpose, consider the following decomposition of the material stress into mean and fluctuating parts:

$$\sigma_{ij} = \overline{\sigma}_{ij}^f + \sigma'_{ij}. \quad (6.19)$$

The quantities,  $\sigma_{ij}$ , are the components of the material stress tensor,  $\overline{\sigma}_{ij}^f$  are the components of the average stress tensor in the permeating fluid field, and  $\sigma'_{ij}$  are fluctuations in the components of the material stress tensor. The momentum source term, therefore, can be written as

$$\overline{A^k \frac{\partial \sigma_{ij}}{\partial x_j}} = \phi^k \frac{\partial \overline{\sigma}_{ij}^f}{\partial x_j} + \frac{\partial \overline{A^k \sigma'_{ij}}}{\partial x_j} - \overline{\sigma'_{ij} \frac{\partial A^k}{\partial x_j}}. \quad (6.20)$$

However,

$$\overline{A^k \sigma'_{ij}} = \phi^k (\overline{\sigma}_{ij}^k - \overline{\sigma}_{ij}^f), \quad (6.21)$$

in which the field-weighted average stress is defined by

$$\overline{\sigma}_{ij}^k \equiv \frac{\overline{A^k \sigma_{ij}}}{\overline{A^k}} \Rightarrow \overline{A^k \sigma_{ij}} = \phi^k \overline{\sigma}_{ij}^k. \quad (6.22)$$



Therefore,

$$\overline{A^k \frac{\partial \sigma_{ij}}{\partial x_j}} = \phi^k \frac{\partial \overline{\sigma}_{ij}^f}{\partial x_j} + \frac{\partial \phi^k (\overline{\sigma}_{ij}^k - \overline{\sigma}_{ij}^f)}{\partial x_j} - \overline{\sigma'_{ij} \frac{\partial A^k}{\partial x_j}}, \quad (6.23)$$

in which  $\overline{\sigma}_{ij}^k$  are the components of the average stress tensor in field  $k$ , and the quantity,  $\overline{\sigma'_{ij} \frac{\partial A^k}{\partial x_j}}$ , represents the momentum exchange resulting from relative motion of the two fields at material interfaces. Each of these quantities requires modeling.

### 6.3.2.1 Momentum Exchange

The force due to momentum exchange is quite possibly the most widely studied aspect of multifield theory. Significant contributions to this discipline date back to the time of Lord Kelvin, who engaged in the study of potential flow around fixed bodies. Later, the viscous flow contributions of Stokes and subsequent researchers provided a significant body of analytical and experimental results forming an important cornerstone of this field today. Rather than reiterate the standard results for the force due to momentum exchange, the interested reader is directed to Ishii [31], Drew and Passman [32], or most general fluid dynamics texts (see, for example, [35]) for extensive discussions of the matter.

Let it suffice to note that

$$\frac{\partial A^k(x_i, t)}{\partial x_i} = \begin{cases} n_i, & x_i \in \partial V^k, \\ 0, & \text{otherwise} \end{cases} \quad (6.24)$$

in which  $n_i$  are the components of the unit normal vector on the interface,  $\partial V^k$ , between two fields. Thus,

$$\overline{\sigma'_{ij} \frac{\partial A^k}{\partial x_j}} = \begin{cases} \overline{\sigma'_{ij} n_j}, & x_i \in \partial V^k, \\ 0, & \text{otherwise}, \end{cases} \quad (6.25)$$

which provides the average normal component of the interfacial stress, usually referred to as the drag. For material systems consisting of only two distinct fields, this drag term is traditionally modeled as

$$\overline{\sigma'_{ij} \frac{\partial A^k}{\partial x_j}} = K_{ij} (\overline{u}_j^k - \overline{u}_j^l), \quad (6.26)$$

in which the quantities,  $K_{ij}$ , are the components of the momentum-exchange-rate tensor and the superscript  $l$  on the quantities,  $\overline{u}_j^l$ , represents the field opposite to field  $k$  (that is, if  $k$  is the solid field, then  $l$  represents the fluid field, and vice versa). This is the simplest manner of representing the momentum exchange between two material fields resulting from processes associated with viscous shear and flow separation (for details, see any general reference on fluid dynamics, for example, [35]). Many other physical mechanisms can be considered and must be for some applications.

A further simplification is made by assuming the momentum-exchange rate does not give rise to forces perpendicular to the mean relative flow (e.g., lift).

Under these circumstances, the components of the momentum-exchange-rate tensor can be expressed as

$$K_{ij} = K \delta_{ij}. \quad (6.27)$$

A model for the scalar quantity,  $K$ , can be taken from the porous media literature (see, for example, [4]). Capillarc models based on conduit flow provide

$$K = \frac{50 \bar{\mu}^f}{\phi_0^f \bar{a}^2}, \quad (6.28)$$

in which  $\bar{\mu}^f$  is the kinematic viscosity of the fluid and  $\bar{a}$  is the average diameter of the apertures, that is, the small open windows between pores or cells. The quantities,  $\delta_{ij}$ , are the components of the Kronecker delta tensor defined by

$$\delta_{ij} \equiv \begin{cases} 1, & i = j, \\ 0, & \text{otherwise.} \end{cases} \quad (6.29)$$

### 6.3.2.2 Fluid-Field and Solid-Field Stresses

Because viscous effects are modeled through the momentum-exchange term, the components of the average stress tensor in the permeating fluid are written as

$$\bar{\sigma}_{ij}^f = -\bar{p}^f \delta_{ij}, \quad (6.30)$$

in which  $\bar{p}^f$  is the average permeating fluid pressure, which is modeled using an appropriate equation of state. (Note that a positive fluid pressure, which will induce a state of compression, will produce negative volumetric stresses, consistent with the standard convention in continuum mechanics:  $p = -1/3 \sigma_{ii}$ .)

The components of the average stress tensor in the solid matrix can be decomposed into volumetric and deviatoric components

$$\bar{\sigma}_{ij}^s = -\bar{p}^s \delta_{ij} + \bar{\tau}_{ij}^s. \quad (6.31)$$

However,

$$\bar{p}^s \equiv \bar{p}^f + \Delta \bar{p}^s, \quad (6.32)$$

in which the quantity,  $\Delta \bar{p}^s$ , represents the difference between the volumetric stress in the solid matrix and the pressure in the permeating fluid. This provides

$$\bar{\sigma}_{ij}^s = -\bar{p}^f \delta_{ij} - \Delta \bar{p}^s \delta_{ij} + \bar{\tau}_{ij}^s. \quad (6.33)$$

Therefore, the stress state in the solid matrix (the solid matrix, or cellular solid, should be differentiated from the bulk, or fully dense, solid) resulting from deformation is defined by

$$\bar{\sigma}_{ij}^{sm} \equiv -\Delta \bar{p}^s \delta_{ij} + \bar{\tau}_{ij}^s, \quad (6.34)$$

and this stress can be modeled using an appropriate constitutive model for the solid matrix.

In this way,

$$\bar{\sigma}_{ij}^k - \bar{\sigma}_{ij}^f = \begin{cases} 0, & k = f, \\ \bar{\sigma}_{ij}^{sm}, & k = s. \end{cases} \quad (6.35)$$

Therefore, the modeled momentum equations for the fluid and solid fields are given, respectively, by

$$\frac{\partial \phi^f \bar{\rho}^f \bar{u}_i^f}{\partial t} + \frac{\partial \phi^f \bar{\rho}^f \bar{u}_i^f \bar{u}_j^f}{\partial x_j} = -\phi^f \frac{\partial \bar{p}^f}{\partial x_i} + K(\bar{u}_i^s - \bar{u}_i^f) \quad (6.36)$$

and

$$\frac{\partial \phi^s \bar{\rho}^s \bar{u}_i^s}{\partial t} + \frac{\partial \phi^s \bar{\rho}^s \bar{u}_i^s \bar{u}_j^s}{\partial x_j} = -\phi^s \frac{\partial \bar{p}^f}{\partial x_i} + \frac{\partial \phi^s \bar{\sigma}_{ij}^{sm}}{\partial x_j} + K(\bar{u}_i^f - \bar{u}_i^s) \quad (6.37)$$

### 6.3.2.3 Solid Matrix Constitutive Models

The final component required to fully close the set of multifield conservation equations developed above is a continuum-scale constitutive model for describing the stress–strain response of the porous or cellular solid. The development of models for describing the mechanical response of porous and cellular solids is a topic that would require a length of presentation that is beyond the scope of this discussion. Indeed, many publications have been devoted to the subject, and using cellular materials as an example, the interested reader is directed to the classic text of Gibson and Ashby [1] for relatively simple mechanical descriptions based on analytical models derived from single cell models; to the work of Warren and Kraynik [24, 25] for numerical studies of idealized, but realistic, cellular material geometries that could be used to guide the development of a constitutive model, at least, for mechanical response in the small-strain regime of behavior; or to Schraad and Harlow [30] for a more advanced stochastic representation of cellular material behavior. And indeed, the model developed by Schraad and Harlow [30] is the one used to close the governing set of equations and the one used in the demonstration simulations to follow.

Equations (6.36) and (6.37) are now fully determined and, along with the multifield conservation of mass equations, may be used to simulate the dynamic response of both the articular cartilage and silicone foam materials. With modest alterations, this same set of equations could be used to represent virtually any porous or cellular material, as well as many other coupled fluid–solid systems.

## 6.4

### Demonstration Simulations

The multifield approach is used to simulate the finite-strain uniaxial compression of coupled fluid–solid systems under dynamic loading conditions. The effects of the interstitial fluid, the aperture size, and the loading rate on the dynamic response of these cellular materials are examined. The materials of interest

represent a relatively dense structural foam used primarily as a stress cushion between much stiffer metallic parts in multicomponent engineering systems, with air (and other light gases) as the interstitial fluid, and articular cartilage, with water as the interstitial fluid.

A scanning electron micrograph of a silicone foam sample is shown in Figure 6.1c. The average initial tangent modulus of the bulk solid is estimated to be  $\bar{E}^s = 15$  Mpa (see [36]), and the average Poisson's ratio is estimated to be  $\bar{\nu}^s = 0.4$ . The average density of the bulk solid was measured to be  $\bar{\rho}^s = 1.2$  g cm<sup>-3</sup>, and the average initial foam density was measured to be  $\bar{\rho}_0^c = 0.41$  g cm<sup>-3</sup>. This particular material, therefore, has an average initial relative density, or average initial solid volume fraction,  $\bar{\phi}_0 = \bar{\rho}_0^c / \bar{\rho}^s = 0.34$ . In other words, this material initially is 66% air by volume, and thus, typical of this class of materials, is lightweight and soft relative to the bulk solid.

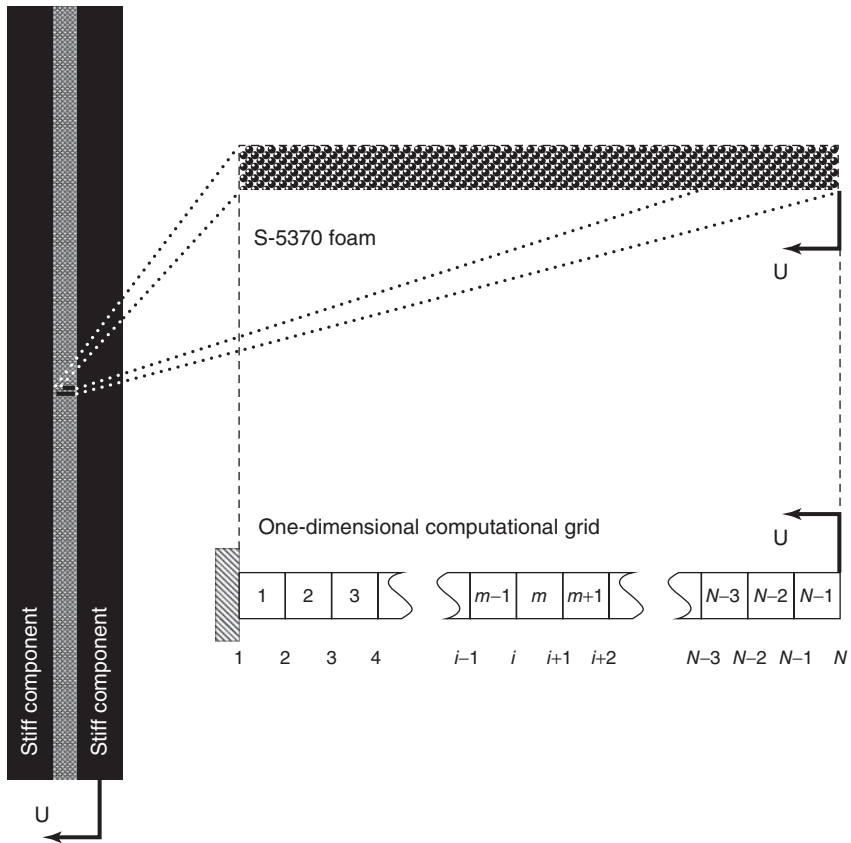


**Figure 6.2** The dynamic compression of a thin sheet of material between two rigid plates, the corresponding 1D problem and the 1D computational grid used in the solution of the multifield equations of motion.

Consider a thin sheet of silicone foam and the dynamic loading of this sheet as it is compressed between two rigid plates, as shown in Figure 6.2. If the thickness of the sheet is small relative to the other spatial dimensions, then a 1D problem can be solved to determine the response of the cellular material. In the 1D problem, a silicone foam sample is compressed between a moving piston, with velocity  $U$ , and a stationary wall, which can be constrained to allow outflow of the interstitial fluid at a rate determined by equilibration with atmospheric pressure. A standard finite-volume computational algorithm is employed, in which the multifield conservation equations are solved in the Lagrangian frame of the solid on the 1D computational grid shown. In other words, a staggered grid moving with the velocity of the cellular solid is used, and the permeating fluid is allowed to flow with a different velocity through this grid.

The total force per unit area required to move the piston at a constant velocity is plotted as a function of uniaxial compression in Figure 6.3. The total force is decomposed into the components due to solid matrix stress and interstitial fluid pressure. These results represent the dynamic response of a silicone foam sample with air as the permeating fluid. Commensurate with the apertures in the foam sample, the cellular material is modeled using an average aperture diameter,  $\bar{a} = 50 \mu\text{m}$ , and a piston velocity,  $U = 1000 \text{ cm s}^{-1}$ , is used for loading. For a sample thickness of 1 cm, this velocity produces an equivalent macroscopic strain rate

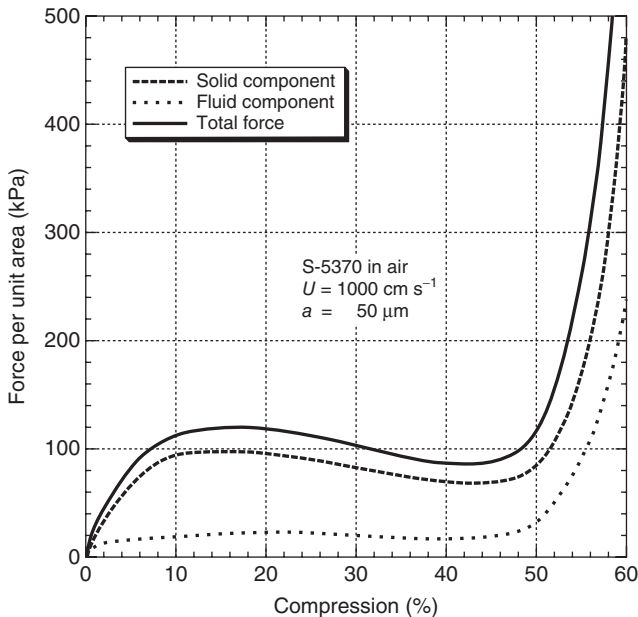


**Figure 6.3** The total force per unit area required to move the piston at a constant velocity for a silicone foam sample modeled using an average aperture diameter,

$\bar{a} = 50 \mu\text{m}$ , and a piston velocity,  $U = 1000 \text{ cm s}^{-1}$ , and the decomposition of the total force into solid and fluid components.

of  $10^3 \text{ s}^{-1}$ . The average initial density of air is taken to be  $\bar{\rho}^f = 1.2 \times 10^{-3} \text{ g cm}^{-3}$ , the average initial air pressure is taken to be  $\bar{p}^f = 1.0 \times 10^2 \text{ kPa}$ , and the average viscosity is taken to be  $\bar{\mu}^f = 1.8 \times 10^{-4} \text{ g m}^{-1} \text{ s}^{-1}$ . Prescribed boundary conditions allow outflow of the permeating fluid at the stationary wall, where the cellular solid is constrained to have zero velocity.

As the piston moves, the cellular material is compressed, and the permeating fluid is forced to flow through the cellular structure. An increase in fluid pressure accompanies the compression and accounts for approximately 20% of the total force for deformations up to approximately 40% compression. The relative contribution of the fluid pressure to the total force on the piston increases by about 35% as the cellular material approaches densification. The rapid increase in total force at the highest levels of compression coincides with the return of the cellular solid stress wave to the piston boundary, at which point the cellular solid is compressed to near full densification. The cellular solid, in turn, compresses the air, which is restricted from flowing freely through the small apertures, producing a significant corresponding rise in the fluid pressure.

In Figure 6.4, results represent the dynamic response of a silicone foam sample in vacuum and with sulfur hexafluoride ( $\text{SF}_6$ ), air, and argon as the permeating fluid. Again, the cellular material is modeled using an average aperture diameter,  $\bar{a} = 50 \text{ }\mu\text{m}$ , and a piston velocity,  $U = 1000 \text{ cm s}^{-1}$ , is used for loading. The significant difference between the various fluid media considered is in their respective compressibilities. For  $\text{SF}_6$  and argon, the average initial densities are taken to

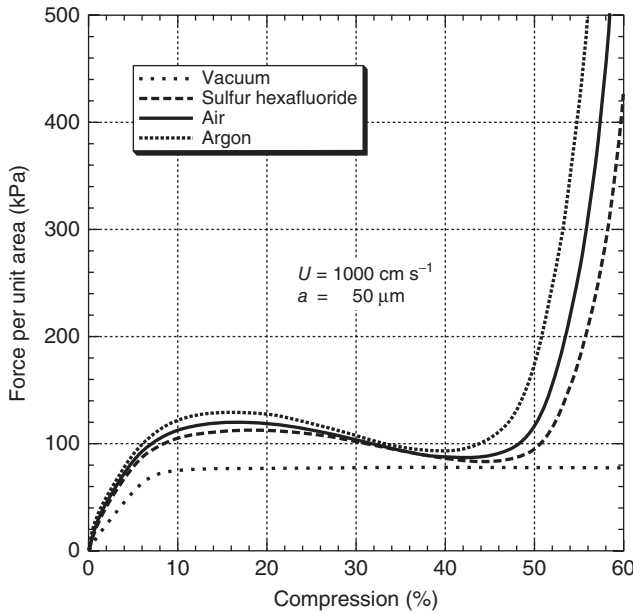


**Figure 6.4** The effects of various fluids on the total force for a silicone foam sample and a piston velocity,  $U = 1000 \text{ cm s}^{-1}$ .

be  $\bar{\rho}^f = 6.1$  and  $1.7 \text{ g cm}^{-3}$ , respectively; and the average viscosities are taken to be  $\bar{\mu}^f = 1.6 \times 10^{-4}$  and  $2.2 \times 10^{-4} \text{ g m}^{-1} \text{ s}^{-1}$ , respectively. The average initial fluid pressure in each of these circumstances remains  $\bar{p}^f = 1.0 \times 10^2 \text{ kPa}$ . And again, prescribed boundary conditions allow outflow of the permeating fluid at the stationary wall.

For the case of a silicone foam sample in vacuum, the total force on the piston reaches a plateau. The cellular solid stress remains constant at the piston boundary, while the stress wave propagates through the sample. The force does not increase again until the stress wave in the cellular solid reflects off of the stationary boundary and returns to the piston (not shown). The results obtained for a silicone foam sample in vacuum reproduce what one would obtain using a purely single-field mechanical model such as Gibson and Ashby [1, 22], Warren and Kraynik [24, 25], or Schraad and Harlow [30]. For the cases of silicone foam in  $\text{SF}_6$ , air, and argon, the total force on the piston reaches a maximum load, as the two fields in each case couple to provide nonmonotonic response. The total force also increases (to various degrees for various levels of compression) with decreasing compressibilities due to the increased pressure required to reach the same level of compression.

The effect of aperture size on the piston force is examined in Figure 6.5. A piston velocity,  $U = 1000 \text{ cm s}^{-1}$ , is used for loading, and the cellular material is modeled using an average aperture diameter,  $\bar{a}$ , ranging from 0 (i.e., closed cells) to  $500 \text{ }\mu\text{m}$  (approximately the size of the largest foam cells). The fluid properties

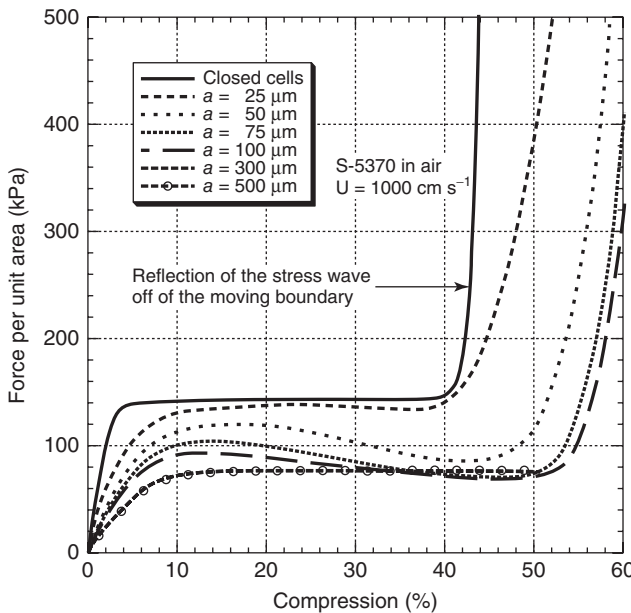


**Figure 6.5** The effect of varying average aperture size on the total force for a silicone foam sample and a piston velocity,  $U = 1000 \text{ cm s}^{-1}$ .

for air provided above are used again here, and for all subsequent simulations involving the silicone foam. And again, prescribed boundary conditions allow outflow of the permeating fluid at the stationary wall.

In general, as the aperture size increases, the total force required to move the piston at a constant velocity decreases, because the smallest aperture sizes significantly restrict the flow of the interstitial fluid through the cellular structure, resulting in the buildup of higher fluid pressures. Similar to the case of a silicone foam material in vacuum, for a silicone foam material with closed cells, the total force on the piston reaches a plateau. In this case, however, the response of the two material fields is fully coupled (e.g.,  $K \rightarrow \infty$ ), and thus, the cellular solid and the permeating fluid are constrained to move with the same average velocity. Both the cellular solid stress wave and the pressure wave in the permeating fluid travel at the same speed, and therefore, the force on the piston does not increase again until this combined stress–pressure wave reflects off of the stationary boundary and returns to the piston, as shown. The results obtained for closed cells (i.e., fully coupled response) reproduce what one would obtain using classic mixture theories such as Mak [5, 19] and Mak *et al.* [20], in which each phase is treated using the average velocity of the mixture and relative motion of the two fields is not considered.

The results obtained for  $\bar{a} = 300$  and  $500\mu\text{m}$  are nearly identical to one another, and again, in both cases, the total force on the piston reaches a plateau. For aperture diameters greater than approximately  $300\mu\text{m}$ , the fluid flows without restriction through the cellular structure, as the coupling between the two fields has been significantly reduced, and in fact becomes negligible for air flowing through this microstructure at these velocities. In other words, for aperture diameters greater than approximately  $300\mu\text{m}$ , the response of the two fields becomes fully uncoupled, and the permeating fluid no longer contributes to the total force on the piston (in fact, the results obtained for  $\bar{a} = 300$  and  $500\mu\text{m}$  essentially are indistinguishable from the results obtained for a silicone foam material in vacuum shown in Figure 6.4. And so, here again, the results obtained for the largest apertures (i.e., uncoupled response) reproduce what one would obtain using a purely single-field mechanical model.

The results presented in Figure 6.5 demonstrate that the microstructure (e.g., in this case, the aperture size) and the coupling of the permeating fluid behavior with the cellular solid response affect signal propagation speeds in cellular materials. The maximum load occurring in each force–compression response, the variation in the level of compression at which these maxima occur, and the variation in the level of compression corresponding to the rapid increase in piston force provide evidence that the cellular solid stress wave and the fluid pressure wave travel at different velocities.

The effect of loading rate on the piston force is examined in Figure 6.6. The cellular material is modeled using an average aperture diameter,  $\bar{a} = 50\mu\text{m}$ , and a piston velocity,  $U$ , ranging from  $100$  to  $1000\text{ cm s}^{-1}$  is used for loading. Again, prescribed boundary conditions allow outflow of the permeating fluid at the stationary wall.



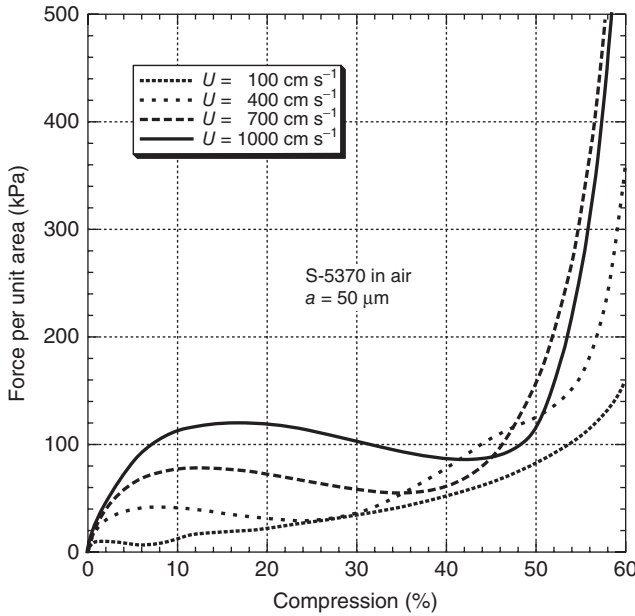


**Figure 6.6** The effect of varying loading rate on the total force for a silicone foam sample modeled using an average aperture diameter,  $\bar{a} = 50 \mu\text{m}$ .

In general, as the loading rate increases, the total force required to move the piston at a constant velocity increases. This certainly is the case for levels of compression less than approximately 35%. This trend does not necessarily hold for higher levels of compression, as the stress wave in the cellular solid and the pressure wave in the permeating fluid propagate at different velocities. For example, for compressions up to 60%, the stress wave in the cellular solid travels to the stationary boundary and back to the piston once for a piston velocity,  $U = 1000 \text{ cm s}^{-1}$ , but many times for a piston velocity,  $U = 100 \text{ cm s}^{-1}$ . In addition, the pressure wave in the permeating fluid travels at a higher velocity and out of phase with the cellular solid stress wave, leading to nonmonotonicity in the results at the higher levels of compression. Note, however, that the continuum-scale constitutive model for the cellular solid is rate independent, so the rate effects exhibited in these simulations are due solely to the coupled behavior of the interstitial fluid.

Now, consider a different material, for example, the articular cartilage shown in Figure 6.1d. Perhaps surprisingly, the bulk solid is quite similar to the silicone of the previous example. Here, collagen fibers replace molecular chains at the molecular scale. However, the solid–volume fractions are similar, ranging between 0.25 and 0.45 for the silicone foam and between 0.20 and 0.40 for articular cartilage. The cellular-scale structures of both materials are highly disordered, and the average cell and aperture sizes for both materials are of the same order of magnitude. The two materials are qualitatively similar in both structure and bulk

material properties; however, for most applications, the interstitial fluids present in these two coupled fluid–solid systems will be different, with air in the case of silicone foams and a biological fluid, with similar properties to water, in the case of articular cartilage. For much denser, less compressible fluids, such as water, the effects of the interstitial fluid on the coupled response of the material are even more pronounced.

So, now consider a thin sample of cartilage and the dynamic loading of this sample as it is compressed between a moving piston and a stationary wall, as shown in Figure 6.2. The total force per unit area required to move the piston at a constant velocity is plotted as a function of uniaxial compression in Figure 6.7. The total force is decomposed into the components due to solid matrix stress and interstitial fluid pressure. Results represent the dynamic response of articular cartilage with water as the interstitial fluid. Reported values of the properties of the bulk solid in articular cartilage vary widely, so the results have been nondimensionalized by dividing the resultant stress on the piston by the initial elastic modulus of the bulk solid, which was assumed to be  $\bar{E}^s = 15 \text{ Mpa}$  (see [37]). The average initial densities of the bulk solid and the porous cartilage were estimated to be  $\bar{\rho}^s = 1.0 \text{ g cm}^{-3}$  and  $\bar{\rho}_0^c = 0.30 \text{ g cm}^{-3}$ , respectively. This particular material, therefore, has an average initial solid–volume fraction,  $\bar{\phi}_0 = \bar{\rho}_0^c / \bar{\rho}^s = 0.30$ .

Commensurate with the apertures in the cartilage sample, the material is modeled using an average aperture diameter,  $\bar{a} = 25 \text{ }\mu\text{m}$ , and a piston velocity,  $U = 1 \text{ cm s}^{-1}$ , is used for loading. For a sample thickness of 1 cm, this velocity produces an equivalent macroscopic strain rate of  $1 \text{ s}^{-1}$ . The average initial

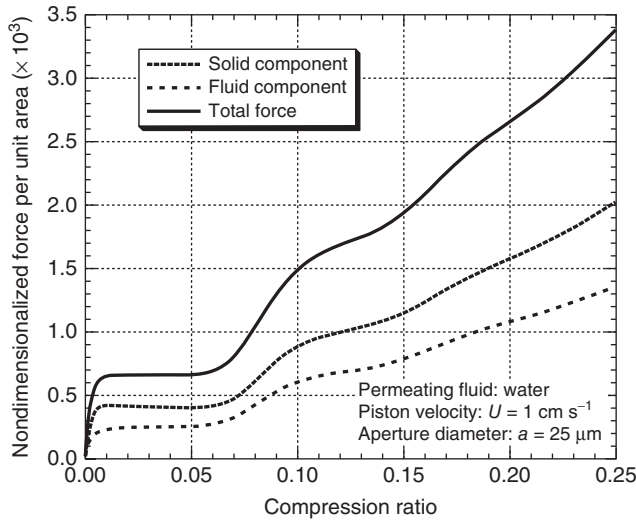


**Figure 6.7** The nondimensionalized total force per unit area required to move the piston at a constant velocity for an articular cartilage sample modeled using an average

aperture diameter,  $\bar{a} = 20 \text{ }\mu\text{m}$ , and a piston velocity,  $U = 1 \text{ cm s}^{-1}$ , and the decomposition of the total force into solid and fluid components.

density of water is taken to be  $\bar{\rho}^f = 1.0 \text{ g cm}^{-3}$ , the average initial water pressure is taken to be  $\bar{p}^f = 1.0 \times 10^2 \text{ kPa}$ , and the average viscosity is taken to be  $\bar{\mu}^f = 1.0 \times 10^{-2} \text{ g cm}^{-1} \text{ s}^{-1}$ , all standard properties of water.

As the piston moves, the cellular material is compressed, and the interstitial fluid is forced to flow through the cellular structure. An increase in fluid pressure accompanies the compression and accounts for approximately 40% of the total force for all deformations. This is roughly twice the effect seen in the silicone foam and represents effects of the higher density, less compressible interstitial fluid, as well as the effects of a smaller average aperture size. It also now represents an effect commensurate with the stress state in the solid, suggesting any modeling approach that neglects the behavior of the interstitial fluid is missing relevant physics. The second step-like increase in the force–compression curves coincides with the return of the cellular solid stress wave to the piston boundary, at which point the cellular solid is compressed to near full densification, producing a corresponding rise in the fluid pressure. These abrupt steps diminish over time due to viscosity in the system.

The effects of varying aperture size on the cartilage response are examined in Figure 6.8. A piston velocity,  $U = 1 \text{ cm s}^{-1}$ , is used for loading, and the material is modeled using an average aperture diameter,  $\bar{a}$ , ranging from 0 (i.e., closed cells) to  $100 \mu\text{m}$  (approximately the size of the largest pores).

Quite similar to the response of the silicone foam, in general, as the aperture size increases, the force required to move the piston decreases, because the smallest apertures significantly restrict the flow of the interstitial fluid, resulting in higher fluid pressures. For a material with closed cells, the response of the two material fields is fully coupled, and for aperture diameters greater than approximately

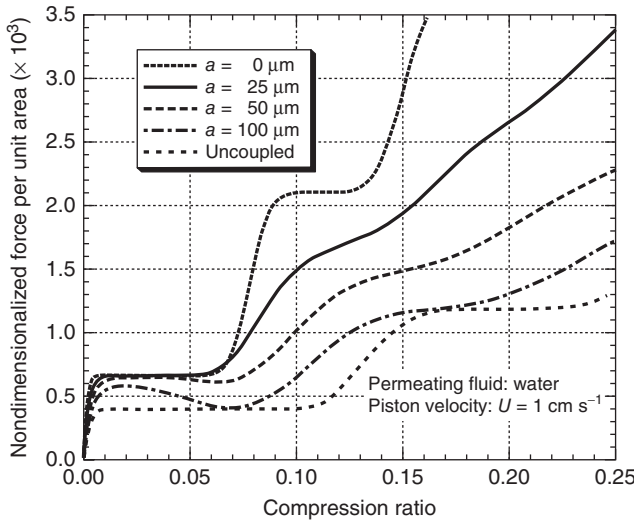


**Figure 6.8** The effects of varying aperture size on the total force for an articular cartilage sample and a piston velocity,  $U = 1 \text{ cm s}^{-1}$ .

100  $\mu\text{m}$ , the interstitial fluid no longer contributes significantly to the total force on the piston. Similar to the silicon foam results, these results reproduce what one would obtain using mixture theory or a purely single-field mechanical model, respectively. And once again, the results provide evidence that the cellular solid stress and fluid pressure waves travel at different velocities.

The effects of varying loading rate on the cartilage response are examined in Figure 6.9. The material is modeled using an average aperture diameter,  $\bar{a} = 25 \mu\text{m}$ , and a piston velocity,  $U$ , ranging from 0.001 to  $1 \text{ cm s}^{-1}$  is used for loading.

In general, as the loading rate increases, the force required to move the piston increases. Because the forces per unit area obtained for the two lowest piston velocities are nearly indistinguishable, the results suggest that an approximately quasistatic loading rate is achieved for  $U \approx 0.01 \text{ cm s}^{-1}$ . Recall; however, that the continuum-scale constitutive model for the cellular solid is, again, rate independent, so the rate effects exhibited in these simulations are due solely to the influence of the interstitial fluid.

Collectively, the results presented here demonstrate the significant influence that the interstitial fluid can have on the general mechanical response of porous and cellular materials, contributing to the overall load-carrying capacity of the material and affecting rate dependence and signal propagation speeds. The results point to the usefulness of the multifield approach and provide evidence to suggest that any modeling approach developed for these materials should provide a proper accounting of the pressure evolution and flow behavior of the fluids permeating the underlying cellular structures.

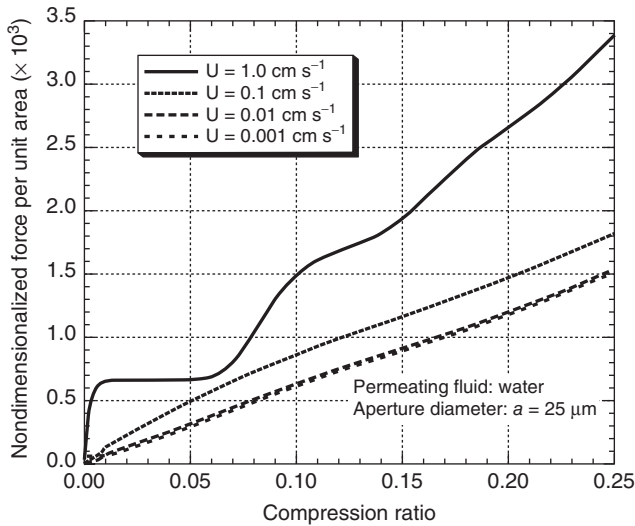


**Figure 6.9** The effects of varying loading rate on the total force for an articular cartilage sample modeled using an average aperture diameter,  $\bar{a} = 20 \mu\text{m}$ .

## 6.5

### Concluding Remarks

Early investigations into the mechanical response of porous and cellular materials demonstrated that these materials stiffen with the increasing fluid pressure that accompanies compressive deformations and dissipate energy through viscous mechanisms as the permeating fluids flow (or are restricted from flowing) through the intricate underlying microstructures. Efforts to model the mechanical response of such coupled fluid–solid systems, however, have primarily ignored the evolving pressure and flow behavior of the gases and liquids permeating these complex material systems.

The geomechanics community has taken the furthest steps, by using a Darcy law approximation to the full multifield equation set for many problems of interest. And indeed, such an approximation is appropriate for most geomechanics applications. Biphasic theory has been used successfully to model the mechanical response of biological materials under many circumstances. However, when the velocities of the interstitial fluid and cellular solid fields are distinctly different from the average velocity of the mixture, a more general formulation is required. And unfortunately, the mechanical engineering community mostly has restricted attention to the mechanical response of the solid matrix, despite evidence to suggest that relevant physical mechanisms associated with the fluid fields are being neglected.

The developments presented herein establish a new approach for modeling both synthetic and natural porous and cellular materials. The innovation in this new approach comes about through the incorporation of advanced constitutive models for the solid matrix material into a general multifield representation of the governing conservation equations. The outcome is a unique modeling approach for use in simulating the continuum-scale mechanical response of geological, biological, and synthetic engineered materials possessing underlying porous or cellular structures. Results establish that the pressure evolution and flow behavior of the interstitial fluids represent relevant physical response mechanisms and suggest that any modeling approach developed for these, or similar, materials gives a proper accounting of the corresponding effects.

The multifield approach to modeling porous and cellular materials offers a unique opportunity to identify the materials, applications, and conditions under which the interstitial fluid affects the response of the surrounding porous or cellular matrix, and to distinguish between the physical mechanisms associated with the solid matrix material and those associated with the interstitial fluid. For example, the effective system stiffness due to the solid matrix stress state is differentiated from the stiffness due to the developing pressures in the interstitial fluid. Likewise, rate dependencies related to the viscoelastic properties of the bulk solid can be differentiated from rate dependencies related to viscous mechanisms associated with the flow of the interstitial fluid through the underlying structure. Similar distinctions are made with regard to the physics governing signal propagation speeds, fluid transport, and susceptibility to failure. In turn, these

distinctions are providing new insight into the coupled fluid–solid response of porous and cellular material systems, leading to less phenomenology-dependent constitutive laws, and thus, a more physically based modeling approach and an improved predictive capability for material response simulations.

## References

- Gibson, L.J. and Ashby, M.F. (1997) *Cellular Solids: Structure and Properties*, 2nd edn, Cambridge University Press, Cambridge.
- Biot, M.A. (1941) General theory of three-dimensional consolidation. *J. Appl. Phys.*, **12**, 155–164.
- Bowen, R.M. (1976) in *Continuum Physics, Mixtures and EM Field Theories*, vol. 3 (ed. A.C. Eringen), Academic Press, New York, pp. 1–127.
- Dullien, F.A.L. (1979) *Porous Media: Fluid Transport and Pore Structure*, Academic Press, New York.
- Mak, A.F. (1986) The apparent viscoelastic behavior of articular cartilage: the contributions from the intrinsic matrix viscoelasticity and interstitial fluid flow. *ASME J. Biomech. Eng.*, **108**, 123–130.
- Simon, B.R. (1992) Multiphase poroelastic finite element models for soft tissue structures. *Appl. Mech. Rev.*, **45**, 191–218.
- Cowin, S.C. (1999) Bone poroelasticity. *J. Biomech.*, **32**, 217–238.
- Wang, H.F. (2000) *Theory of Linear Poroelasticity*, Princeton University Press, Princeton, NJ.
- Biot, M.A. (1956) Theory of propagation of elastic waves in a fluid saturated porous solid. I. Low frequency range. *J. Acoust. Soc. Am.*, **28**, 168–178.
- Biot, M.A. (1956) Theory of propagation of elastic waves in a fluid saturated porous solid. II. Higher frequency range. *J. Acoust. Soc. Am.*, **28**, 179–191.
- Biot, M.A. (1962) Mechanics of deformation and acoustic propagation in porous media. *J. Appl. Phys.*, **33**, 1482–1498.
- Biot, M.A. (1962) Generalized theory of acoustic propagation in porous dissipative media. *J. Acoust. Soc. Am.*, **34**, 1254–1264.
- Darcy, H. (1856) *Les Fontaines Publiques de Ville de Dijon*, Dalmont, p. 590.
- Gray, W.G. and O'Neill, K. (1976) On the general equations for flow in porous media and their reduction to Darcy's law. *Water Resour. Res.*, **12**, 148–154.
- Neuman, S.P. (1977) Theoretical derivation of Darcy's law. *Acta Mech.*, **25**, 153–170.
- Mow, V.C., Kuei, S.C., Lai, W.M., and Armstrong, C.G. (1980) Biphasic creep and stress relaxation of articular cartilage in compression: theory and experiments. *J. Biomech. Eng.*, **102**, 73–84.
- Mow, V.C. and Guo, X.E. (2002) Mechano-electrochemical properties of articular cartilage: their inhomogeneities and anisotropies. *Annu. Rev. Biomed. Eng.*, **4**, 175–209.
- Lim, C.T., Zhou, E.H., and Quek, S.T. (2006) Mechanical models for living cells—a review. *J. Biomech.*, **39**, 195–216.
- Mak, A.F. (1986) Unconfined compression of hydrated viscoelastic tissues: a biphasic poroviscoelastic analysis. *Biorheology*, **23**, 371–383.
- Mak, A.F., Lai, W.M., and Mow, V.C. (1987) Biphasic indentation of articular cartilage. 1. theoretical analysis. *J. Biomech.*, **20**, 703–714.
- Gent, A.N. and Thomas, A.G. (1963) Mechanics of foamed elastic materials. *Rubber Chem. Technol.*, **36**, 597–610.
- Gibson, L.J. and Ashby, M.F. (1982) The mechanics of three-dimensional cellular materials. *Proc. R. Soc. London, Ser. A. Math. Phys. Sci.*, **382**, 43–59.
- Ashby, M.F. (1983) The mechanical properties of cellular solids. *Metall. Mater. Trans. A Phys. Metall. Mater. Sci.*, **14**, 1755–1769.
- Warren, W.E. and Kraynik, A.M. (1987) Foam mechanics: the linear elastic

- response of two-dimensional spatially periodic cellular materials. *Mech. Mater.*, **6**, 27–37.
25. Warren, W.E. and Kraynik, A.M. (1988) The linear elastic properties of open-cell foams. *J. Appl. Mech.*, **55**, 341–346.
  26. Zhu, H.X., Mills, N.J., and Knott, J.F. (1997) Analysis of the high strain compression of open-cell foams. *J. Mech. Phys. Solids*, **45**, 1875–1904.
  27. Zhu, H.X., Hobdell, J.R., and Windle, A.H. (2000) Effects of cell irregularity on the elastic properties of open-cell foams. *Acta Mater.*, **48**, 4893–4900.
  28. Triantafyllidis, N. and Schraad, M.W. (1998) Onset of failure in aluminum honeycombs under general in-plane loading. *J. Mech. Phys. Solids*, **46**, 1089–1124.
  29. Zhu, H.X. and Windle, A.H. (2002) Effects of cell irregularity on the high strain compression of open-cell foams. *Acta Mater.*, **50**, 1041–1052.
  30. Schraad, M.W. and Harlow, F.H. (2006) A stochastic constitutive model for disordered cellular materials: finite-strain uni-axial compression. *Int. J. Solids Struct.*, **43**, 3542–3568.
  31. Ishii, M. (1975) *Thermo-Fluid Dynamic Theory of Two-Phase Flow*, Eyrolles, Paris.
  32. Drew, D.A. and Passman, S.L. (1999) *Theory of Multicomponent Fluids*, Springer-Verlag, New York.
  33. Zhang, D.Z. and Prosperetti, A. (1994) Averaged equations for inviscid disperse two-phase flow. *J. Fluid Mech.*, **267**, 185–219.
  34. Zhang, D.Z. and Prosperetti, A. (1997) Momentum and energy equations for disperse two-phase flows and their closure for dilute suspensions. *Int. J. Multiphase Flow*, **23**, 425–453.
  35. White, F.M. (1986) *Fluid Dynamics*, 2nd edn, McGraw-Hill.
  36. Orler, E.B. (1999) The aging of silica filled polysiloxane composites. Report LA-UR-99-936, Los Alamos National Laboratory.
  37. Haut Donahue, T.L., Hull, M.L., Rashid, M.M., and Jacobs, C.R. (2003) How the stiffness of meniscal attachments and meniscal material properties affect tibio-femoral contact pressure computed using a validated finite element model of the human knee joint. *J. Biomech.*, **36**, 19–34.

## 7

**Swelling of Wood Tissue: Interactions at the Cellular Scale**

*Dominique Derome, Jan Carmeliet, Ahmad Rafsanjani, Alessandra Patera, and Robert Alan Guyer*

## 7.1

**Introduction**

Swelling of wood superposes two interesting phenomena: the displacement by adsorbed moisture of an oriented polymeric material and the geometrical interactions of the layered structures of adjacent cell walls. In this chapter, experimental and simulation observations are made at the cellular scale to consider the relative roles of cellular geometry and material organization during the swelling and shrinkage of the material.

In wood, swelling is the increase in volume that results from the adsorption of water molecules on the polar sites of the hygrophilic polymers that compose the cell wall. The porosity of the cell wall in dry state is very low, so the presence of water molecules soon results in a displacement of the polymeric components. The level of moisture adsorption is dependent on the water vapor chemical potential (or on the relative humidity, RH) in the ambient air. In addition, the sorption of water leads to a breaking or a softening of some component interactions, reducing the dry modulus of elasticity of the cell wall by 50–75% depending on the orthotropic direction. Water vapor sorption can lead up to a moisture content (MC) of  $125 \text{ kg water m}^{-3}$  (for an average dry wood density of  $450 \text{ kg m}^{-3}$ , i.e., porosity of 70%) or 28% MC in mass per mass. Above this level, or namely the hygroscopic range, additional moisture has almost no impact on the swelling or on the mechanical properties as this additional water is in bulk liquid state and resides within the void, or lumen, of the wood cells.

Studying swelling may provide open views into both the moisture and the mechanical behavior of such cellular polymeric materials, toward a full description of this moisture/mechanical interaction.



7.2  
Description of Wood

Wood is a biological hierarchical cellular polymeric composite. The cell wall material organization reflects the biological formation of this exoskeleton. First, the cell extrudes strings of cellulose crystal. Then, a further polymerization leads to the embedding and agglomeration of the crystalline cellulose by polysaccharides, mainly amorphous cellulose, but also some hemicellulose, to produce cellulose microfibrils, of 15–20 nm diameter range, which are laid in a quasiparallel manner. Once the fibrils are in place, the living cell flushes additional material of which chemical composition and organization vary from layer to layer during the formation of the cell wall. The thin P layer is formed as the cell grows and reaches its full size; it is a malleable structure that presents little organization and is very thin, as schematically shown in Figure 7.1. In the remaining three layers, the cellulose microfibrils are laid out in specific arrangements, with a crisscrossing pattern at an angle of 70° with the trunk direction in the S1 layer, then all parallel with a small angle in the S2 layer forming a right-handed helix, and then all parallel at 70° in the S3 layer. It is more and more suspected that, during placement, the microfibrils somewhat relax from the deposited position until touching their neighbors on both sides [1], maybe resulting in the netlike configuration. The arrangement of

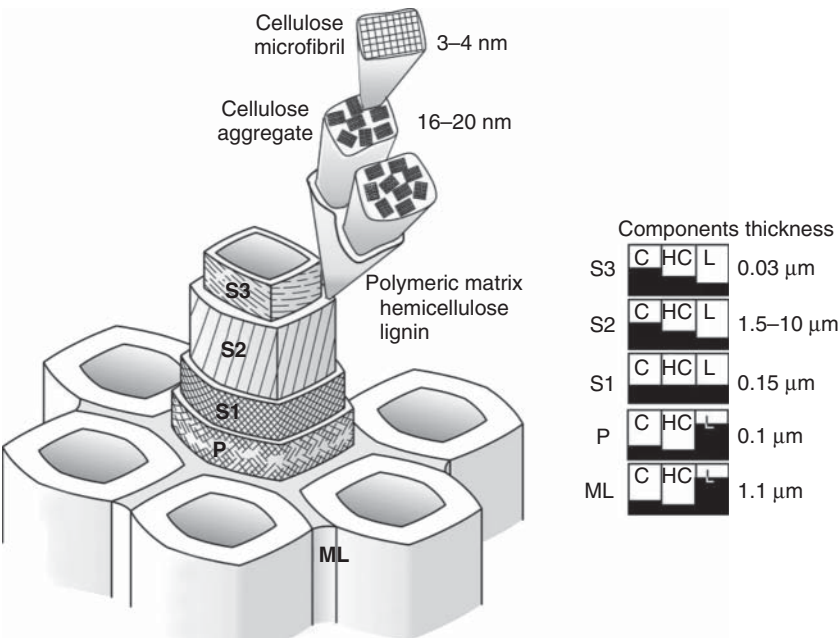


**Figure 7.1** (a) Schematic representation of the organization of the cell wall components. (b) Chemical composition of the different cell wall layers. ML refers to middle lamella; P, primary cell wall; S1, S2, and S3, layers of the secondary cell wall; C, cellulose; HC, hemicellulose; and L, lignin. (from Derome *et al.* (2012) with permission of Taylor & Francis)

the different chemical components in between the lenticularly undulating cellulose microfibrils suggests interfibrils distance in the order of 4–10 nm in dry cell walls [2]. It is likely that the different polysaccharide layers are oriented along the direction of these cellulose microfibrils [3, 4]. In a softwood like spruce, the cellulose fibrils and glucomannan, an hemicellulose, bond via hydrogen bonds, resulting in a strong but also flexible connection of both polymers. Lignin is covalently bound to hemicelluloses (glucomannan and xylan) and does not bound directly to cellulose. The hemicelluloses thus interface the hydrophilic (amorphous phase) and stiff (crystalline phase) cellulose with the more hydrophobic and pliant lignin. Salmén and Burgett [5] see hemicelluloses as templates leading to a strengthening of the cell wall polymers bonding, performed in a highly organized manner as revealed by the orientation of both hemicelluloses and lignins in relation to the cellulose microfibrils. Finally, the middle lamella, that is, the space between cells, is filled with a lignin-rich matrix, labeled as ML in Figure 7.1.

Thus, the cell wall material is akin to a multilayer fiber-reinforced composite, as represented on Figure 7.1. The very thin internal and external cell wall layers (namely, S3 and S1) act as corsets due to the winding of the fibers, namely cellulose fibrils, around the cell. In the central and, by far, thickest cell wall layer, namely S2, the helicoidal organization of the fibrils stiffens the cell wall material along its circumference. The P layer is often considered together with the middle lamella as forming the quasi-isotropic layer bonding the cells.

Softwood consists mainly of longitudinal tracheid cells and of some radially oriented ray cells, the latter representing only 5% of the wood volume. In temperate climate regions, the tree growth occurs in the warmer part of the year and is modulated by the environmental conditions and biological needs of the tree. The result is a mesoscale feature, the growth ring, where thin-walled earlywood cells (grown in spring) with large internal lumens gradually change to thick-walled latewood cells (grown in summer) with small-sized lumens. In earlywood cells, given their delicate configuration, the S2 layer can account to less than 50% of the cell wall, while the S2 may account to more than 80% of cell wall of the bulky latewood cells. For example, Fengel and Stoll [6] have measured the percentage of the thickness of the cell wall layers, showing that S2 is the thicker layer in both earlywood and latewood, but the thickness of the two stiffer layers S1 and S3 is in percentage higher in earlywood than in latewood (total of 18% of wall thickness (13% for S1 and 5% for S3, respectively) in earlywood and 12% (9% and 3%) in latewood).

### 7.3

#### Absorption of Moisture in Wood

For the species under discussion, that is Norway spruce (*Picea abies* (L.) Karst.), the macroscopic swelling and shrinkage strains occur between dry state and 28% MC (in the ratio of mass of water to mass of dry wood) and are known to be orthotropic. In the hygroscopic range, moisture-induced deformation strains are typically in the order of 0.5% longitudinally, 4% radially, and 6% along the

tangential direction. The maximal difference between the MC during adsorption and desorption for a given RH has been identified to be as much as 4% MC at the mid-point [7]. Strain hysteresis between swelling and shrinkage in function of MC has been observed macroscopically, to be in the range maximally of 1% for maple [8]. The source of swelling/shrinkage strains is normally attributed to the process of water sorption in the cell wall, where water molecules bind with hydrogen bonds to sorption sites, primarily hydroxyl sites, of the amorphous cellulose, hemicellulose, and lignin. As water adsorption and desorption occur within the cell wall material, the cell wall and the overall cellular structure experience swelling and shrinkage, thus inducing swelling/shrinkage at macroscale. Both the cellular and the growth ring structures affect the resulting moisture-induced deformations at the macroscale, as described by Hernandez [8].

As mentioned earlier, wood exposed to a closed-loop RH protocol shows sorption hysteresis. Water is a polar molecule that binds with hydrogen bonds to the hydroxyl sites of the polar molecules. A common explanation for hysteresis is that, in dry state, a pair of hydroxyl sites are bonded together until this bond is broken due the general displacement resulting from moisture adsorption, at which point these hydroxyl sites become available for bonding to water. In desorption, moisture can thus desorb at lower RH than when it sorbed. Except for crystalline cellulose, all wood polymers demonstrate, to different extents, an affinity for water. Hemicelluloses adsorb almost twice as much moisture than lignin does at the same RH, and so does amorphous cellulose at high relative humidities. In the dry state, the cell wall has a low porosity where water molecules can readily find a few available sorption sites. For further sorption to take place, that is, above 2–3% MC, the creation of new porosity by the displacement of molecules is required. Thus, sorption of water molecules in between the hydrophilic molecules pushes the constituents apart, resulting in swelling and a reduction of stiffness of the matrix. The whole process of swelling and shrinkage, which is known to be anisotropic at the cellular scale and is expected to be also anisotropic at the cell wall scale, is yet to be understood.

Salmen and Burgett [5] indicate that knowing better the distribution of the different hemicelluloses in the cell wall and their *in situ* mechanical and moisture properties would solve a main hurdle to understand wood hygroexpansivity. In the interim that such molecular-level behavior becomes available, the main tool available to understand swelling/shrinkage at the cellular, and maybe subcellular scale, is imaging.

#### 7.4

##### Swelling of Wood Tissue – Investigations by Phase Contrast Synchrotron X-Ray Tomographic Microscopy

This moisture-induced deformation process has been described over the last century at the macroscale (lumber) and, recently, at the cellular scale with optical or confocal scanning laser microscopy, such as reported by Murata and Masuda [9],

Gu *et al.* [10], Ma and Rudolph [11], Sakagami *et al.* [12], or with X-ray tomographic microscopy [13, 14]. In this latter work, the swelling strains of homogeneous wood tissues of different density subjected to a hygroscopic loading cycle in RH were measured and presented in function of RH and MC. Here, we summarize this work. At the microscale, when considering homogeneous wood tissues with uniform density, it is possible to decouple the effects of the growth ring layered arrangement of denser and lighter wood tissues and thus to focus especially on the role of the cell geometry and the cellular structure on these deformations.

X-ray tomographic microscopy is an efficient technique for three-dimensional characterization of the deformation of the cellular structure. The synchrotron radiation is a beam with parallel geometry, that is monochromatic, highly brilliant and highly coherent, which allows to achieve high spatial resolution (here submicrons range), while the flux permits very rapid imaging. The cellular configuration of the wood samples is thus captured at different moisture states using synchrotron radiation-based phase contrast X-ray tomographic microscopy (srPCXTM). A brief description of the experimental setup and srPCXTM is presented here, more details can be found in Derome *et al.* [13]. The measurements were performed at the TOMCAT beamline of the Swiss Light Source, Paul Scherrer Institute, Villigen, Switzerland.

Housed in an environmental chamber with controlled RH conditions, as shown in Figure 7.2, different samples are exposed to five RH steps in adsorption and five in desorption, covering the 10–85% RH range. The RH conditions at each step are maintained long enough to ensure moisture equilibrium in the



**Figure 7.2** Photo at TOMCAT beamline experimental station, showing (i) end of the X-ray tube, (ii) shutter, (iii) environmental chamber with the sample inside and the

inlet/outlet tubes connected the chamber to the RH control system, and (iv) the camera (from Patera *et al.* (2013) with permission from Elsevier).

samples, that is 1 h as verified earlier by dynamic vapor sorption apparatus. Each adsorption–desorption experiment lasts between 12 and 16 h.

The srPCXTM 3D datasets consist in 1024 radiographic images of  $1024 \times 1024$  pixels of  $0.70 \mu\text{m pixel}^{-1}$  spatial resolution. Phase contrast imaging is here used. The method can be used to highlight edges and internal boundaries of a sample as a technique complementary to absorption contrast, which is more sensitive to the bulk of the sample. Moreover, phase contrast can be used to image low-density materials such as wood, which present a low X-ray attenuation coefficient [15–17]. The difference in density, thus the X-ray index of refraction, at the boundary between air and wood is the source of phase contrast. We used the modified Bronnikov algorithm (MBA) [18, 19]. The MBA method is simple, very fast, and well suited for small objects where the needed resolution is around  $1 \mu\text{m}$ . The basic idea of the MBA is to introduce a correction factor to the low-pass filter function.

To determine the swelling and shrinkage strains along the radial, tangential, and longitudinal directions between a reference state and each subsequent state, we perform an affine registration as explained in detail in [13]. In general, a 3D affine transformation,  $f$ , which maps 2 volumes by a linear function, is defined by 12 parameters: 3 for translation, 3 for rotation, 3 for scaling, and 3 for shear and is described by

$$\overline{x'} = f(\overline{x}) = \overline{A}\overline{x} + \overline{T} \quad (7.1)$$

where  $\overline{x'}$  is the transformed and  $\overline{x}$  the original image coordinates;  $\overline{A}$  is a  $3 \times 3$  matrix of real numbers referring to the shear, scale, and rotation contributions; and  $\overline{T}$  is a column translation vector. We assume here that the affine relation is a good approximation for describing the deformation between the two volumes. The state at the lowest RH is considered the reference state from which the transformation matrix  $\overline{A}$  at the subsequent states is calculated, using the software Slicer 3D [20]. Starting from these parameters and under the approximation of small displacement gradients, it is possible to calculate the principal strains along the tangential, radial and longitudinal directions.

#### 7.4.1

##### Behavior of Homogeneous Tissues

The four samples are homogeneous tissues, two earlywood samples, named EW1 and EW2, and two latewood samples, LW1 and LW2, of high to low porosity, that is, from 78% to 45%. The swelling/shrinkage strains in radial and tangential directions of the four samples as function of RH are shown in Figure 7.3a, with decreasing porosity from top to bottom. Each point corresponds to one tomographic dataset taken at one RH. The points are joined with a dash line in adsorption and with a full line in desorption.

Considering first the swelling range in tangential direction, the samples behave similarly except for the highest porosity sample that shows a lower value. In radial

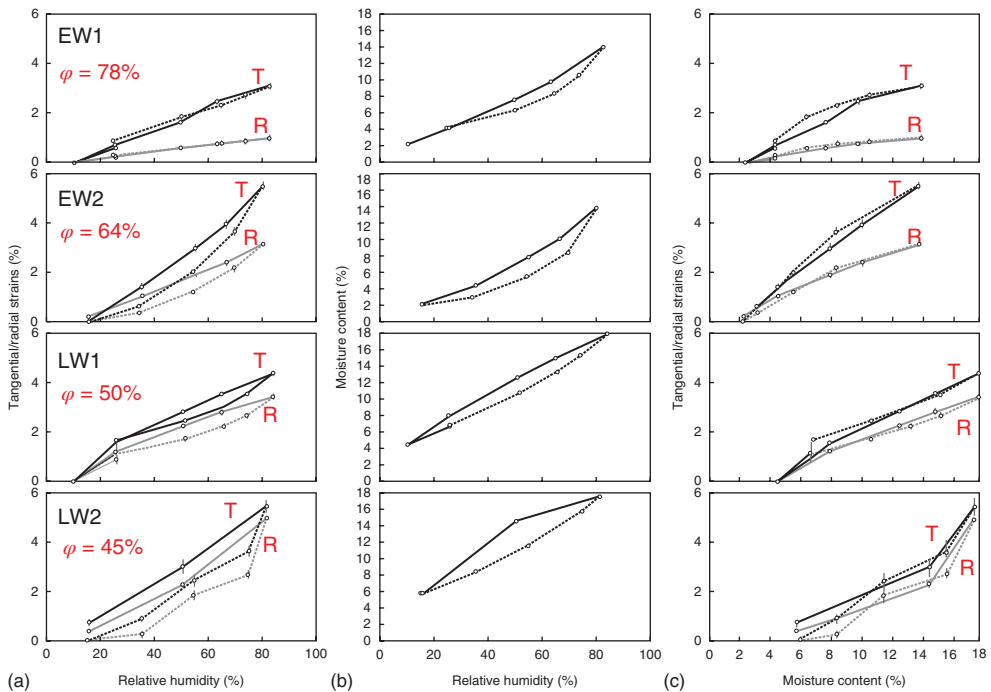


**Figure 7.3** (a) Strain versus RH in tangential (black lines) and radial (gray lines) directions for earlywood samples EW1 and EW2 and latewood samples LW1 and LW2. (b) Sorption curves for the four samples in moisture content versus RH. (c) Strain versus moisture content in tangential and radial directions for the four samples (from Patera *et al.* (2013) with permission from Elsevier).

direction, the highest porosity sample swells also much less than the other three. However, here the two middle porosity samples (64% and 50%) swell less than the lowest porosity one (45%). The magnitude of the swelling strains is generally higher in tangential than in radial directions, and much more so for the highest porosity sample. The ratios of tangential-to-radial swelling differences for the four samples, in the order of decreasing porosity, are 3.1, 1.7, 1.3 and 1.1. Figure 7.4 plots these ratios plus the tangential to radial ratios of the slopes in adsorption and desorption in function of porosity. These ratios are the slopes of the linear trend lines that fit plots of Figure 7.3, so each point considers the full hygroscopic range. It is clear that the anisotropy increases with the porosity, while a quasi-isotropic behavior is seen for the denser sample.

Coming back to Figure 7.3a, all samples clearly show hysteresis in swelling/shrinkage strains versus RH, except the one with highest porosity. We also observe that most strain–RH curves are closed loops, meaning that the starting and ending points of the respective adsorption and desorption coincide. The measurements display the expected reversibility of the sorption process.

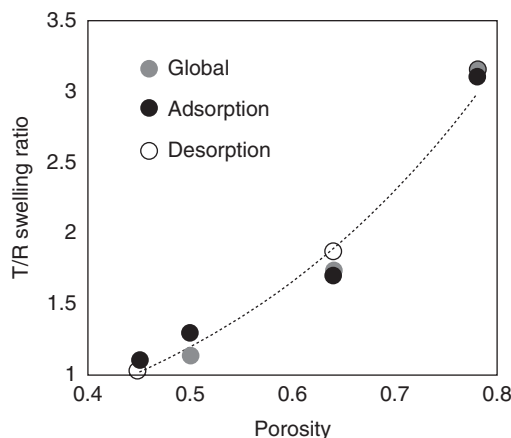


**Figure 7.4** Ratios of total tangential (T) to radial (R) strains versus porosity, in adsorption, desorption, and globally (adapted from Patera *et al*, 2013).

In addition, sorption isotherms were determined using a dynamic sorption apparatus, exposing the samples to the same steps of RH. All adsorption–desorption curves display a clear hysteresis of MC versus RH, as shown in Figure 7.3b. Going one step further, combining the two first columns, the radial and tangential strains are plotted in function of MC for all the samples, as shown in Figure 7.3c. In all plots, the swelling and shrinkage strain curves almost collapse on each other. Hysteresis is thus reduced, even more so in the radial direction where it vanishes. The plots of strains versus MC illustrate that, at the same MC, the swelling strains produced by the swelling of the cell wall is the same in adsorption or desorption. As it is the sorbed moisture that is at the origin of the deformation of the cellular structure, deformation which is quantified in swelling/shrinkage strains, it is logical that the same amount of moisture entering or exiting the cell wall material leads to the same deformation of the cell material. This means that the main origin of the hysteresis has to be sought in the sorption behavior and not in the swelling itself. Furthermore, in homogeneous wood tissues, the absence of hysteresis in the swelling strains in terms of the MC indicates that the MC history does not play a role in the current deformation state.

Moreover, we see that the strain–MC curves are quite linear over the total RH range with some small deviations. The slopes of linear trend lines that fit the strains versus MC plots provide the linear swelling coefficients. The swelling anisotropy ( $\beta_T/\beta_R$ ) confirms the anisotropic behavior in earlywood and the more isotropic behavior in latewood. For the clearly observed dependence of anisotropy on porosity, three explanations are considered:

- 1) At the cellular structure level, the presence of rays lying in the radial direction could also explain in part the anisotropy. Globally, all samples have the same number of rays, although EW1 has less stacks. The rays could restrain the



swelling of the thin-walled tissues. In contrast, the thicker S2 layer of the low porosity tissues results in a bulky tissue that could override the reinforcing effects of rays.

- 2) The wood sample with highest porosity, thus showing very thin cell walls, manifests the highest swelling anisotropy. As mentioned earlier, the cell wall is composed of a core, the S2 layer of varying thickness, bounded on both sides with restraining thin sheets, the S1 and S3 layers. Thus, the thin earlywood cells have very little S2 material compared to the other tissues. So the anisotropy of highly porous wood tissue may come from a stronger presence (in proportion) of the corseting action of the S1 and S3 layers. Conversely, the quasi-isotropy of the low porosity tissues may stem from the overriding presence of the S2 layer. This experimental result confirms previous studies.
- 3) To be more complete, a full discussion of the origin of anisotropy should also include the role of the cellular geometry and alignment, as wood structure is far from regular (disorder in alignment, in adjacency and in cell shapes) with earlywood cells that display a quasi-brick arrangement and the latewood cells, which are more like thick tubes change of paragraph. We pursue these two latter avenues using computer simulation using a surrogate cellular geometry.

## 7.5

### Parametric Investigation of Swelling of Honeycombs – Investigation by Hygroelastic Modeling

In an attempt to generalize the geometry of the wood cellular structure, we use a honeycomb structure. The basic geometrical features are the shape angle  $\theta$ , the aspect ratio  $\alpha$ , and the density ratio  $\gamma$ , which relate the height  $h$ , length  $l$ , and thickness  $t$ , as shown in Figure 7.5.

Using  $\theta$ ,  $\alpha$ , and  $\gamma$ , a domain of possible geometry can be mapped for symmetric honeycombs, as shown in Figure 7.6. From the analysis of wood geometry, it is concluded that wood geometry is confined to shape angles of  $0-30^\circ$ , aspect ratio

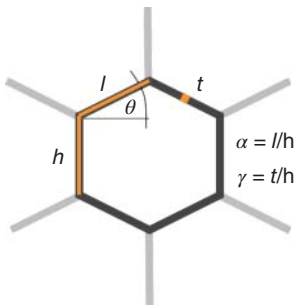


**Figure 7.5** Geometrical features used to describe honeycombs.



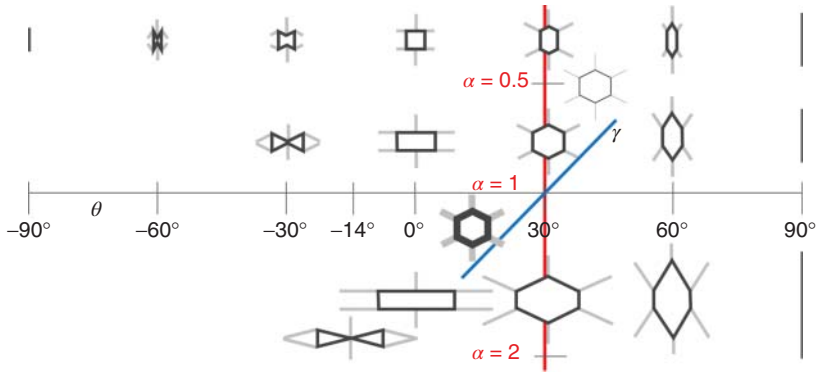


**Figure 7.6** Domain of possible geometry for symmetrical honeycomb structures. The axis variables  $\theta$ ,  $\alpha$ , and  $\gamma$  are defined in Figure 7.5.

of 0.5–2, and density ratio of 0.1–0.5. Recent simulation work indicates that part of the anisotropy may stem from the variety of layered structure, shape and wall thickness of the cells [21, 22]. We report some findings here.

#### 7.5.1

##### Simulation Methodology

We consider the wood cellular structure and accept to simplify it to a regular honeycomb, where the dimensions of one hexagonal cell are based on microscopy measurements. The hygroelastic constitutive equation of the linearly elastic solid with moisture-induced swelling is expressed as

$$\sigma_{ij} = C_{ijkl}(\epsilon_{kl} - \beta_{kl}\Delta m) \quad (7.2)$$

in which  $\sigma_{ij}$  and  $\epsilon_{kl}$  are, respectively, the second-order strain and stress tensors,  $C_{ijkl}$  is the fourth-order stiffness tensor,  $\beta_{kl}$  is the second-order tensor of hygroexpansion or swelling, and  $\Delta m$  is the change in MC in mass of water per mass of dry wood. The expression for moisture-induced swelling is formally similar to thermal expansion in which the MC plays the role of temperature. The cellular solids are composed of a network of connected struts and contain void space in between. If the struts in a cellular material are composed of homogeneous isotropic material, the macroscopic thermal or hygric expansion is the same as that of the solid from which it is made.

We describe the macroscopic behavior of periodic cellular solids with an energetically equivalent continuum following the micromechanics of solids [23]. An efficient computational upscaling scheme is devised in the finite element package ABAQUS (Rising Sun Mills, Providence, RI, USA) and the effective swelling coefficients of honeycombs are computed [22].

## 7.5.2

## Layered Cell Wall

We consider first that the cell wall is composed of three layers, where the material properties of each layer are assumed to be isotropic and where the internal and external sheath layers of the cells are assumed much stiffer than the cell wall core material. Despite the fact that experimental data for the transverse elastic properties of the wood cell wall are scarce in literature, given that reported values range between 1 and 10 GPa, we used  $E_c = 1$  GPa and  $E_s = 10$  GPa with an assumed Poisson's ratio of  $\nu = 0.3$  in our simulations. We look at swelling anisotropy considering the effects of the shape angle and of the thickness and stiffness of the sheaths. The results are presented in Figure 7.7. Looking at the swelling of two-sheath-layered

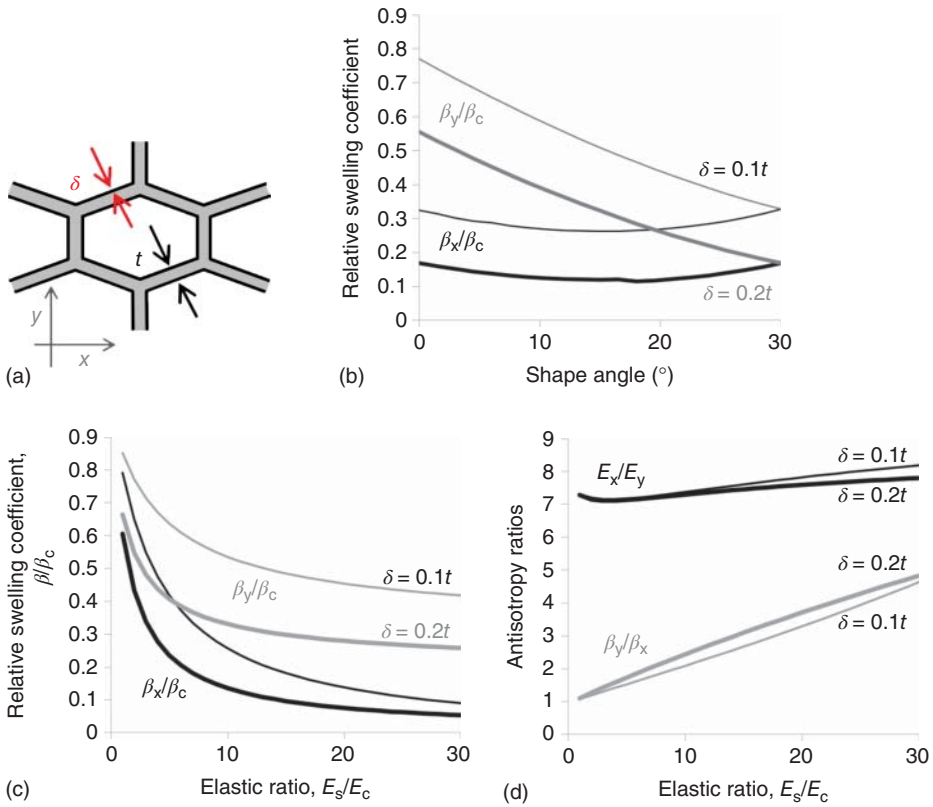


**Figure 7.7** Two-sheath-layered honeycomb. (a) Schematic representation of a honeycomb cell with the inner and outer sheaths have a width of  $\delta$ ; results for two thicknesses of the sheath layers, that is,  $d = 0.1t$  and  $d = 0.2t$ , where  $h = 1$ ,  $t = 0.1h$ . (b) Swelling coefficients, normalized to the core  $\beta_c$ , in function of

shape angle where sheath-to-core elastic ratio  $E_s/E_c = 10$ . (c) Swelling coefficients normalized to the core  $\beta_c$ , in function of  $E_s/E_c$ , where shape angle =  $15^\circ$ . (d) Anisotropy swelling and elastic ratios as function of  $E_s/E_c$ , where shape angle =  $15^\circ$  (adapted from Rafsanjani *et al*, 2013).

honeycomb with varying shape angle, we see that the swelling along the long axis of the cell, that is,  $x$ -direction, almost does not vary with shape, although the swelling in the perpendicular direction is drastically increasing with reducing shape angle. This is due to the progressive alignment of the top and bottom struts, as the hexagonal honeycomb becomes a rectangle, which let the middle layer, that form a more and more horizontal layer, as seen on Figure 7.7a, to swell in the  $y$ -direction with less and less restraining effects of the sheaths. The effect of the thickness of the sheaths is also displayed on Figure 7.7b, as thicker sheaths result in smaller swelling coefficients across the board. Considering how stiff the sheaths should be compared to the core to lead to some effects, Figure 7.7c illustrates that the swelling coefficients are very sensitive to stiffer sheaths, reducing dramatically as the ratio of elastic constant of the sheaths to the  $E$  of core increases by about 10, after which ratio this decreasing effect is much less perceptible. In addition, Figure 7.7d shows that the anisotropy of the swelling coefficients increases quasi-linearly with increasing the sheath to core elastic constants ratio, independent of the thickness ratio of the sheaths. It is worth noting that, for the same variation, the anisotropy of the elastic properties of the honeycomb is quite constant. It is therefore demonstrated that one manner to increase the swelling anisotropy is to increase the stiffness of the sheaths of a multilayer honeycomb structure.

The two-sheath layered model used above is a simplification of the multilayered system that is present in wood. To verify the effect of this simplification, we compare the behavior of honeycombs where the cell wall has three different configurations: with a single sheath in its middle, with both inner and outer sheaths, and with the three sheaths, that is, inner, middle, and outer, as depicted in Figure 7.8d. Considering more layers has almost no effect in the  $x$ -direction for the thin sheaths and has little effect when the sheaths are thicker, Figure 7.8a,b. In the  $y$ -direction, increasing the number of sheaths restrains more and more swelling, and more so at lower shape angle. The different honeycomb structures behave very similarly at shape angle close to the regular hexagon. At lower shape angle and only for the  $y$ -direction, the swelling behavior becomes increasingly different. In terms of anisotropy, as shown in Figure 7.8c, the shape angle has the most impact. However, doubling the thickness of the sheaths results in an increase in the anisotropy by  $\sim 50\%$  for shape angles of more than  $10^\circ$ . The number and position of the sheaths have a less but still interesting effect. A single middle layer sheath results in less swelling anisotropy than a pair of inner and outer sheaths. This is undoubtedly due to the continuous nature of this superposed stiff web, while in the double sheaths scheme, it is the soft core that is continuous. Considering this, it is not surprising that the anisotropy of the three-sheath-layered configuration lies in between the anisotropy of the other two configurations. Thus, the number of layers and their respective configuration can further modulate the anisotropic swelling behavior of honeycomb structures.

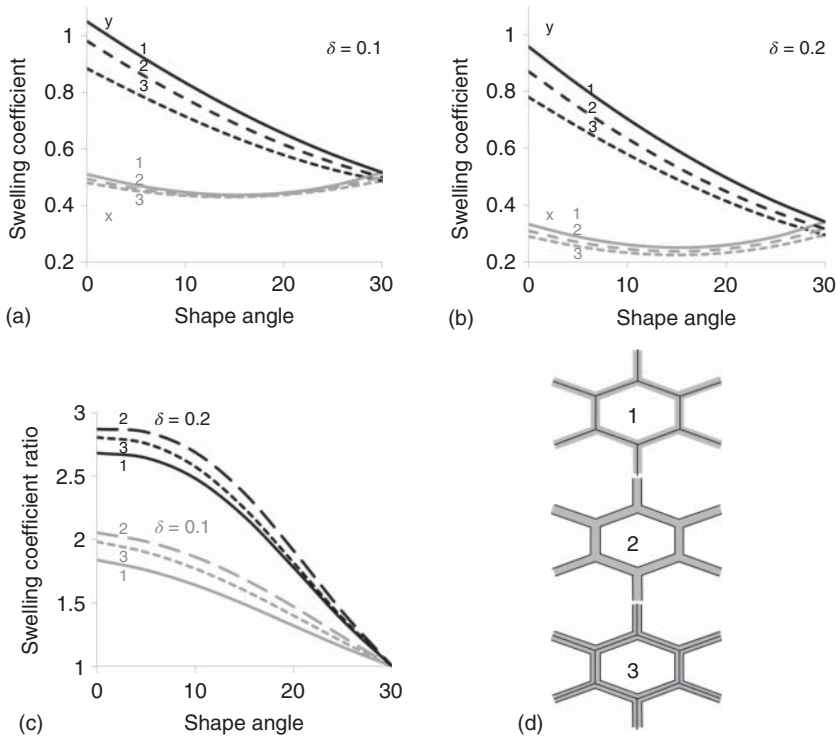


**Figure 7.8** Comparison for single-, two-, and three-sheath-layered honeycomb of the swelling coefficient normalized to the core  $\beta_c$  in function of shape angle where  $h = 1$ ,  $t = 0.1h$ , and sheath-to-core elastic ratio  $E_s/E_c = 10$  (a) in the x-direction and

y-direction for inner and outer sheaths of thickness  $d = 0.1t$ ; (b) in the x-direction and y-direction  $d = 0.2t$ ; (c) anisotropy swelling ratios; and (d) schematic representation of a single-, two-, and three-sheath-layered honeycomb.

### 7.5.3

#### Effects of Geometric Variations

In the previous section, the role of the sheath layers has been demonstrated. Continuing with simulation, we now look at the role of geometry of the honeycomb structure as a source of anisotropy in its swelling behavior. We use a single-layer cell wall with varying anisotropic material properties as a surrogate multilayered cell wall. We vary the shape angle of the honeycomb structure for three basic cell configurations: a high porosity elongated cell, a median porosity even-proportioned cell, and a low porosity stocky cell the configurations together with all the results are presented in Figure 7.9.

The shape angle is once again found to have a strong effect on the swelling coefficient in the y-direction, more as porosity increases. The swelling coefficients in the x-direction display all slightly concave curves with slightly lower swelling

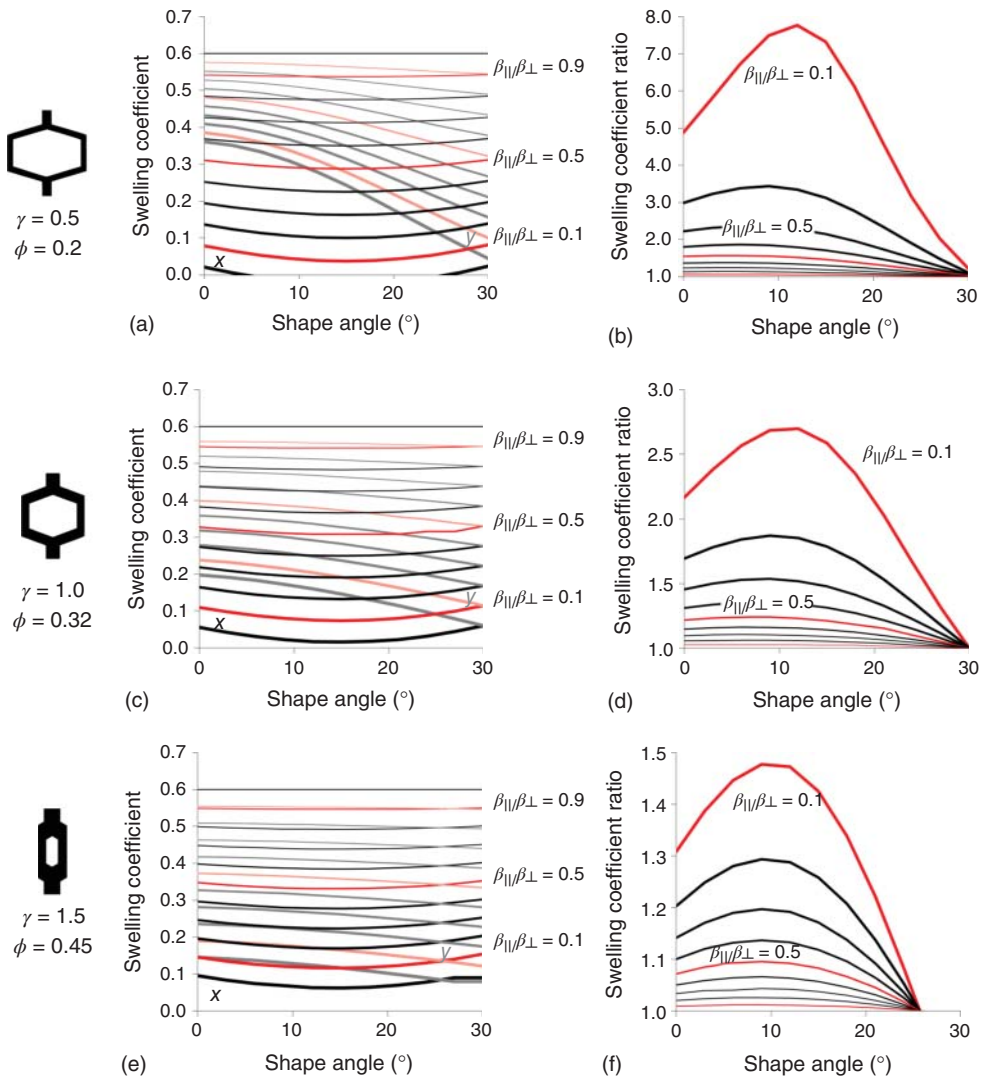


**Figure 7.9** A: (a,c,e) Swelling coefficients in the x-direction and y-direction versus shape angle for different anisotropy of the swelling coefficient of the cell wall. B: (b,d,f) Swelling

coefficient ratios for the same and for three basic cells from high porosity at the top to low at the bottom.

coefficients for shape angle between 10° and 20° and become larger as porosity decreases. The resulting swelling coefficient ratios are strongly dependent on shape angle when the anisotropy of the cell material is increased. The magnitude of the anisotropy is most influenced by the configuration of the cells, as the stocky cell shows here a maximum anisotropy of a bit less than 1.5, the evenly proportioned cell gets to 2.7, while the light elongated cell almost reaches 8 for the same

ratio of cell material anisotropy and similar shape angle. Despite the important effect of the shape angle, it seems that the basic cell configuration has the most effect on the capacity to display swelling anisotropy.

The above exploration of the domain of possible geometry and the respective effects of different parameters on the capacity of honeycomb to swell and to display anisotropic swelling has been inspired by wood, but could be expanded to the full space domain as represented in Figure 7.6.

## 7.6

### Beyond Recoverable Swelling and Shrinkage: Moisture-Induced Shape Memory

As a note before concluding this chapter, we bring up two series of observations made by exposing wood samples to different RH and imaging with srPCXTM as presented at the beginning of the chapter. The first series documents a cell that was situated at the corner of the sample (see Figure 7.10a). Imaged at a RH of 25% RH, the cell is initially partly collapsed and sheared due to the sample cutting. As the cell is exposed to air with higher relative humidity, sorption takes place, but more interestingly, in addition to general swelling discussed so far in this chapter, some large deformations take place and the cell realigns with its neighbor to a configuration that is apparently close to the original one before cutting. Furthermore, upon drying, this reacquired shape persists. Thus, beyond swelling, the cell has also shape memory capacity. In Derome *et al.* [24], we saw that this capacity is also found for rows of cells and for a half-cell that closes during drying, as shown in Figure 7.10b. The latter case then indicates that, at least, part of the shape memory capacity lies not at the cellular scale, but at the subcellular scale, that is, the organization of the cell wall material. Further probing on the role of the polymeric organization and specially of the stiff cellulose microfibrils would thus seem to

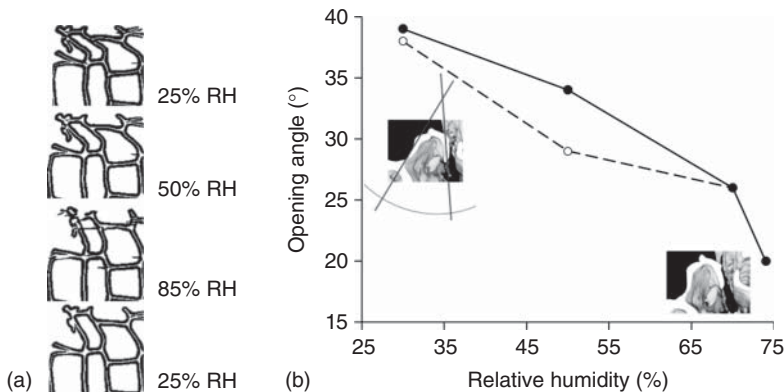


**Figure 7.10** Wood samples exposed to increasing and then decreasing relative humidity: (a) segmented tomographic slice of the corner cells of a wood sample; (b) angle

of opening of a half-cell during adsorption, in continuous line, and in desorption, in dash line.

provide a more complete portrait of the moisture-induced deformation of cellular structures.

## 7.7

### Discussion

#### 7.7.1

##### On the Origin of Hysteresis of Sorption as a Function of Relative Humidity

The RH in the air is a yardstick of the energy level of the water molecule in air, namely, its chemical potential ( $\mu$ ), as  $\mu \cong \ln(\text{RH})$ . We can thus use the chemical potential ( $\mu$ ) to discuss the state of energy of the water molecules in the air or in adsorbed state. The sorption of a water molecule on a sorption site requires a certain chemical potential,  $\mu_0$ , as sorption is achieved via hydrogen bonding and where 0 refers to stress-free conditions such as occurring in free swelling. So if sorption and desorption would occur at  $\mu_0$ , it would occur at the same RH of the ambient air and no hysteresis would be observed. This is not the case for wood cellular tissues, as shown in Figure 7.3a.

We can thus consider that the chemical potential at adsorption and desorption is different, that is,  $\mu_a \neq \mu_d$ . Our hypothesis is that internal strain/stress resulting from sorption play a role in hysteresis. The sorption sites in the material may be considered to be stretched by the neighboring sorption sites being filled by water molecules. This stretching makes the sites to adsorb extra water molecules more easily. So the chemical potential at which the sorption site fills depends also on the strain, and the chemical potential for sorption can be thus taken as  $\mu = \mu_0 + \lambda \epsilon$ , where  $\lambda$  is coupling factor and  $\epsilon$  the local strain. In reverse, desorption occurs only when sufficient shrinkage occurs around the sorption site to make it spatially untenable and make desorption desirable. The difference of forces induced by swelling and shrinkage is thus reflected by the difference of chemical potential required for adsorption and desorption, which is actually the difference in RH to obtain the same MC in a sorption loop [25].

The presence of the hysteresis loop in the sorption isotherms is a typical experimental observation for hygroscopic materials. Such hysteresis can be understood to be the results of different mechanisms: capillary condensation, fluid–fluid interactions, or fluid–solid interaction. Swelling of wood clearly belongs to this last category, with fluid–solid interaction at the origin of the hysteretic swelling behavior, interaction which has been ascribed formally in the preceding paragraph in this  $\lambda$  factor.

#### 7.7.2

##### On the Effects on Moisture Sorption

The graphs of Figure 7.3c demonstrate that a change of MC results in a proportional change in strain. We mentioned that the absence of hysteresis in these



strain–MC curves indicates that cell wall reconfiguration due to shrinkage and swelling is found to be independent of MC history. Swelling is almost linearly related to MC, although the sorption curve and the dependence of stiffness on RH are not linear. In fact, the stiffness reduces with MC while the moisture capacity, also referred to as the *Biot modulus*, increases with MC. It results that these two variations compensate the influence of each other, resulting in a linear swelling behavior, where high MC can be reached in part due to the mechanical softening of the material. Such observation highlights how swelling results from the pressure induced by the presence of moisture within the anisotropic nanoporous materials of the cell walls. A further consideration would be to study the dynamics of the honeycomb swellings.

Although the process rate is controlled by diffusion, it would be interesting to study whether the long time required to achieve equilibrium is mainly due to diffusion, or whether to the actual deformation process as the water molecules require sometime to push apart the cell wall constituents. The deformation process might also have a role to play in the higher magnitude of hysteresis observed in lower porosity cellular structures.

### Acknowledgment

The authors are grateful for the financial support of the Swiss National Science Foundation (SNF) under Grant No. 125184. Prof. Dr. Marco Stampanoni (ETHZ and Paul Scherrer Institute) is greatly acknowledged. The experiments were carried out at the TOMCAT beamline of the Swiss Light Source, Paul Scherrer Institute, Villigen, Switzerland, with the help of beamline scientist Dr. Rajmund Mokso. Finally, we acknowledge Dr. Michele Griffa, Dr. Matthias Kobel, Dr. Pavel Trtik, and Dr. Hannelore Derluyn, for their participation in the data acquisition and specially Roger Vonbank and Stephan Carl for their precious technical support to carry out the experimental work.

### References

1. Xu, P., Donaldson, L.A., Gergely, Z.R., and Staehelin, L.A. (2007) Dual-axis electron tomography: a new approach for investigating the spatial organization of wood cellulose microfibrils. *Wood Sci. Technol.*, **41**, 101–116.
2. Fahlén, J. and Salmén, L. (2005) Pore and matrix distribution in the fiber wall revealed by atomic force microscopy and image analysis. *Biomacromolecules*, **6**, 433–438.
3. Bernsen, J. (1986) Dynamic thresholding of grey-level images. Proceeding of the 8th International Conference on Pattern Recognition, Paris, France, pp. 1251–1255.
4. Salmén, L. (2004) Micromechanical understanding of the cell-wall structure. *C.R. Biol.*, **327**, 873–880.
5. Salmén, L. and Burgert, I. (2009) Cell wall features with regard to mechanical performance. A review COST Action E35 2004–2008: wood machining – micromechanics and fracture. *Holzforschung*, **63**, 121–129.
6. Fengel, D. and Stoll, M. (1973) Variation in the cell cross-sectional area, cell-wall thickness and wall layers of



- spruce tracheids within an annual ring. *Holzforschung*, **27** (1), 1–7.
7. Zillig, W. (2009) Moisture transport in wood using a multiscale approach. PhD Thesis. KU Leuven.
  8. Hernandez, R.E. (1993). Influence of moisture sorption history on the swelling of sugar maple wood and some tropical hardwoods. *Wood Sci. Technol.*, **27**, 337–345.
  9. Murata, K. and Masuda, M. (2001) Observation of the swelling behaviour of coniferous cells using a confocal scanning laser microscope and digital image correlation method. *Mater. Sci. Res. Int.*, **7**, 200–205.
  10. Gu, H., Zink-Sharp, A., and Sell, J. (2001) Hypothesis on the role of cell wall structure in differential transverse shrinkage of wood. *Holz Roh Werkst.*, **59**, 436–442.
  11. Ma, Q. and Rudolph, V. (2006) Dimensional change behavior of Caribbean pine using an environmental scanning electron microscope. *Drying Technol.*, **24**, 1397–1403.
  12. Sakagami, H., Matsumura, J., and Kazuyuki, O. (2007) Shrinkage of tracheid cells with desorption visualized by confocal laser scanning microscopy. *IAWA J.*, **28**, 29–37.
  13. Derome, D., Griffa, M., Koebel, M., and Carmeliet, J. (2011) Hysteretic swelling of wood at cellular scale probed by phase-contrast x-ray tomography. *J. Struct. Biol.*, **173**, 180–190.
  14. Patera, A., Derome, D., Griffa, M., and Carmeliet, J. (2013) Hysteresis in swelling and in sorption of wood tissue. *J. Structural Biology*, **182**, 226–234.
  15. Ando, M. and Hoyosa, S. (1972) in *Proceedings of the 6th International Conference of X-ray Optics and Microanalysis* (eds G. Shinoda, K. Kohra, and T. Ichinokawa), University of Tokyo Press, Tokyo, pp. 63–68.
  16. Momose, A., Takeda, T., and Itai, Y. (1994) Phase-contrast X-ray computed-tomography for observing biological specimens and organic materials. *Proceedings of 5th International Conference on Synchrotron Radiation Instrumentation*, Stony Brook, NY, July 18–22, pp. 1434–1436.
  17. Schmahl, G., Rudolph, D., Schneider, G., Guttman, P., and Niemann, B. (1994) Phase-contrast x-ray microscopy studies. *Optik*, **97**, 181–182.
  18. Bronnikov, A.V. (1999) Reconstruction formulas in phase-contrast tomography. *Opt. Commun.*, **171**, 239–244.
  19. Bronnikov, A.V. (2002) Theory of quantitative phase-contrast computed tomography. *J. Opt. Soc. Am. A*, **19**, 472–480.
  20. Pieper, S., Halle, M., and Kikinis, R. (2004) 3D SLICER. *Proceedings of the 1st IEEE International Symposium on Biomedical Imaging: From Nano to Macro*, pp. 632–635.
  21. Rafsanjani, A., Derome, D., Wittel, F.K., and Carmeliet, J. (2012) Computational up-scaling of anisotropic swelling and mechanical behavior of hierarchical cellular materials. *Compos. Sci. Technol.*, **72** (6), 744–751.
  22. Rafsanjani, A., Derome, D., and Carmeliet, J. (2013) Micromechanics investigation of hygroelastic behavior of cellular materials with multi-layered cell walls. *Compos. Struct.*, **95**, 607–611.
  23. Hill, R.J. (1963) Elastic properties of reinforced solids: some theoretical principles. *J. Mech. Phys. Solids*, **11**, 357–372.
  24. Derome, D., Rafsanjani, A., Patera, A., Guyer, R., and Carmeliet, J. (2012) Hygromorphic behaviour of cellular material: hysteretic swelling and shrinkage of wood probed by phase contrast X-ray tomography. *Phil. Magazine*, **92**, 3680–3698.
  25. Guyer, R., Kim, A., Derome, D., Carmeliet, J., and TenCate, J. (2012) “Hysteresis in modeling of poroelastic systems: Quasistatic equilibrium”. *Physical Review E*, **83** (6), 061408.

## 8

### Hydro-Actuated Plant Devices

*Khashayar Razghandi, Sebastien Turcaud, and Ingo Burgert*

#### 8.1

##### Introduction

In terms of movement, plants are commonly the last to come to mind because plants, in general, are reflected to be stationary living organisms and are not as much known for their ability to move in a detectable timescale for human eyes. Nevertheless, movement is an essential part of a plant life from movement associated with plant growth to acquiring nutrition, spatial reorientation, fixation, seed dispersal, defense, and so on [1, 2]. To satisfy such needs, plants have evolved a variety of mechanisms for stress generation and organ movement actuation. In all stress generation or movement-related mechanisms, water plays a crucial role. The interaction of water with the plant material at the nanoscale of cells and cell walls can be controlled and transferred to the macroscale through a sophisticated structural design at different hierarchical levels of plants, comprising the cell wall composition and architecture, cell size and shape, and tissue structure up to the organ [1].

Two general principles of plant–water interactions that induce stresses and plant movements can be distinguished. On the one hand, the active variation of the volume of the living plant cells due to water influx/efflux is achieved by an increase in the cell inner pressure [3–9]. On the other hand, in terms of dead cells with a thick and rigid cell wall, swelling/shrinkage of the cell wall leads to the generation of internal stresses or organ movements. In both cases, the structural information necessary for passive actuation is embedded at different hierarchical levels of the system that allows even dead organs to be actuated by various environmental stimuli to perform a targeted deformation or movement. As a result, these latter systems are independent of any control or energy input from the plant metabolism [10, 11]. Spatial adjustment of the organs such as leaning of stems and branches is a widespread example of slow movements [12–16], while opening and closing of pine cone scales [10] or moisture-dependent bending of wild wheat awns [11] are examples of relatively faster passive hydro-actuated deformation. Some plants such as Venus flytrap combine a turgor pressure-based mechanism with geometrical instabilities to go beyond the speed limitation of fluid transport

and perform much faster movements as the so-called snap-buckling movements [4, 17, 18]. Other plants developed an explosive seed dispersal strategy through which the release of the stored elastic energy is accompanied by sudden rupture of pre-stressed tissues [19].

Skotheim and Mahadevan have categorized different plant movements according to their speed in three basic groups (Figure 8.1) [20]. The slow deformations limited by the speed of fluid transport categorized as swelling/shrinking movements can be found above the dotted line. The relatively faster deformations are based on the storage and sudden release of elastic energy via geometrical constraints and are shown in between the dotted line and above the limit of the

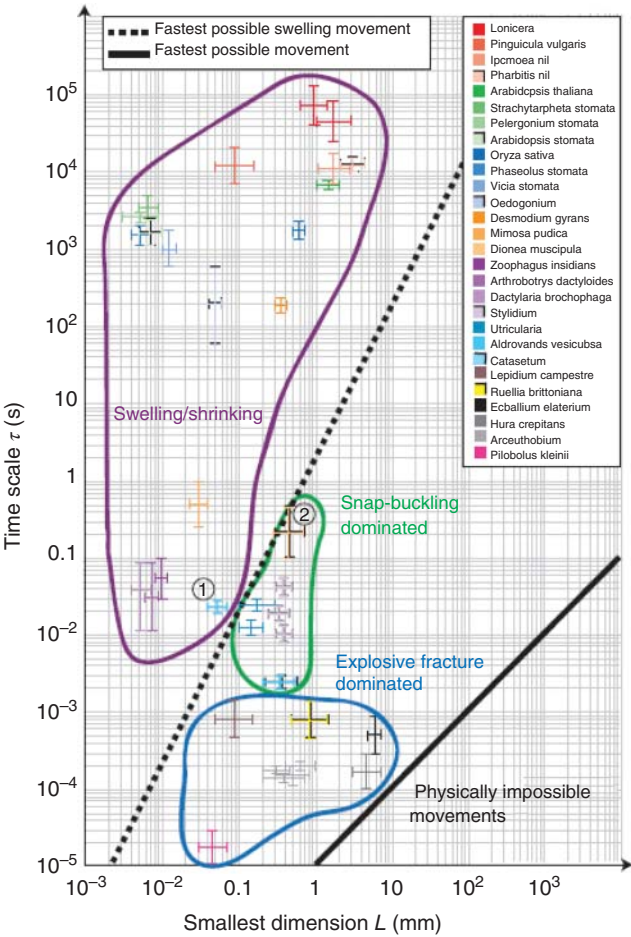


**Figure 8.1** Classification of plant and fungal movements. The duration of the movement ( $t$ ) is plotted against the smallest macroscopic dimension of the moving part

( $L$ ). (Reprinted from Ref. [20] with permission. Copyright by American Association for the Advancement of Science.)

physically possible movements. The two subcategories of the fast movements, snap-buckling and explosive fracture, are only different in the mechanism of how the stored energy is released.

In this chapter, we will review the basic physiochemistry and mechanics of how water can be utilized as an “engine” for stress generation and movement. First, the general aspects of a mechanical response of a material are introduced, followed by some reflections on the water–plant material interactions. Next, the underlying structural and physiochemical principles of plant hydrodriven movements and stress generation strategies will be discussed by going through some well-known examples.

## 8.2

### General Aspects of Plant Material–Water Interactions

#### 8.2.1

##### Principle Mechanics: Stress and Strain

In the context of plant movements, two fundamental notions are introduced, stress that accounts for the interior forces within the solid body and strain as a measure of deformation. Unlike most fluids in hydrostatic equilibrium, solids are capable of not only transmitting forces normal to their surfaces but also tangential forces. The magnitude of these forces may also depend on the loading direction as happens, for instance, when a body is stretched along one particular direction. The well-known notion of hydrostatic pressure for fluids has, therefore, been extended to solids to account for the so-called shear stress and also for possible anisotropy of stress. Deformation characterizes the change of size and shape of a body and describes how the relative positions of neighboring points change in terms of distances and angles. As with stresses, changes in distances are called normal strains while changes in angles are called shear strains. These notions of stress and strain are quite rich as their magnitude usually varies inside the object (heterogeneity) and may also be different in various directions (anisotropy). Without going into technical details, the current mechanical state of a solid is locally represented by three normal stresses (and associated strains) and three shear stresses (and associated strains). Stress has the dimension of a pressure (Newton per square meter or Pascal) and corresponds to a force divided by a reference area, while strain is dimensionless and corresponds to a length divided by a reference length. As the amount of deformation varies, different variants of stress and strain can be defined mainly depending on the choice of reference state. If the deformed state is not too far from the undeformed state, then the so-called engineering stress and strain are used where the reference state is simply the undeformed state. In the following, engineering stress and strain will be used. For small strains, most materials are linear elastic (Hook’s law) meaning that the normal stress is proportional to the normal strain and that the deformation is reversible. The coefficient of proportionality is called the Young

modulus and characterizes the stiffness of the material or its resistance to elastic deformations. Some materials such as rubber stay actually elastic for a wider range of strains, but the relation between stress and strain is no longer linear. The two normal strains perpendicular to the pulling direction have to be considered as the cross section becomes thinner upon stretching of the material. This is expressed by the Poisson's ratio defined as the negative ratio of the transverse strain and the longitudinal strain.

Once the so-called yield strength is reached, deformation is no longer reversible and the material deforms plastically. If unloaded, the elastic deformation will go back, but plastic strains will remain. Finally, at a sufficient strain, fracture occurs and the body is no longer a continuum.

Natural materials are often half-solid and half-fluid, so they sometimes display some fluid properties such as viscosity. This implies that the mechanical response may also depend on the loading rate. Such time dependency can be seen for instant in creep behavior, which describes the tendency of a material to deform under a constant stress over time. This behavior in addition to the hierarchical nature of biological materials makes it both nontrivial and challenging to characterize them.

## 8.2.2

### **Water as an Engine**

Water can work as an engine in various ways. The well-known example of water mills shows how flow of a liquid can be harvested to produce a desired movement. But in addition to that, water can also be utilized as an inflating or swelling media to generate stresses or movements in plants. Inflation is defined as a change in the volume of a confined geometry due to the variation of pressure of the gas/liquid inside the cell, while swelling is referred to the changes in the volume of a porous material due to the adsorption of a liquid into the solid body.

Water possesses a large dipole moment that enables it to participate in a wide range of reactions from acid–base reactions to the ability to build up hydrogen bonds with itself and with other available solutes. The energy of a hydrogen bond lies in between the strong covalent bonds and relatively loose van der Waals forces, which gives it a perfect compromise to have a degree of dynamics as well as stability. Its ability to form hydrogen bonds with a large variety of biomolecules makes water a crucial media for evolution of life and many of its fascinating features.

#### 8.2.2.1 Inflation

Water can work as an engine when filling a thin-walled cell (sphere, cylinder, etc.). Changes in water pressure inside such confined geometry can exert stress on the walls. The generated stresses in the walls of a sphere or cylinder are illustrated in Figure 8.2.

The hoop or tangential stress equilibrates the internal pressure that can be due to water uptake in the cell. The expressions are derived simply by balancing the

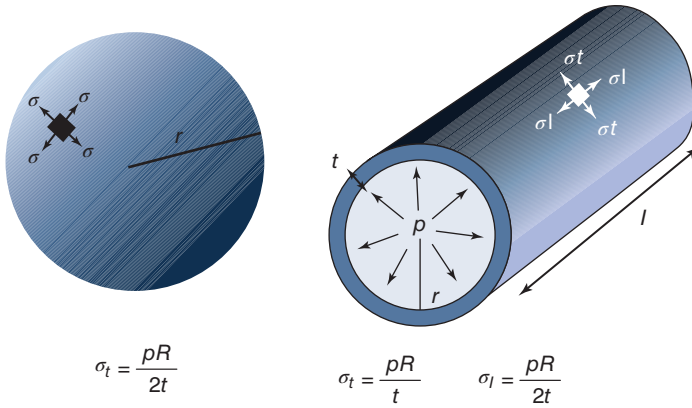


**Figure 8.2** Inflation. Variation in the pressure of a gas–liquid inside a close sphere or cylinder leading to the generation of stress in the cell walls.

pressure with the hoop stress in a cylinder or a sphere:

$$\text{for a sphere : } \sigma_t = \frac{pR}{2t} \quad (8.1)$$

$$\text{for a cylinder : } \sigma_t = \frac{pR}{t} \quad \sigma_l = \frac{pR}{2t} \quad (8.2)$$

where  $P$  is the internal pressure,  $R$  is the radius,  $t$  is the thickness of the cylinder or sphere, and  $\sigma_t$  and  $\sigma_l$  are the hoop stress and longitudinal stress, respectively.

Depending on the mechanical properties of the wall, the generated stresses can result in reversible or irreversible inflation/deflation of the volume. This principle is utilized by plants to change the volume of living cells via active changes of the pressure inside the cell to introduce irreversible (growth) or reversible (pre-stress) increase in the cell volume.

The water potential in the cells ( $\Psi$ ) is a determining factor for the volume change of living cells:

$$\Psi = \frac{\mu - \mu^*}{\bar{V}_w} \quad (8.3)$$

with  $\mu$  being the chemical potential of the solution,  $\mu^*$  the chemical potential of the pure water, and  $\bar{V}_w$  the water molar volume [21].

Active delivery of the solutes through the cell membrane results in lower water potential. Cell turgor pressure ( $P$ ) is related to water potential ( $\Psi$ ) and osmotic pressure ( $\Pi$ ) as follows:

$$\Psi = P - \Pi \quad (8.4)$$

As a result, an increase in osmotic potential of the cells results in a decrease in water potential. To maintain the equilibrium, water flows into the cells. The result can be a reversible or irreversible change of cell volume, depending on cell wall properties [21].

Plant movements can be based on irreversible plastic deformation and volume changes of the cells during growth processes and on reversible elastic deformation of the cells due to changes in cell turgor pressure, which will be discussed in Section 8.3.

#### 8.2.2.2 Swelling

Swelling phenomena refer to the uptake of a liquid by a solid that causes the solid dimensions to change while maintaining the macroscopic homogeneity. Flory–Huggins theory describes the swelling pressure ( $\Pi$ ) for a polymer–liquid solution and its relation to the Gibbs’ free energy of mixing  $\Delta G_{\text{mix}}$  as [22–24]:

$$\Pi = -\frac{\partial \Delta G_{\text{mix}}}{\partial V} + \Pi_{\text{el}} = -\frac{RT}{V_s} \left( \ln(1 - \nu) + \left(1 - \frac{1}{r}\right) \nu - \chi \nu^2 \right) + \Pi_{\text{el}} \quad (8.5)$$

The  $\Pi_{\text{el}}$  term corresponds to the counteracting elastic force associated with elastic expansion of the polymer chains, the  $-\chi \nu^2$  part corresponds to the enthalpic term, and the  $\ln(1 - \nu) + \left(1 - \frac{1}{r}\right) \nu$  part represents the entropic contribution, where  $V_s$  is the solvent molar volume,  $\chi$  is the apparent interaction parameter depending on the specific properties of the particular polymer–liquid mix,  $r$  is the number of repeating unit in a polymer chain,  $\nu$  is the polymer volume fraction,  $R$  is the gas constant, and  $T$  is the absolute temperature.

According to Flory–Huggins theory, the water uptake and swelling of polymer networks, in general, can be described as a three-step process: in the first step, water molecules hydrate the most polar hydrophilic groups and form the first “primary bound” water layers. Then the water molecules interact with more hydrophobic groups to make the secondary bound water. These two enthalpy-driven steps form the total bound water. In these stages, the interaction parameter  $\chi$  defines the affinity of a polymer to water and is related to the polymer solubility parameters. Hansen described the solubility of a solute in a solvent in three distinct parts: a nonpolar part coming from the energy of dispersion bonds between molecules ( $\delta_d$ ), a polar part showing the energy from dipolar intermolecular force ( $\delta_p$ ), and a component representing the energy from hydrogen bonds between molecules ( $\delta_h$ ) [24]. Total solubility parameter  $\delta_T$  is expressed as follows:

$$\delta_T^2 = \delta_h^2 + \delta_p^2 + \delta_d^2 \quad (8.6)$$

In the final step, when all bonding sites are occupied by bound water, the main mechanism for further water uptake is entropy-driven with the entropy of the mixing being related to polymer volume fraction ( $\nu$ ) and number of repeating units in polymer chains ( $r$ ) [22, 23]:

$$\Delta S_{\text{mix}} = -R \left[ \ln(1 - \nu) + \left(1 - \frac{1}{r}\right) \nu \right] \quad (8.7)$$

The adsorbed water at this stage fills mainly the spaces between the network chains and centers of larger pores, macro pores, and voids. The infinite dilution at this stage is restricted by counteracting force because of the associated elastic expansion of the hydrogel network, and swelling continues only to the point



at which the entropic gain of the mixing and the elastic entropy of the network reach an equilibrium level. The plant cell wall is a relatively dense network of various macromolecules, thus its swelling can also be described as water uptake in a composite of polymeric chains.

### 8.2.3

#### Plant Cell Walls

Growing plant cells possess a so called primary cell wall. Beside protecting the cell against environmental factors, it also determines the structural support and shape of the cell [46–48]. Plant cell walls are a complex composite of various macromolecules. The architecture can be described as a fiber-reinforced composite, where stiff cellulose microfibrils are embedded in a much softer matrix that consists of hemicelluloses, pectin or lignin [25–33]. The microfibrils are formed and extruded into the cell wall by complex “machines” called cellulose synthase complexes [34]. A cell can control the direction of the cellulose deposition via its cytoskeleton (cortical microtubules) that guides the movement of the cellulose synthase complexes along the plasma membrane [35–38]. Natural cellulose (cellulose I) is a linear chain of (1,4)-linked  $\beta$ -D-glucan, which can be found in various organisms such as higher plants, algae, and so on. It is basically a composite of two polymorphs, I $\alpha$  and I $\beta$ , which can coexist at different ratios, with I $\beta$  being the more dominant polymorph in the cell walls of higher plants [39]. The intermolecular hydrogen bonding and van der Waals forces between the neighboring chains result in a packing of the cellulose chains into relatively ordered aggregates [40]. These cellulose fibrils are paracrystalline consisting of crystalline regions with highly ordered parallel arrangement of cellulose chains and more disordered amorphous regions. Depending on the species, fibrils can possess a diameter of 3–5 nm [41]. Their exact length is not yet clear, but fibrils are probably long enough to spiral around the circumference of a cell. Covalent bonds between the sugar units along the chain and the dense network of hydrogen bonds in and in between the chains result in a high stiffness of the fibrils in the axial direction [41].

The space between the microfibrils is filled with a more pliant matrix forming repeating lamellae [42]. Hemicelluloses are one of the main building blocks of the matrix. Their main role is to work as cellulose-binding agents, forming a strong yet resilient network with cellulose fibrils on the basis of hydrogen bond formation. These polysaccharides consist of various sugar units but have almost the same hygroscopicity as amorphous cellulose. Lignin is another constituent of the cell wall matrix which contains different phenyl groups making the macromolecule more hydrophobic than the other constituents. Pectins make up a complex and heterogeneous family of water-soluble structural polysaccharides which provide a relatively flexible matrix for the cellulose–hemicellulose network and play a crucial role in the extension of the primary cell wall during cell growth. In combination with lignin, they are among the main constituents of the middle lamella



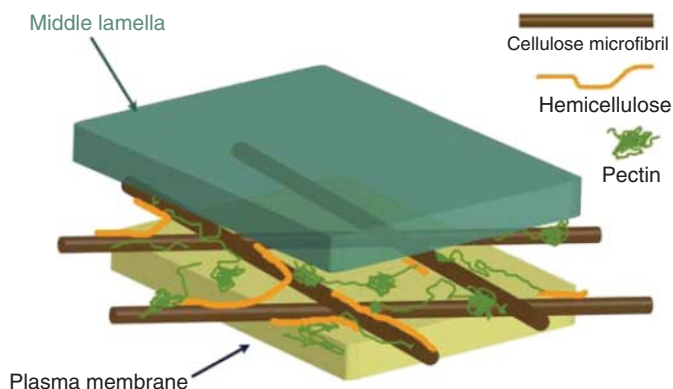


**Figure 8.3** Simple schematic of the structure and composite of the primary cell wall. Cellulose microfibrils are embedded in a relatively soft polymeric matrix of hemicellulose and pectin. To allow for plastic deformation

as a consequence of turgor-driven cell growth, primary cell walls should be rather pliant and must be able to loosen some of the load-bearing linkages between the fibrils while bearing the inner pressure load.

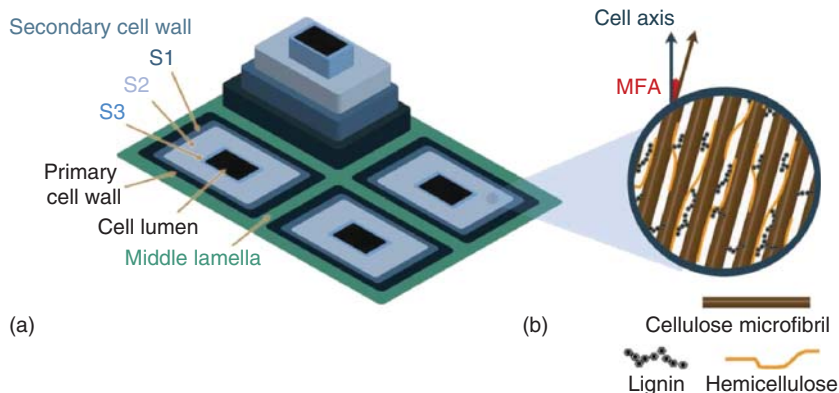


**Figure 8.4** Simple schematic of wood cell wall architecture and composition. Primary cell wall and different layers of the secondary cell wall (S1–S3) are depicted schematically separating the cell lumen (black) from the intercellular middle lamella (green). Hemicelluloses and lignin work as a cross-linking

and filling agent in the secondary cell wall, respectively, connecting and separating the cellulose fibrils from each other. The fibril angle toward the cell axis is known as microfibril angle (MFA) and is one of the crucial factors determining the anisotropy of the cell wall swelling (right).

between the cells gluing the neighboring cells together (Figure 8.3) [27–29, 31, 32, 41, 42].

Secondary cell walls, have a distinct lamellar structure with a specific arrangement of cellulose fibrils (Figure 8.4). The angle between the microfibrils and the cell wall axis is known as microfibril angle (MFA) and is an important parameter in defining the mechanical and swelling properties of the cell wall as a whole. S1 and S3 being the inner and outer layers of the secondary cell wall in wood have a

relatively large MFA almost perpendicular to the cell axis. The middle layer (S2) is the thickest and dominant layer, determining the stiffness and the anisotropy of the cell wall. In cell walls of “normal” wood, cellulose fibrils are oriented almost parallel to the cell axis (MFA 0–10°) while specific reaction tissues in trees such as compression wood can possess an MFA up to almost 60° [1, 43–45].

The matrix–microfibrils interaction is an important determining factor in cell wall properties as the mechanical response of the fiber composite largely depends on the interface between the stiff and pliant components. Cellulose interactions with hemicelluloses and pectin are of specific importance in primary cell walls during cell growth, since these cell walls need to be not only stiff enough to bare the hydrostatic pressure inside the cells and external loads, but also have to be compliant to allow for the cell wall extension accompanied by cell enlargement [46–48].

#### 8.2.4

##### Cell Wall–Water Interaction

To study the plant cell wall–water interaction, the equilibrium moisture content of the tissue under investigation is usually monitored upon increasing/decreasing relative humidity at a specific temperature. The result is the sorption isotherm

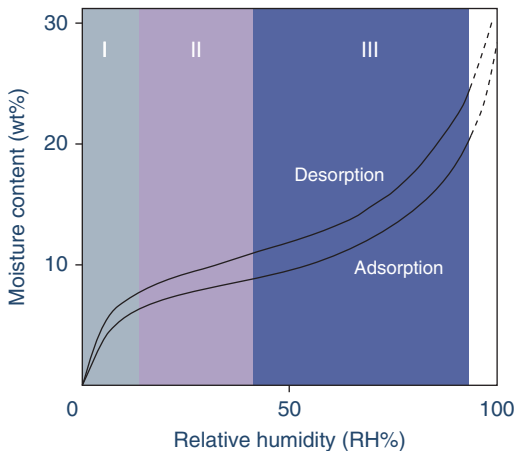


**Figure 8.5** A typical sorption isotherm for wood plotting the equilibrium moisture content (the weight of the adsorbed water per weight of the dry wood) against the relative humidity (RH%). (I) The initial adsorption region where first few layers of water are adsorbed into the wood cell wall to make strong bonds with cell wall polymers. (II) Beginning of the multilayer adsorption where more and more layers of water molecules are adsorbed onto the already adsorbed

first layer. (III) Adsorption of more mobile condensed water known as capillary water. The slope of the adsorption increases rapidly as the capillary adsorption becomes the dominant, but due to inaccurate equilibrium conditions at high relative humidity close to 100%, the precise measurement of the moisture content is problematic. (Redrawn with permission from Ref. [49]. Copyright by Springer-Verlag.)

that provides an entire picture of the different stages of interaction with water (Figure 8.5).

Various models have been developed to understand the different adsorption stages in cell wall-water interaction with each stage corresponding to a different state of water in the cell wall. Due to various interpretations of the results the true nature of each state is still under debate. However, the different adsorption stages discussed for polymer-liquid solutions can describe the water-cell wall interaction to some extent. At low relative humidity, the initial adsorption of water into the cell wall is a hydration process, mainly involving free hydroxyl groups of hemicellulose or the amorphous regions of cellulose aggregates where a mono layer of water molecules gets strongly fixed onto the chains [50, 51]. The adsorption of water at this stage (region I in Figure 8.5) was suggested to follow the Langmuir monolayer adsorption model [49, 52]. Desorption of this primary bond water is not easy and requires high energy input to open the strong bonding between the water molecules and the polymer chains. At higher relative humidity Brunauer-Emmett-Teller theory (BET) multilayer adsorption is suggested as the main adsorption mechanism where more and more layers of water molecules are adsorbed onto the already existing first layer [49, 52–55]. In the beginning of the multilayer adsorption, newly adsorbed water surrounds the already present water molecules to build ordered compact multiple layers, which due to the interaction with neighboring macromolecules have a restricted mobility. The multilayer water molecules help to open up the intermolecular hydrogen bonds between the saccharides and ease the conformational changes and mobility of the chains [49, 52–57]. In these stages, the reaction is exothermic, and the enthalpic gain of the system is the main driving force for adsorption of the first few layers. At higher relative humidity (region III in Figure 8.5) the hydrogen bonding between the water molecules and cellulose chains gets weaker with distance, and most of the newly adsorbed water is mainly interacting with other water molecules. Thus, further adsorption is mainly condensation of water vapor into the voids that are already covered with first layers of adsorbed water, as there is some degree of energetic gain by reducing the liquid surface due to the filling of the pores [23, 49, 52–57]. The increase in the slope of adsorption at this stage was formerly explained as sorption of free water in capillaries. However, recently it was shown both theoretically and experimentally that the capillary sorption is not that significant at this RH and the change in the slope cannot be contributed to the capillary sorption alone [58–60]. Technical problems and inaccurate equilibrium conditions prevent accurate measurements at high relative humidity near 100% dominant.

#### 8.2.4.1 Swelling/Shrinkage of Wood

Water adsorption at all three aforementioned stages results in the swelling of the cell wall matrix and consequently the bulk tissue. The swelling/shrinkage of wood is one of the big challenges in wood and paper industries and is considered to be avoided or at least controlled [61]. Wood has a hierarchical nonhomogeneous

structure with various levels of organization, which have severe influence on the macroscopic deformation based on the interaction of wood cell walls with water. In freshly cut wood, the water can exist as free water in the lumen of the cells as well as bound water in the cell wall. Upon drying the water inside the lumen is the first to leave till the point where the only water in the tissue is the water saturated inside the cell wall, known as fiber saturation point (about 26–32 wt% moisture content) [49]. Up to this point, water uptake/loss has no influence on wood dimension. However, adsorption/desorption of water into the cell wall below this point results in anisotropic swelling/shrinkage of the bulk tissue, and if restricted can exert huge stresses on the restricting frames [49]. In normal wood, the swelling/shrinkage can range from ~0.1% to 0.3% along the longitudinal direction, ~3% to 6% in the radial direction, and ~6% to 12% in the tangential direction, upon drying from the moisture content of about 30 wt% at fiber saturation point to the dry state [49]. The relatively low swelling/shrinkage in the longitudinal direction can be explained by the cellulose fibril orientation, as the main swelling occurs in the cell wall matrix and results in deformation perpendicular to the longitudinally oriented fibrils [49].

### 8.2.5

#### Principles of Anisotropic Deformation

The swelling/shrinkage of wood tissue is just a passive deformation that occurs mainly below the fiber saturation point and needs to be avoided in various wood applications. However, some plants even make use of such basic swelling principles for generating internal stresses and organ movement. Due to the significant difference in swelling/shrinkage capacity and stiffness between the reinforcing cellulose fibrils and the soft matrix, the orientation of the microfibrils in the cell wall is the main controlling factor to determine the directionality of the swelling. By having control over the anisotropy of the cell wall via controlling the orientation of the cellulose microfibrils in the cell wall formation process, plants can (i) control the final geometry of the cell in the growth process, (ii) generate the desired stress or deformation, and/or (iii) determine the mechanical properties of an organ in general [1, 10, 11, 14, 43, 62–64]. In a simple model of a composite consisting of almost undeformable stiff fibrils in a much softer matrix, when both elements are subjected to same strain (tensile loading in the direction of the fibrils), the extension is mainly controlled by the resistance of the fibrils. Whereas in case where both elements face the same stress field (force perpendicular to the fibrils), the extension is achieved mainly via the stretching of the matrix [63]. The same is valid for the cell wall as high stiffness of cellulose fibrils resists the expansion of the cell wall in the direction of the cellulose and makes it easier to stretch the cell wall perpendicular to the fibrils orientation [62, 63]. Examples of such plant hydro-driven stress generation due to swelling of anisotropic cell walls will be discussed in Section 8.3.

### 8.3

#### **Systems Based on Inner Cell Pressure – Living Turgorized Cells**

##### 8.3.1

##### **Cell Growth – Turgor: Plastic Deformation of the Cell Wall**

Differential growth movements are probably the simplest way for a plant to perform a specific deformation in its organ. Cell growth is achieved through an irreversible plastic extension of the cell wall caused by an increase in the cell volume via water uptake. In the normal state, the internal stress in the cell wall and the turgor pressure are in mechanical equilibrium. To allow the plastic deformation of the cell wall for growth, stress relaxation occurs via selective loosening of the load-bearing linkages between cellulose microfibrils. Loosening can be a result of the scission of cellulose-connecting molecules or the opening of load-bearing bonds, and in both cases stress relaxation occurs without significant changes in wall dimensions. The resulting drop in the turgor pressure results in further water uptake and expansion of the cell. The process relies mainly on the changes in the cell wall (visco)plastic deformation behavior [1, 41, 65–68]. The unequal irreversible differential growth of the cells on opposite sides of an organ results in an imbalance volumetric change, which can lead to the required organ deformation. Growth-induced bending of the coleoptiles of grasses or tropic movements as response of the plant to environmental stimuli are examples of plant movements related to the differential irreversible growth of the cells [1, 2, 69].

##### 8.3.2

##### **Movement via Elastic Deformation of the Cell Wall**

During growth processes, cell walls undergo a plastic deformation. However, for more rapid movements, plants need an elastic response of the cell wall to introduce stresses in specific cells or perform a desired movement by a change in inner cell pressure. Changes in the inner cell pressure exerted by so-called motor cells deform the cell walls elastically and enable the plant to build up the driving force for the actuation of the entire organ [3, 7, 70]. Light-induced or Circadian movements of the leaves of many species are controlled by variation of the inner pressure of these special motor cells in the joint-like hinges at base of the stalk of the leaves called pulvini [8, 71]. The same principle is applied to achieve relatively rapid leaf folding of *Mimosa* upon external stimuli [17, 19, 72–74]. The carnivorous Venus flytrap uses a similar mechanism combined with a special metastable geometry of its leaves to perform one of the fastest plant organ movements [1, 18, 75]. However, the most common turgor-based systems in plants are the stomatal movements for control of gas exchange of the leaves through small pores [4, 70, 76, 77].

### 8.3.2.1 Stomatal Movement

One of the most abundant examples of reversible turgor-driven movements at the cellular level is the opening/closing of stomata in plants. Stomata are small gates in the epidermis of most leaves and young stems, which control the gaseous exchange between the plant interior and its environment. The environmental conditions such as  $\text{CO}_2$  level, light, and humidity dictate the opening and closing of these valves through stimulating the stomatal motor cells called “guard cells.” The guard cells can sense the changes in air humidity and moisture status of distant tissues. In general, opening and closing of the pathways is governed by the volume and shape changes of guard cells that cover and regulate the pore size for  $\text{CO}_2$  uptake or maintain the desired water level in the leaves [1, 4, 70, 76–80].

Hydrodriven movement of the stomata guard cells is completely reversible and is generally driven by variation in the water potential of the cells. Active delivery of the solutes (such as cationic potassium salts) through the membrane of the motor cells and accumulation of them in the cells results in a lower water potential. Water flows into the guard cells in order to retain the equilibrium, thus the turgor pressure rises and the cell volume increases. The whole process is directly related to active ion transport by the ion-transport proteins in the guard cells. Presence of  $\text{K}^+$ -selective ion channels in the plasma membrane of guard cells was shown to facilitate the  $\text{K}^+$  uptake and regulate the volume change of the guard cells (Figure 8.6) [77, 81].

During the stomatal opening, the guard cells' volume increases about 40%, which is accompanied by almost the same amount of stretching in the cell surface area. Radial arrangement of the cellulose microfibrils in the cell wall results in an anisotropic deformation of the cells along the longitudinal axis, which leads to bending of the cells and opening/closing of the valve [77, 82, 83].

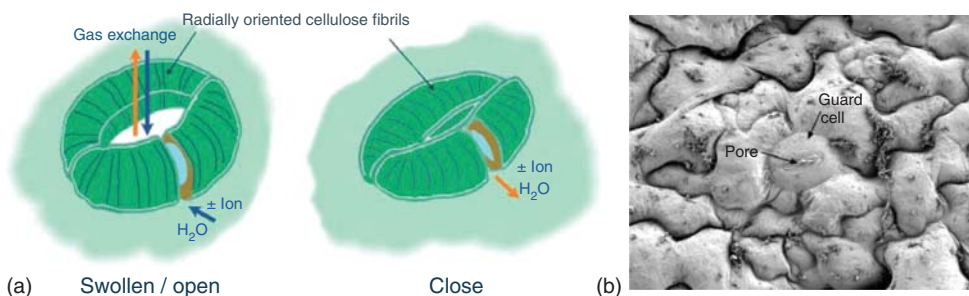


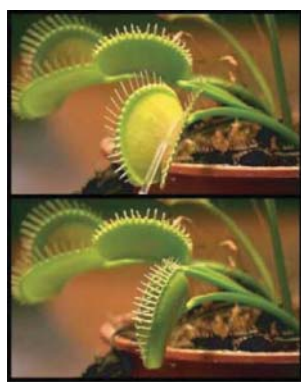
**Figure 8.6** Schematic illustrates the guard cells during stomatal movements. Cell volume increases during the opening and causes the cells to bend. The cross section of the cells changes from flat oval in close state to circle in open state (left).

Scanning electron microscopy of a single stomatal pore on an abaxial leaf surface of *Arabidopsis thaliana* is shown on the right side. (Reprinted from Ref. [79] with permission. Copyright by Cambridge University Press.)

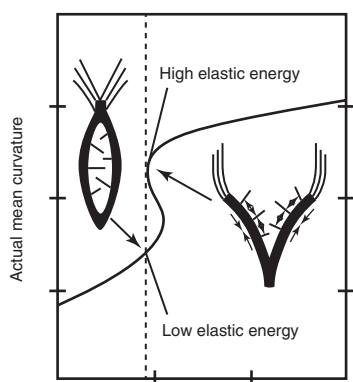
### 8.3.2.2 Venus Flytrap: A Turgor-Based Rapid Movement

One of the famous examples of turgor pressure-driven movement in plant kingdom is the rapid closure of *Dionaea muscipula* leaves, better known as Venus flytrap. It is one of the fastest organ movement in plant kingdom with 60% of the total displacement occurring in about 100 ms [1, 17]. The trap is stimulated when a relatively large prey deflects at least two of the sensory hairs located in the inner side of the leaves. The signal is then translated into propagation of action potentials changing the membrane permeability and followed by a volume change of the leaf [2, 4–6, 17, 84].

The actuation can be described as a combination of two distinct mechanisms: the biochemical response of the plant to the external stimuli results in water flow, and the mechanical response by means of changes in leaf geometry results in the rapid closure of the leaves. The underlying mechanism for the plant biochemical response and water exchange in the leaves has been debated, and different models have been proposed. A rapid loss of turgor pressure in motor cells or an irreversible acid-induced wall loosening is considered to be the possible mechanism responsible for the plant response to the external stimuli [5, 75, 85, 86]. Despite the different underlying mechanisms proposed, all models agree on significant volume changes of the leaves' tissue on adaxial and abaxial sides upon movement. In addition, it has been debated that the process based on simple water flow in the leaf tissue would be relatively slow and cannot explain the astonishing speed of the leaf folding [4, 75, 85–87]. Forterre *et al.* redefined the problem in a biomechanical model, explaining the mechanism in terms of mechanical constraints leading to a pre-stressed trap system [17]. The fascinating translation of the small and slow



(a)



(b) Natural curvature in the direction of the midrib

**Figure 8.7** (a) Venus flytrap; the leaves close in a fraction of a second when triggered by a prey (Adapted from Ref. [17] with permission. Copyright by Nature Publishing Group). (b) Schematic of the Venus flytrap leaf in open and closed state. The mechanical metastable border is shown by the curve

in the diagram with two possible folding states. The leaf snaps rapidly as the folding state flips from the high elastic energy level into the low elastic energy level. (Adapted from Ref. [1] with permission. Copyright by Royal Society.)



cellular movement based on water flow to a much faster macroscale movement of the organ in Venus flytrap is achieved by coupling the cell turgor pressure variation with instabilities in the geometry of the entire organ. In the open state, the leaf is curved outwards (concave), holding the leaves in an intermediate mechanically metastable state through a high turgor pressure inside the responsive motor cells. Stimulation of hair sensors by a prey triggers the leaf volume change through the water flow between the inner and outer faces of the leaf, which consequently destabilize the metastable folding state. To release the stress, the leaf goes through an elastic relaxation via a sudden curvature conversion to a convex (inward) folding, which results in a rapid closure and snapping of the trap (Figure 8.7) [1, 4, 17, 88].

## 8.4

### Systems Based on Water Uptake of Cell Walls

The principles of anisotropic swelling in the cell wall and the role of cellulose MFA in that process have been discussed in Section 8.1 in general. By controlling the architecture of the cell wall during the differentiation process of the living cell, plants can utilize the anisotropic deformation via swelling/shrinkage after cell death to generate relatively huge compressive or tensile stresses or perform a desired movement [1, 89, 90].

#### 8.4.1

##### Bilayered Structures for Bending

One of the simple yet ingenious strategies used by various plants is to use a bilayer structure to perform bending movements. When two elements with different mechanical response to an external stimulus (temperature, humidity, etc.) are connected to each other, the extension/compression of one side is hindered or resisted by the more passive part. The compromise for the element with more extensibility (active part) is to satisfy the elongation through bending (Figure 8.8).

The curvature of a bilayer can be calculated in analogy to the analytical approach for the curvature of a bimetallic strip derived by Timoshenko [91]. In the absence



**Figure 8.8** Principles of the bilayered structure bending. The layer on top (blue) has a strong response to a specific stimulus (temperature, humidity, etc.) while the layer on the bottom (gray) is passive or resistive.

When connected tightly together, the active part goes under tensile stress upon actuation while the passive part resists the elongation. The compromising result is the bending of the whole structure.



of external loads, both force and torque are balanced:

$$F_1 = F_2 \quad (8.8)$$

$$\frac{F_1 h_1}{2} + \frac{F_2 h_2}{2} = \kappa (E_1 l_1 + E_2 l_2) \quad (8.9)$$

where  $F_1 = \epsilon_1 E_1 h_1 t$  and  $F_2 = \epsilon_2 E_2 h_2 t$  are the forces in each layer,  $l_1 = \frac{th_1^3}{12}$  and  $l_2 = \frac{th_2^3}{12}$  the moments of area,  $t$  the width,  $h_1$  and  $h_2$  the thickness of the lower and upper layers,  $E_1$  and  $E_2$  the respective Young modulus, and  $\kappa$  the curvature.

In addition, the strain at the interface between the two layers must be equal:

$$\epsilon_1^* + \frac{F_1}{E_1 h_1 t} + \frac{\kappa h_1}{2} = \epsilon_2^* + \frac{F_2}{E_2 h_2 t} + \frac{\kappa h_2}{2} \quad (8.10)$$

where  $\epsilon_1^*$  and  $\epsilon_2^*$  are the swelling strains in the two layers.

Solving these equations, the curvature  $\kappa$  leads to

$$\kappa = \frac{6(\epsilon_2^* - \epsilon_1^*)(1 + m)^2}{(h_1 + h_2) \left( 3(1 + m)^2 + (1 + mn) \left( m^2 + \frac{1}{mn} \right) \right)}$$

where  $m = h_1/h_2$  and  $n = E_1/E_2$ .

When  $m = n = 1$  the curvature is given by  $\kappa = 3(\epsilon_2^* - \epsilon_1^*) / 2(h_1 + h_2)$ , so it is proportional to the difference in swelling strains between the two layers and inversely proportional to the thickness of the bilayer.

#### 8.4.1.1 Passive Hydro-Actuation in Pine Cones

A well-known example of passive hydro-actuation movement is the pine cone opening for seed dispersal. The pine cone scales are closed in wet state and

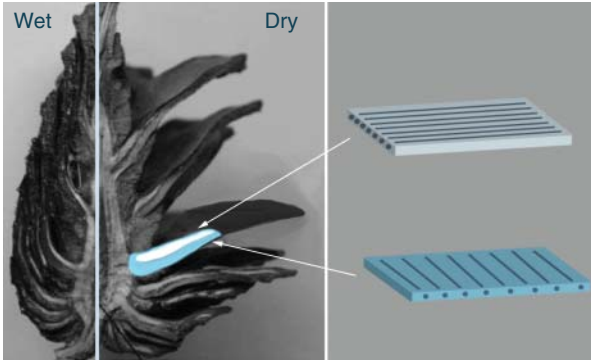


**Figure 8.9** Passive hydro-actuated bending of the pine cone scales. A cross section of a pine cone along its longitudinal axis in wet and dry states is shown with schematic of the two layers on upper (white) and lower (blue) side of a scale. In the upper layer, fibrils are oriented along the longitudinal

direction while in the lower layer fibrils are more perpendicular to the cell axis. The different swelling properties of the two layers result in the bending and opening of the scales upon drying. (Redrawn from Ref. [1] with permission. Copyright by Royal Society.)

open upon drying to unveil the seeds. The reversible hydroresponsive bending movement of the scales is realized through a sophisticated architecture of the cell wall. Each scale is made up of two differently structured layers on the upper and lower sides. Here again, the specific orientation of the cellulose microfibril in the cell wall during the plant growth results in different shrinking responses of the two layers. On the upper side, fibrils are almost parallel to the cell's axis, which restricts the upper side to shrink only in the direction perpendicular to the scale. The lower side, on the other hand, has an MFA of about  $90^\circ$ , thus water desorption of the cell wall matrix results in the shrinkage of the cells along the longitudinal direction. The combined material response of the two sides with different directionality of the swelling leads to the bending of the scale upon humidity changes (Figure 8.9) [1, 10].

#### 8.4.1.2 Wheat Awns Hydro-Actuated Swimming Movement

A similar mechanism enables the wild wheat awns to actuate seed dispersal units via a swimming-like movement upon natural day–night humidity cycles.

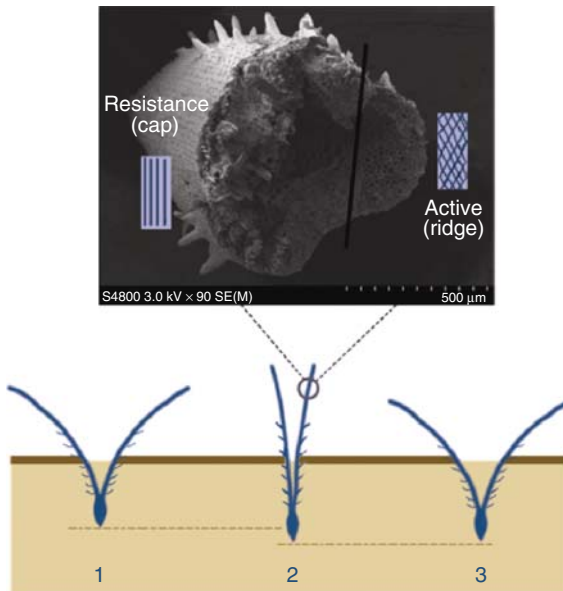


**Figure 8.10** Hydrodriven movement of wild wheat awns. The swimming movement of the wild wheat awns is shown schematically. An Scanning electron microscope (SEM) micrograph of the cross section of the wheat awn depicts the active (ridge) and resistive (cap) parts. The cellulose fibrils are oriented parallel to cell axis in the cell walls of the passive part (inner side), preventing the swelling of the cells in the longitudinal

direction. The random orientation of the microfibrils in the cell walls of the cells in the outer ridge makes the active part swell more than the inner tissue. This leads to a periodic bending movement of the awns upon the humidity changes during day (1, 3) and night (8.2), which pushes the seed case into the soil [11, 89]. (Adapted from Ref. [11] with permission. Copyright by American Association for the Advancement of Science.)

The seed cases are connected to two antenna-like awns that land the seeds in helical-descending movement to the ground. Each awn consists of two layers with different swelling properties. On the inner side of the awns (cap), the cellulose microfibrils are oriented almost parallel to the cell axis that only allows the swelling/shrinkage in the direction perpendicular to the cell axis. The cells on the ridge (the outer part of the awns) have multilayered cell walls with alternating MFA, which leads to an isotropic shrinkage/swelling of the tissue upon humidity changes. Although this cellulose orientation is not entirely optimized for large longitudinal swelling, this swelling is by far larger than the longitudinal swelling at the cap. As a result, the difference in the swelling/shrinkage of the inner and outer parts of the awns leads to a slow bending movement of the awns upon ambient humidity changes (Figure 8.10) [11].

The passive tissue is more densely packed to support the active part, and a soft intermediate layer improves the connection between the two parts and optimizes the movement. The cyclic changes in between the relatively dry air during the day and higher humidity at nights result in a very slow swimming movement of the seed dispersal unit. Small spike-like silica hairs on the outside of the awns ensure the forward movement of the seeds by preventing the unit to move backwards and out of the soil [11].

#### 8.4.2

##### **Bilayered Structures for Twisting Movements**

Although bending movements are quite ubiquitous in natural systems, other types of actuation patterns can be observed as well. In case of elongated objects such as the pine cone scales or the wheat awns, actuation patterns can be understood by looking at the change of a shape of a line in space. In these objects where the dimensions of the cross sections are much smaller than the length, this line approximately connects the barycenter of the cross sections together. Bending corresponds to changing the curvature of this line staying in a plane. Uniform bending results in a circular arc so that any bending actuation is locally circular. Instead of changing the shape of this line as in bending, the line can stay straight while the cross sections rotate around it. This deformation is called twisting and represents the second fundamental actuation pattern of elongated objects. While bending is related to a linear distribution of normal strains in the bending plane, twisting results from a radial distribution of shear strains around the centerline. A combination between bending and twisting results in curling. For a constant curvature and twist, the actuation pattern is helical. A simple way to produce these strains is to take a band consisting of two layers that contract in opposite directions at an angle with the main line. Just by changing this angle, the layered structure performs a bending, coiling, or twisting movement (Figure 8.11) [92, 93].

##### **8.4.2.1 Curling of *Erodium* Awns**

A natural hydrodriven actuator illustrating twisting movements is the *Erodium* stork's bill. After being catapulted from the seed pod due to the active drying of

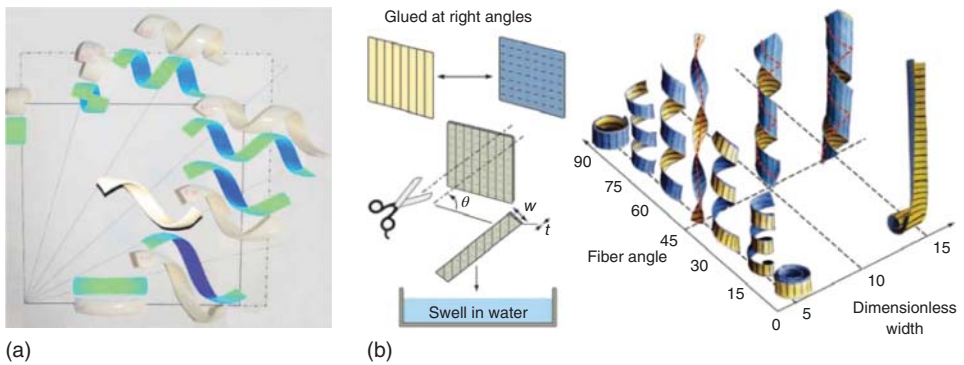


**Figure 8.11** Principles of bilayered structure for twisting movement. (a) Biaxially pre-stretched latex sheet cuts into thin strip at different angles leading to different deformation upon stimulation from bending to different curling. (Reprinted from Ref. [92] with permission. Copyright by American

Institute of Physics.) (b) Schematic illustration of a simple paper-bilayer model where the dimensionless width and the fiber angle control the actuation pattern. (Reprinted from Ref. [93] with permission. Copyright by American Association for the Advancement of Science.)

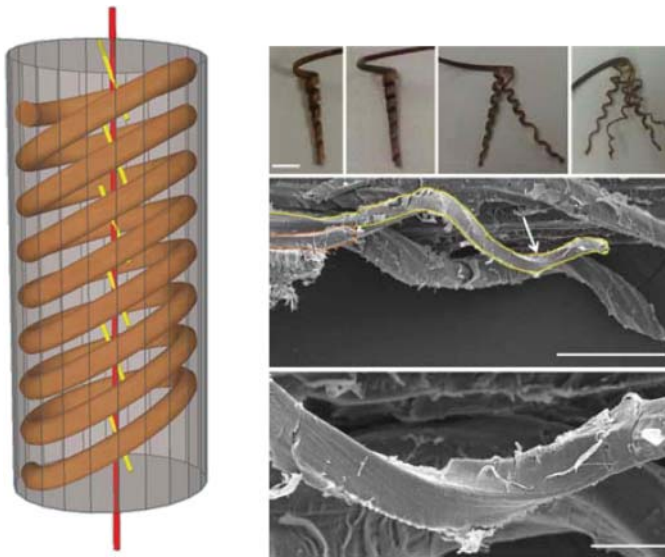


**Figure 8.12** The underlying mechanism for twisting of *Erodium gruinum*. (a) Schematic of the cellulose microfibrils in the coiling cells of the stork's bill possessing a specific tilted helical arrangement. (b) Hierarchical coiling; at top the coiling section of a complete awn and separated inner layers of the awn.

Scanning electron micrographs of the inner layer shows couple of coiling cells. The SEM image on the bottom shows the closer look at the region indicated with arrow. Scale bars are top, 5 mm; middle, 100 mm; and bottom, 20 mm. (Reprinted from Ref. [94] with permission. Copyright by Royal Society.)

the awn relative to the passive resistance of the central column, each of the five awns undergoes helical actuation thus propelling the seed on and into the ground. The unidirectionality of the movement is granted by the presence of silica hairs aligned similar to those in wheat awns. Surprisingly, the awn appears to be made of a uniform material, thus contradicting the previous tilted bilayer models. In fact, a tilted orientation of the microfibrils in relation to the awns' long axis was observed by Small-angle X-ray scattering (SAXS) measurements. As longitudinal sections show that cells are parallel to the awns' axis, the tilt has to be achieved at the level of the cellulose microfibrils in the cell walls. Indeed, single cells with a tilted helical arrangement of microfibrils curl as confirmed by scanning electron micrographs. This novel cellulose arrangement leads to a curling building block, thus enriching the available mechanisms for passive actuation (Figure 8.12) [94].

## 8.5

### Systems Based on a Differential Swelling of Cell Wall Layer

#### 8.5.1

##### Tension Wood Fibers

Tension wood is the reaction wood of hardwoods on the upper side of leaning stems, responsible for the bending and uprighting of the stems and branches. Tension wood can generate extremely high longitudinal tensile stresses in the organ [13]. Many hardwood species utilize a nonlignified cellulose-rich layer, the so-called gelatinous layer (G-layer), which swells more easily than the surrounding lignified cell wall layers. The G-layer that can fill the whole lumen of the fibers consists of aggregates of cellulose microfibril with a diameter of about 30–40 nm, running parallel to the cell's axis [16, 95, 96]. The microfibril orientation makes the G-layer axially stiff and laterally swellable. The role of the G-layer and the underlying mechanism of the stress generation in the tension wood fibers are still under debate [14, 97–106]. It has been shown that the MFA of the cellulose microfibrils in the secondary cell walls of such G-fibers is much larger and is required to translate the tangential stress from the transverse swelling of the G-layer into a maximum axial contractile stress in an optimized range [16, 99]. Based on this theory, the combination of a highly swellable G-layer inside the cell lumen, with a suitable arrangement of the cellulose microfibrils in the surrounding secondary cell wall, enables some hardwoods to exert such high tensile stresses by tension wood fibers (Figure 8.13).

Other models on the active role of the G-layer in tension wood fibers have proposed different stress generation mechanisms that are related to an important role of xyloglucan in the stress generation process, a honeycomb cellulose structure in the G-layer, or variations in the cellulose fibril orientation in the surrounding secondary cell wall layers, respectively [100, 103–105]. However, it

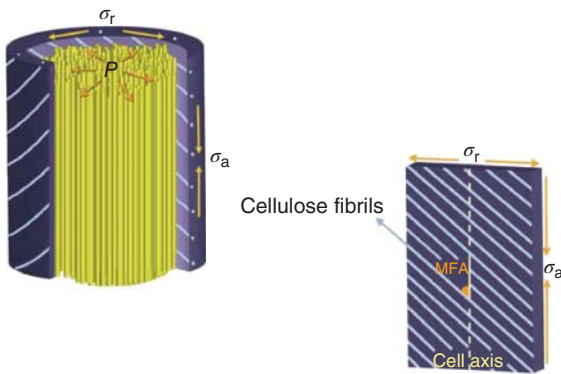


**Figure 8.13** One of the proposed mechanisms for tensile stresses generation in tension wood fibers. The lateral swelling of the cellulose-rich G-layer inside the cell lumen (yellow fibers) exert a tangential pressure ( $P$ ) on the secondary cell wall that results in a circumferential stress  $\sigma_r$  within the cell wall.

The specific orientation of the cellulose fibrils in the cell wall translates this stress into an axial tensile stress  $\sigma_a$ , so that the microfibril angle (MFA) determines the  $\sigma_a/\sigma_r$  ratio and leads to the shortening of the tension wood fibers (Redrawn after Ref. [16]).

should be noted that hardwood species that do not form a G-layer are also capable to generate tensile stresses that allow for uprighting leaning stems and branches [101, 102, 104, 106].

### 8.5.2

#### Contractile Roots

Root contraction has been found among many species [107–110]. The contraction of the roots can serve for a variety of functions from reassuring a safe position for renewing the underground organs, vegetative spreading of daughter bulbs or corms, and seedling establishment [110]. In *Trifolium pratense*, the proximal part of the storage root can contract up to 30% in the longitudinal direction to drag the foliage buds deeper into the soil [111]. The mechanism behind the movement of the contractile roots was found to follow the same principles that may generate high tensile stresses in the tension wood fibers. The cells in the root were found to have a similar structure to those of tension wood in hardwoods, with the characteristic feature of having the G-layer in the lumen of the cells, with cellulose microfibrils running parallel to the cell axis. The surrounding secondary cell wall also resembles that of the tension wood fibers with relatively high cellulose MFA. Here, the significant contraction of the proximal root part is the result of a consecutive contraction of newly formed G-fibers during organ growth, which further compresses the already existing and contracted fibers and vessels (Figure 8.14) [111].



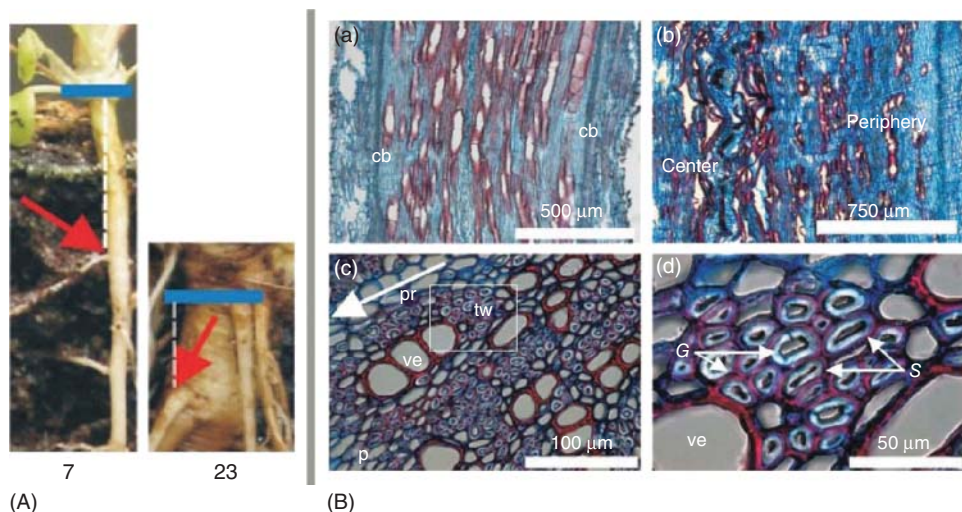


**Figure 8.14** Contractile roots. (A) The uppermost contractile region of a single *Trifolium pratense* plant depicted from week 7 and 23 after germination. The blue bars show the border between the cotyledon and the hypocotyl and the red arrow tracks a lateral root. The distance between the hypocotyl (blue bars) and this root, depicted as white dashed line, resembles the contraction of this part of the storage root. (B) FCA (fuchsin-chrysoidine-astra blue)-stained sections of the root with lignified parts stained in red and nonlignified parts

stained in blue. (a) Longitudinal section of the straight vessels of distal uncontracted part. (b) Bent vessels in the center and straight vessels at periphery of a proximal contracted part. (c) Transverse section of proximal part. (d) Higher magnification of the white box in (c) showing the presence of the G-layer in the tension wood region. cb, Cambium; G, G-layer; p, parenchyma; pr, pith ray; S, S-layers; tw, tension wood; and ve, vessel element. (Reprinted from Ref. [111] with permission. Copyright by Blackwell Publishing Ltd.)

### 8.5.3

#### Ice Plant Seed Capsule

The plant species *Delosperma nakurense*, belonging to the Aizoaceae also known as ice plants utilize a kind of G-layer such as swellable inner layer in a completely different way to actuate a relatively large movement. Ice plants grow in semiarid areas and have evolved a sophisticated seed dispersal mechanism (Figure 8.15). The seed capsule consists of five protective valves that unfold and unveil the seeds only when wetted with liquid water. The active muscle responsible for this reversible movement is a hygroscopic tissue located along the center of the valve inner surface, which consists of a network of hexagonal/elliptical shape cells with a highly swellable cellulose-rich inner layer (CIL) inside their lumen. The shape of the cells dictates a high anisotropy in the swelling direction with the main swelling occurring in the shorter axis of the transverse cell cross section (fourfold in the *Y*-direction). The cells at the edge of the keel are free and swell more than

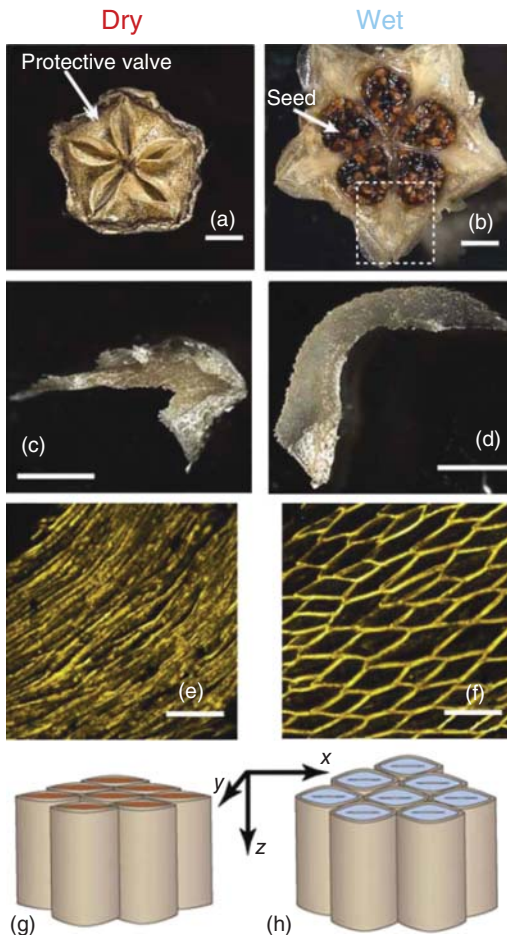


**Figure 8.15** Hierarchical morphology of ice plant seed capsule. The morphology of the ice plant capsule and the hygroscopic keel tissue are shown at different hierarchical levels by light and confocal microscopy: seed capsule in close/dry and open/wet state (a, b), hygroscopic keel in close/dry and open/wet state (c, d), and network of

hexagonal/ellipsoid cells in close/dry and open/wet state (e, f). Schematics show that the main swelling occurs in the width (Y-direction) of the cells (g, h). Scale bars are a, b = 2 mm; c, d  $\approx$  1 mm; and e, f = 0.1 mm. (Adapted from Ref. [112] with permission. Copyright by Nature Publishing Group, a division of Macmillan Publishers Limited.)

those attached to the valve backing tissue. This gradient in the swelling properties translate the cooperative swelling/shrinkage of the cells into an origami similar to unfolding/folding of the seed capsules [112, 113].

What separates the hydroresponsive unfolding of ice plants from other hygroscopic plant movements is that an incremental increase in relative humidity (even up to 90%) does not trigger any movement in the system and actuation starts only in presence of liquid water [114]. The initial water adsorption in ice plant keels



follows a somehow similar trend observed in wood cell wall, where the first few layers of water are adsorbed into the cell wall matrix and onto cellulose chains. However, this initial water adsorption does not trigger the movement of the keels.

#### 8.5.3.1 Ice Plant Capsule Opening as a Case Study for the Capacity of Water as a Plant Movement Actuator

The peculiar capability of water as swelling agent becomes obvious when monitoring the ice plant keel moving in different media. To be able to compare the swelling ability of different solvents, the ice plant keels were placed in different media and their opening angles were measured at equilibrium state and normalized to the initial dry state, so that the reported opening factor ranges from 0% at completely dry and close state to 100% at fully open state. The swelling behavior depends on different parameters such as solvent molar volume and solubility parameter, which are shown in Figure 8.16. The solubility is directly related to the internal energy of solvents and solutes. The relation between the total solubility parameter and the cohesive energy density (CED, as the energy that binds the molecules in 1 cm<sup>3</sup>), is defined as follows:

$$\delta_T = CED^{1/2} = \left( \frac{\Delta E}{V_m} \right)^{1/2} = \left( \frac{\Delta H - RT}{V_m} \right)^{1/2} \quad (8.11)$$

where  $T$  is the absolute temperature,  $R$  is the gas constant,  $V_m$  is the molar volume,  $H$  is the enthalpy of vaporization, and  $E$  is the energy of vaporization [115, 116].

In Figure 8.16, keel opening in each solvent is plotted against solvents CED, where the bubble size depicts the molar volume of the comparative solvents (cm<sup>3</sup> mol<sup>-1</sup>).

In general, according to solubility theory, dissolution can occur when a solute is surrounded by a solvent of similar CED value [115, 116]. Here, it can be seen that solvents with higher CED (higher values of Hansen solubility parameters) showed more swelling power. On the other hand, osmotic pressure as an ability of a network to adsorb an adsorbent is inversely related to solvent molar volume represented by Flory–Huggins equation [29]. Hence, the swelling power of a solvent is expected to decrease with increasing molar volume. This can explain the comparatively minor swelling of the cells in glycerol compared to ethylene glycol. Despite slightly higher CED, glycerol's molar volume is significantly higher than ethylene glycol, which makes it a weaker actuator. All three alcohols induce only a partial swelling of the CIL, although their minor actuation follows the same trend and keel's opening decreases for solvents with lower solubility parameters and higher molecular size. Comparison of keel's opening in glycerol and methanol put even more weight on the impact of hydrogen bonding power of the Hansen solubility parameters compared to the other parameters; despite similar value of the polar part of the Hansen solubility parameter ( $\delta_p$ ) and relatively higher molar volume, glycerol shows double the actuation power of methanol, thanks to its significantly higher hydrogen bonding power ( $\delta_h$ ). It is obvious that water with the highest CED and the lowest molar volume ( $V_m$ ) is the best solvent for CIL and opens the keel immediately after soaking.

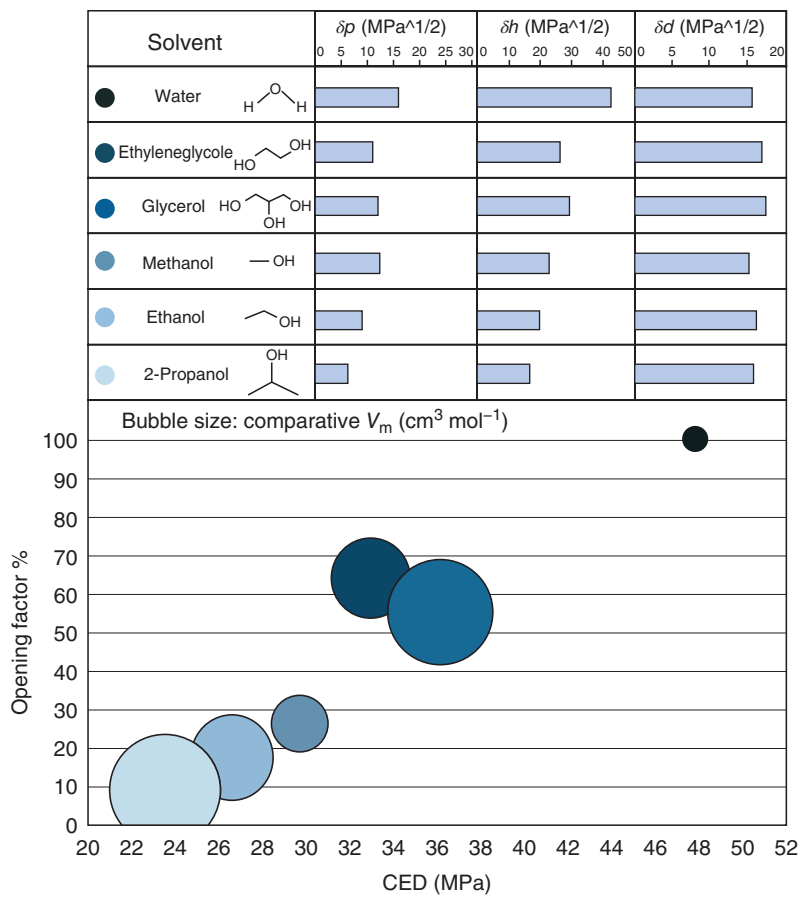


**Figure 8.16** Role of different parameters in opening of the ice plant keel. The table shows the different solvents used as actuating media for the keels with their Hansen solubility parameters shown in blue bars. The three partial solubility parameters  $\delta_p$ ,  $\delta_h$ , and  $\delta_d$  represent a polar interaction, hydrogen bonding component, and a nonpolar part of the total Hansen solubility parameter, respectively [62, 116, 117]. The correlation

between keel's opening in different solvents and the solvents' cohesive energy density (CED) calculated from the solubility parameters is shown at the bottom. The bubble size represents the solvents molar volume (cm<sup>3</sup> mol<sup>-1</sup>). The yellow region highlights solvent's CED range that can promote a relatively significant CIL swelling and keel's opening.

8.6  
Biomimetic Potential

Various stress generation or movement mechanisms in plant kingdom can be a source of inspiration for extracting and transferring biomimetic principles. Passive actuation systems are probably most interesting for a biomimetic transfer and further development of smart systems as, unlike the movements that depend

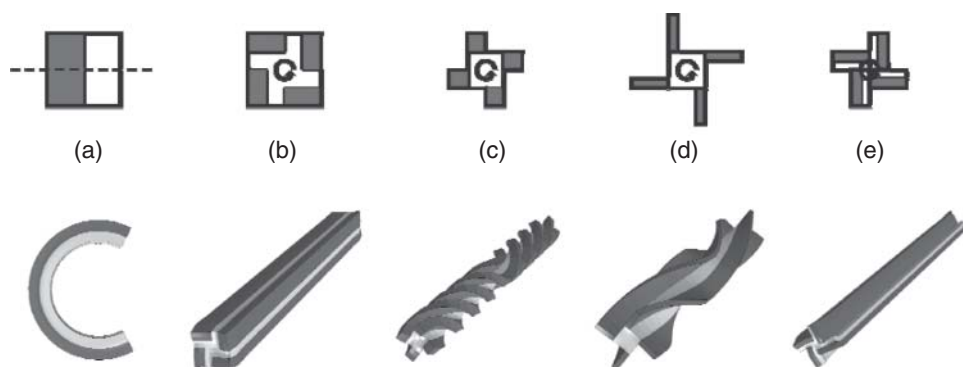


**Figure 8.17** Actuation patterns simulated for a variety of cross-sectional distributions of the active and passive elements: (a) bilayer bending in mirror plane; (b) closed fourfold cross section with bilayer remaining straight; (c) opened fourfold cross section with bilayer showing a large twist;

(d) opened fourfold cross section with bigger moment of inertia resulting in less twisting than (c); and (e) opened fourfold section with differently oriented bilayer unit cell remaining straight. (Reprinted from Ref. [121] with permission. Copyright by Carl Hanser Verlag GmbH & Co. KG.)

on the active role of the living organism, these systems can react autonomously [17, 76, 90, 117–120]. By applying the same principles observed in the passive actuation systems in plants, one can embed the desired response (deformation or stress generation) to specific stimuli by modeling and tailoring the mesoscopic features at different hierarchical scales.

A lesson to be learned from plant actuation is that the different arrangement of an expanding and a resisting phase can lead to a variety of responses and performances [121]. In particular, when the two phases are no longer arranged along a mirror plane, but around a rotational axis, twisting occurs (Figure 8.17). This behavior enriches the design space of biphasic actuated structures.

To recognize the potential of how the basic principles from plant hydro-actuated movements can inspire the development of new smart systems, Mahadevan and coworkers utilized the basic mechanism behind the bending movement of the wheat awns and pine cone scales to model and develop a simple bilayer that responds to changes in the surrounding humidity and undergo a bending movement [120]. Their flower pellets were made up of an active paper layer with a directional swelling along the leaf axis and a passive polymer film glued to the other side. The flower undergoes a reversible opening and closing upon wetting and drying cycles (Figure 8.18).

Abstracting from the biological actuators, the source of actuation can be multiple. In fact, any physical phenomenon leading to a reversible volume change is a potential candidate for passive actuation. Some examples are thermal expansion, solvent absorption (water or other proper solvents), or even electromagnetic couplings. By looking through various examples of hydrodriven actuations, one might think of water as a potential engine for developing novel passive hydro-actuated systems. Another abstraction consists of changing the source of heterogeneity. As

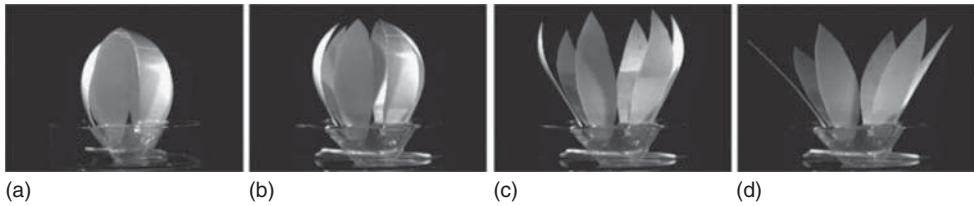


**Figure 8.18** (a–d) “Hygromorph model.” A biomimetic model of a hydroresponsive flower made up of paper–plastic bilayer petals. The blooming of the flower can be

controlled by humidity so that the petals open when wetted with water and close as they dry. (Reprinted from Ref. [120] with permission. Copyright by Royal Society.)

it can be observed in bending of the paper strip upon wetting, water needs time to diffuse through the paper, so the activation field of water is heterogeneous while the swelling properties are approximately homogeneous. Therefore, in terms of a biomimetic transfer, the question of size and shape is of tremendous importance. The role of gravity and structural integrity becomes more and more fundamental as the size of the actuator increases. Hence, a sufficient material selection process must be stimulated in order to find or invent adequate actuating materials that can be used for large-scale applications.

### Acknowledgments

The authors would like to acknowledge the fruitful comments and insights of Dr. Luca Bertineti on the experiments in Section 8.5.3.1. We like to thank the Max Planck Society and the German Research Foundation (DFG) for financial support in the framework of the priority program SPP1420. IB thanks Lignum and BAFU (Bundesamt für Umwelt), Switzerland, for the financial support of the professorship.

### References

1. Burgert, I. and Fratzl, P. (2009) *Philos. Trans. R. Soc. London, Ser. A*, **367**, 1541–1557.
2. Hart, J.W. (1990) *Plant Tropisms and Other Growth Movements*, Unwin Hyman Ltd, London, p. 208.
3. Toriyama, H. and Jaffe, M.J. (1972) *Plant Physiol.*, **49** (1), 72–81.
4. Hodick, D. and Sievers, A. (1988) *Planta*, **174** (1), 8–18.
5. Hodick, D. and Sievers, A. (1989) *Planta*, **179** (1), 32–42.
6. Sibaoka, T. (1991) *Bot. Mag.-Tokyo*, **104**, 73–95.
7. Fromm, J. and Lautner, S. (2007) *Plant Cell Environ.*, **30** (3), 249–257.
8. Moran, N. (2007) *FEBS Lett.*, **581** (12), 2337–2347.
9. Uehlein, N. and Kaldenhoff, R. (2008) *Ann. Bot.*, **101** (1), 1–4.
10. Dawson, J., Vincent, J.F.V., and Rocca, A.M. (1997) *Nature*, **390**, 668.
11. Elbaum, R., Zaltzman, L., Burgert, I., and Fratzl, P. (2007) *Science*, **316**, 884–886.
12. Wardrop, A.B. and Harada, H. (1965) *J. Exp. Bot.*, **16**, 356.

13. Okuyama, T., Yamamoto, H., Yoshida, M., Hattori, Y., and Archer, R.R. (1994) *Ann. Sci. For.*, **51** (3), 291–300.
14. Burgert, I., Eder, M., Gierlinger, N., and Fratzl, P. (2007) *Planta*, **226** (4), 981–987.
15. Coutand, C., Fournier, M., and Moulia, B. (2007) *Plant Physiol.*, **144** (2), 1166–1180.
16. Goswami, L., Dunlop, J.W.C., Jungnickl, K., Eder, M., Gierlinger, N., Coutand, C., Jeronimidis, G., Fratzl, P., and Burgert, I. (2008) *Plant J.*, **56** (4), 531–538.
17. Forterre, Y., Skotheim, J.M., Dumais, J., and Mahadevan, L. (2005) *Nature*, **433**, 421–425.
18. Volkov, A.G., Adesina, T., and Jovanov, E. (2008) *Bioelectrochemistry*, **74** (1), 16–21.
19. Levin, S.A., Muller-Landau, H.C., Nathan, R., and Chave, J. (2003) *Annu. Rev. Ecol. Evol. Syst.*, **34**, 575–604.
20. Skotheim, J.M. and Mahadevan, L. (2005) *Science*, **308**, 1308–1310.
21. Nobel, P.S. (1970) *Introduction to Biophysical Plant Physiology*, Freeman, San Francisco, CA.
22. Teraoka, I. (2002) *Polymer Solutions, An Introduction to Physical Properties*, Wiley-Interscience Publication.
23. Treloar, L.T.G. (1975) *The Physics of Rubber Elasticity*, Oxford University Press Inc., New York.
24. Hansen, C.M. (1969) *Ind. Eng. Chem. Prod. Res. Dev.*, **8** (1), 2–11.
25. Salmén, L. (2002) in *Proceedings of 1st International Conference of the European Society of Wood Mechanics* (ed. P. Navi), EPFL, Lausanne, pp. 385–398.
26. Kerstens, S., Decraemer, W.F., and Verbelen, J.P. (2001) *Plant Physiol.*, **127**, 381–385.
27. Fratzl, P., Burgert, I., and Gupta, S. (2004) *Phys. Chem. Chem. Phys.*, **6**, 5575–5579.
28. Fengel, D. and Wegener, G. (1984) *Wood – Chemistry, Ultrastructure, Reactions*, De Gruyter, Berlin.
29. McNeil, M., Darvill, A.G., Fry, S.C., and Albersheim, P. (1984) *Annu. Rev. Biochem.*, **53**, 625–663.
30. McCann, M.C. and Roberts, K. (1991) in *The Cytoskeletal Basis of Plant Growth and Form* (ed. C.W. Lloyd), Academic Press, New York, pp. 109–129.
31. Carpita, N.C. and Gibeaut, D.M. (1993) *Plant J.*, **3**, 1–30.
32. Bacic, A., Harris, P.J., and Stone, B.A. (1998) in *The Biochemistry of Plants* (ed. J. Priess), Academic Press, New York, pp. 297–371.
33. Fahlén, J. and Salmén, L. (2005) *Biomacromolecules*, **6**, 433–438.
34. Saxena, I.M. and Brown, R.M. (2000) *Curr. Opin. Plant Biol.*, **3** (6), 523–531.
35. Paredez, A., Wright, A., and Ehrhardt, D.W. (2006) *Curr. Opin. Plant Biol.*, **9**, 571–578.
36. Paredez, A., Somerville, C.R., and Ehrhardt, D.W. (2006) *Science*, **312**, 1491–1495.
37. Emons, A.M., Höfte, H., and Mulder, B.M. (2007) *Trends Plant Sci.*, **12**, 279–281.
38. Lloyd, C. and Chan, J. (2008) *Curr. Opin. Plant Biol.*, **11**, 641–646.
39. Kovalenko, V.I. (2010) *Russ. Chem. Rev.*, **79** (3), 231–241.
40. Moon, R.J., Martini, A., Nairn, J., Simonsen, J., and Youngblood, J. (2011) *Chem. Soc. Rev.*, **40**, 3941–3994.
41. Cosgrove, D.J. (2005) *Nat. Rev.*, **6**, 850–861.
42. Salmen, L. and Fahlen, J. (2006) *Cellul. Chem. Technol.*, **40**, 181–185.
43. Reiterer, A., Lichtenegger, H., Tschegg, S., and Fratzl, P. (1999) *Philos. Mag.*, **79**, 2173–2184.
44. Burgert, I., Keckes, J., Frühmann, K., Fratzl, P., and Tschegg, S.E. (2002) *Plant Biol.*, **4**, 9–12.
45. Groom, L., Mott, L., and Shaler, S. (2002) *Wood Fiber Sci.*, **34**, 14–27.
46. Cleland, R. (1971) *Annu. Rev. Plant Physiol.*, **22**, 197–222.
47. Taiz, L. (1984) *Annu. Rev. Plant Physiol. Plant Mol. Biol.*, **35**, 585–657.
48. Veytsman, B.A. and Cosgrove, D.J. (1998) *Biophys. J.*, **75** (5), 2240–2250.
49. Skaar, C. (1988) *Wood-Water Relations*, Springer-Verlag, New York, p. 283.
50. Christensen, G.N. and Kelsey, K.E. (1959) *Holz Roh Werkst.*, **17**, 189–203.
51. Wallenberger, F.T. and Weston, N.E. (2003) *Natural Fibers, Plastics and Composites*, 1st edn, Springer, London.

52. Avramidis, S. (1997) The basics of sorption. International Conference of COST Action E8, Mechanical Performance of Wood and Wood Products, Theme: Wood-Water Relations, Copenhagen, Denmark, 1997.
53. Rouquerol, F., Rouquerol, J., and Sing, K. (1999) *Adsorption by Powders and Porous Solids Principles, Methodology and Applications*, Academic Press, London.
54. Berthold, J., Rinaudo, M., and Salmén, L. (1996) *Colloids Surf., A*, **112**, 117–129.
55. Newsome, P.T. and Sheppard, S.E. (1930) The Kodak Research Laboratories. 1930, Communication No. 392, p. 483.
56. Banik, G. and Bruckle, I. (2010) *J. Restaurator*, **31**, 164–177.
57. Kimura, M., Hatakeyama, T., and Nakano, J. (1974) *J. Appl. Polym. Sci.*, **18**, 3069–3076.
58. Englund, E.T., Thygesen, L.G., Svensson, S.H., and Callum, A. (2013) *Wood Sci. Technol.*, **47**, 141–161.
59. Thygesen, L., Englund, E.T., and Hoffmeyer, P. (2010) *Holzforschung*, **64**, 315–323.
60. Englund, E., and Thygesen, L.H.P. (2010) *Holzforschung*, **64** (3), 325–330.
61. Mantanis, G.I., Young, R.A., and Rowell, R.M. (1994) *Wood Sci. Technol.*, **28**, 119–134.
62. Baskin, T.I. (2005) *Annu. Rev. Cell Dev. Biol.*, **21**, 203–222.
63. Burgert, I. and Fratzl, P. (2006) in *Plant Cellmonogr (5) The Expanding Cell* (eds J.P. Verbelen and K. Vissenberg), Springer-Verlag, Berlin, Heidelberg, pp. 191–215.
64. Kohler, L. and Spatz, H.C. (2002) *Planta*, **215** (1), 33–40.
65. Fry, S.C., Smith, R.C., Renwick, K.F., Martin, D.J., Hodge, S.K., and Matthews, K.J. (1992) *Biochem. J.*, **282**, 821–828.
66. Cosgrove, D.J. (2000) *Nature*, **407**, 321–326.
67. Schopfer, P. (2001) *Plant J.*, **28** (6), 679–688.
68. Lockhart, J.A. (1965) *J. Theor. Biol.*, **8** (2), 264–275.
69. Firn, R.D. and Myers, A.B. (1989) *Environ. Exp. Bot.*, **29** (1), 47–55.
70. Morillon, R., Lienard, D., Chrispeels, M.J., and Lassalles, J.P. (2001) *Plant Physiol.*, **127** (3), 720–723.
71. Iino, M., Long, C., and Wang, X.J. (2001) *Plant Cell Physiol.*, **42** (11), 1219–1227.
72. Campbell, N.A. and Thomson, W.W. (1977) *Ann. Bot.*, **41**, 1361–1362.
73. Samejima, M. and Sibaoka, T. (1980) *Plant Cell Physiol.*, **21** (3), 467–479.
74. Haupt, W. (1977) *Bewegungsphysiologie der Pflanzen*, Thieme Verlag, Stuttgart, p. 406.
75. Fagerberg, W.R. and Allain, D. (1991) *Am. J. Bot.*, **78**, 647–657.
76. Hill, B.S. and Findlay, G.P. (1981) *Q. Rev. Biophys.*, **14** (2), 173–222.
77. Roelfsema, M.R.G. and Hedrich, R. (2005) *New Phytol.*, **167**, 665–691.
78. Cutler, D.F., Botha, T., and Stevenson, D.W. (2007) *Plant Anatomy An Applied Approach*, Blackwell Publishing Ltd, Oxford.
79. Rudall, P.J. (2007) *Anatomy of Flowering Plants*, Cambridge University Press, New York.
80. Hetherington, A.M. and Woodward, F.I. (2003) *Nature*, 901–908.
81. Fischer, R.A. (1968) *Science*, **160**, 784–785.
82. Sharpe, P.J.H., Wu, H.-I., and Spence, R.D. (1987) in *Stomatal Function* (eds E. Zeiger, G.D. Farquhar, and I.R. Cowan), Stanford University Press, Stanford, CA, Honolulu, HI, ILLUS, pp. 91–114.
83. Franks, P.J. (2001) *Tree Physiol.*, **24**, 865–878.
84. Stuhlman, O. and Darden, E. (1950) *Science*, **111**, 491–492.
85. Williams, S.E. and Bennet, A.B. (1982) *Science*, **218**, 1120–1121.
86. Fagerberg, W.R. and Howe, D.G. (1996) *Am. J. Bot.*, **83**, 836–842.
87. Brown, W.H. (1916) *Am. J. Bot.*, **3**, 68–90.
88. Fratzl, P. and Barth, F.G. (2009) *Nature*, **462**, 442–448.
89. Burgert, I. and Fratzl, P. (2009) *Integr. Comp. Biol.*, **49** (1), 69–79.
90. Fratzl, P., Elbaum, R., and Burgert, I. (2008) *Faraday Discuss.*, **139**, 275–282.

91. Timoshenko, S. (1925) *J. Opt. Soc. Am. Rev. Sci. Instrum.*, **3**, 233–255.
92. Chen, Z., Majidi, D., Srolovitz, D.J., and Haataja, M. (2011) *Appl. Phys. Lett.*, **98**, 011906.
93. Forterre, Y. and Dumais, J. (2011) *Science*, **333** (6050), 1715–1716.
94. Abraham, Y., Tamburu, C., Kelvin, E., Dunlop, J.W., Fratzl, P., Raviv, U., and Elbaum, R. (2011) *J. R. Soc. Interface*, **9** (69), 640–647.
95. Daniel, G., Filonova, L., Kallas, A.M., and Teeri, T.T. (2006) *Holzforschung*, **60** (6), 618–624.
96. Müller, M., Burghammer, M., and Sugiyama, J. (2006) *Holzforschung*, **60**, 474–479.
97. Côte, W.A. Jr., and Day, A.C. (1965) in *Cellular Ultrastructure of Woody Plants* (ed. W.A. Coté), Syracuse University Press, Syracuse, NY, pp. 391–418.
98. Clair, B., Ruelle, J., and Thibaut, B. (2003) *Holzforschung*, **57**, 189–195.
99. Burgert, I. and Fratzl, P. (2010) *Integr. Comp. Biol.*, **50** (1), E20.
100. Mellerowicz, E.J., Immerzeel, P., and Hayashi, T. (2008) *Ann. Bot.*, **102**, 659–665.
101. Qiu, D., Wilson, I.W., Gan, S., Washusen, R., Moran, G.F., and Southerton, S.G. (2008) *New Phytol.*, **179**, 94–103.
102. Clair, B., Gril, J., Baba, K., Thibaut, T., and Sugiyama, J. (2005) *IAWA J.*, **26**, 189–196.
103. Clair, B., Alméras, T., Pilate, G., Jullien, D., Sugiyama, J., and Riekkel, C. (2011) *Plant Physiol.*, **155**, 562–570.
104. Clair, B., Gril, J., Di Renzo, F., Yamamoto, H., and Quignard, F. (2008) *Biomacromolecules*, **9**, 494–498.
105. Mellerowicz, E. and Gorchkova, T.A. (2012) *J. Exp. Bot.*, **63**, 551–565.
106. Clair, B., Ruelle, J., Beauchene, J., Prevost, M.F., and Fournier, M. (2006) *IAWA J.*, **27** (3), 329–338.
107. Stroeve, V. (1892) *Ueber die Verbreitung der Wurzelverkürzung*, Universität Jena, Jena.
108. Rimbach, A. (1927) *Ber. Dtsch. Bot. Ges.*, **45**, 127–130.
109. Rimbach, A. (1929) *Ber. Dtsch. Bot. Ges.*, **47**, 22–31.
110. Pütz, N. and Sukkau, I. (2002) *Flora*, **197**, 385–393.
111. Schreiber, N., Gierlinger, N., Putz, N., Fratzl, P., Neinhuis, C., and Burgert, I. (2010) *Plant J.*, **61**, 854–861.
112. Harrington, M.J., Razghandi, K., Ditsch, F., Guiducci, L., Ruggeberg, M., Dunlop, J.W., Fratzl, P., Neinhuis, C., and Burgert, I. (2011) *Nat. Commun.*, **2**, 337.
113. Garside, S. and Lockyer, S. (1930) *Ann. Bot.*, **44**, 639–655.
114. Razghandi, K., Bertinetti, L., Guiducci, L., Dunlop, J.W.C., Fratzl, P., Neinhuis, C., and Burgert, I. (2014) *Bioinspired, Biomimetic Nanobiomater.*, **3**, 1–14.
115. Hansen, C.M. (1916) *Ind. Eng. Chem. Prod. Res. Dev.*, **8** (1), 2–11.
116. Barton, A.F.M. (1990) *Handbook of Polymer-Liquid Interaction Parameters and Solubility Parameters*, CRC Press, Boca Raton, FL.
117. Shahinpoor, M. and Thompson, M.S. (1995) *Mater. Sci. Eng.*, **C2**, 229–233.
118. Taya, M., Almajid, A.A., Dunn, M., and Takahashi, H. (2003) *Sens. Actuators, A-Phys.*, **107** (3), 248–260.
119. Matthews, L., Giurgiutiu, V., Sundaresan, V.B., and Leo, D. (2006) *J. Mater. Res.*, **21** (8), N8.
120. Reyssat, E. and Mahadevan, L. (2009) *J. R. Soc. Interface*.
121. Turcaud, S., Guiducci, L., Fratzl, P., Brechet, Y.J.M., and Dunlop, J.W.C. (2011) *Int. J. Mater. Res.*, **102** (6), 607–612.



## Index

### **a**

- adsorption-induced strain
  - adsorbate–adsorbent couple 33
  - hysteresis loop 33–34
  - MCM-41 and SBA-15 silicas 33
- Aizoaceae (ice plants) 192
- anisotropic deformation 181

### **b**

- bilayered structures
  - bending 185–187
  - twisting 187–189
- biomimetic model 195–197
- Biot coefficient 109

### **c**

- carbon dioxide injection
  - axisymmetric 122–123
  - cleats 115, 123
  - coal matrix thermodynamic equilibrium, 123
  - fractured coal 116
  - intrinsic permeability 123
  - Kozeny–Carman relation 123
  - mass balance equations 122
  - methane recovery process 116
  - methane-free coal seam, finite-element simulations 124
  - permeability 123
  - pressures 115
- carnivorous Venus flytrap 182
- cavitation
  - Cohan's model 47
  - duplex porous layer 51
  - elemental isotherms 47–48
  - evaporation process 47
  - heterogeneous nucleation and elastic strain 52–55
  - homogeneous nucleation 51–52
  - ink-bottle geometry 47
  - nitrogen adsorption isotherm 48
  - pore-blocking/percolation mechanism 47
  - Si/A/B and Si/B/A configuration 49–51
- CBM. *see* coal bed methane (CBM) production
- CED. *see* cohesive energy density (CED)
- cell walls
  - actuation patterns 187
  - anisotropic swelling 184
  - bilayered structure, twisting 189
  - contractile roots 191–192
  - curvature of bilayer 185
  - elastic deformation. *see* elastic deformation
  - Erodium awns 189
  - force and torque 186
  - hydro-actuation in pine cones 186
  - ice plant seed capsule. *see* ice plant seed capsule
  - plastic deformation 182
  - radial distribution, shear strains 188
  - tension wood fibers 189–191
  - wheat awns hydro-actuated swimming movement 186–188
- cell wall–water interactions
  - adsorption stages 180
  - “free water” 180
  - “freezing bound water” 180
  - “non-freezing bound water” 180
  - swelling/shrinkage, wood 180–181
  - typical sorption isotherm, wood 179
- cellular solid
  - empty pore space 60
  - geometry 61
  - hexagonal. *see* hexagonal cellular solid
  - honeycomb. *see* honeycomb cellular solid
  - ice plant 61–62



cellular solid (*contd.*)

- numerical tests, elastic properties 62–63
- wood 61–62

## cellulose-rich inner layer (CIL) 194

## chemical potential

- molar chemical potential 111
- protocol 68, 70, 72

## closure models

- fluid-field and solid-field stresses 138–139
- governing equations 135
- material stress gradients 136–137
- momentum exchange 137–138
- Reynold's stress and body forces 136
- solid matrix constitutive models 139

## coal bed methane (CBM) production 115

## coal seams

- CO<sub>2</sub> injection. *see* carbon dioxide injection
- coal bed methane (CBM) production 115
- CO<sub>2</sub>-ECBM 115–116
- ECBM applications 115–116
- fractured coal 116
- hysteresis source 119–122
- representative elementary volume, modeling 116–117
- volumetric strain 115

CO<sub>2</sub>-enhanced coal bed methane recovery (CO<sub>2</sub>-ECBM) 115

## Cohan's model 28, 47

## cohesive energy density (CED)

- definition 194
- ice plant keel 195

## contractile roots 191–192

## coupling

- macroscopic damage and damage-dependent PM model 93–94
- porous materials. *see* fluid–solid coupling, porous materials

**e**

## elastic deformation

- carnivorous Venus flytrap 182
- light-induced/Circadian movements 182
- stomatal movement 183
- turgor-based rapid movement 184–185

## elastic strain 52–55

## elemental isotherms 47–48

## Erodium awns curling 189

## evaporation

- porous silicon 30–31
- porous Vycor glass 28–29
- SBA-15 silica 31–33

**f**

## fluid–solid coupling, porous materials

- ice plant 61–62
- mechanical response, applied external forces 63–66
- pore space 73–76
- quantities of interest 62–63
- skeleton 66–73
- systems and models 57–60
- wood 61

## Fontainebleau sandstone

- description 1
- longitudinal vibration modes 16
- temperature control 21–22
- thin section 1–2

**g**

## gelatinous layer (G-layer) 190–191

## generic (and potentially microporous) media

- deviatoric behaviors 110
- Gibbs–Duhem relation 111
- isotropy 110
- pore fluid, molar chemical potential 111
- tangent Biot coefficient 111–112
- thermodynamic pressure 111

**h**

## Hertz–Mindlin model 4

## heterogeneous nucleation 52–55

## hexagonal cellular solid

- extension ratio 65–66
- swelling ratio 67

## HF/EtOH solution 47

## high-pressure preferred orientation (HIPPO)

neutron diffraction measurements. *see* neutron diffraction measurements

- sample holder and can 13
- sample with thermocouple junctions and piezoelectric disks 12

## homogeneous nucleation 51–52

## honeycomb cellular solid

- anisotropy 61–62
- extension ratio 65–67
- fluid response 69–71, 74–78
- frame 57–58
- geometry 61, 64
- isotropic 62
- swelling ratio 66–67

## honeycombs

- anisotropy, swelling behavior 165
- geometrical features 161, 162
- layered cell wall 163–165
- micromechanics 162

- moisture-induced swelling 162
- second-order strain and stress tensors 162
- shape angle 165
- swelling coefficients 165–167
- wood geometry analysis 161
- Hook's law 173
- hydro-actuated plants
  - anisotropic deformation 181
  - biomimetic potential 195, 197
  - cell walls. *see* cell walls
  - cell wall–water interactions. *see* cell wall–water interactions
  - and fungal movements 172
  - movement 171
  - physiochemistry and mechanics 173
  - plant cell walls 177–179
  - plant–water interactions 171
  - snap-buckling movements 171–172
  - stress and strain 173–174
  - swelling/shrinking movements 172–173
  - water. *see* water

## i

- ice plant seed capsule
  - CIL 192
  - hierarchical morphology 192–193
  - hydroresponsive unfolding 193–194
  - plant movement actuator 194–195
  - swelling/shrinkage 192–193
- inflation, water engine 174–176
- ink-bottle geometry 47, 49–50

## l

- Lagrangian frame 141
- Los Alamos Neutron Science Center (LANSCE) 8

## m

- macroporous media
  - Biot coefficient 109
  - Gibbs–Duhem relation 108
  - Lagrangian porosity 108
  - linear poroelasticity 109
  - micromechanical relations 109
- macroscopic damage model
  - coupling 93–94
  - damage loading function 87
  - damage variable 85–86
  - loading conditions 87
  - pre-peak regime 87
  - stress–strain curve 85–86
  - uniaxial scalar formulation 85

- macroscopic measurements
  - Hertz–Mindlin model 4
  - humidity measurements, hysteresis 5–6
  - hysteretic macroscopic strain 3
  - Preisach–Mayergoyz (PM) model 4
  - rate effects 4
  - rock grain skeleton 4
  - slow dynamics 6–7
  - stress–strain hysteresis 4–5
  - temperature vs. modulus/sound speed 4
- MCM-41 28

## mechanical testing

- extension ratio 63–64
- swelling ratio 64
- mesoporous materials
  - adsorption-induced strain 29–34
  - cavitation. *see* cavitation
  - Cohan's model 28
  - deformation 27
  - evaporation. *see* evaporation
  - external stress 45–47
  - hysteresis loop 27–28
  - MCM-41 and SBA-15 28
  - porous Si layers 43
  - stress and strain effects 27

## mesoporous media

- Gibbs adsorption isotherm 113
- grand potential 112
- isotropic linear elastic mesoporous medium 114
- pore volume 112
- Shuttleworth equation 113
- surface tension 113

## microfibril angle (MFA)

- anisotropic swelling 184
- description 177–178
- tensile stress generation 191

## moisture dependence

- damage and PM model 99–102
- disjoining pressure 95
- fluid–solid interactions 95–96
- mechanical experiments 96–98
- porous media classification 94
- multifield equations 134–135

## n

- neutron de Broglie wavelength 8
- neutron diffraction measurements
  - average temperature and frequency 19, 21–22
  - elastic behavior, sandstone 12
  - Fontainebleau sandstone 13–14
  - HIPPO. *see* high-pressure preferred orientation (HIPPO)

- neutron diffraction measurements (*contd.*)
  - hysteresis loop 19–20
  - longitudinal vibration modes, Fontainebleau sample 16
  - neutron scattering data 17
  - nonporous sample (steel) 20–21
  - Pochhammer modes 16
  - PZT-5A material 14
  - quality factor  $Q$  18
  - sample cell 14–15
  - stress–strain 9–12
- neutron scattering measurements
  - crystalline structure 7–8
  - elastic/macroscopic 7
  - grains and bonds, rock surface 7
  - HIPPO 8–9
  - *in situ* uniaxial loading 8
  - LANSCE 8
  - magnetic hysteresis 7
  - neutron de Broglie wavelength 8
  - ordered and disordered materials 7
  - powder diffraction 8
  - SMARTS 8
  - X-ray diffraction techniques 7
- nitrogen adsorption isotherm 48
- nonlinear, hysteretic and damage behavior of
  - quasi-brittle materials
    - continuum modeling 84
    - cyclic loading 81
    - load-deformation behavior 81–83
    - oolitic limestone, cracking pattern 81–82
    - PM model 84–85
    - quasistatic compressive tests 84
    - stiffness reduction and recovery 82
    - strain-softening curve 82–83
    - nonlinear hysteretic elastic behavior. *see* Preisach–Mayergoyz (PM) model
- p**
- PDSC. *see* primary descending scanning curve (PDSC)
- Peltier stage 21–22
- phase contrast synchrotron X-ray tomographic microscopy (PCXTM) 157–158
  - column translation vector 158
  - confocal scanning laser microscopy 157
  - controlled relative humidity (RH) 157–158
  - 3D affine transformation 158
  - geometry and alignment 161
  - homogeneous tissues behavior 158
  - modified Bronnikov algorithm (MBA) 158
  - porosity, adsorption and desorption ratios 160
  - sorption process, reversibility 159
  - strain vs. relative humidity (RH) 159
  - strain–moisture content curves 160
  - swelling anisotropy 161
  - tangential to radial strain, ratios 160
- Piezoelectric disks (PZT-5A) material 14
- pine cones 186
- plant cell walls 177–179
- plant material–water interactions
  - strain 173–174
  - stress 173–174
- plastic deformation 182
- PM. *see* Preisach–Mayergoyz (PM) model
- Pochhammer modes 16
- pore size distribution (PSD)
  - nitrogen adsorption isotherm 48
  - TEM plane views 47
- pore space, solid structural features
  - description 57
  - fluid in 73–76
- porous and cellular materials
  - aperture size, piston force 143–144
  - articular cartilage, aperture size 147–148
  - cartilage response, loading rate 148
  - cellular solid stress wave 142
  - compression response 144
  - continuum-scale mechanical response 149
  - dynamic compression, thin sheet 140
  - engineering applications 127
  - equations governing 131
  - finite-strain uniaxial compression 139–140
  - finite-volume technique 131
  - fluid pressure and flow 127
  - force-compression curves 147
  - interstitial fluids 127
  - Lagrangian frame 141
  - mechanical response 149
  - multifield equations and systems 132–135
  - multifield theory 130–131
  - natural/synthetic material 131–132
  - physical mechanisms and material response 130
  - piston force, loading rate 144–145
  - piston velocity 146–147
  - scanning electron micrograph 140
  - silicone foam 141–143
  - single-field equations and averaging 133–134
  - traditional modeling approaches 128–130

- uniaxial compression 141
- viscoelastic properties 149
- porous sedimentary rocks
  - acoustic field 23
  - cementation 2
  - diagenesis 1
  - Fontainebleau sandstone 1–2
  - grains 2
  - macroscopic measurements. *see* macroscopic measurements
  - neutron diffraction measurements. *see* neutron diffraction measurements
  - neutron scattering measurements. *see* neutron scattering measurements
  - oil and gas extractions 1
  - Peltier stage 21–22
  - petrographic techniques 2
  - pore space 2
  - sandstone 1
  - thermal expansion coefficients, quartz 23
  - vibration 3
- porous Si layers 43–45
- porous solids, poromechanical modeling
  - adsorption 105
  - coal seams. *see* coal seams
  - mercury intrusion porosimetry 2
  - pores, subcategories 105
  - saturated porous media. *see* saturated porous media
- porous Vycor glass 28–29
- Preisach–Mayergoyz (PM) model
  - compliance 89
  - cyclic tensile loading 91
  - high damage levels 93
  - inelastic strain 90
  - magnetic domains 4
  - non-classical units (NCUs) 88–89
  - parameters 92
  - residual strength 90
  - reversible nonhysteretic NCUs 88
  - tensile and tensile-compressive hysteretic loops 90–91
- primary descending scanning curve (PDSC)
  - nitrogen adsorption isotherm 27–31
  - pore-blocking/percolation model 32–33
  - Xenon adsorption isotherm 29
- PSD. *see* pore size distribution (PSD)

## q

- quasi-brittle materials
  - concrete 84
  - crack bridging phenomenon 81

- description 81
- macroscopic damage model 85–88
- moisture dependence. *see* moisture dependence
- nonlinear, hysteretic and damage behavior 81–85

## r

- representative elementary volume, coal seams
  - characteristic size 117
  - cleats 117
  - definition 116
  - first-order expansion 118
  - fluid, adsorbed amount 118
  - poromechanical behavior 119
  - scales 117
  - state variables, coal matrix 118
  - thermodynamic equilibrium 117

## s

- saturated porous media
  - generic (and potentially microporous) media 110–112
  - grand potential 108
  - macroporous media 108–109
  - mesoporous media 112–114
  - rock mechanics, triaxial cell 108
  - thermodynamics 107
- SBA-15 silica 31–33
- shear strains 173
- Si/A/B and Si/B/A configuration 49–51
- skeleton, solid structural features
  - description 57
  - fluid 59, 66–73
- slow dynamics 6
- SMARTS. *see* Spectrometer for Materials Research at Temperature and Stress (SMARTS)
- snap-buckling movements 171–172
- solid–fluid interface
  - 2D strains 35
  - displacement component 36
  - elastic and thermodynamics properties 34
  - elastic energy, infinitesimal deformations 36
  - homogeneous phases 35
  - interfacial excess 35
  - interfacial free energy 37
  - strain and stress tensor elements 35
  - tangential trains 35
- solid–liquid interface 40–43
- solid–solid interface 36
- solid–vapor interface 37–40

Spectrometer for Materials Research at  
Temperature and Stress (SMARTS)  
– neutron diffraction measurements. *see*  
neutron diffraction measurements  
– polycrystalline materials 8  
spreading pressure 33, 38  
stomatal movement 183  
swelling  
– adjacent cell walls, geometrical interactions  
153  
– adsorbed moisture displacement  
153  
– description 154–155  
– honeycombs, parametric investigation. *see*  
honeycombs  
– investigation. *see* phase contrast synchrotron  
X-ray tomographic microscopy  
– moisture adsorption 153, 155–156,  
168–169  
– moisture-induced shape memory  
167–168  
– sorption hysteresis, relative humidity (RH)  
168  
swelling/shrinkage, ice plant seed capsule  
192–193

## t

tension wood fibers 189–191  
time-of-flight (TOF)  
– diffractometers 8  
– neutron 10, 23  
*Trifolium pratense* 191–192  
turgor pressure 182

## v

Venus flytrap 184–185  
volumetric confining stress 108

## w

water  
– hydrogen bonds 174  
– inflation 174–176  
– stresses/movements in plants 174  
– swelling 176–177  
– uptake. *see* cell walls  
wheat awns 186–187  
wood  
– cellulose microfibrils 154  
– closed-loop RH protocol 156  
– hemicelluloses 155  
– hygroexpansivity 156  
– interfibril distance 155  
– macroscopic swelling and shrinkage strains  
155  
– middle lamella (ML) 155  
– multilayer fiber-reinforced composite 155  
– polymerization 154  
– softwood 155  
– strain hysteresis 156  
– swelling. *see* swelling  
– swelling/shrinkage 180–181

## x

Xenon adsorption isotherm 29

## y

Young modulus 173–174